A Novel UV Laser System for Electric Field Calibration in Liquid Argon Time Projection Chambers

Inauguraldissertation
der Philosophisch-naturwissenschaftlichen Fakultät
der Universität Bern

vorgelegt von

Matthias Lüthi

von Rüderswil

Leiter der Arbeit
Prof. Dr. Igor Kreslo
Prof. Dr. Michele Weber

Albert Einstein Centre for Fundamental Physics
Laboratory for High Energy Physics
Physics Institute

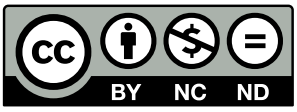

A Novel UV Laser System for Electric Field Calibration in Liquid Argon Time Projection Chambers

Inauguraldissertation
der Philosophisch-naturwissenschaftlichen Fakultät
der Universität Bern

vorgelegt von

Matthias Lüthi

von Rüderswil

Leiter der Arbeit
Prof. Dr. Igor Kreslo
Prof. Dr. Michele Weber

Albert Einstein Centre for Fundamental Physics
Laboratory for High Energy Physics
Physics Institute

Von der Philosophisch-naturwissenschaftlichen Fakultät angenommen.

Bern, 17.Januar 2019

Der Dekan:
Prof. Dr. Z. Balogh

ABSTRACT

At the core of any time projection chamber lies the electric field. The field is responsible for the separation of electron-ion pairs created during charged particle interactions as well as their transport to the readout plane. Any non-uniformity in the electric field causes distortions to a drifted ionization track, impacting the detectors spatial resolution and calorimetric capabilities. Both the spatial and calorimetric capabilities are central to the time projection chamber and provide their key advantage over other detector technologies The effect is particularly prominent in large scale liquid argon time projection chambers used for precision neutrino experiments. Sampling the detector with intrinsically straight ultraviolet laser beams while recording the distorted ionization signal provides a probe of the electric field. In this thesis the necessary hard- and software of such an ultraviolet laser system used to characterize the electric field in a liquid argon time projection chamber is outlined. Furthermore, the deployed methods to recover a spatial distortion and electric field map are described and verified against simulations. In case of the MicroBooNE detector, a map of the spatial distortion was obtained and a maximal spatial distortion of $20 \pm 4\,\mathrm{cm}$ has been observed. Furthermore, the electric field has been reconstructed within the coverage limits of the laser system, a maximal distortion from the nominal field of $15 \pm 4\,\%$ has been measured. The temporal distortion variation of the spatial distortion in drift direction has been observed to be $2.2 \pm 0.3\,\mathrm{mm}$ over two hours. Correlations between neighboring wires suggest that these features extend up to $20\,\mathrm{cm}$.

CONTENTS

LIST OF FIGURES

LIST OF TABLES

TPC Time Projection Chamber

LAr Liquid Argon

LArTPC Liquid Argon Time Projection Chamber

LArTF Liquid Argon Test Facility

BNB Booster Neutrino Beam

LEE Low Energy Excess

PMT Photomultiplier Tube

UV Ultra Violet

DAQ Data Acquisition

ADC Analog Digital Converter

AOI Angle of Incidence

NIM Nuclear Instrumentation Standard

TTL Transistor-Transistor Logic

AC Alternating Current

DC Direct Current

HV High Voltage

UPS Uninterruptible Power Supply

NTP Network Time Protocol

UDP User Datagram Protocol

1 INTRODUCTION

Time Projection Chambers have become an indispensable tool in particle physics. With this type of detector it is possible to obtain precise three-dimensional trajectories and calorimetric information in the same instrument, allowing for precision particle identification. Moving from the inert gaseous low-density target media towards high density media, such as liquid argon, greatly increases particle interaction probabilities. Yet, for the notoriously low cross-section of the neutrino, a massive multi-tonne-scale detector is necessary to boost the interaction rate to an acceptable level. Paired with a high flux neutrino beam, produced by a particle accelerator, liquid argon time projection chambers are a state-of-the-art technology to probe the nature of the neutrino.

Neutrinos were proposed more than 80 years ago, it took 30 years until they were first detected. In the remaining 50 years, improvements in all aspects of detector technology has slowly enabled to probe the nature of the neutrino in more detail. Together with advances in other fields of physics, this has brought fascinating insights into the fundamental forces of nature, but has also risen new questions. Among these are the origin of the observed matter and anti-matter asymmetry, the nature of the neutrino mass (Dirac or Majorana) and the neutrino mass hierarchy. Answers to these questions have come within reach with the progression of neutrino detectors to precision experiments, such as DUNE, a massive liquid argon time projection chamber. This technology will provide the required precision not only to answer questions in the neutrino sector, but also in the astroparticle sector, i.e proton decay and supernovae observations. Until today neutrino oscillation searches have determined three mixing angles and two mass splittings with a high confidence, meanwhile LSND and MiniBooNE have recorded signals incompatible with these measurements. Both experiments observed an excess of low energetic neutrino signals, but were unable to determine its origin. As a successor of the two experiments, MicroBooNE's primary objective is to investigate this anomaly using a liquid argon time projection chamber in the Booster Neutrino Beam at Fermilab. While MicroBooNE has a strong physics objective in itself, technologies deployed and know-how gained during its entire lifetime will greatly influence the design of DUNE.

Using large quantities of liquid argon as a dense target material to perform precision measurements poses several challenges. Among these are the cryogenic operation, low signal amplification and argon purity considerations. In addition to these challenges, the most crucial parameter to control in a time projection chamber is the electric field. The electric field is responsible for the separation of electrons from ions, preserving the ionization track. The electric field governs the speed at and path trough which this cloud of ionization electrons drifts towards to the readout plane. Hence, the electric field ultimately defines the spatial resolution and calorimetric precision of the detector. Many factors influence the electric field,

for example the detector geometry or the electric potentials applied to establish it. But the main contribution to field inhomogeneities, for a detector located on the earth's surface, is the accumulation of positive charge produced by the constant penetration by cosmic radiation. These minimum ionizing particles create a constant source of positive argon ions. Opposite to the fast electrons ($v_d = 1\,\mu\mathrm{m\,s^{-1}}$), these drift along the field at speeds of the order of $1\,\mathrm{mm\,s^{-1}}$, thus remaining in the detector for minutes before neutralization at the cathode. In this way space charge builds up and severely impacts the nominal electric field, affecting the fiducial volume as well as tracking and calorimetric capabilities of the detector.

Therefore, accurate knowledge of the spatial and electric field distortion is necessary to characterize a liquid argon time projection chamber used as a high precision instrument. Ionization tracks introduced by an ultraviolet laser with a well-defined straight trajectory can be used to recover this information. A distortion map can be obtained by sampling the detector volume with such tracks and calculating the residuals compared to the expectations. An electric field map can subsequently be derived from this distortion map. Within this thesis all the necessary hardware and software developed to steer an ultra violet laser beam into the active volume of a liquid argon time projection chamber are presented. Furthermore, the commissioning, operation and initial calibration of the system are discussed. This concludes the first ever deployment of a laser calibration system on a liquid argon time projection chamber. Finally, the methodology for the derivation of the distortion and electric field maps are presented and validated against a full detector simulation. The magnitude of the variation in time of the electric field is investigated.

2

NEUTRINOS AND NEUTRINO OSCILLATION

2.1 BRIEF HISTORY OF NEUTRINOS

After Pauli postulated the neutrino to fulfill conservation of energy and angular momentum in β-decays in 1930 [1], almost 25 years passed until Cowan and Reines provided experimental proof [2] for the existence of neutrinos. Since then many other experiments were conducted to investigate neutrino properties, but still open questions exist. In 1968 strong evidence was found for neutrino flavor oscillation when R. Davis Jr and collaborator attempted to detect neutrinos produced in thermonuclear reaction in the solar core [3, 4]. Later the oscillation model was confirmed with measurements of the angular distribution of neutrinos induced by cosmic rays penetrating the upper atmosphere [5, 6]. The picture was completed by the exposure of detectors to man-made neutrinos (accelerators and reactors) [7, 8, 9, 10, 11]. All this experimental evidence leads to the conclusion that neutrinos are massive particles, however oscillation experiments are unable to provide information about the absolute masses. Experiments carefully measuring kinematics of the β-decay have so far set upper limits to absolute neutrino masses [12, 13]. Observations of the cosmic microwave background constrain the sum of the neutrino masses [14].

2.2 NEUTRINOS IN THE STANDARD MODEL

The standard model is a physical description of the interactions between elementary particles. The elementary particles are divided in three generations. The electron, the electron neutrino and the up- and down quarks (e, ν_e, u, d) together are called the first generation. Placed in the second generation are the muon, the muon neutrino, the charm and strange quarks (μ, ν_μ, c, s). The third generation contains the tau, the tau neutrino and the bottom and top quarks (τ, ν_τ, b, t). Within the standard model framework, three interactions between these particles exist: the electromagnetic, strong and weak force. Each force is mediated by one or more force carrier particles, the photon (γ) mediates charge in electromagnetic interactions, gluons (g) mediated so called color in strong interactions and intermediate vector bosons mediate the weak charge $(W^{\pm}, Z)$ for the weak interaction. There are electrically charged and neutral particles, and in the same fashion there are colored and colorless particles, but all particles carry weak charge. The elementary particles can be divided into the spin-1/2 group called leptons and the spin-1 group called bosons. All mediators of forces are bosons, whereas all particles in the first to the third generation are fermions. Furthermore, the recently discovered Higgs boson is part of the Standard Model, giving mass to all fermions. All particles listed above are shown in Figure 2.1

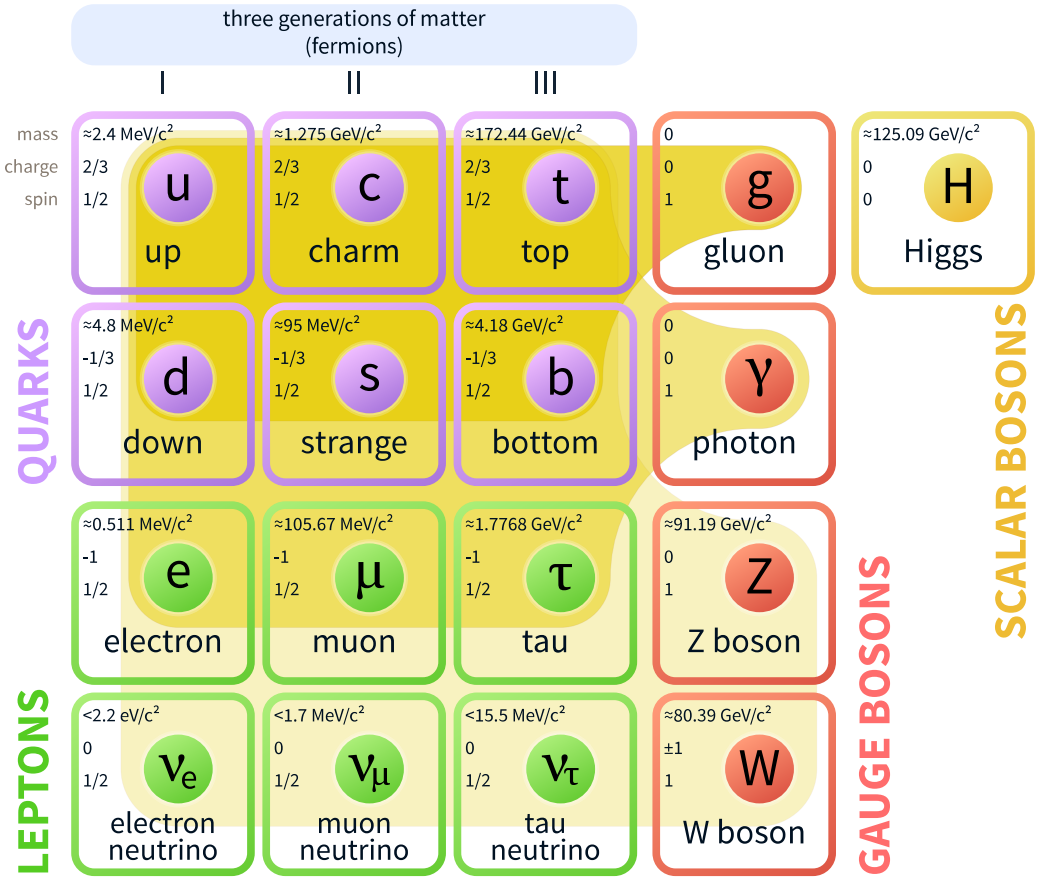

Figure 2.1: Overview of the particles described in the Standard Model, adapted from [15].

Quarks carry color and are electrically charged ($\pm 1/3$ or $\pm 2/3$), hence they are subject to strong, weak and electromagnetic forces. The other two particles in each generation are called leptons and are only subject to interactions via the electromagnetic and weak force, since both of them are colorless. The electrically neutral neutrinos are even more restricted and can only interact trough the weak force. There are two fundamentally different kinds of weak interactions: charged (mediated by $W^{\pm}$) and neutral (mediated by Z). For both interactions the fundamental Feynman graphs are shown in Figure 2.2. Neutral interactions include any lepton or quark, example processes are neutrino electron scattering $e^- + \nu_\mu \rightarrow e^- + \nu_\mu$ and neutrino proton scattering $p + \nu_\mu \rightarrow p + \nu_\mu$. Notice that any process mediated by a photon can also mediated by a Z. Charged interactions are special in the sense that in these the flavour of the incoming and outgoing particle changes, in no other interaction of the standard model this is possible. For example a negative lepton (could be e^-, μ^- or τ^-) is converted to the corresponding neutrino ν_l under the emission of an W^-. As usual the primitive vertex is combined to form more complex interactions, such as the electron or muon neutrino scattering $\nu_\mu + e^- \rightarrow +\nu_\mu + \mu^-$. Since their flavor changing behavior, charged neutral currents represent the only true mode for particle decay, in which neutrinos are produced. An unique behaviour of neutrinos arises from their handedness. A par-

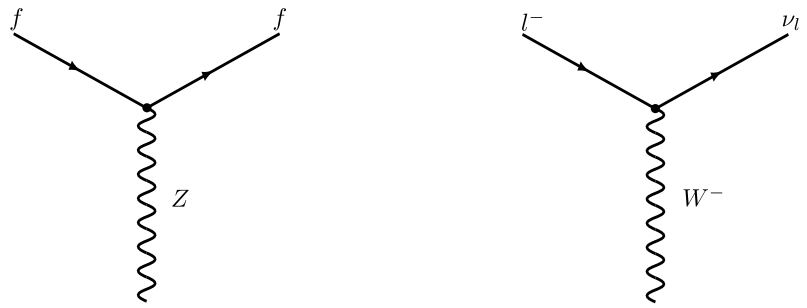

Figure 2.2: Fundamental Feynman graphs for the weak interactions, neutral (right) and charged (left) current. For the neutral interaction f can be any quark or a lepton.

ticle's handedness is related to its helicity, which is the projection of a particles spin (σ) onto its momentum vector ($\vec{p}$). The particle has a positive helicity if this projection is aligned with the momentum vector. Vice versa, if the projection is not aligned with the particles momentum. If a particle is massive the helicity is dependent on the reference frame, an observer can always 'overtake' the particle and so change its helicity. Massless particles however cannot be overtaken since they travel at the speed of light. The handedness of a particle can be determined by applying the chiral projection operators

$$P_R = \frac{1}{2}(1 + \gamma^5), P_L = \frac{1}{2}(1 - \gamma^5). \tag{2.1}$$

Here the Dirac γ-matrices are defined as in [16]. Each particle spinor can be decomposed into right- and left-handed chiral components

$$u = \frac{1}{2}(1 + \gamma^5)u + \frac{1}{2}(1 - \gamma^5)u = P_R u + P_L u \tag{2.2}$$

A unique feature of the charged weak interaction is that only the left-handed particles and right-handed antiparticles are affected by it. Because of this only left-handed neutinos and right-handed antineutrinos can be observed.

2.3 NEUTRINO OSCILLATION

As mentioned in the introductory chapter, neutrino oscillations have been observed, where a neutrino of a certain flavour has a non-zero transition probability into a different flavour after a certain propagation time and distance. This behaviour can not be explained in a minimalistic Standard Model. Only by adding masses to the individual neutrinos the observed behaviour can be reproduced. The following discussion is largely based on [16]. An in-depth review of neutrino oscillations can be found in [17] or [18].

The mass eigenstates, which describe the physical states of particles, are the free-particle Hamiltonian which satisfy,

$$H|\psi\rangle = i\frac{\partial\psi}{\partial t}|\psi\rangle = E|\psi\rangle. \tag{2.3}$$

The time evolution of mass eigenstates is described in a first approximation as a simble plane wave by

$$\psi(\vec{x},t) = \phi(\vec{x})e^{-iEt}. \tag{2.4}$$

Neutrinos are produced in flavour eigenstates but are propagated in space and time in mass eigenstates. There is no physical reason for identity of the mass and flavour eigenstates. This leads to the conclusion that, for example, the electron flavour state is a linear combination of the three mass eigenstates. In quantum mechanics the relation between the different eigenstates can be expressed as a unitary matrix U:

$$\begin{pmatrix}\nu_e\\ \nu_\mu\\ \nu_\tau\end{pmatrix} = \begin{pmatrix}U_{e1} & U_{e2} & U_{e3}\\ U_{\mu1} & U_{\mu2} & U_{\mu3}\\ U_{\tau1} & U_{\tau2} & U_{\tau3}\end{pmatrix}\begin{pmatrix}\nu_1\\ \nu_2\\ \nu_3\end{pmatrix}. \tag{2.5}$$

The flavour eigenstate propagates as a linear superposition of the mass eigenstates until the wave function is collapsed, producing a observable flavour eigenstate. When the masses of ν_1, ν_2 and ν_3 differ, phase differences between the mass eigenstate components of the wavefunction arise. This phenomenon is then leading to neutrino flavour oscillation.

It is instructive to describe the neutrino oscillation in a two neutrino scenario, as it will permit to showcase the underlying mathematical patterns in an easily understandable framework. Hence, we consider only the e and μ flavour eigenstates, correspondingly only two mass eigenstates are necessary. The mass eigenstates propagate in the form of plane waves,

$$\begin{aligned}|\nu_1(t)\rangle &= |\nu_1\rangle e^{\vec{x}\vec{p}-E_1t} = e^{-ip_1x},\\ |\nu_2(t)\rangle &= |\nu_2\rangle e^{\vec{x}\vec{p}-E_2t} = e^{-ip_2x},\end{aligned} \tag{2.6}$$

where $(E_i, \vec{p})$ and $i = 1, 2$ are the respective energy and three-momenta of the ν_i and $p_i x = Et - \vec{p}_i \vec{x}$ is the Lorentz-Invariant phase. In the two flavour case the unitary mixing matrix can be expressed by a single mixing angle ϕ,

$$\begin{pmatrix} \nu_e \\ \nu_\mu \end{pmatrix} = \begin{pmatrix} U_{e1} & U_{e2} \\ U_{\mu 1} & U_{\mu 2} \end{pmatrix} \begin{pmatrix} \nu_1 \\ \nu_2 \end{pmatrix} = \begin{pmatrix} \cos\theta & sin\theta \\ -\sin\theta & \cos\theta \end{pmatrix} \begin{pmatrix} \nu_1 \\ \nu_2 \end{pmatrix}. \tag{2.7}$$

Suppose we start out with an electron neutrino (e.g from a muon decay) at $t = 0$. The wavefunction at this time is the superposition of the two mass eigenstates of the electron.

$$|\psi(\vec{x}, t)\rangle = |\nu_e\rangle = \cos\theta|\nu_1\rangle + \sin\theta|\nu_2\rangle \tag{2.8}$$

The wavefunction at any given time t is therefore given by the superposition of the two mass eigenstates and the propagation description from Equation 2.3,

$$|\psi(\vec{x}, t)\rangle = \cos\theta|\nu_1\rangle e^{-ip_1 x} + \sin\theta|\nu_2\rangle e^{-ip_2 x} \tag{2.9}$$

If the neutrino interacts at time T and distance L, the phases can be expressed as

$$\phi_i = p_i x = E_i T - p_i L. \tag{2.10}$$

hence,

$$|\psi(L, T)\rangle = \cos\theta|\nu_1\rangle e^{-i\phi_1} + \sin\theta|\nu_2\rangle e^{-i\phi_2} \tag{2.11}$$

Inverting Equation 2.7 yields,

$$\begin{pmatrix} \nu_1 \\ \nu_2 \end{pmatrix} = \begin{pmatrix} \cos\theta & -\sin\theta \\ \sin\theta & \cos\theta \end{pmatrix} \begin{pmatrix} \nu_e \\ \nu_\mu \end{pmatrix} \tag{2.12}$$

Using this expression, the mass eigenstates can be expressed in terms of flavour eigenstates in Equation 2.3, this yields

$$\begin{aligned} |\psi(L, T)\rangle &= \cos\theta(\cos\theta|\nu_e\rangle - \sin\theta|\nu_\mu\rangle)e^{-i\phi_1} \\ &\quad + \sin\theta(\sin\theta|\nu_e\rangle + \cos\theta|\nu_\mu\rangle)e^{-i\phi_2} \\ &= (e^{-i\phi_1}\cos^2\theta + e^{-i\phi_2}\sin^2\theta)|\nu_e\rangle + (e^{-i\phi_2} - e^{-i\phi_1})\sin\theta\cos\theta|\nu_\mu\rangle \\ &= e^{-i\phi_1}\left[(\cos^2\theta + e^{i\Delta\phi_{12}}\sin^2\theta)|\nu_e\rangle + (1 - e^{i\Delta\phi_{12}})\sin\theta\cos\theta|\nu_\mu\rangle\right], \end{aligned} \tag{2.13}$$

with

$$\Delta\phi_{12} = \phi_1 - \phi_2 = (E_1 - E_2)T - (p_1 - p_2)L. \tag{2.14}$$

From the last expression of Equation 2.13 it becomes apparent that if there is no phase difference ($\Delta\phi_{12} = 0$) the muon component of the wavefunction vanishes. In this case only electron neutrino states remain in the wavefunction. If there is a phase difference ($\Delta\phi_{12} \neq 0$), muon neutrino components are present in the wavefunction. The amplitudes of the electon and muon neutrino components can be written as

$$|\psi(L, T)\rangle = c_e|\nu_e\rangle + c_\mu|\nu_\mu\rangle, \tag{2.15}$$

where $c_e = \langle \nu_e | \psi \rangle$ and $c_\mu = \langle \nu_\mu | \psi \rangle$. The probability that a electron neutrino will appear as an muon neutrino after the distance L and time T is given by

$$\begin{aligned} P(\nu_e \to \nu_\mu) &= c_\mu c_\mu^* = (1 - e^{i\Delta\phi_{12}})(1 - e^{-i\Delta\phi_{12}}) \sin^2\theta \cos^2\theta \\ &= (2 - (e^{i\Delta\phi_{12}} + e^{-i\Delta\phi_{12}})) \sin^2\theta \cos^2\theta \\ &= (2 - 2\cos\phi_{12}) \frac{1}{4} \sin^2 2\theta \\ &= \sin^2 \frac{\phi_{12}}{2} \sin^2 2\theta \end{aligned} \tag{2.16}$$

Therefore the neutrino flavor changing probability depends on the mixing angle θ and the phase difference ϕ_{12}. Assuming that the momenta of the two eigenstates are equal ($p_1 = p_2 = p$) without any physical justification, Equation 2.14 reduces to $\Delta\phi_{12} = (E_1 - E_2)T$. A detailed discussion, treating the neutrino as a wave-packet instead of a plain wave can be found in [19]. Expressing the energy in terms of momentum and mass $E_i^2 = m_i^2 + \vec{p}^2$ yields,

$$\Delta\phi_{12} = (E_1 - E_2)T = \left[p\sqrt{1 + \frac{m_1^2}{p^2}} - p\sqrt{1 + \frac{m_2^2}{p^2}} \right] \tag{2.17}$$

The square root can be approximated by $1 + \frac{m_i^2}{2p^2}$ because $m \ll E$, hence the phase difference reduces to

$$\Delta\phi_{12} = \frac{m_1^2 - m_2^2}{2p} L \tag{2.18}$$

where $T \approx L$ (in natural units) because the neutrino mass is very small. Inserting Equation 2.18 into Equation 2.16 and writing $E_\nu = p$ gives the transition probability in terms of the square mass difference and neutrino energy,

$$P(\nu_e \to \nu_\mu) = \sin^2 \left(\frac{(m_1^2 - m_2^2)L}{4E_\nu} \right) \sin^2 2\theta \tag{2.19}$$

This term can be rewritten in terms of units encountered in neutrino experiments, where L[km], E[GeV], $\Delta m^2 = m_1^2 - m_2^2$[eV],

$$P(\nu_e \to \nu_\mu) = \sin^2 \left(1.27 \frac{\Delta m^2[\text{eV}] L[\text{km}]}{4E_\nu[\text{GeV}]} \right) \sin^2 2\theta \tag{2.20}$$

Figure 2.3 shows three oscillation probability curves, each corresponding to a different mass splitting. For increasing mass splitting the wavelength of the oscillation increases. The amplitude of the oscillation probability is determined by $sin^2 2\theta$, the mixing matrix governs the amplitude. Also, for relatively small distances oscillation probabilities are very small, which explains why neutrino oscillation was not observed in experiments with a relatively small distance between neutrino source and their detection.

As mentioned above, the equal momentum assumption has no physical basis, it is therefore necessary to treat the dispersion relation in Equation 2.14 in a wave-packet framework. Luckily, however, the equal momentum assumption is irrelevant in the derivation of the oscillation probability, as the wave-packet treatment

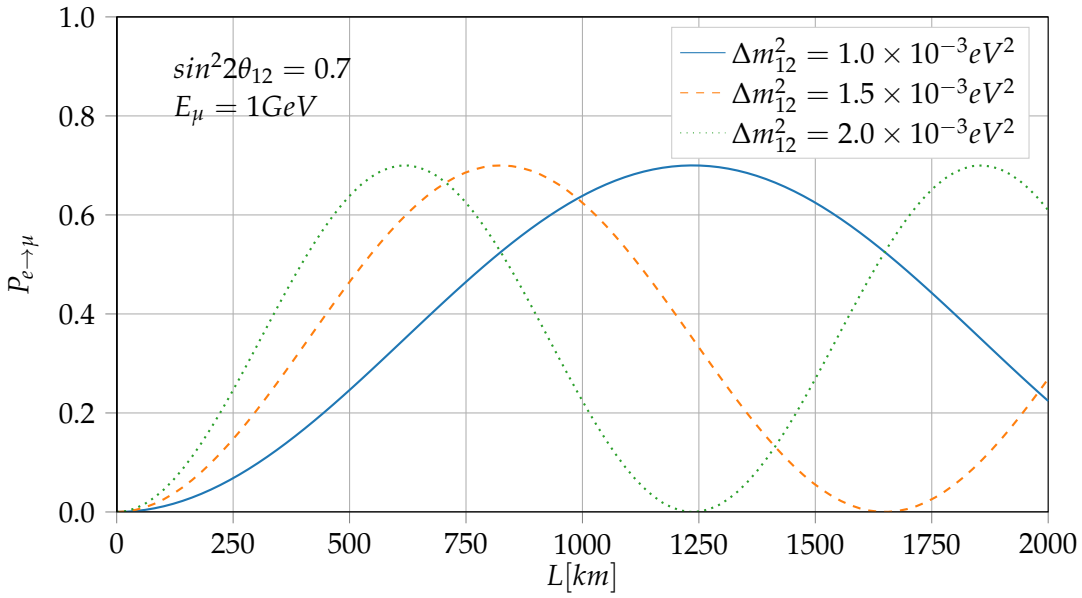

Figure 2.3: Neutrino oscillation probabilities versus propagation distances. Different colours correspond to different mass splitting.

yields the same results. A detailed wave-packet treatment of neutrino oscillation can be found in [17].

Although the simplification of considering only two neutrino flavours instead of three, nearly all relevant physics has been present in the above derivation. The fact that the neutrino oscillation arises from the relationship between mass- and flavour-eigenstates and a phase difference in the time dependant wavefunction stays valid in the three neutrino case.

In the three-flavour treatment of neutrino oscillations, the three weak eigenstates are related to the mass eigenstates by the 3×3 unitary Pontecorvo-Maki- Nakagawa-Sakata (PMNS) matrix shown in Equation 2.5. Due to the unitary nature of the mixing matrix, the matrix can be parameterized by three mixing angles and one phase. In general 6 phases are necessary to define a unitary matrix, but 5 phases can be absorbed into non-observable phases. The three mixing angles are denoted by θ_{12}, θ_{23}, θ_{13} and the phase, which is actually violating charge-parity (CP) symmetry is δ_{CP}.

$$\begin{aligned} U_{PNMS} &= \begin{pmatrix} U_{e1} & U_{e2} & U_{e3} \\ U_{\mu 1} & U_{\mu 2} & U_{\mu 3} \\ U_{\tau 1} & U_{\tau 2} & U_{\tau 3} \end{pmatrix} \\ &= \begin{pmatrix} 1 & 0 & 0 \\ 0 & c_{23} & s_{23} \\ 0 & -s_{23} & c_{23} \end{pmatrix} \begin{pmatrix} c_{13} & 0 & s_{13}e^{-i\delta} \\ 0 & 1 & 0 \\ -s_{13}e^{-i\delta} & 0 & c_{13} \end{pmatrix} \begin{pmatrix} c_{12} & s_{12} & 0 \\ -s_{12} & c_{12} & 0 \\ 0 & 0 & 1 \end{pmatrix}, \end{aligned} \tag{2.21}$$

where $c_{ij} = cos\theta_{ij}$ and $s_{ij} = sin\theta_{ij}$. Given the PNMS matrix the three neutrino oscillation probability can be written in a very similar fashion to Equation 2.19,

$$P(\nu_\alpha \to \nu_\beta) = \delta_{\alpha\beta} - 4\sum_{j>i} U_{\alpha i}U_{\beta j}U^*_{\alpha i}U_{\beta j}\sin^2\Delta_{ij} \quad , \tag{2.22}$$

with

$$\Delta_{ij} = \frac{(m_i^2 - m_j^2)L}{4E_\nu}. \tag{2.23}$$

As in the two neutrino case, the mixing matrix elements affect solely the amplitude of the flavor changing probability. Whereas the phase difference or the mass splitting respectively define the frequency of the oscillation pattern. An individual oscillation probability may depend on three possible mass splitting. As an example the electron survival probabily depends on the three mass splittings Δm^2_{12}, Δm^2_{32} and Δm^2_{13}. But only two of them are independent because of $\Delta m_{31} = \Delta_{32} + \Delta_{21}$. As we have seen in the previous section the neutrino oscillation probabilities depend on the square mass splitting. Therefore, it is not possible to measure the absolute mass of a neutrino with any oscillation experiment. Experiments suggest that the neutrino mass spectrum is formed by a duo of small splitting and by a third lone neutrino state. The lone neutrino may be much heavier or much lighter than the duo, denoted as normal and inverted hierarchy, respectively. The two cases are illustrated in Figure 2.4. In a third scheme, the lightest neutrino's mass squared is large compared with the mass squared differences. Consequently, all neutrinos have a similar mass. This scheme is called quasi-degenerate hierarchy.

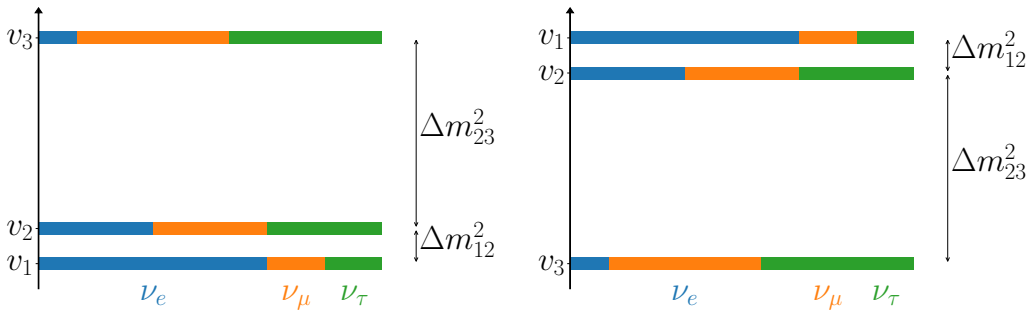

Figure 2.4: Mass splitting for normal (left) and inverted (right) neutrino hierarchy.

2.4 THE NEUTRINO OSCILLATION LANDSCAPE

Neutrino oscillation experiments at many different baselines and neutrino energy ranges have been conducted. Neutrinos of different flavor are produced in nuclear reactors, proton accelerators, the sun and cosmic rays, all of them are used as neutrino source for oscillation measurements. These experiments have confirmed that the neutrino flavor eigenstates produced in weak interactions are linear combinations of mass eigenstates, according to Equation 2.5. However, the limitation to three neutrino flavors, has no theoretical foundation. But it has been experimentally established that at least three types of neutrino exist and participate in oscil-

lations [20]. The so called Euler angles in Equation 2.21 have been measured to be $\sin^2\theta_{12} = 0.307 \pm 0.013$, $\sin^2\theta_{23} = 0.51 \pm 0.04$ and $\sin^2\theta_{13} = 0.0210 \pm 0.0011$ [20]. In the three neutrino case on can write two distinct differences of the square mass, combining all measurements the current values are $\Delta m^2_{12} = 7.37 \pm 0.51 \times 10^{-5}\,\mathrm{eV}^2$ and $\Delta m^2_{23} = 2.56 \pm 0.12 \times 10^{-3}\,\mathrm{eV}^2$ [21]. In Figure 2.7 for each of the three mixing angles and the two mass splittings an experimental result is depicted. The quoted values are valid for normal hierarchy, the values and error estimates vary if inverted hierarchy is assumed. An extensive discussion of all neutrino oscillation experiments would go beyond the scope of this introduction. A detailed discussion of long-baseline neutrino oscillation experiments can be found in [22], reactor based experiments are treated in [23] and a review of solar and atmospheric neutrino experiments can be found in [24, 25]. Neutrino oscillation experiments are unable to measure the absolute mass, however future experiments will be able to determine the mass hierarchy and the value of the CP-violating phase δ_{CP}.

The main motivation for MicroBooNE are anomalies found within the 3×3 oscillation picture described so far. Among these hints, LSND and MiniBooNE have been the most influential for the physics case of MicroBooNE. Both experiments observed an oscillation signal for $\nu_\mu \to \nu_e$ in the mass splitting rage of $\Delta m \approx 1\,\mathrm{eV}$. Which is well outside the established mass splittings quoted above.

LSND, short for Liquid Scintillator Neutrino Detector, was the first experiment to obtain evidence of the anomaly [26]. LSND used a stopped pion souce neutrino beam produced at Los Alamos National Laborator, where 798 MeV protons were impinged onto a target-dump construction, producing pion and muon decays at rest. A cylindrical tank, 8.3 m long and 5.7 m in diameter, placed 29.8 m away from the neutrino source was filled with 167 t of liquid scintillator(CH_2 with $0.031\,\mathrm{g\,L^{-1}}$ butyl-PBD). 1220 Photomultiplier Tubes (PMTs) mounted on the inner surface of the tank were recording promt positron signals from the inverse β-decay ($\bar{\nu_e} + p \to e^+ + n$) followed by a correlated 2.2 MeV photon emission from neutron capture. LSND recorded a total event excess over the expected backround of 87.9 ± 22.4 [27], the corresponding event distribution as a function of neutrino energy is shown in Figure 2.5. The best fit parameters for two neutrino oscillation (according to Equation 2.20) reported by LSND are $\sin^2\theta = 0.003$ and $\Delta m^2 = 1.2\,\mathrm{eV}^2$ [27], which are the parameters used to estimate the beam excess in Figure 2.5.

MiniBooNE was build to investigate the excess observed by LSND, it is hosted at the Booster Neutrino beam at Fermilab and used a beam of neutrinos produced by a high energetic proton hitting a beryllium target producing pions and Kaons. These mesons sequentially decay in a 50 m long tunnel into muon neutrinos. Due to the beam construction, the beam could be configured to either produce muon neutrinos or anti-neutrinos. The same beam is used in MicroBooNE, also see Section 4.1 for more details. Neutrinos were detected in a spherical tank (diameter 12.2 m) filled with CH_2 (806 t) [28]. Very similar to LSND, 1280 PMTs covered the inner surface of the sphere, observing Cerenkov rings produced by final state charged particles from neutrino interactions. During its 10 years of operation an excess of 162.0 ± 47.8 in neutrino and 78.4 ± 28.5 in anti-neutrino mode were observed. The energy distribution of the found events in both modes are shown in Figure 2.6. The main background in the excess region of MiniBooNE is due to mis-

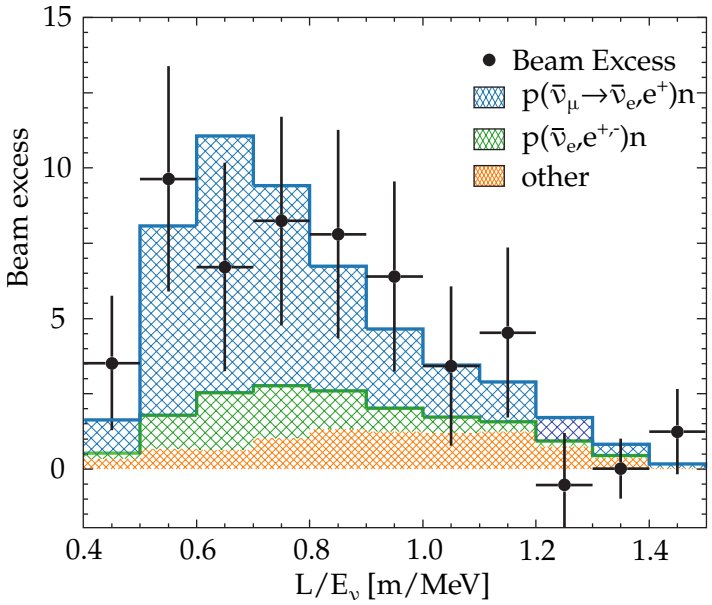

Figure 2.5: LSND neutrino excess as a function of L/E_ν. Adapted from [27].

identified chargeless pions. The neutral pion decays into two photons, the decay is isotropic in the rest frame of the particle [29]. The momentum of the two photons in the laboratory frame can therefore be asymmetric and possibly lead to a single observable photon. Which in turn can be mis-identified as an electron neutrino event. Furthermore, the neutral pion production is enhanced at lower energies trough a resonant process of the electron neutrino and a nucleon [30].

The excess of events observed in MiniBoonE is below the energy of 475 MeV, in the neutrino case the excess is marginally compatible with the LSND excess. However, the excess observed in the anti-neutrino channel is compatible with the LSND excess. In 2018 the MiniBooNE released a study where the excess was confirmed using additional data, furthermore the excess in is now compatible with LSND results [31]. Allowed regions for a two neutrino observation case in terms of $\sin^2\theta$ and Δm^2 for both experiments are shown in Figure 2.7. The surplus of events recorded in MiniBooNE and LSND in the lower energy region is also known as the Low Energy Excess (LEE). Further anomalies were observed in reactor [32] and gallium [33] experiments. Although, recently these deficiencies in the so called reactor sector have been accounted for by taking into account reactor fuel dynamics in the flux predictions [34]. As already mentioned, oscillation limits from both experiments are not compatible with the established three neutrino scenarios. Theoretical effort is made to explain the observed oscillation anomalies with the introduction of one or more sterile neutrinos [35]. The sterility of the neutrino has its origin in the concept that only three mass eigenstates couple to the electroweak gauge bosons, whereas the additional orthogonal eigenstates do not interact with these. This opens the possibility of neutrino oscillation trough the sterile neutrino channel, while not interfering with the well-established measurement of the number of three active neutrinos (by measureing the Z-boson decay width [36]). MicroBooNE's objective is to investigate the LEE using the capabilities of Liquid Argon

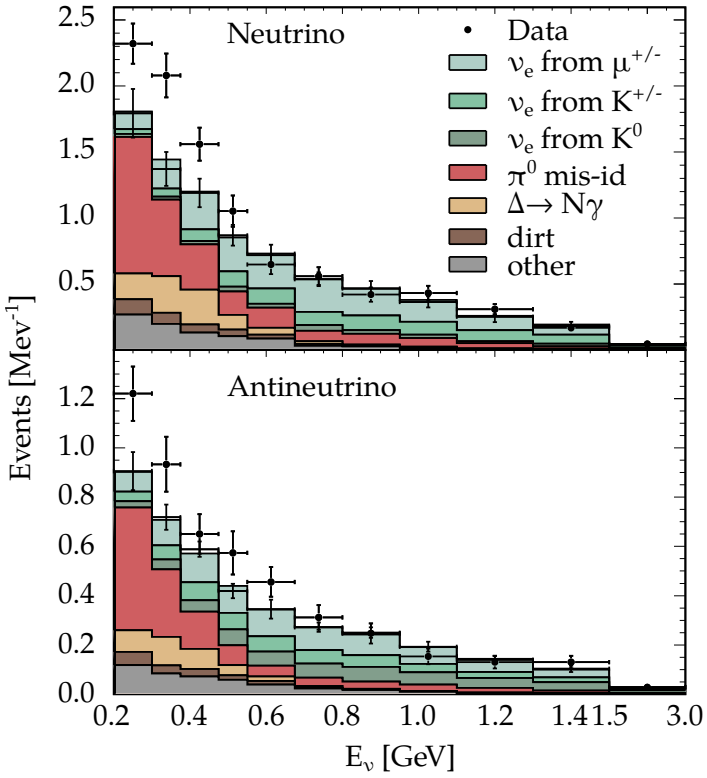

Figure 2.6: The reconstructed energy distribution of MiniBooNE in neutrino and anti-neutrino mode. Adapted from [28].

Time Projection Chambers (LArTPCs) to determine if the excess is due to electrons or photons, as mentioned earlier a question LSND and MiniBooNE are unable to answer.

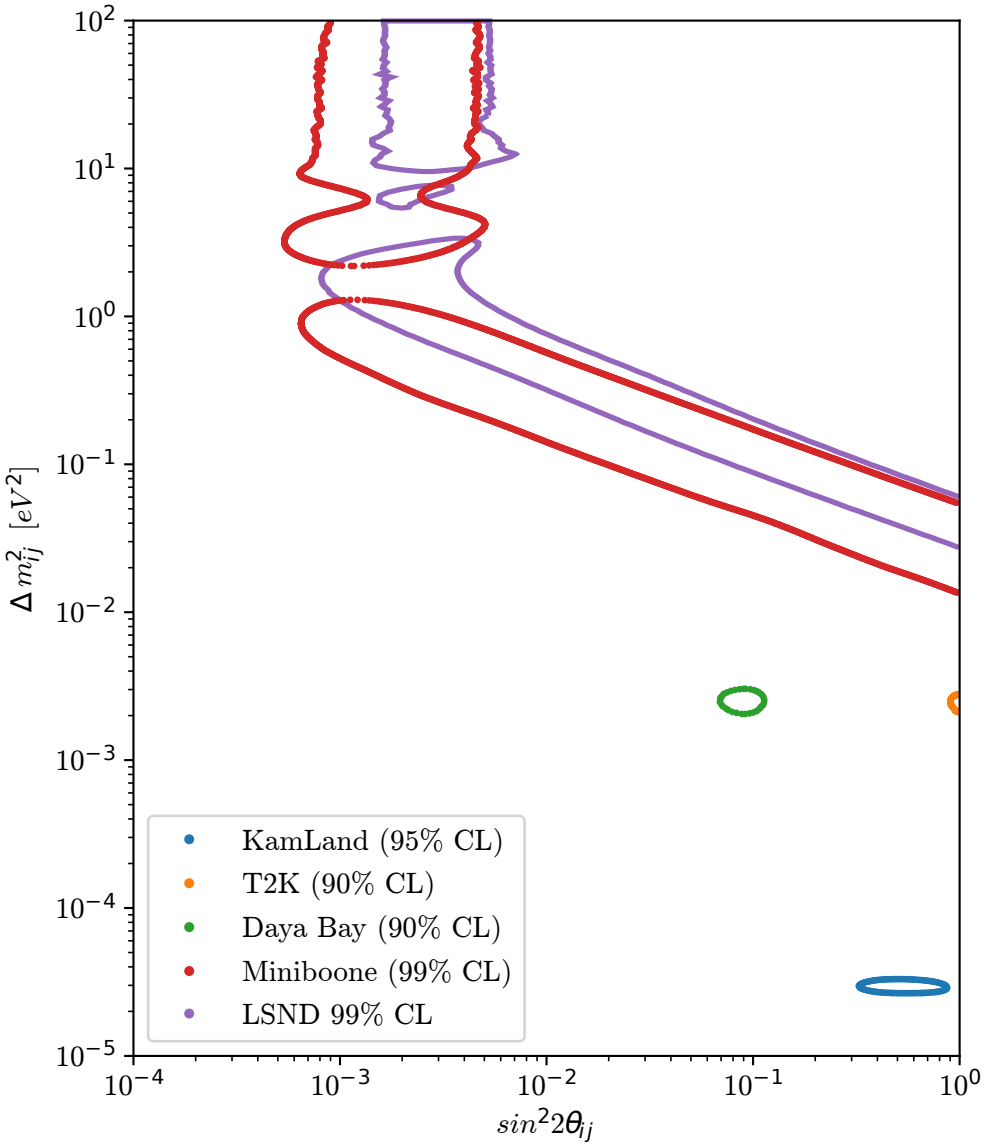

Figure 2.7: Allowed regions from different experiments for two-neutrino oscillation models with different mass splitting and angle combinations. Data points for KamLand [37], T2K [38] and Daya Bay [39], represent limits for $(\sin^2\theta_{12}, \Delta m^2_{12})$, $(\sin^2\theta_{23}, \Delta m^2_{23})$ and $(\sin^2\theta_{13}, \Delta m^2_{13})$, respectively. These three experiment represent the three neutrino model. Allowed regions for LSND [26] and MiniBooNE (combined neutrino and anti-neutrino mode) [40], represent the anomalous high-Δm^2 region.

3

LIQUID ARGON TIME PROJECTION CHAMBERS

The Time Projection Chamber (TPC) was introduced by David Nygren in 1974 at Lawrence Berkeley National Laboratory [41]. It was a successor of the the multi-wire proportional chamber invented by Georges Charpak in 1968 [42], who was awarded the Nobel Prize in Physics in 1992 for this work. The invention of these two techniques marked a milestone in the detection of ionizing radiation, introducing electronically readout capabilities for tracking detectors superior to those of bubble chambers. Because of simpler detector setup, TPCs were initially filled with noble gases where argon was the first choice in most cases. Liquefied Argon as detector medium were first proposed by Carlo Rubbia in 1977 [43]. In this chapter the working principle of a liquid Argon TPC is discussed in detail.

3.1 WORKING PRINCIPLE

In a TPC two parallel planes, anode and cathode, enclose the drift gap, which can extend from a few millimeter to several meters depending on the application. The cathode is connected to a negative electric potential, whereas the anode is held at ground. Therefore, an electric field is present within the gap in between the plates, in analogy to a plate capacitor. Field strengths typically reach several $100\,\mathrm{V\,cm^{-1}}$ for large scale experiments and $10\,\mathrm{kV\,cm^{-1}}$ for shorter drift distances. Maximum uniformity of the field within the drift gap is achieved by placing field-shaping electrodes equally spaced between cathode and anode. The potential of each electrode is tuned such that the field within the cathode is homogeneous, this is typically achieved by a high-ohmic resistors chain. A sensing plane spans up the anode, in which the detector output signals are formed, by means of a spatially segmented readout, consisting of two or more wireplanes oriented along different directions. A wireplane consists of a collection of equally spaced conductive wires, each used as a readout channel of the detector. It is possible to replace the wires with pad electrodes, so to form a pixelated readout. A drawing of a TPC with a two-wireplane read-out is shown in Figure 3.8.

An ionizing particle traversing a LArTPC creates pairs of positively charged argon ions Ar^+ and quasifree electrons e^- along its path (ionization track). Instead of being ionized, an argon atom may be raised to an excited state, which eventually leads to the emission of argon scintillation light during its de-excitation. The situation is illustrated in Figure 3.1 for a passing-through muon. Right after creation, an electric field dependent amount of the electron-ion pairs recombines, resulting in the emission of more scintillation light. Liquid argon is transparent to its own scintillation light. It can thus be measured by photodetectors to use it as a trigger, to provide the precise event time stamp t_0 and to gain additional information about an event to facilitate its reconstruction. The residual electrons and argon cations, left after recombination, are separated by the presence of the electric field forcing

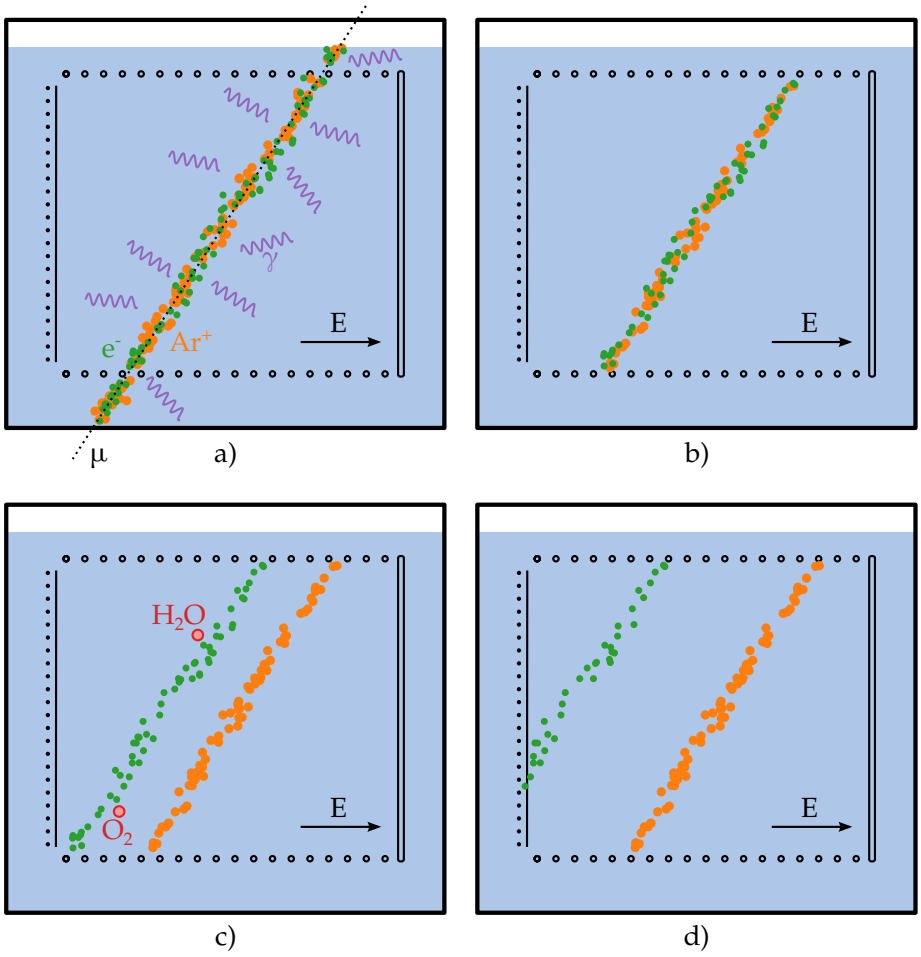

Figure 3.1: LArTPC working principle in four steps. Each frame contains the basic mechanical structure, the anode with readout wires on the left and the cathode on the right, in between the field shaping rings are indicated on the top and bottom. The electric field inside the detector points from left to right. The structure is fully immersed in liquid argon, indicated in light blue. a) A muon passes trough the detector from top to bottom, creating an ionization track in the liquid argon electrons (e^{-}) in green, argon (Ar^{+}) ions in orange. Additionally scintillation light is emitted (γ), drawn in purple, which is recorded by light sensitive detectors. b) A certain fraction of the electron-ion pair is separated from each other by the electric field present in the detector, the remaining fraction recombines. c) Electrons drift towards the readout plane argon ions drift towards the cathode. Electronegative impurities in capture a fraction of the drifting electrons. The homogeneous electric field conserves the ionization track left behind by the muon. d) The Electrons arrive at the readout plane and are registered, together with the arrival time, by the readout wires.

them to drift towards the anode or the cathode respectively. Their movements are described by phases of acceleration, interrupted by collisions with the surrounding atoms of the medium. This can be modelled by a finite average electron or ion drift speed. Compared to the argon ions, electrons have a mobility which is higher by orders of magnitude and, at a given electric field strength, they have much higher drift speeds. In terms of overall detector performance, a fast charge transport is favourable which is why the electrons rather than the ions are read out to obtain information about the ionization track 2. Due to the high uniformity of the electric field, the integrity of the original ionization track is kept during the drifting process (c). Any field disuniformities would cause distortions of the track and strongly affect the detector spatial resolution. During the drift, two physics processes have an impact on the detector performance. Firstly, the drifting electrons are subject to longitudinal (along the drift direction) and transverse (perpendicular to the drift direction) diffusion, meaning that they do not strictly keep their positions relative to one another, but rather they disperse. This limits the spatial resolution of the device. Secondly, electronegative impurities, such as oxygen and water molecules dissolved in the sensitive liquid argon volume, tend to attach electrons and thus reduce the amount of charge drifting towards the read-out (c).

Consequently, impurities diminish the detector output signals and hence one is interested in keeping their concentration in the device as low as possible. At the sensing plane, the electrons are registered by the x-y segmented readout (d) and the signals produced are subsequently amplified electronically. In addition to measuring the x and y spatial coordinates, the electron arrival times are recorded. Having knowledge of the event time stamp t_0 , for instance from the measurement of the scintillation light, the actual drift times t_d can be calculated from the arrival times. Since t d is proportional to the drift distance, it is possible to obtain the third spatial coordinates z of the ionization track to allow full 3D tracking. After doing a thorough detector calibration and applying appropriate corrections for attachment and recombination losses, the number of electrons collected at the read-out plane yields calorimetric information about an event.

3.2 LIQUEFIED ARGON AS A DETECTION MEDIUM

Because atoms of noble liquids have fully occupied valence shell, they do not tend to attach electrons. Together with the high electron mobility, these media allow an efficient transport of electrons across long distances, a property of major relevance for TPCs. Additionally, the availability of technology needed to reduce electron capturing impurities in noble liquids make such detectors feasible. Key characteristic of liquefied argon is summarized in Table 3.1. The ionization yield, stopping power and operation temperature liquid xenon would be favourable over liquid argon. However, argon is the third-most abundant gas in the earth atmosphere (relative abundance of 1 %), whereas xenon is extremely rare (relative abundance 9.7×10^{-10} %). Therefore the yield, hence reducing the cost, to obtain liquid argon from liquefied air is much smaller compared to xenon. This rather low production cost makes liquid argon a suitable candidate as a detector medium for kilo-ton scale LArTPCs. From a safety standpoint the high density of argon leads to oxy-

QUANTITY	SYMBOL	VALUE	
Atomic number	Z	18	
Molar mass	M	39.948(1)	g/mol
Atmospheric abundance	η_{atm}	0.934	%vol.
Boiling point (BP)	T_{BP}	87.26	K
Melting point (MP)	T_{MP}	83.8(3)	K
Density at normal BP	ρ_{BP}	1396(1)	kg/m^3
Dielectric constant	ϵ_r	1.505(3)	
Ionization energy	I	13.84	eV
Effective ionization potential	I_c	188	eV
W-value for ionization	W_i	23.6(3)	eV/pair
W-value for scintillation	W_s	19.5(10)	eV/photon
Radiation length	X_0	14.0	cm
Nuclear interaction length	λ_I	85.7	cm
Mean specific energy loss	$\langle dE/dx \rangle$	2.12	MeV/cm
Critical energy (e^-)	E_c	32.84	MeV
Scintillation emission peak	λ_s	128	nm
e^- drift velocity	v_e	1.60(2)	mm/μs
e^- mobility	μ_0^e	518(2)	cm^2/(Vs)
Ar^+ drift velocity	v_i	$8.0(4) \cdot 10^{-6}$	mm/μs
Ar^+ mobility	μ_0^i	$6.0 \cdot 10^{-4}$	cm^2/(Vs)

Table 3.1: Liquid argon properties [44, 45, 46]. T_{BP} and T_{MP} are at a pressure of 1 atm. W_i, W_s and $\langle dE/dx \rangle$ are obtained for minimum ionizing particles. μ_0^e, μ_0^i and v_e, v_i are specified at T_{BP} and $E = 00\,\mathrm{kV\,cm^{-1}}$ and $E = 0.5\,\mathrm{kV\,cm^{-1}}$.

gen deficiency hazards, because in confined spaces gaseous argon will displace all air. This must be considered during building and operation of LArTPCs, especially when underground. Being chemically inert no fire hazards arise from argon.

The need for cryogenic environment is a major challenge to overcome when using liquid argon as a detector medium. Handling and running of the detector become more complicated. Radioactive and scintillation light absorbing impurities, such as Radon and Nitrogen, have to be addressed when operating LArTPCs. Despite all the above mentioned disadvantages and challenges, liquid argon serves as an excellent detector medium, particularly for kilo-ton scale experiments.

3.3 ENERGY DISSIPATION IN LIQUID ARGON

The mechanism for energy dissipation in a medium is depending on the type of incident radiation. Charged particles, such as electrons or heavy charged particles, continuously interact trough the Coulomb force with electrons present in

the medium trough which they pass. Neutral particles, such as neutrons, are not exposed to Coulomb interaction, therefore this type of radiation have to undergo catastrophic interactions with the constituent atoms. The photon represents a special case of uncharged radiation, it is either fully absorbed and the interaction product then ionizes the detector medium, or it is scattered at a relatively large angle. Concerning neutrinos and antineutrinos crossing the detector, they can be absorbed by the nuclei of the medium in weak interactions [47, 48, 49, 20].

Photons lose their energy via the processes of photoelectric absorption, Compton scattering, pair production and photo-nuclear interactions. In the process of photoelectric absorption, an incoming photon undergoes an interaction with an atom in which the incident photon is fully absorbed. In its place a photoelectron is ejected from the bound shells of the atom. For a photon with sufficient energy to overcome the binding energy E_B the energy of the outgoing electron is given by

$$E_{e^-} = E_\gamma - E_B. \tag{3.1}$$

For photons with energies above a few hundred keV, the photoelectron carries the majority of the original photon energy. The interaction creates also an ionized absorber atom, which is quickly neutralized trough capture of an free electron from the medium and/or rearrangement of the electrons from the other shells. This leads to the emission of a characteristic X-ray photon. In the process of Compton scattering an incident photon is deflected by an absorber material electron. The incoming photon is scattered at an angle θ with respect to its original direction. A portion of its energy is transferred to the electron. All scattering angles are possible, the energy transferred can range from zero to a substantial part of the photon energy. Using the conservation of momentum and energy it is possible to derive the photon energy after the scattering to be

$$E^{'} = \frac{E}{1 + \frac{E}{m_0 c^2}(1 - \cos\theta)}. \tag{3.2}$$

The m_c^2 term corresponds to the electron rest mass (0.511 MeV). The cross section of Compton scattering falls off gradually with increasing energy. Pair production is only possible whenever the incoming photon energy exceeds twice the rest mass of an electron (1.02 MeV). In the process, which can only happen in the Coulomb field of a nucleus, the incoming photon is replaced by an electron position pair. All excess kinetic energy is equally shared. The importance of pair production raises sharply after the threshold energy and becomes dominant at several hundred MeV. The absorption coefficients in liquid argon for the three processes described above are summarized in Figure 3.2.

Heavy charged particles, such as muons or alpha particles, predominately interact with matter trough Coulomb forces between them and the negatively charged orbital electrons. Electromagnetic interactions with the atomic shell lead to ionization, excitation and transfer of momentum (heat) [48, 49]. The latter process becomes dominant when only elastic collisions in the medium are possible, this happens when the charged particle energy falls below the ionization threshold. Hence heat transfer losses are not measured in a TPC. Depending on the proximity of the encounter (known as the impact parameter) the energy transfer from the

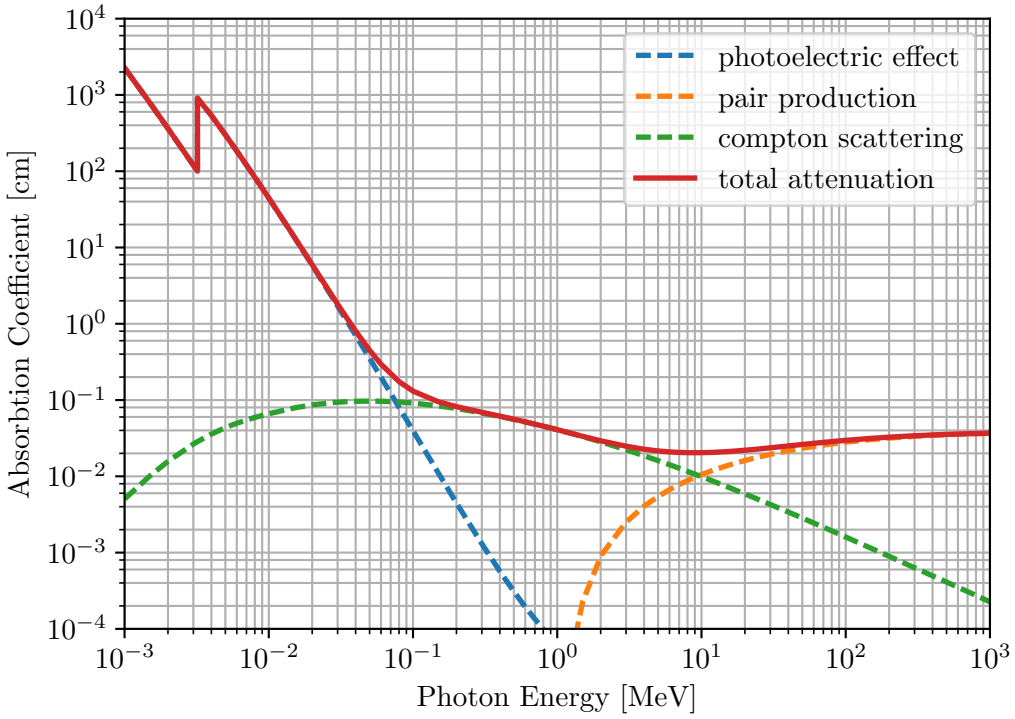

Figure 3.2: Energy dependence of the main photon interaction processes in liquid argon (86 K, standard pressure). Data provided by [50].

incoming particle to the shell electron can either be lifted to a high lying shell (excitation) or can be completely removed from the atom (ionization). As the maximum energy transfer on a single encounter is limited to $E_{max} \approx 4Em_e/m$, where E and m are the kinetic energy and the mass of the incoming particle and m_e the electron mass [47]. Because this is a small fraction of the total energy, the incoming particle must loose its energy in many such encounters during the passage trough the absorber material. In the process of ionization, enough energy is transferred from the ionizing particle to one of the shell electrons of an atom to overcome its binding energy

$$\mathrm{Ar} + \chi \rightarrow \mathrm{Ar}^{+} + e^{-} + \chi', \tag{3.3}$$

where χ and χ' indicate the incoming particle before and after the interaction respectively and Ar represents the argon atom. Until it looses all its energy, the outgoing electron may have enough energy E_e for further ionization or excitation of atoms. If the energy transferred to the shell electron is smaller than the ionization potential of the medium, the atom may end up in a highly excited state Ar^{**} [51]

$$\mathrm{Ar} + \chi \rightarrow \mathrm{Ar}^{**} + \chi'. \tag{3.4}$$

These excited states are short-lived. Either trough non-radiative energy exchange or by the emission of photons in the vacuum ultraviolet spectrum (at 104.8 nm and 106.7 nm) the excited atom de-excites to

$$\mathrm{Ar} + \mathrm{Ar}^{**} \rightarrow \mathrm{Ar} + \mathrm{Ar}^{*} + \text{heat}, \tag{3.5}$$

$$\mathrm{Ar} + \mathrm{Ar}^{**} \rightarrow \mathrm{Ar} + \mathrm{Ar}^{*} + \gamma. \tag{3.6}$$

The photons produced in the optical de-excitation of the Ar^{*} can be re-absorbed by other argon atoms, hence these transitions do not contribute to scintillation in liquid argon. The mechanism responsible for the emission of scintillation light to which argon is self-transparent is discussed in detail in Section 3.5.

When a heavy singly charged charged particle traverses trough a medium its energy loss per unit distance is given by the Bethe-Bloch equation [20],

$$\frac{1}{\rho}\frac{dE}{dx} = -\frac{4\pi\hbar^2\alpha^2 N_A}{m_e}\frac{z}{\beta^2}\frac{Z}{A}\left[\ln\left(\frac{2m_e c^2\gamma^2\beta^2}{I}\right) - \beta^2 - \frac{\delta}{2}\right] \tag{3.7}$$

where

ρ is the density of the absorber material,

$\hbar$ is the Planck constant,

α is the fine structure constant,

N_A is the Avogadro number,

m_e is the electron mass,

z is the charge of the incident particle,

Z is the atomic number of the absorber,

A is the atomic weight of the absorber,

$\beta = \frac{v}{c}$ with v the velocity of the incident particle,

$\gamma = \frac{E}{m_0 c^2}$ with E the energy and m_0 the rest mass of the incident particle,

I is the effective ionization potential of the material,

δ is a parameter describing the screening of the extended transverse electric field of relativistic incident particles by the charge density of the atomic electrons of the absorber.

The expression in brackets varies slowly with particle energy for non-relativistic speeds ($v \ll c$). Thus, the general behavior can be inferred from the behavior of the multiplicative factor. Therefore dE/dx varies with $1/v^2$, inversely with particle energy. Equation 3.7 is generally valid for multiple particles as long as the particle velocity is well above the speed of the orbital electrons of the absorber medium. In the case of highly relativistic particles ($v \approx c$), dE/dx depends logarithmically on $(\beta\gamma)^2 = (p/mc)^2$, this results in a relativistic rise. Since Z/A stays roughly constant, due to the equal number of protons and neutrons in the nuclei, dE/dx

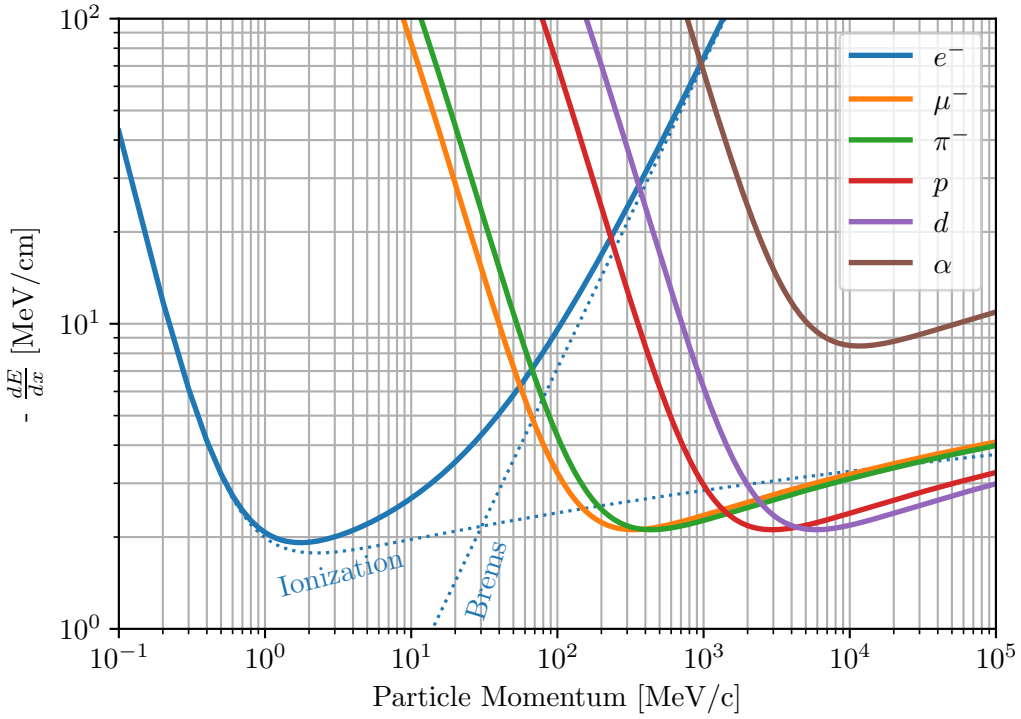

Figure 3.3: Energy loss of different particles in liquid argon, using liquid argon properties from Table 3.1.

only depends on the material trough the density ρ. For muons, pions, protons, deuterons and alpha particles the energy loss per unit distance in liquid argon is depicted as colored lines in Figure 3.3.

Equation 3.7 well describes the energy loss mechanism of particles below 100 GeV in liquid argon. The main signal event in MicroBooNE are muons produced in quasi-elastic neutrino scattering off an argon atom [52]. The expected energy range of the muons is 0.2 GeV to 1.5 GeV. Assuming a minimum ionizing energy loss of roughly 2.1 MeV cm^{-1}, these muons will penetrate liquid argon from 1 m to 7 m and leave a trail of ionization, allowing tracking. An additional source of muons in the detector is the bombardment of the atmosphere with cosmic rays. Trough a cascade of decays, muons with energies in the range 1 GeV to 100 GeV are produced and propagate to the earth surface [20]. Due to their high energy, these muons will almost always fully penetrate the detector.

So far only heavy particles ($m \gg m_e$) where treated. Fast electrons and positrons have to be treated differently since in this case the incident particle and the absorber particle have the same mass, the discussion of maximum energy transfer do not hold anymore. A throughout discussion of the relevant processes is given in [53]. Since the electron is considerably lighter, minimum ionization occurs ar much smaller momenta compared to heavier particles, nevertheless the minimum energy loss stays comparable. At higher particle velocities, the energy loss is not anymore dominated by ionization but radiation losses within the Coulomb field present in

the atom. The incident particle looses energy by emitting a photon. This process is called Bremsstrahlung and its energy loss per unit distance is described by

$$\frac{1}{\rho}\frac{dE}{dx} = -\frac{E}{X_0} \tag{3.8}$$

where the radiation length X_0 is defined as

$$X_0 \approx \frac{1}{4\alpha n Z^2 r_e^2 \ln(287/Z^{1/2})} \tag{3.9}$$

The critical energy defines where both ionization and Bremsstrahlung losses have equal amplitude. For liquid argon $E_C^e = 32.84\,\text{MeV}$ [20]. It can be shown that the critical energy scales with the square particle mass (see [53]), hence the $E_C^\mu = 1300\,\text{GeV}$. Hence, the Bremsstrahlungs effects can be neglected for heavy particles with momenta in the range up to 100 GeV. The ionization and Bremsstrahlung energy losses (dashed), as well as the total energy loss (solid) are drawn in blue in Figure 3.3.

The energy deposited per unit track length dE/dx is an important quantity for particle identification and can be precisely measured in LArTPCs thanks to their excellent 3D tracking and calorimetric capabilities. For moderately relativistic heavy ($m \geq m_\mu$) charged particles, the Bethe-Bloch formula provides a good description of dE/dx [20].

In addition to the above discussed energy loss processes, a particle traversing a medium is deflected by many small angle scatters. This scattering occurs in the Coulomb field of the nucleus and can is well described by the Molière's theory [54]. The scattering angle is distributed around $\theta = 0°$. The central part (98 %) is Gaussian while the tails are extended (larger than Gaussian). The root mean square width of the central part is given by

$$\theta_0 = \frac{13.6\,\text{MeV}}{\beta pc} z \sqrt{\frac{x}{X_0}} [1 + 0.038 \ln(\frac{x}{X_0})] \tag{3.10}$$

where βc, p and z are the particle velocity, momentum and the electric charge. X_0 denotes the radiation length of the traversed medium and x specifies the thickness of it. Figure 3.4 shows θ_0 for muons for momenta from 200 MeV to 2000 MeV traveling trough liquid argon of thickness from 0 cm to 500 cm.

3.4 RECOMBINATION MECHANISMS

Due to the applied electric field, a fraction of the electron-ion pairs produced during the ionization process are separated fast enough to prevent recombination. Several models describing the processes involved in recombination exist [55, 56, 57]. The basic idea is that the ionized particles loose energy trough collisions with surrounding particles within a few nanoseconds [58]. The free electron, created during ionization, may remain in the vicinity of an ion, enabling re-capture. An increase in electric field, and therefore the Coulomb force acting on the charged particles, has a strong impact on the fraction of recombination. The higher the field, the further (away from the ion) can the free electron travel, hence reducing

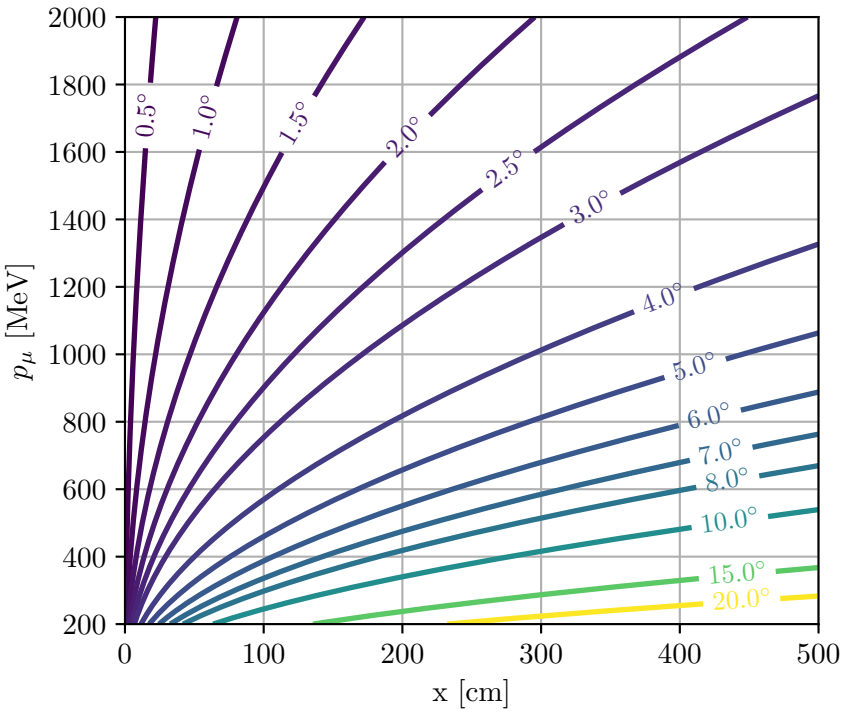

Figure 3.4: θ_0 contours in degrees for muons with various momenta (y-axis) after passage trough multiple columns (x-axis) of liquid argon.

the chance of recombination. Figure 3.5 shows the dependence of recombination on the field strength and the specific energy loss dE/dx as a saturation curve. Also shown is the fraction of light collected as a fraction of total light collected at zero field.

Early models by Onsager [55] did only take into account the electron ion pair individually, not taking into account any neighboring charge. In contrast, Jaffé introduced a column of charge density along the ionization track, to account for collective effects from the surrounding charge. Hence, the electron will not only recombine with its parent ion but with all nerby ions. Therefore, the recombination fraction will depend on ionization density and thus on the particle type responsible for ionization. The charge density will evolve in time, due to diffusion and as the applied electric field will separate negative and positive charges. During this separation process, any electron might recombine with a nearby ion, the charge left after this is given by,

$$Q = \frac{Q_0}{1 + q_0 F(E \sin \phi)}, \tag{3.11}$$

here Q_0 is the initially produced charge, q_0 is the initial density of electron-ion pairs and F is a function that depends on the electric field strength and the relative angle ϕ of the ionization track with respect to the field lines. The fraction of electrons left after recombination is given by $R = Q/Q_0$. The electron and ion drift speeds are assumed equal and their mobilities are regarded as constants.

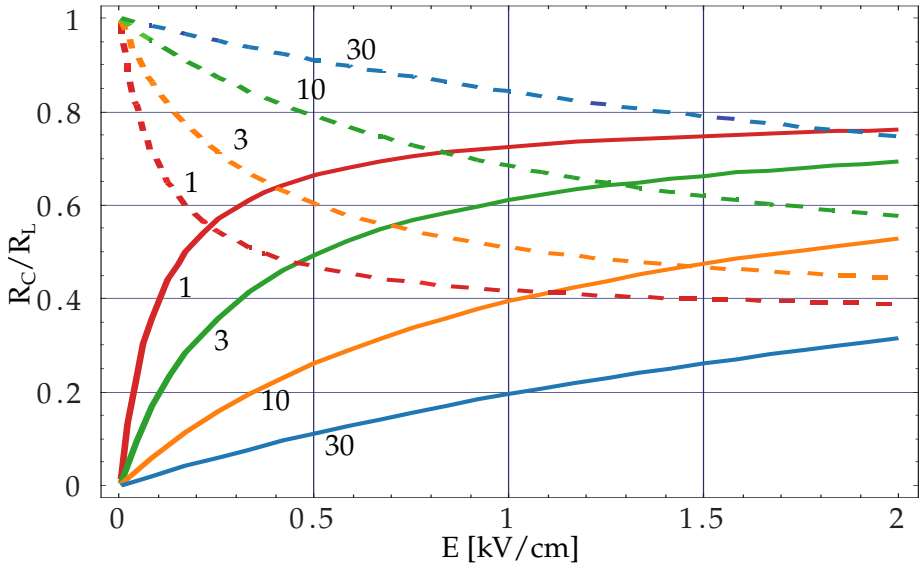

Figure 3.5: The recombination factors for charge R_C (solid lines) and light R_L (dashed lines) as functions of the electric field strength. The factors represent the charge and light collected with respect to zero field and infinite field, respectively. Different colors are associate with different energy loss dE/dx in units of minimum ionizing particles. Adapted from [44].

With the knowledge of W_i and dE/dx in liquid argon it is possible to calculate the average distance between ionization centers to be of the order of 10 nm. In comparison, electrons travel around 10×10^3 nm before thermalization [59]. The comparison between ion-ion distance and the electron thermalization distance indicated that collective recombination processes dominate over parent-ion recombination. It has been measured that the fraction of electrons remaining after recombination depends on ionization density [59, 60].

The Jaffé columnar Equation 3.11 was extended by Thomas and Imel [57]. In their model the diffusion and ion mobility was ignored, leaving only the electrons moving. Within a box an uniform charge distribution is introduced, this leads to the following expression for the remaining charge

$$Q = \frac{Q_0}{\psi} \ln(1 + \psi), \tag{3.12}$$

where $\psi = \alpha Q_0 / E$. Here α is a free (fit) parameter. In experiments using liquid argon as detector medium, a functional form of either Equation 3.11 or Equation 3.12 fitted to data is typically used. Birks'law [61] is typically used to approximate the Jaffé model, this leads to

$$Q = A \frac{Q_0}{1 + k_E / E}, \tag{3.13}$$

where k_E and A are fit parameters. The ICARUS collaboration [60] found,

$$A = 0.800 \pm 0.003 \quad \text{and} \quad k_E = 0.0486 \pm 0.0060 \,\text{kV/cm} \frac{\text{g/cm}^2}{\text{MeV}} \tag{3.14}$$

by fitting experimental data to Equation 3.13, the fitted parameters were confirmed by [59].

For inferring calorimetric information about an event in a LArTPC using the collected charge signal, recombination and electron attachment losses (caused by impurities) must be corrected. Corrections for recombination are introduced by transforming the collected charge (corrected for attachment losses) at the detector readout ΔQ to the corresponding deposited energy ΔE using,

$$\Delta E = \frac{\Delta Q}{R} W_i \quad \text{or} \quad \frac{dE}{dx} = \frac{dQ/dx}{R} W_i \tag{3.15}$$

where dE/dx is the deposited energy and dQ/dx is the deposited charge per unit length. Combining the above equation with Equation 3.13 yields

$$\frac{dE}{dx} = \frac{dQ/dx}{A/W_i - k(dQ/dx)/E}. \tag{3.16}$$

Here k is the fit parameter given in Equation 3.14 normalized to argon density $k = k_E/\rho_{Ar}$.

The process of deexcitation can happen trough two mechanism. Either directly via $Ar^+ + e^- \rightarrow Ar^*$, where the excited atom reaches the ground state trough the emission of an Ultra Violet (UV) photon or relaxation (analog to Equation 3.5. Or trough the very efficient tripple collision of argon cations with closby argon atoms [62], forming eximer states (stable state only in an excited state),

$$Ar^+ + 2Ar \rightarrow Ar_2^+ + Ar. \tag{3.17}$$

Because of conservation of momentum a second argon atom has to participate in the reaction. The excimer subsequently absorbs a free electron, leading to recombination, leaving behind an highly excited argon atom,

$$Ar_2^+ + e^- \rightarrow Ar^{**} + Ar \tag{3.18}$$

Once again, the excited atom decays to the ground state via the processes described in Equation 3.5. Hence under the impact of an electric field, less electron-ion pairs recombine resulting in a lower light yield. Also the light yield increases with higher dE/dx under a constant electric field.

3.5 SCINTILLATION

The deexcitation of liquid argon linked to the emission of a photon (104.8 nm and 106.7 nm) could be interpreted as scintillation, however the process is possible in the opposite direction too, absorbing the emitted photon again. This behaviour is known as radiation trapping, the characteristic photon is only observed in very low pressure gaseous argon [63].

Therefore other processes are responsible for efficient scintillation in liquid argon. The main path is the following: Excited argon atoms Ar^{**} reach the lowest excited states Ar^* through collisions with other argon atoms or optical transitions [64]. These excited states can subsequently decay into the ground state of the argon atom, but as already mentioned above, the emitted photon will be absorbed by argon atoms preventing the photon to leave the liquid argon. But through collisions with neighboring atoms the excited argon atoms Ar^* can form excited argon

molecules, called excimers, which are only stable as an excited state. Due to the different possible lowest excited states, corresponding to different electron shell configurations (namely $^3P_1$ and $^3P_2$), two distinguishable excimer states can form. These states are formed within picoseconds after the ionization because of the high density of liquid argon [65], a detailed description of the formation and structure of argon excimers can be found in [66]. The formation of argon excimers is summarized in the following reaction diagram:

$$\begin{aligned}
\mathrm{Ar}^{**} &\longrightarrow \mathrm{Ar}^{*} + \gamma && \text{optical}\\
\mathrm{Ar}^{**} + \mathrm{Ar} &\longrightarrow \mathrm{Ar}^{*} && \text{collisional}\\
&\quad \mathrm{Ar}^{*}(^3\mathrm{P}_1) + 2\,\mathrm{Ar} && \longrightarrow \mathrm{Ar}_2^{*}(^1\Sigma_u^+) + \mathrm{Ar}\\
&\quad \mathrm{Ar}^{*}(^3\mathrm{P}_2) + 2\,\mathrm{Ar} && \longrightarrow \mathrm{Ar}_2^{*}(^3\Sigma_u^+) + \mathrm{Ar}
\end{aligned}$$

These two excimer states are singlet $(^1\Sigma_u^+)$ and $(^3\Sigma_u^+)$ triplet states. Both states decay to the excimer ground state via the emission of a deep ultraviolet photon:

$$\begin{aligned}
\mathrm{Ar}_2^{*}(^1\Sigma_u^+) &\longrightarrow \mathrm{Ar}_2(^1\Sigma_g^+) + \gamma_s\\
\mathrm{Ar}_2^{*}(^3\Sigma_u^+) &\longrightarrow \mathrm{Ar}_2(^1\Sigma_g^+) + \gamma_t
\end{aligned}$$

Because the repulsive electric force of the two argon atoms in the excimer ground state is not any more compensated by the electric bounding which was present in the excited state, the excimer will separate into two isolated argon atoms:

$$\mathrm{Ar}_2(^1\Sigma_g^+) \longrightarrow 2\,\mathrm{Ar}$$

The singlet decay represents the allowed decay channel with a lifetime τ_s of several nanoseconds whereas the triplet decay is suppressed and therefore has a enhanced lifetime τ_t of the order of microseconds [67]. The emitted photons have very similar wavelengths of 126.6 nm for the singlet decay and 127.6 nm for the triplet decay and a width (FWHM) of about 10 nm [68]. Because of the large separation in time and the close emission peaks the two lifetimes are well measurable as seen in Figure 3.6. Due to the very short time needed for the formation of argon excimers and the subsequent decay after ionization, the detection of the emitted photons is well suited for the measurement of the absolute time when an particle interaction happened inside the detector.

3.6 CHARGE CARRIER TRANSPORT

The velocities of free charged particles in a medium are Maxwellian distributed and are isotropic. If an electric field (with field strength E) is applied, these particles will be accelerated along the field lines up to a certain velocity, named drift velocity $\vec{v_d} = const$. Unlike in vacuum where no counter-part to the acceleration by the electric field is present, the medium restricts acceleration trough collisions with

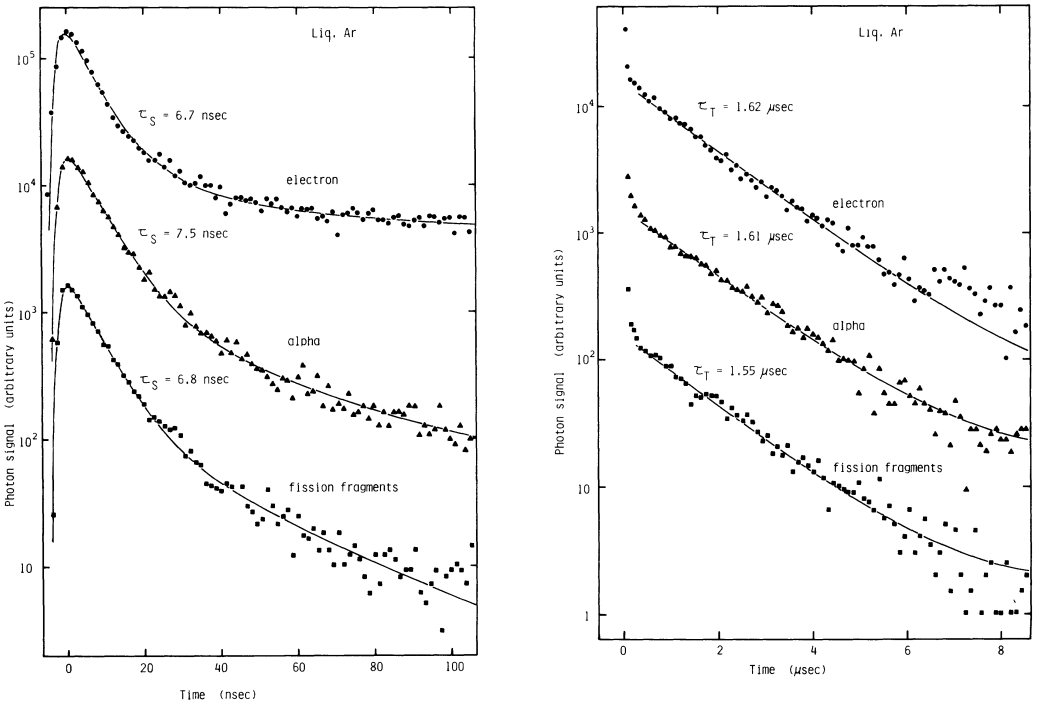

Figure 3.6: Time resolved scintillation intensity in the VUV-range for different ionizing particles (electrons α-particles and ions). Two different lifetimes (τ_S and τ_T) (singlet and triplet) are distinguishable in the two different time scales. Graph from [69].

the surrounding medium. The mean drift velocity is governed by the electric field and the mobility of the free charge. The mobility itself depends on the electric field strength, the free charge type (subscript p) and the temperature T of the medium. The expression for the drift velocity is given by

$$\vec{v_d} = \mu_i(E_d, T) \cdot \vec{E_d}. \tag{3.19}$$

An overview of measurements and fits of the drift velocity for electron in liquid argon as a function of electric field and for different liquid temperatures is shown in Figure 3.7. In liquid argon in the region of low electric field up to 200 V cm^{-1}, μ can be considered constant [70, 71]. This leads to a linear dependence of v_d on E_d in this region. Above these field strengths, the behaviour becomes non-linear and from the aforementioned figure, it becomes apparent that μ decreases with higher electric field strengths. For a TPC the precise knowledge of the drift speed is essential, it governs the spatial resolution in drift direction. Another factor that has to be considered is the drift speed of ions. Since the mobility is 6 orders of magnitudes lower (see Table 3.1) compared to electron drift speeds (1 mm s^{-1} vs. 1 mm μs^{-1}), ions remain much longer in the detector than electrons. In large scale detectors (such as MicroBooNE) with high event rates, this will lead to the accumulation of positive space charge towards the cathode. This cloud of positive charge will distort the electric field introduced by the anode-cathode configuration and ultimately lead to deviations from the ideal scenario of straight line electric field lines in the detector. The high event rate originates mainly from the high flux of cosmic

radiation interacting in the detector, if the device is installed at the earths surface or at shallow depths. The distortions must be accounted for, either by introducing systematic error, or by means of a calibration.

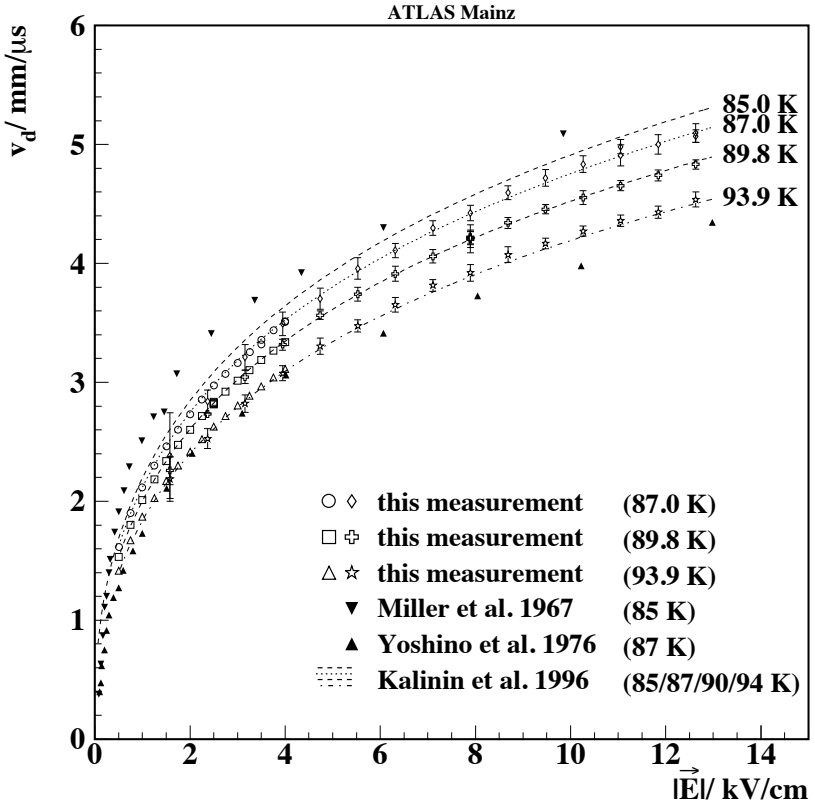

Figure 3.7: Drift velocity in liquid argon versus electric field strength for different temperatures [71].

Another effect acting on free charge traversing a medium is diffusion, describing the spatial broadening of a cloud charge over time. In the case of zero electric field, diffusion is isotropic and can be described by a diffusion constant D. When an electric field is applied the Einstein equation has to be modified and results in [20]

$$\frac{eD}{\mu} = f(v_d) \cdot \langle E \rangle, \tag{3.20}$$

where e is the elementary charge, μ is the carrier mobility (introduced above), f a constant depending on the drift velocity and $\langle E \rangle$ is the mean electron energy. Furthermore, the electric field breaks the isotropy of the diffusion into transverse and longitudinal directions. This requires the introduction of two independent diffusion coefficients D_T and D_L. With the knowledge of the diffusion coefficients the width of an originally infinitely small charge cloud as a function of time can be determined to

$$\sigma_{L,t} = \sqrt{2tD_{L,T}}. \tag{3.21}$$

Via the charge carrier mobility the diffusion again depends on the electric field. As can be see from rearranging Equation 3.20, the diffusion is lower for higher electric

fields. For long drift distances or long drift times, the spatial diffusion can limit the detector resolution.

A third process affecting the electrons drifting in Liquid Argon (LAr) is the attatchement to an impurity. Impurities of concern are molecules or atoms with a high electron negativity, which describes their tendency to attract an electron to form a negative ion. Main contaminants in LArTPCs are oxygen and water. The rate of electron attachment losses in a charge cloud formed by $N_e(t)$ electrons at time t can be modeled by [48]

$$\frac{dN_e}{dt} = -k_{tot} \cdot N_e t. \tag{3.22}$$

Here $k_{tot} = \sum_i k_i$ is the sum over all individual probabilities k_i for a molecule or atom i to attatch an electron. Individual probabilities are directly proportional to the number density of the kind of impurity in LAr. Integrating the above equation yields

$$N_e(t) = N(0)e^{-k_{tot}t} = N_0 e^{-t/\tau}. \tag{3.23}$$

In the second form N_0 denotes the number of electrons present after recombination and τ is known as the electron lifetime. A rule of thumb relating the oxygen equivalent impurities and the electron life time is given by [72]

$$\rho(O_2 \text{ equiv.})[ppt] \approx \frac{300}{\tau[ms]}. \tag{3.24}$$

Where *ppt* stands for parts per trillion (number of impurities per 1×10^{12} atoms).

3.7 WIREPLANE READOUT AND SIGNAL FORMATION

At the wireplane, which marks the end of the drift field spanned in the anode-cathode configuration, the electrons produced during the ionization process are converted to an electric signal on an array of thin wires. Spatial resolution is obtained by spanning two wire meshes perpendicular to each other at the anode end of the detector (x-y plane). Within the mesh, the wire spacing is typically 2 mm to 4 mm, and the wire diameter is of the order of few µm. The two meshes are usually spaced in a similar rage as the inter-wire distance. Here the electric field is shaped such that the drifting electrons will induce a current on the inner wireplane and will be solely collected at the last wireplane. The signals of the wireplanes are read out simultaneously allowing to determine the relative arrival times. This relative timing information enables the reconstruction of the particle track in the detector, Figure 3.8 illustrates the described procedure.

To ensure that no charge is collected at the induction wireplane, the field $\vec{E_b}$ behind the induction wires has to be larger than the field $\vec{E_f}$ in front of it. A so called transparency condition for the two field strhengths is given by [73]

$$|\vec{E_b}| \; > \; \frac{1+\rho}{1-\rho} |\vec{E_f}|, \tag{3.25}$$

where $\rho = 2\pi r/d$ with r and d being the wire radius and the inter-wire spacing. The charge carriers approaching the induction wireplane induce a negative potential drop in the wires located at corresponding spatial coordinate. After the

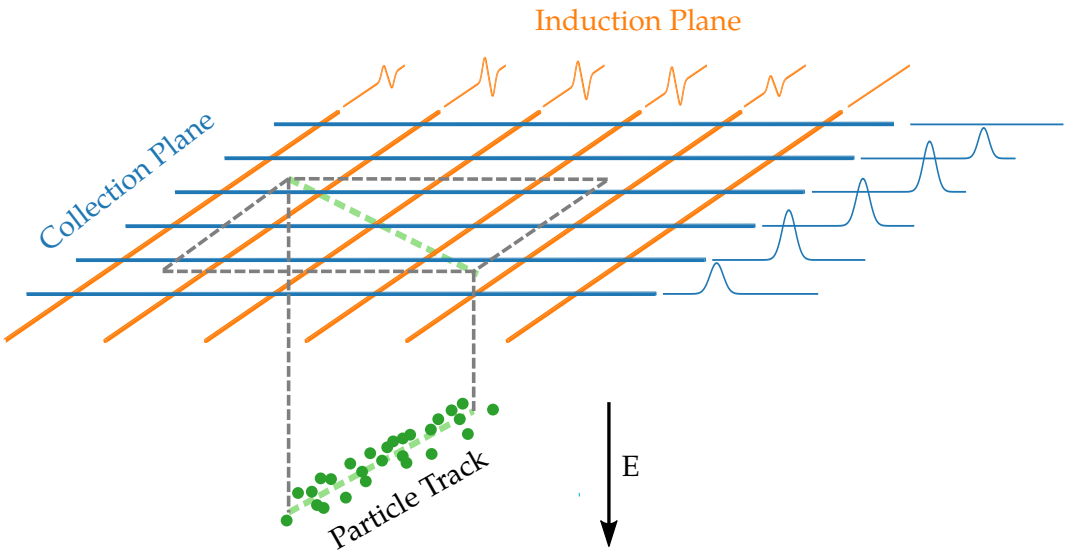

Figure 3.8: Generation of signals on the lower induction (orange) and upper collection (blue) wireplane induced by electrons drifted to the wireplane. The green line represents the projected particle track onto the wireplanes. Signals formed on the wires are shifted relative in time by th later arrival time due to the longer drift distance (time) inside the detector.

charge carriers pass the the first wireplane, the distance to the wireplane increases again and a current in the opposite direction is induced. This behaviour leads to an bipolar signal in induction wires. Whenever the transparency condition is fulfilled, no charge is collected at the induction wireplane. Field lines end at the last wireplane, hence the drifting charge is collected and the electrical signal is unipolar. For typical configurations in LArTPCs, a minimum ionizing particle track produces roughly $6000\,\mathrm{mm}^{-1}$ electrons, corresponding to 1 fC per wire at the readout [74]. Pre-amplifiers are usually installed as close as possible to the wires to enhance the signal before digitization. To resolve ambiguities in later event reconstruction, a setup with more that two wire meshes is usually deployed. In this configuration two induction wireplanes at a specific angle with respect to the collection wire plane are installed.

3.8 ELECTRIC FIELD

In this section the impacts of the electric field onto the detector performance are summarized. A summary of the involved processes is also given in Figure 3.9. The shape and strength of the electric field are governed by two design parameters. First, the detector geometry, with the cathode, field cage rings and anode plane define the shape of the electric field. Secondly, the voltage potential applied to the cathode defines the strength of the electric field. Usually the geometry is constant for an LArTPC, the applied electric potential is a variable parameter and can be adjusted to the requirements of the measurement campaign. Although, if chosen too low, all electrons from the signal might be absorbed by impurities present in the detector, see Section 3.6 for details. Any space charge, large enough to compete

with the applied potential at the cathode, present in the detector will alter the electric field as well. Since ions produced in the ionization process drift slowly (of the order of $cm\,s^{-1}$, see Table 3.1) and the penetration by cosmic muons is high (discussed later), significant charge can accululate.

The electrons and ion formed during the ionization process are subject to recombination described in Section 3.4, with an increased field, fewer pairs recombine and an electron cloud is formed. Hence, the light yield is diminished for increased field strengths. The light and charge yield is a crucial parameter in a LArTPC, both directly influence the calorimetric capabilities of the detector. With the exact knowledge of the local electric field, the recombination rate can be determined and variations in the produced charge can be calibrated. The electron cloud drifts trough the LAr along the field lines (see Section 3.6 for details), hence inhomogeneities in the electric field of any kind will distort the electron cloud, resulting in a distortion of the 2D projection recorded at the wireplane. Trough the dependence of the drift speed on the electric field strength the picture is further complicated, the linear back-projection (in time) of a recorded charge signal on the wireplane becomes invalid when the electric field is non-linear. Hence, a distortion in the electric field will result in a 3D distortion of the naively reconstructed (assuming a uniform field) charge cloud. This distortion will again affect calorimetry performance as the track length is affected. Furthermore, it will affect spatial cuts applied for event selection trough the distortion of the track and track length. Calibration of distortion effects is possible with an exact mapping of the electric field in the detector.

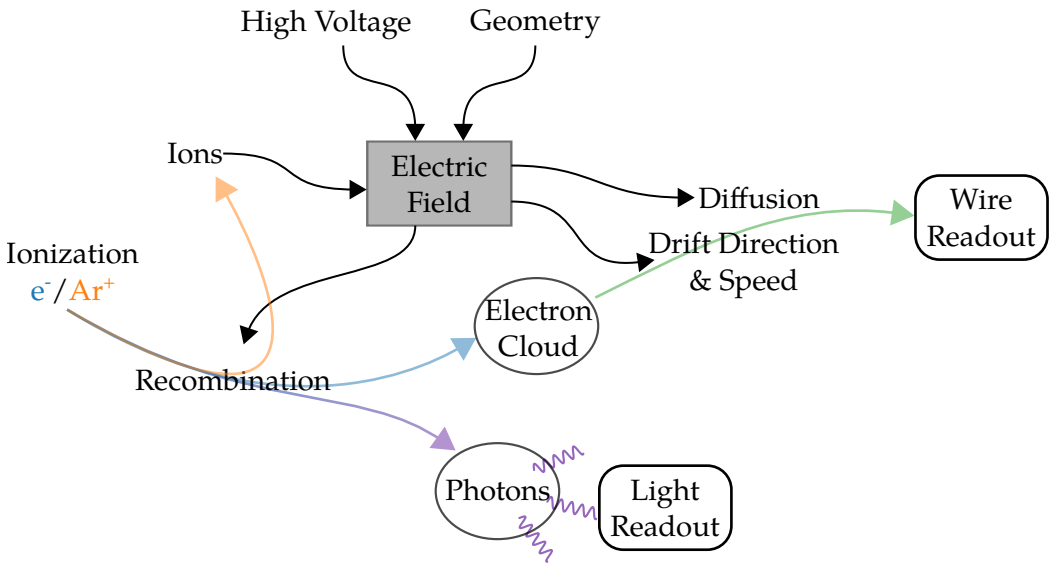

Figure 3.9: Impacts of the electric field onto detector performance.

4

MICROBOONE

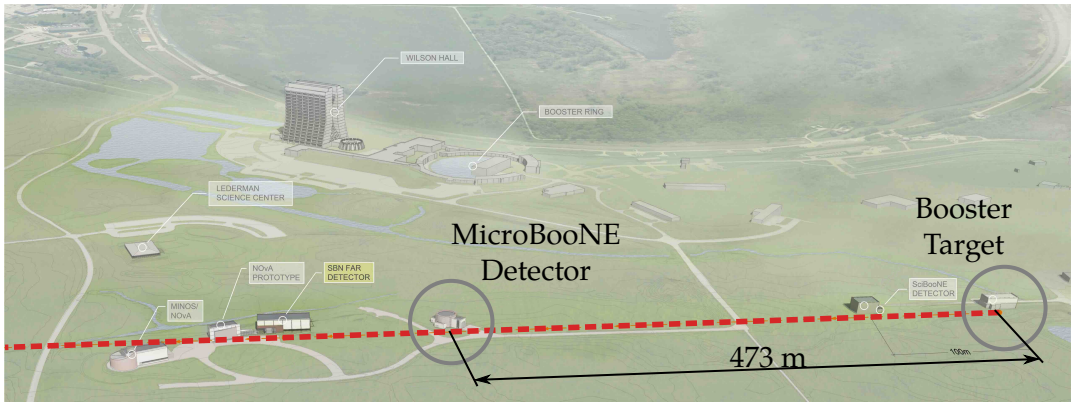

Figure 4.1: Aerial view of the booster neutrino beamline with MicroBooNE situated in the middle of the image, 473 m downstream from the neutrino source (Booster Targer). The neutrino beam is shown as a dashed red line.

The MicroBooNE detector at Fermilab in Batavia Illinois, is hosted in the Liquid Argon Test Facility (LArTF), 470 m downstream of the neutrino production target. Neutrinos with a peak energy of 700 MeV are produced in the Booster Neutrino Beam (BNB) mainly by decaying pions, produced by protons impinged onto a beryllium target. The neutrinos are then detected in a large scale Liquid Argon Time Projection Chamber (LArTPC). It's main physical goal is to understand the nature of the Low Energy Excess (LEE) observed in MiniBooNE (see Section 2.4), in contrast to MiniBooNE, LArTPCs are capable of distinguishing between electrons and photons produced in electron neutrino interactions. For the objective of a precision measurement of the neutrino signal it is crucial to characterize the electric field in the detector. This will be achieved by a laser calibration system developed in the scope of this thesis. Additionally, MicroBooNE will perform neutrino cross-section measurements helping to obtain a clearer picture of neutrino interactions with argon. Each sub-system of the experiment is described in the sections below, tightly following the main publication of the detector construction [52].

4.1 BOOSTER NEUTRINO BEAM

The Booster Neutrino Beam (BNB) is an evolution of the neutrino horn proposed and realized by Van der Meer [75] at CERN. An in detail description of the BNB can be found in [76, 77], the following discussion is based on these references. Protons with an energy of 8 GeV are extracted from the Fermilab booster rapid-cycling synchrotron at a rate of 5 Hz The extracted protons are impinged onto a beryllium target, in the target interactions mainly pions and a small fraction of kaons are produced. The target has the shape of a long rod with a length of 71.1 cm and a radius

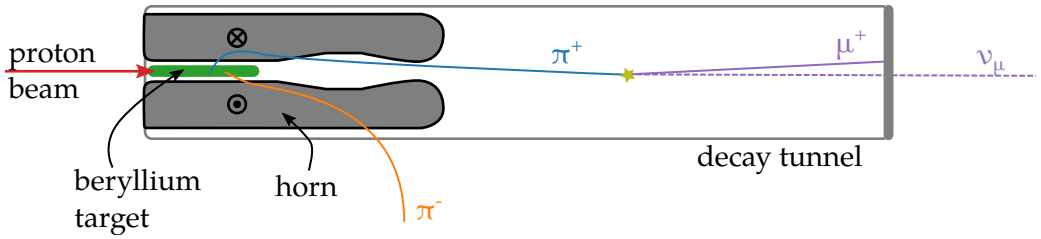

Figure 4.2: Beam operation principle, an incident proton beam produces mainly pions in a beryllium target. The pions of the positive charge are focused in the horn, whereas the negative pions are defocused. Finally the pion decays into a muon and a muon neutrino. The muon is absorbed at the end of the decay tunnel and the neutrino travels to the detector, where it hopefully interacts.

of 0.51 cm. Its form is governed by the absorption length of protons in the target, so to optimize the conversion of protons into mesons. Although, the incident high energetic proton governs the forward direction of the decay products, neutrino intensities directed at the MicroBooNE detector would still be too low to conduct neutrino studies within an acceptable time-frame. Therefore, the beryllium target is placed inside a magnet focusing the decay products into a beam towards the detector. The focusing electro-magnet is made of aluminum and has a toroidal shape, it is pulsed with a peak current of 174 kA synchronized with the arrival of a proton beam bunch. The magnetic horn consists of two axially-symmetric conductors with a current sheet running down the inner conductor and returning on the outer conductor. Between the conductors a torodial magnetic field is produced, the resulting force $F = q\vec{v} \times \vec{B}$ from the magnetic field acts as a restoring force, thus focusing particles of one sign (π^+ or π^-) and defocusing particles of the other sign. Thus, the horn construction not only enhances the pion flux towards the detector but also selects the sign. Pions produced, selected for sign and focused in the horn will eventually decay into a muon and a neutrino according to Equation 6.1. For this a 50 m long decay tunnel filled with air is foreseen. The emitted muon is then absorbed at the end of the decay tunnel before decaying, preventing the electron neutrinos emitted in the muon decay to pollute the pure muon neutrino beam. Although optimized for muon neutrino purity, other neutrino flavours can leak into the beam content, due to the decay of the muon inside the decay tunnel or very forward going pions (which are not defocused by the horn) of the wrong sign. Furthermore, primary kaons produced in addition to the pions have several decay channels leading to the production of electron neutrinos. The discussed principle of the neutrino beam generation is illustrated in Figure 4.2 and the expected neutrino energy at the MicroBooNE detector is shown in Figure 4.3.

4.2 CRYOGENIC SYSTEM

The temperature range of 83 K to 87 K, where argon is in the liquid aggregate state at normal pressure, requires cryogenic systems to operate a LArTPC. The system is

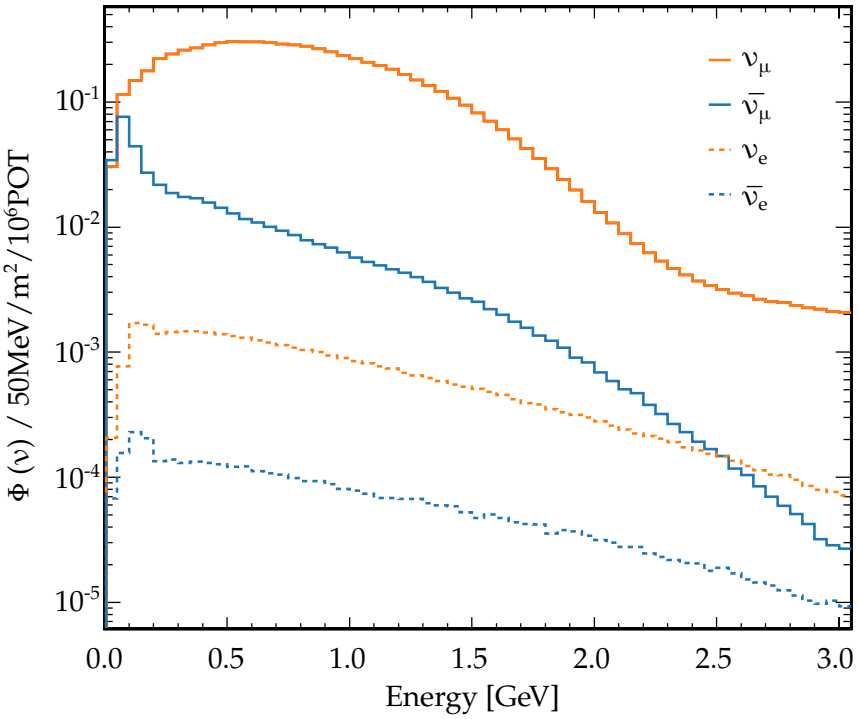

Figure 4.3: Flux for different neutrino flavors in MicroBooNE. Adapted from [78].

complicated by the requirement of low levels of oxygen equivalent impurities has to be achieved and maintained.

The cryostat itself has three major components: a stainless steel vessel hosting all the liquid argon and the detector, front and rear support structure and 41 cm foam insulation, restricting heat input from ambient air, covering the entire cryostat surface. The cryostat is of cylindrical shape enclosed by domed caps closing each end, with a total length of 12.2 m and a diameter of 3.81 m and a wall thickness of 11.1 mm. Requiring a low level of oxygen equivalent impurities of 100 ppt, corresponding to a electron lifetime of roughly 3 ms, requires the minimization of outgassing within the gas phase and avoid leakage and diffusion of air into the cryostat. Furthermore, to maintain the high liquid argon purity it is necessary to constantly remove these impurities. For this purpose a re-circulation and filter system is build, consisting of two identical subsystems. Each system deploying a liquid argon pump[1] and two distinct filters, using different adsorber materials[2,3], removing mainly water or oxygen, respectively. Impurity concentration is monitored with two purity monitors [79] immersed in the liquid argon within the cryostat volume. The filters are regenerated in-situ and as needed, removing the acquired and bound oxygen and water by heating the filter material while flushing with an argon-hydrogen gas mixture. This exothermic reaction forms water with the captured oxygen that is sub-sequentially flushed out with argon gas. The heat input to

1 Barber-Nichols BNCP-32B-000 magnetically-driven partial-emission centrifugal pump
2 Molecular sieve supplied by Sigma-Aldrich
3 BASF CU-0226 S, a pelletized material of copper impregnated on a high-surface-area alumina

the cryostat by the ambient air as well as the detector electronics immersed in the not instrumented liquid argon leads to evaporation. To maintain the liquid argon level constant and to keep temperature and pressure inside the cryostat constant, a nitrogen refrigeration system is deployed. This system contains two condensers in parallel, one for operational use and another one for backup. Each condenser contains two liquid nitrogen coils, an inner and an outer, with the gas argon on the shell side. The system can handle a heat load of up to 6 kW, using 3400 L of liquid nitrogen per day.

4.3 TIME-PROJECTION CHAMBER

The LArTPC is composed of three main structures: the cathode, the field cage, and the anode. A negative voltage is introduced via a feedthrough passing through the cryostat connected to the cathode, defining the electric potential at the cathode. A uniform electric field between the cathode and the anode planes is achieved by a series of field cage rings connected by a voltage divider chain starting at the cathode and ending at the anode plane. The field cage structure is held in place by a G-10[1] support structure. Facing the cathode planes are the sense wire planes: two induction planes (referred to as the "U" and "V" planes) with wires oriented at ± 60 deg from vertical, followed by one collection plane (referred to as the "Y" plane) with vertically-oriented wires. The wires of the anode planes are the sensing elements that detect the ionization created by charged particles traveling through the LArTPC. Figure 4.5 depicts the assembled MicroBooNE LArTPC after insertion into the cryostat, showing details of the cathode, field cage, and anode plane. Table 4.1 lists the main parameters of the MicroBooNE LArTPC.

4.4 LIGHT COLLECTION SYSTEM

Liquid argon is a bright scintillator (see Section 3.5), sampling the light is essential for 3D event reconstruction and can be used for calorimetry. The light produced by neutrino interactions in MicroBooNE is an important input for both event selection and reconstruction. One of the critical capabilities the light collection system provides is the ability to form a beam-event trigger when a pulse of light is observed in coincidence with the beam spill. Such a trigger will substantially reduce the overall data output rate. For non-beam physics studies, the light system provides triggering and an event t_0 for the LArTPC system.

The light collection system consists of primary and secondary sub-systems. The primary light collection system is made up of optical units, each one consisting of a Photomultiplier Tube (PMT)[2] located behind a wavelength-shifting plate. In total, 32 optical units were installed, yielding 0.9% photocathode coverage. The secondary system consists of four light guide paddles. These paddles were introduced for R&D studies for future LArTPC, and are placed near the primary optical units to allow a comparison of their performances. A flasher system, used for calibration, consists of optical fibers bringing visible light from an LED to each PMT face.

1 A glass epoxy composite laminate material well suited for liquid argon temperatures
2 8-inch diameter Hamamatsu 5912-02MOD cryogenic PMT

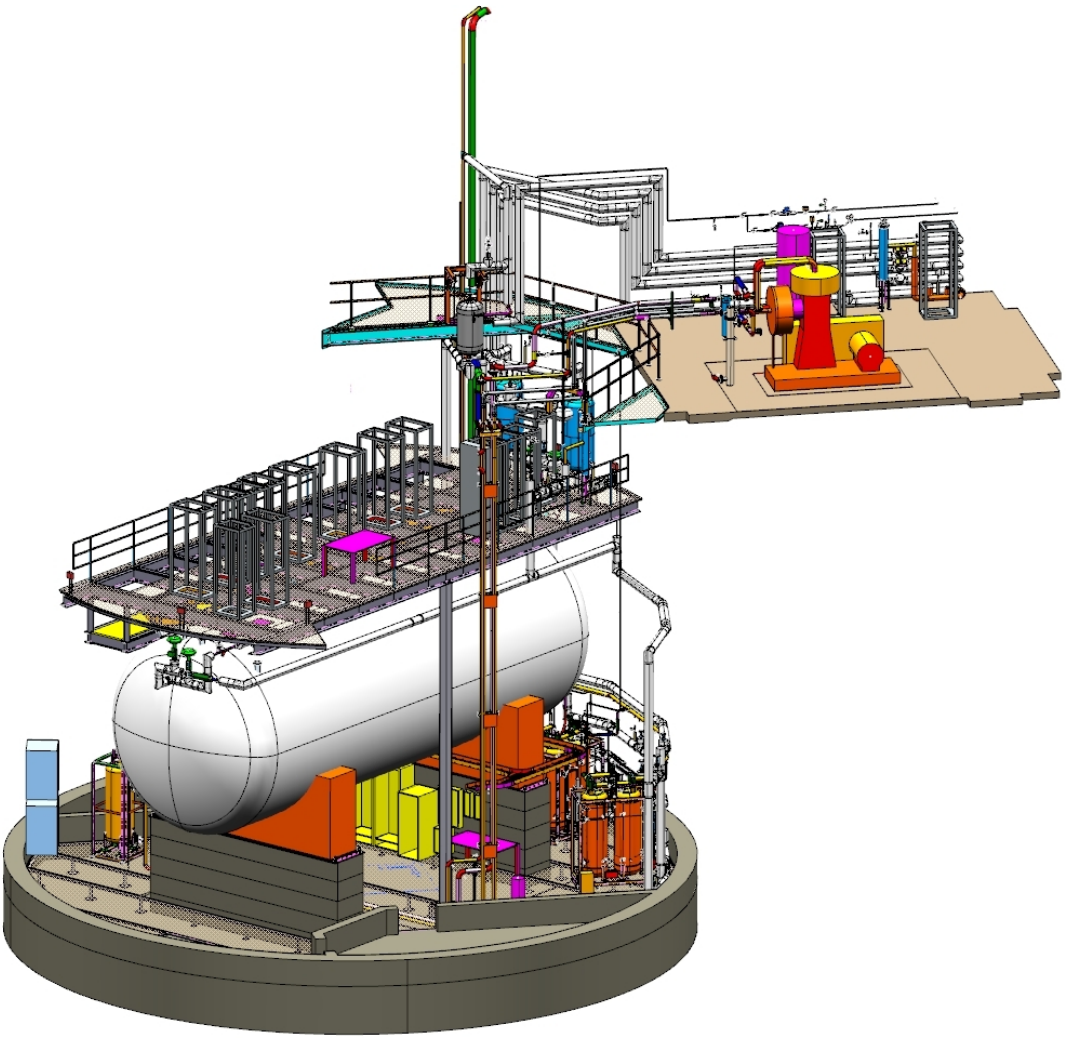

Figure 4.4: MicroBooNE cryogenic system overview. Centrally (in white) the cryostat is shown sitting on the front and rear support structure. Below the cryostat, the filter and recirculation components are placed. The (re-)filling system and refrigeration components are hosted on the ground platform on the top right of the figure. Right above the cryostat a platform is installed, hosting computer racks for readout and control systems. [52].

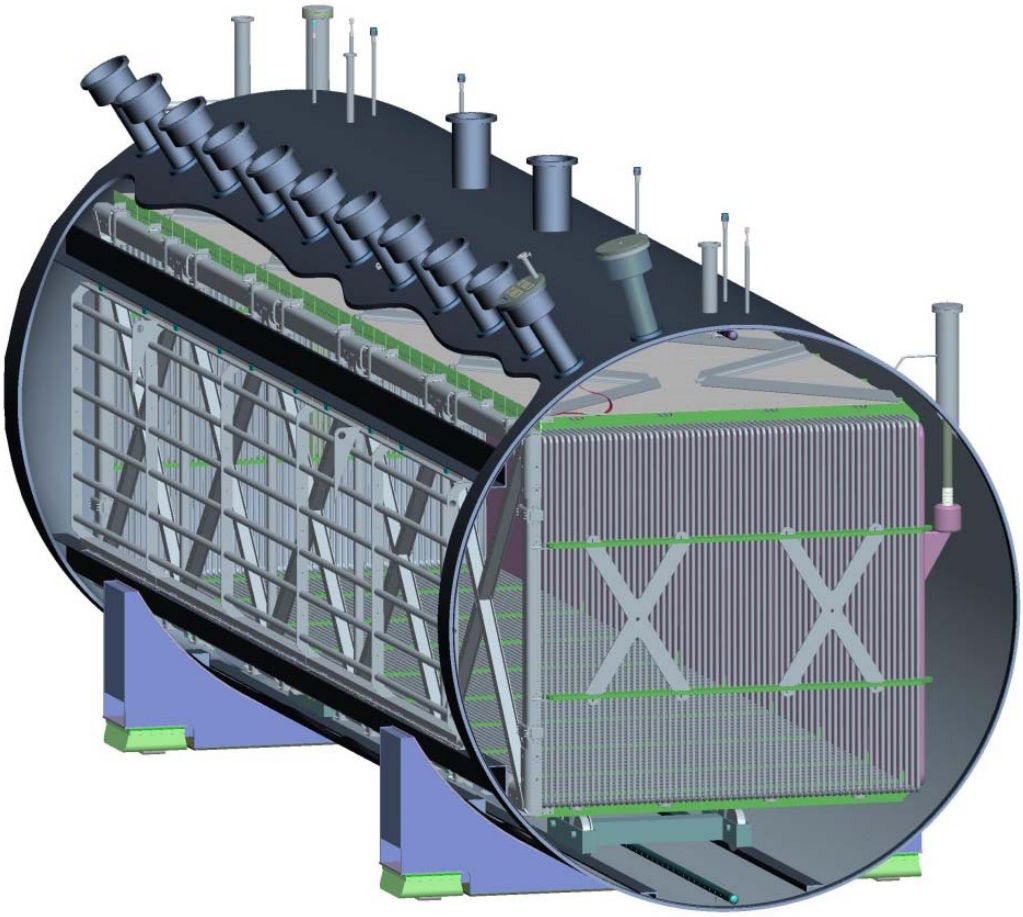

Figure 4.5: Microboone TPC assembly in cryostat, the anode is situated on the left hand side, 64 field cages span the horizontal axis, reaching to the cathode ot the right hand side.

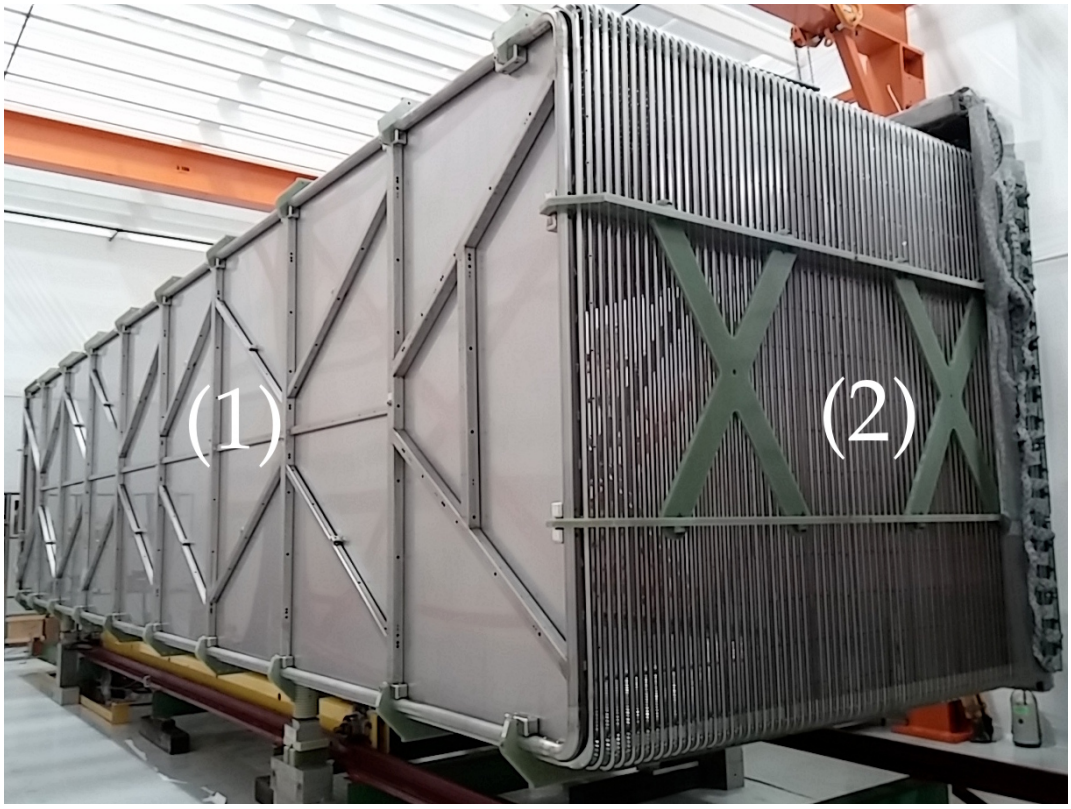

Figure 4.6: Photograph of the Microboone TPC assembly showing the back of the cathode (1) an the field cage rings (2).

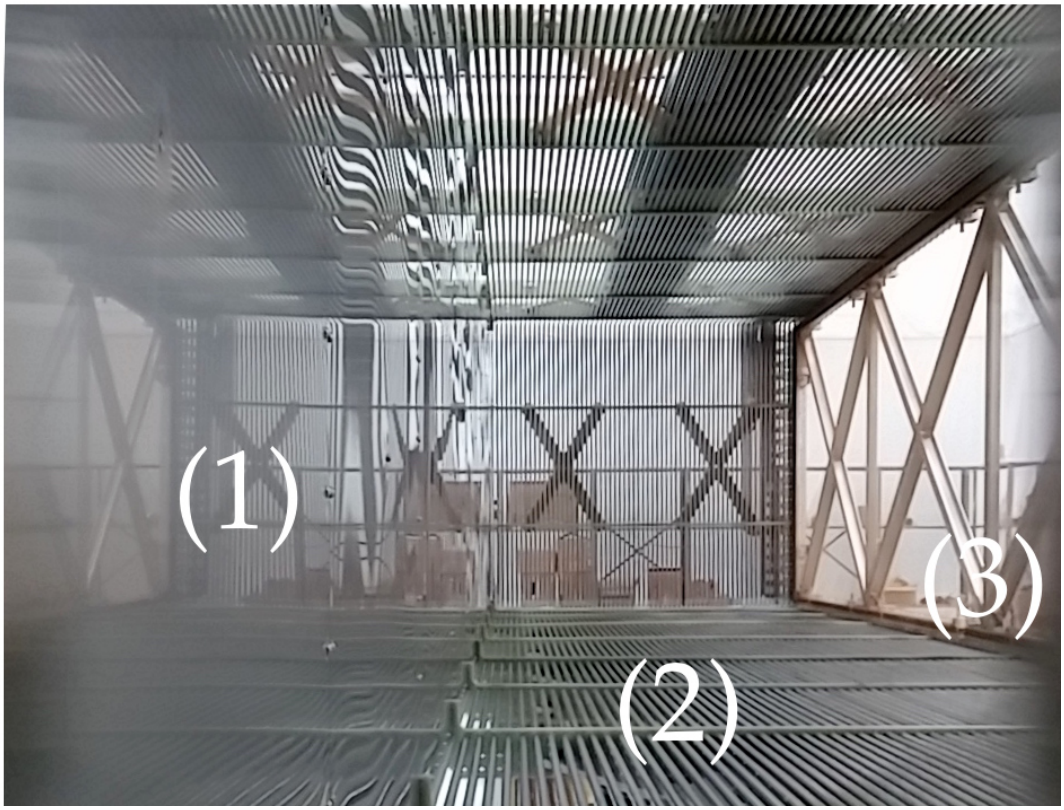

Figure 4.7: Interior Photograph of the Microboone TPC assembly showing the cathode (1) on the left hand side, the field cage rings (2) in the central region and the wireplane (3) to the right

PARAMETER	VALUE
LArTPC (active) dimensions ($h \times w \times l$)	2.325 m × 2.560 m × 10.368 m
LArTPC (active) mass	85 tons
Number of Anode planes	3
Anode planes spacing	3 mm
Wire pitch	3 mm
Wire type	Stainless Steel, $d = 150\,\mu$m
Wire coating	2 µm Cu, 0.1 µm Ag
Design Wire tension	6.0 ± 1.0 N
# wires (total)	8256
# Inductiono plane (U) wires	2400
# Induction1 plane (V) wires	2400
# Collection plane (Y) wires	3456
Wire orientation (w.r.t. vertical)	60 deg,−60 deg,0 deg (U,V,Y)
Cathode voltage (operational)	−70 kV
Bias voltages (U,V,Y)	−110 V, 0 V, 230 V
Drift-field	273 V/cm
# Field-cage steps	64
Ring-to-ring voltage step	2 kV
Field cage ring diameter	2.54 cm
Field cage ring thickness	0.51 cm
Ring-to-ring distance (center to center)	4 cm
Corner curvature radius	5.24 cm
Support structure material	G-10

Table 4.1: MicroBooNE LArTPC design parameters and operating conditions. [52]

The light collection detectors are located in the y-z plane behind the anode planes of the LArTPC. The combined transparency of the three anode planes is 86% for light at normal incidence. This transparency value assumes 100% of VUV photons impinging on the wires are absorbed. The detectors were placed so as not to be obscured by the LArTPC structural cross-bars.

4.5 READOUT AND DATA ACQUISITION

Both, the 8256 sense wires and the 32 PMTs produce analog signals that must be amplified, digitized and stored for later analysis. While the LArTPC and PMT readout systems share the same back-end design that organizes and packages the data for delivery to the Data Acquisition (DAQ) system, each of them employ different analog front-end and digitization designs.

To obtain optimum detector performance, MicroBooNE uses cryogenic low-noise front-end electronics for readout of the sense wires. An ASIC[1] containing a preamplifier, shaper, and signal driver is connected to each sense wire as close as possible on the wire carrier boards, so reducing total input impedance. The ASIC was custom designed for the use in LArTPCs [80]. Individual wires are in addition connected to the wire bias voltage distribution system, decoupling capacitors, and calibration networks. The output signal of the ASIC is then brought outside the cryostat trough a feedthrough hosting a custom designed intermediate amplifiers. The amplified warm signal is then routed to an Analog Digital Converter (ADC) module[2] situated in a standard rack on the MicroBooNE platform above the detector. The ADC module digitizes the signals continuously at 16 MHz. Each channel has a configurable baseline, which is either set low (450 ADC counts) for collection channels or at the middle of the dynamic range (2055 ADC counts) for induction channels. This configuration ensures that both the collection plane unipolar signals and the induction plane bipolar signals can make optimal use of the ADCs dynamic range. Behind the ADCs a FPGA[3] is responsible for data processing and reduction (lossless Huffman encoding), as well as preparation for readout by the DAQ. One FPGA handles 64 digitized channels and employs a circular DRAM[4] buffer.

The signal path of the PMTs is considerably less complex compared to the sense wires. The PMT itself produces a large enough signal that is able to overcome the distance to the cryostat volume, hence no cold preamplification is necessary. From each PMT a low-gain and high-gain is extracted and wired to a shaper and preamlifier situated outside the cryostat. The pre-processed analog signal is then digitized with at a sampling rate of 64 MHz by a 12-bit ADC[5].

The data from each crate (hosting either TPC or PMT ADCs) of the backend electronics is sent to a dedicated server via optical fibers. A real-time application places this data in an internal buffer, collects all segments belonging to an event (from all crates), and creates a sub-event fragment. The beam-triggered data readout stream, in which the data arrives with every trigger, these fragments are sent to a single event-building machine over an internal network. Full events are checked for consistency and written to local disk on the event builder before being sent offline for further processing and storage. A high-level software trigger, is applied to the data to determine whether events should be written locally or ignored.

1 Application-specific integrated circuit
2 each module hosts eight AD9222 octal-channel 12-bit ADCs
3 Field programmable gate array
4 Dynamic random-access memory
5 ADS5272 octal-channel 12-bit ADC

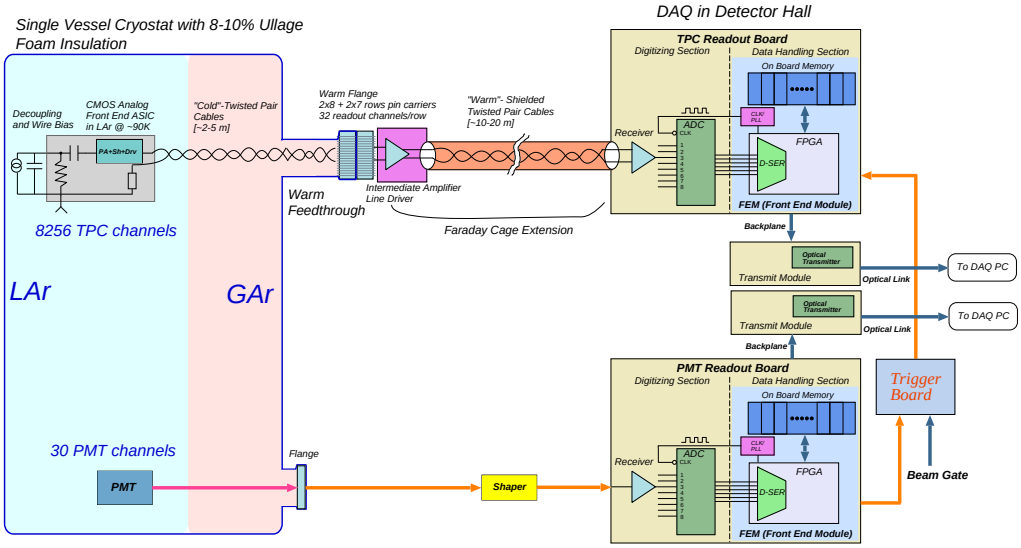

Figure 4.8: Schematic path of the TPC and PMT readout front- and back-end. Analog signals are generated on the right hand side and evolve to the right trough different amplification, shaping and digitization steps. Adapted from [52].

5

UV-LASER CALIBRATION SYSTEM

Introducing well-defined ionization tracks into a Liquid Argon Time Projection Chamber (LArTPC) can be achieved by steering a high-energetic Ultra Violet (UV) laser beam into the detector volume. These signals have the unique feature that their precise ionization location along the track is known a priori. This information can be used to characterize and calibrate the detector response, especially the electric field responsible for the electron drift. This chapter will give a thorough description of the hardware and software necessary to operate such a UV laser calibration system, as well as the underlying physical processes involved. Moreover, initial measurements, required before a precsision mesaurement of the electric field can be performed, are discussed. Two identical UV laser are at the heart of the MicroBooNE laser calibration system, these illuminate the Time Projection Chamber (TPC) at various angles from each end of the cryostat. On an optical bench, an UV laser beam is generated and its properties are optimized for later ionization in the detector. To route the UV beam into the cryostat an optical feedthrough is necessary. Finally, to scan the detector volume with laser beams a movable mirror is needed to deflect the beam in the desired direction. The UV laser beam will then ionize the liquid argon and so mimic particle tracks in the TPC, with a known original ionization trajectory in the detector. Two identical laser systems are installed at each end of the detector for optimal coverage of the detector volume. In the following discussion only where necessary the two individual systems are portrayed separately. So far several laser calibration systems have been implemented into gas time projection chambers [81, 82, 83], but no previous realization of such a system has been employed in a LArTPC prior to the work being presented in this thesis.

5.1 WORKING PRINCIPLE

The ionization potential of liquefied argon has been determined to be 13.84 eV (Table 3.1). This would require a photon with wavelength of 89 nm to create an ion-electron pair. Laser systems emitting light in this wavelength region are not commercially available. However, an additional path to ionization by below ionization wavelength photons exist, namely multiphoton-absorbtion. As the name suggests, two or more photons are simultaneously absorbed, their total energy is transferred to a shell electron which can overcome the ionization potential. The process can be understood and described as a ladder effect, where a single photon absorption forms a virtual state, enabling a second photon to be absorbed and form an even higher energetic state. This can continue until the ionization potential is reached (or even further). The ionization rate W can be described by [84]

$$W = \sigma^{(K)}(\lambda, \rho)\left(\frac{I}{\omega}\right)^{K}, \tag{5.1}$$

here I is the laser beam intensity, ω the laser frequency, $\sigma^{(K)}$ is the generalized K-th cross-section and K is the number of photons required for ionization. In the case of $K = 1$, Equation 5.1 becomes the relation for the rate (single) of photo ionization and $\sigma^{(1)}$ is the photon cross-section. The cross section is characterized by the atomic structure and the parameters of the incoming laser beam, specifically the wavelength λ and the ellipticity ρ. Expressions for the cross-section can be obtained by time-dependent perturbation theory, but this is not presented here. A detailed discussion can be found in [84, 85]. The two photon cross section for gaseous argon is of the order of $1 \times 10^{-50}\,\mathrm{cm}^{-4}\mathrm{s}^{-1}$[86]. Quantitatively, the ladder process, mentioned above, can be used to understand the cross-section behavior. Each step has a small finite lifetime to complete the ladder and so it becomes increasingly unlikely that another photon is absorbed within this time frame. Hence, the more steps are present in the ladder to reach the continuum, the lower the cross section. In the same picture, if a virtual excited state is replaced with a bound excited state, having a considerably longer lifetime, the cross-section is significantly enhanced. Exclusion rules have to be considered when a bound state exists, since angular momentum is conserved. For example since a single photon has spin of $J = \pm 1$, the final excited state reached by a 2-photon absorption process is required to have a spin orbital with a change of $\Delta J = +2, 0$ or -1.

Furthermore, the liquid state of the argon has to be taken into account when energy levels are considered for multi-photon absorption. In the liquid a fully filled valence band and an empty conduction band is formed. The valence band width in liquid argon was measured to be $E_{val} = 0.1\,\mathrm{eV}$ [87]. Similarly, the conduction band lowers the ionization potential (the width of this band is commonly labeled as V_0). Measurements have determined V_0 for liquid argon to be 0.2 eV [88]. Additionally, when electric charge is present in a dielectric material, such as liquid argon, electric polarization occurs. The effect can be quantified by means of the Born model, here the difference in energy of the electric field for the ion in vacuum and the dielectric medium is determined for a Coulomb field [89]. This difference is called the polarization energy P_+, and is given by

$$P_+ = W(\epsilon_r) - W(\epsilon_0) = -\frac{e^2}{8\pi\epsilon_0 R}\left(1 - \frac{1}{\epsilon_r}\right) \tag{5.2}$$

where R is the ion radius and e the electron charge. Using $\epsilon_r = 1.59\,\mathrm{nm}$ and $R = 0.088\,\mathrm{nm}$ the polarization energy was estimated to be $P_+ = 1.79\,\mathrm{eV}$ [90]. The discussed effects on the ionization potential present in the liquid argon can be summarized by,

$$I_{liquid} = I_{gas} + E_{val} + V_0 + P_+ = 13.8\,\mathrm{eV}. \tag{5.3}$$

This results in a energy shift of $\Delta E = -1.9\,\mathrm{eV}$ compared to gaseous argon. In addition to the decrease of the ionization potential in the liquid phase, the energy lines are broadened. The width is weakly density dependent and has been determined to be of the order of 0.1 eV [91]. The energy levels in the liquid and gas phase are sketched in Figure 5.1, also included is the broadening of the ground, excited, and ionization levels. In the figure even spin states are shown in orange and odd states in blue, respectively.

Commercial lasers with an acceptable form factor, price range and beam intensities can reach wavelengths of 266 nm using the well-established Nd:YAG pump

medium and Q-Switch technique. A thorough description of the deployed laser is given in following section. This wavelength translates into a photon energy of 4.66 eV. Since $3E_\gamma > I_{liquid}$, three-photon ionization in liquid argon is possible with this configuration. From the energy level diagram (Figure 5.1) it becomes apparent that with this photon energy a two-photon absorption by the excited state at configurations $3s^2 3p^5(2P^\circ_{1/2})4s$ ($J = 0$) and $3s^2 3p^5(2P^\circ_{3/2})4s$ ($J = 2$) become feasible. Due to the odd spin state change, other transitions are not allowed. As discussed earlier this greatly increases the cross-section of the total three-photon process and was measured in [90]. The third photon then lifts the excited state above the ionization potential, transferring the surplus energy to the ionized electron.

Three-photon ionization of argon gas was used in the STAR TPC for E-Field calibration at the Relativistic Heavy Ion Collider at Brookhaven National Laboratory [92]. In liquified argon, the ICARUS collaboration [93] was the first experiment to use an UV laser to introduce artificial tracks in a TPC. The herein presented laser system has its roots in the liquid argon efforts of the Laboraroty for High Energy Physic based at University of Bern. Within this program the two-photon absorption cross-section was measured [90] and the laser system was extensively used in the ARGONTUBE detector [94, 95, 96] for E-Field characterization and liquid argon purity measurements.

Deonle [84] introduces two regimes of multi-photon absorption, based on the relation of the electric field strength defined by [98] and the binding energy of the atomic electron. The criterion is defined as

$$\gamma = \frac{\omega}{\omega_t} = \omega \frac{\sqrt{2m_e E_i}}{eF}, \tag{5.4}$$

where ω is the radiation frequency and ω_t is the frequency up to which the tunneling probability is independent of the radiation frequency. E_i the binding energy of the electron and F the field strength of the incident radiation. ω_t is estimated from the mean free path l of an electron inside the atomic potential ($l \approx E_i/eF$) and the approximate velocity $v_e \approx \sqrt{I/m}$ of the electron therein. Only if $\gamma^2 \gg 1$, Equation 5.1 is applicable. Otherwise, the ionization rate depends exponentially on the field strength, hence also on the intensity. The electric field of a plane wave laser pulse with a Gaussian beam profile is given by [99]

$$F = \sqrt{\frac{2I}{c\epsilon_r\epsilon_0}} = 776 \times 10^3\,\mathrm{V/cm} \tag{5.5}$$

with c the speed of light and ϵ_0 and ϵ_r are the vacuum and relative dielectric constants. Here I the intensity of a Gaussian beam; $I = \frac{P}{\pi w^2/2}$, where P is the pulse power and w is the beam spot diameter. The pulse power can be determined for a Gaussian beam by $P = E_p/\tau_p$ where E_p and τ_p are the pulse energy and the pulse duration. For the deployed laser, $P = 9.4\,\mathrm{MW}$, $I = 11.9\,\mathrm{MW/cm^2}$. Using this field strength and the ionization potential given in Table 3.1, $\gamma = 189703$ and Equation 5.1 is applicable for the presented configuration.

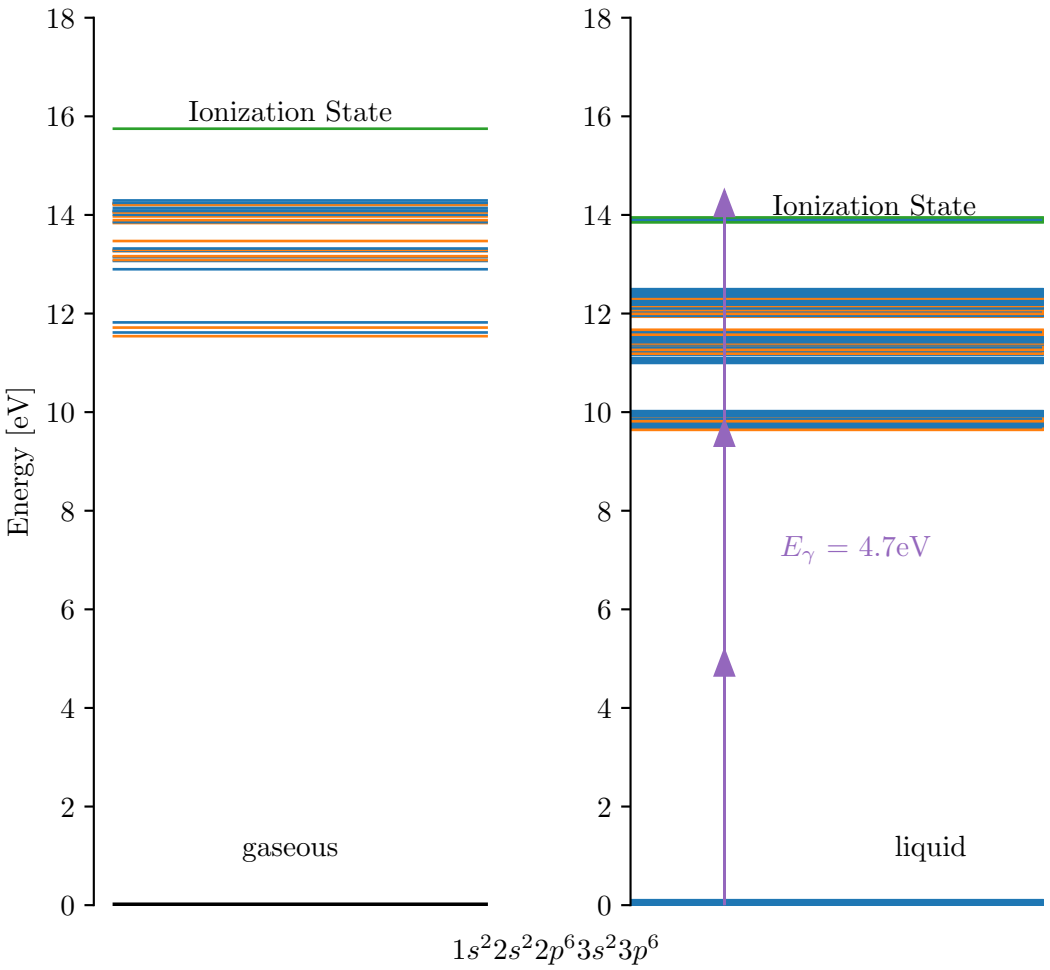

Figure 5.1: Energy levels of gaseous (left) and liquid (right) argon relevant for UV-laser absorption, data from [97]. The ionization state is shown in green. In orange and blue, excited states with even and odd spin states are depicted, respectively. Three stacked photons with a wavelength of 266 nm are introduced in purple.

5.2 OPTICAL SYSTEM

The optical system is split into two parts. Firstly, an aluminum box containing the UV laser head and additional optics for beam generation and control. Secondly, a feedthrough used to introduce the UV beam into the cryostat and steer it into the detector's active volume.

A schematic diagram of all components and laser paths in the laser box is depicted in Figure 5.2. In Figure 5.6 a photograph of the installation is shown. The laser box contains the laser head, where a Neodymium-doped yttrium aluminum garnet (Nd:YAG) gain medium exposed to a flash lamp is emitting light with a wavelength of 1064 nm. The laser[1] uses the Q-switch technique [100] to produce the infra-red light pulses with a duration of 5 ns to 7 ns and pulse energy of 450 mJ. Two frequency doubling (also know as second harmonic generating) crystals are installed in the beam path inside the laser head, producing pulses with wavelengths of 532 nm, 355 nm and 266 nm. These pulses have the same pulse duration as the originating infra-red pulse but reduced energies of 200 mJ, 65 mJ and 60 mJ, respectively. The emitting beam has a diameter of 6 mm, a divergence of 0.5 mrad and a pointing stability of 30 µrad. The shot-to-shot beam energy stability for the 266 nm wavelength is less than ± 7 % and the power drift over 8 h is less than 8 %. The beam shape in the far field is Gaussian-like and has a horizontal polarization. The repetition rate is configurable, with a maximum rate of 10 Hz. A supply unit, placed in the control rack, is connected to the laser head which houses a high voltage power supply for the flash lamp and providing water cooling to the gain medium. To separate the UV pulse from all other wavelengths, dichroic mirrors reflecting UV and transmitting other wavelengths are used in the optical layout, the transmitted light is absorbed in rugged Teflon beam stops. For pulse energy control the horizontal polarization of the UV light is taken advantage of by an attenuator[2]. A rotatable $\lambda/2$ waveplate is placed in the beam path separating the UV pulse into s and p-polarization components. After the waveplate,two thin film polarizers are installed at the Brewster angle relative to the incident beam direction to reflect the p-polarized component and transmit the s-component of the UV pulse. Therefore, the beam is split in two paths, where the orientation of the waveplate defines the ratio of energy in each path. Control of the beam diameter is achieved by installing an aperture in the beam path after the attenuator. For precise remote alignment a motorized two axis optic mount[3] is used to hold the mirror that connects the laser box and the feedthrough. An additional visible class 1[4] laser is installed and aligned with the UV laser path as a reference during installation and commissioning. During normal operation this alignment laser is disabled. For trigger signal generation a photodiode[5], sensitve in the wavelength region from 200 nm to 550 nm is installed in the laser box, detecting direct and scattered light when the laser is fired.

1 Continuum, Surelite I-10
2 Altechna, Laser Beam Attenuator (Watt Pilot), https://www.altechna.com/products/
3 Zaber, T-OMG, a truly magnificant product, https://www.zaber.com/products/optical-mounts/T-OMG/details/T-OMG
4 Classification according to [101]
5 Thorlabs, DET10A/M, https://www.cljk.ch/obs/det10A

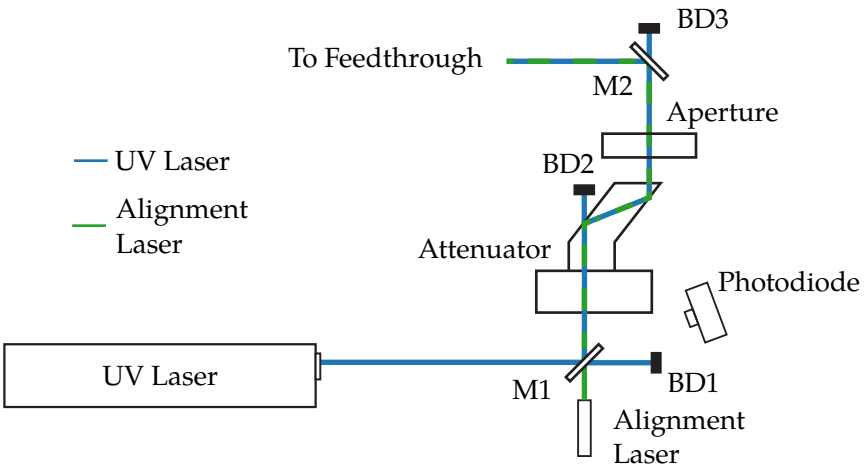

Figure 5.2: A schematic drawing (not to scale) of the components used for laser beam control. A visible (calss 1) laser is aligned onto the UV-laser path at the first dichroic mirror (M1) The attenuator allows to control the pulse energy, the diameter of the beam is controlled by an aperture. A motorised mirror (M2) deflects the mirror into the direction of the feedthrough. Behind all mirrors beam dumps (BD) are installed to absorb the non-reflected laser light.

The second part of the optical system is tightly connected to the feedthrough system. Here, a mirror is placed at the centre of a rotational feedthrough, directing the optical laser path downwards into the cryostat. This mirror is held in place by an motorized mount (identical to the one used for M2 in the laser box), the remote control feature is used for path alignment during commissioning, see Section 5.8 for details. To optically penetrate the cryostat insulation a custom built quartz glass pipe is installed. The pipe is evacuated to prevent condensation due to cooling when in contact with liquid argon. Both faces of the pipe are fabricated of highly transmissive glass in the 266 nm wavelength region to ensure low beam losses. Direct Penetration of the inhomogeneous gas to liquid interface of the argon will result in a large spread of laser paths in liquid argon. To overcome this issue, the length of the quartz glass pipe is chosen such that the lower end is immersed in liquid argon. The end of the vertical laser path inside the cryostat is marked by a last mirror (also called cold mirror). The mount of this mirror can be tilted and rotated to steer the laser beam into the active volume of the detector. Due to the position of the cold mirror in front of the field cage rings, some regions of the detector volume are not accessible with laser beams. The mechanical details of the feedthrough construction are discussed in Section 5.3.

The two mirrors installed in the feedthrough structure are commercially available dichroic mirrors optimized for maximal reflectance for 266 nm wavelengths at an angle of incidence Angle of Incidence (AOI) of 45°. In this mirror type two types of materials, with high and low refractive index are stacked in multiple layers. The thickness of the layers is optimized, such that at a certain AOI constructive interference is achieved, going along with a high reflectivity. If the AOI is changed away from the optimised angle the reflectivity will change accordingly. In air deviations from the optimal AOI do not affect the reflectivity significantly. However in liquid

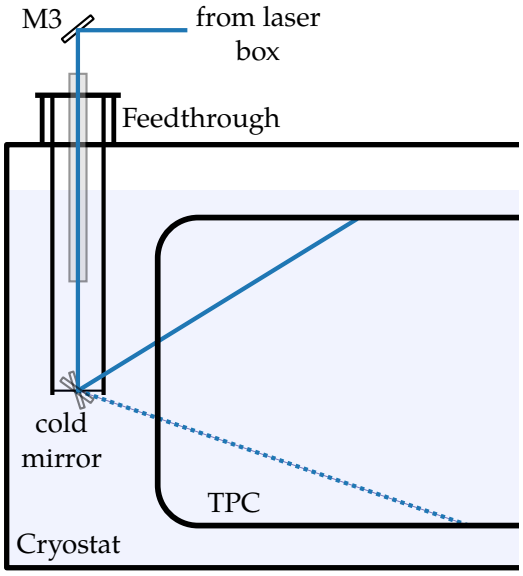

Figure 5.3: Schematic drawing (not to scale) of the laser path in the feedthrough construction. The laser beam arrives from the laser box and is reflected into the cryostat by the mirror M3 trough a quartz glass. Inside the cryostat the laser is steered into the time projection chamber by the cold mirror.

argon the refractive index changes to $n = 1.3$ for $\lambda = 266\,\text{nm}$ according to [48]. The manufacturer [1] of the mirrors supplied a simulation of the reflectivity curves vs. AOI for this configuration shown in Figure 5.4. Since the cold mirror is tilted for scanning the detector, the AOI varies from 0° to 80°. Therefore, the pulse energy has to be adjusted during scanning, the procedure to obtain a optimal beam energies is described in Section 5.8.

Ambient light entering the cryostat will prevent proper operation of the photomultipliers installed in the detector. Furthermore if the laser enclosure is not light tight, personnel working on the detector might get exposed to dangerous invisible laser light[1]. Therefore the laser box and the laser feedthrough parts hosting the laser and laser components are light tight. All light sources, such as indicator LEDs were disabled or dismounted to prevent emission of light within the sealed volume. To ensure light tightness after breakage of the light seals (for maintenance work), the photomultiplier event rate is compared before and after seal breakage. To prevent unitended or unauthorized access to the laser box, multiple locks were installed on the enclosure.

5.3 MECHANICAL SYSTEM

The major mechanical system of the laser calibration system is the feedthrough, which allows the laser beam to be steered into the UV laser into the TPC. Another component are the laser boxes, which host the UV laser sources and beam control

1 Edmund Optics

1 The deployed laser is a class 4 laser according to [101]

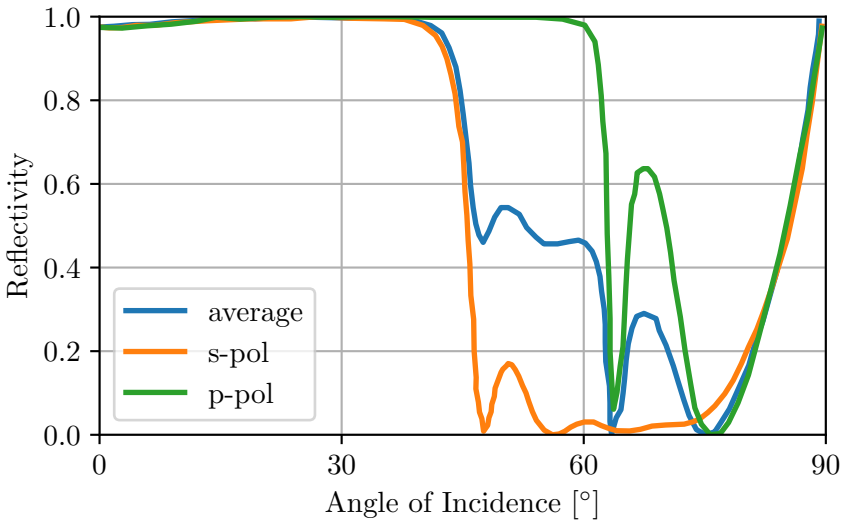

Figure 5.4: Reflectivity dependency on the Angle of Incidence for the installed mirrors. Simulation performed for light with 266 nm wavelength and surrounding medium with refraction index of 1.3 provided by Edmund Optics[1].

optics. The location of the two subsystems, at the down- and upstream end of the detector, is shown in Figure 5.5.

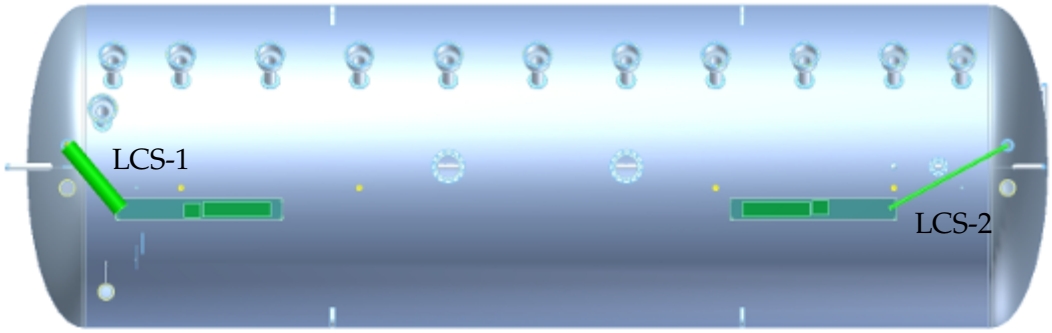

Figure 5.5: Top view of the MicroBooNE cryostat (rendered). The upstream (LCS-1) and downstream (LCS-2) laser systems are colored in green.

All optical systems are installed in the laser boxes associated with the individual system, which is 2 m long, 0.5 m wide and 0.5 m high. All sides are manufactured out of 2 cm thick aluminum sheets and are held together by screws placed on the edge surfaces. Lips in the top lid prevent light leakage into and out of the box. On an aluminum stand the optical devices (for details see Section 5.2 and Figure 5.6) are assembled vertically. A cut out on the top lid lets the top of the structure stick out of the box, such that the laser beam path can be directed towards the feedthrough part. This extension is enclosed in an aluminium box with a hole marking the exit of the beam towards the feedthrough. The laser beam path is delivered to the feedthrough construction by a stainless steel pipe. To ensure light tightness the pipe ends are insulated with black tape. The laser box is attached onto

the cryostat trough four stainless steel legs. The joint of the legs to the bottom of the box is fabricated out of plastic for galvanic separation of cryostat and building ground. For safety reasons the laser box is equipped with two locks, to prevent unauthorized personnel from opening the laser box accidentally.

A major mechanical challenge of the system is the introduction of an UV beam into a cryogenic liquid without disturbing the laser beam profile while keeping the cryogenic liquid isolated from the surrounding atmosphere for safety and purity reasons. This is achieved by the use of an evacuated quartz glass immersed into the liquid argon on the lower end, this guarantee a flat interface between glass and liquid. Sealing to the outer atmosphere is achieved by three rubber seals squeezed against the glass tube at the feedthrough glas holder. Another mechanical challenge of the laser system is to precisely steer the UV beam into the detector. Additionally constraints have to be met not to interfere with detector operation. A main driver for constrains is the fixed location of the feedthrough mount on the cryostat. When the design of the laser calibration system was initiated very limited ports into the cryostat were available. The selected locations at either end of the cryostat govern most mechanical design choices. To maximize coverage of the detector with laser beams under the given constraints, a construction with a steerable mirror immersed in liquid argon in front of the field cage rings was chosen. The position in the x-y plane (horizontal plane) is fixed by the location of the chosen feedthrough. The support structure defines the position of the mirror is z, and is chosen such that the mirror resides at the mid-height of the field cage structure. Due to the presence of the field cage rings, regions with no laser beam coverage arise. Coverage would be maximized with a mirror position as far away from the field cage as possible. But a direct path onto the immersed mirror from the outside is preferable, other options would complicate the beam path inside the cryostat significantly, without greatly increasing laser coverage. The proximity of the mirror to the field cage, prevents the use of conductive materials in the mirror support structure, due to the potential high voltage breakdowns implied by it. This excludes the use of a motorized mirror mount for beam steering. All these constraints lead to the following design. To achieve horizontal scanning abilities, the mirror is fixed onto the inner surface of a rotatable flange. The support structure consists of segments of four vertical rods connected by horizontal beams for stability, with a length of 15 cm Segments are combined to place the mirror in front of the TPC at the desired height. Vertical scanning capabilities are achieved by a piston and rod construction. The rim of the piston is held in place by the aforementioned mirror support structure. This construction translates the rotation of the mirror along the horizontal axis into a linear movement. The rod is held in place by the beams of the support structure and is attached to a linear motor trough a vacuum tight bellow. To electrically insulate the devices placed on the feedthrough from detector ground, a ceramic circuit breaker is installed between the cryostat and rotary feedthrough flange. The upper part of the feedthrough structure, where the laser beam is deflected into the cryostat, is enclosed in an aluminium housing with a cut-out for the pipe, delivering the laser beam from the laser box.

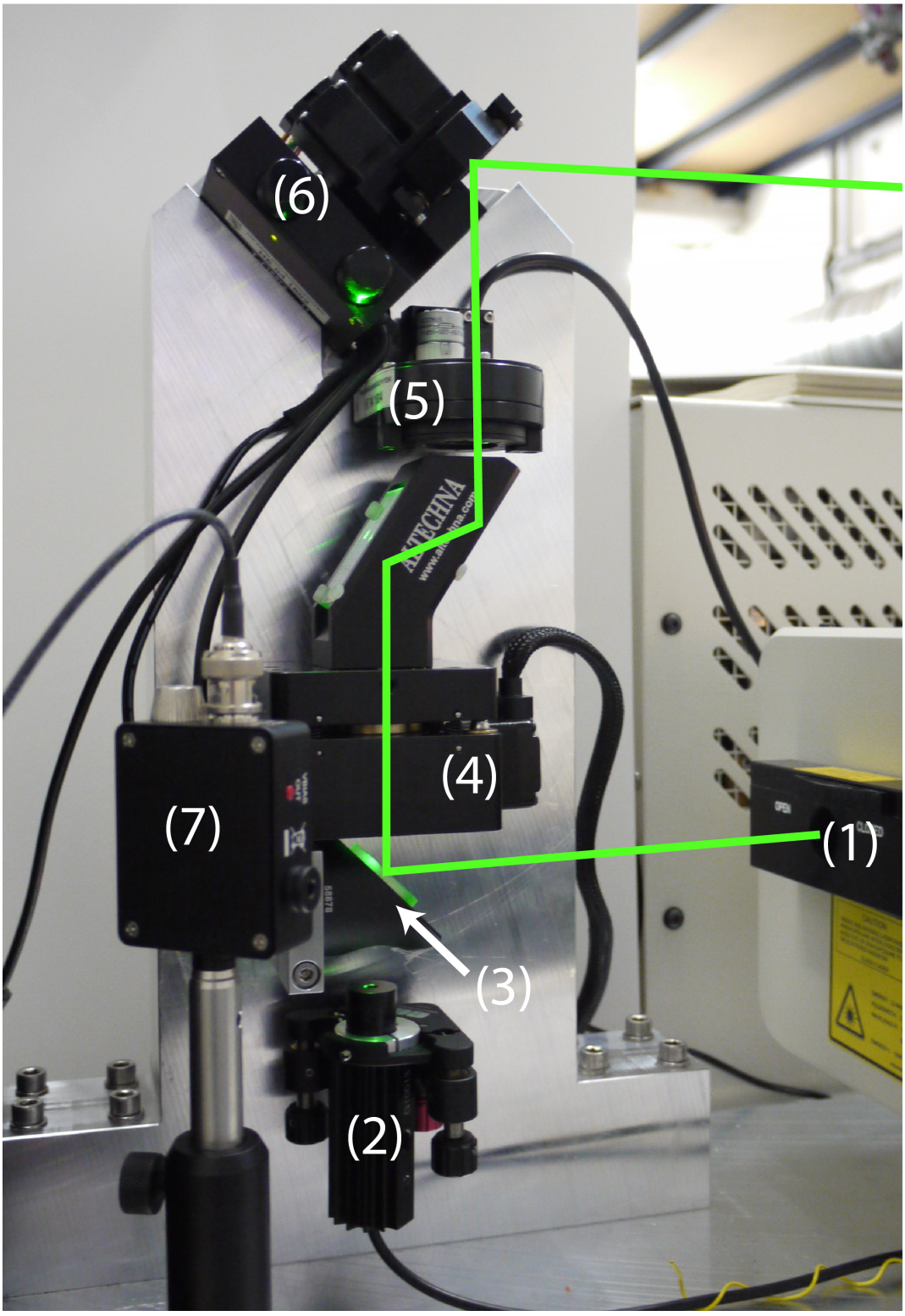

Figure 5.6: Photograph of the optical table with an overlay of the UV-laser beam path in green. (1) UV laser head; (2) green alignment laser; (3) 45° mirror holder; (4) attenuator; (5) aperture; (6) mirror mount; (7) photodiode.

Figure 5.7 shows a cut view of the upper feedthrough construction discussed in detail in the following paragraphs. The mirror support and polar steering construction is shwon in Figure 5.8.

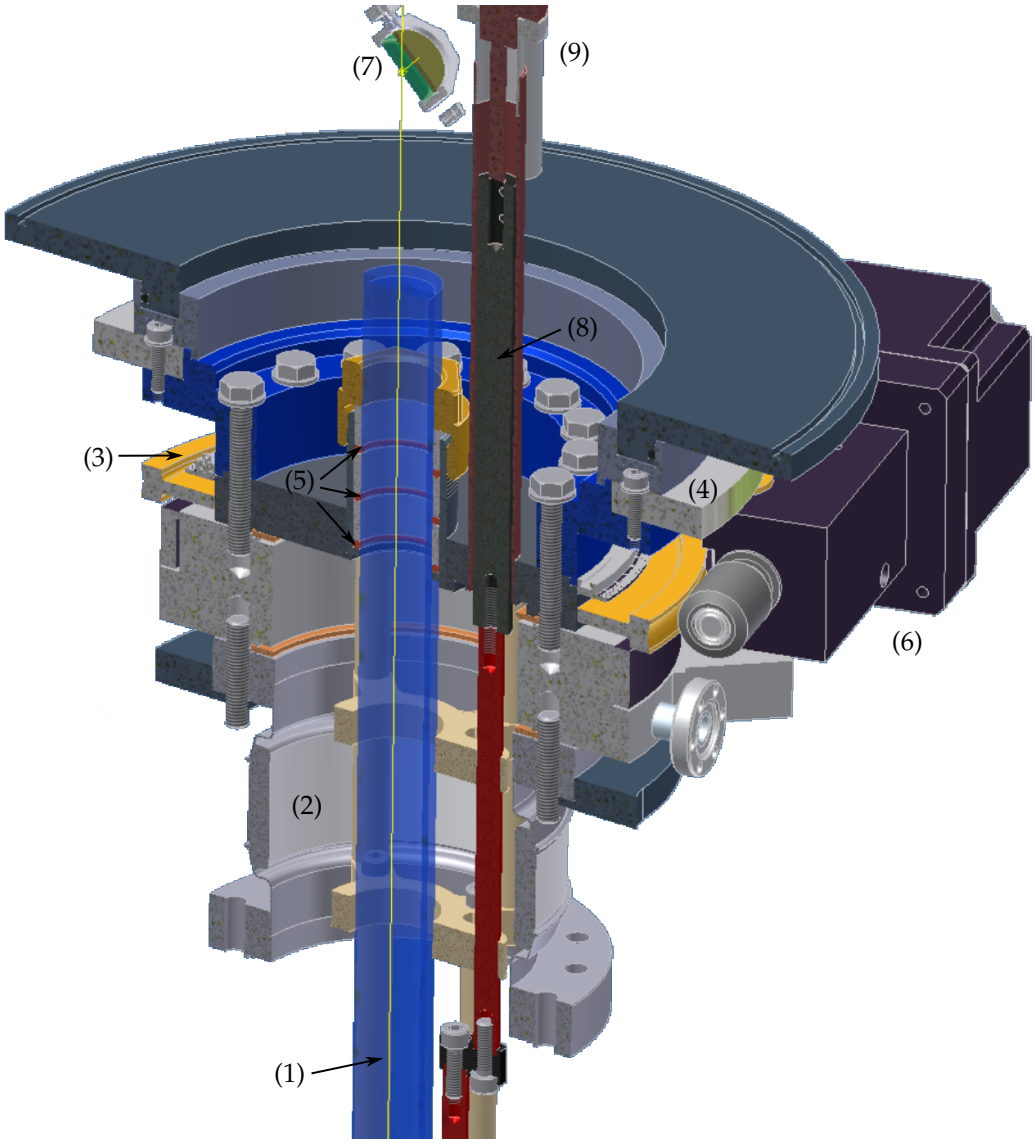

Figure 5.7: A sliced view of the feedthrough construction. (1) The evacuated glass tube, (2) ceramic dielectric braker, (3) rotary thread, (4) rotary encoder ring, (5) three rubber seals for the glass feedthrough, (6) rotary motor, (7) steerable mirror (M3), (8) linear feedthrough and (9) linear actuator.

For the rotational feedthrough, a motorised differentially pumped feedthrough from Thermionics [1] (RNN Series) was chosen. This rotational feedthrough has three U-shaped ceramic seals which enclose two cavities which are evacuated. This is designed for high vacuum applications, since the differentially pumped seals will close preferentially in one direction. However, during operation in MicroBooNE an opposite pressure difference is present when the liquid argon is inside the vessel. A motorised precision linear feedthrough (FLMR) from the same

1 https://thermionics.com/

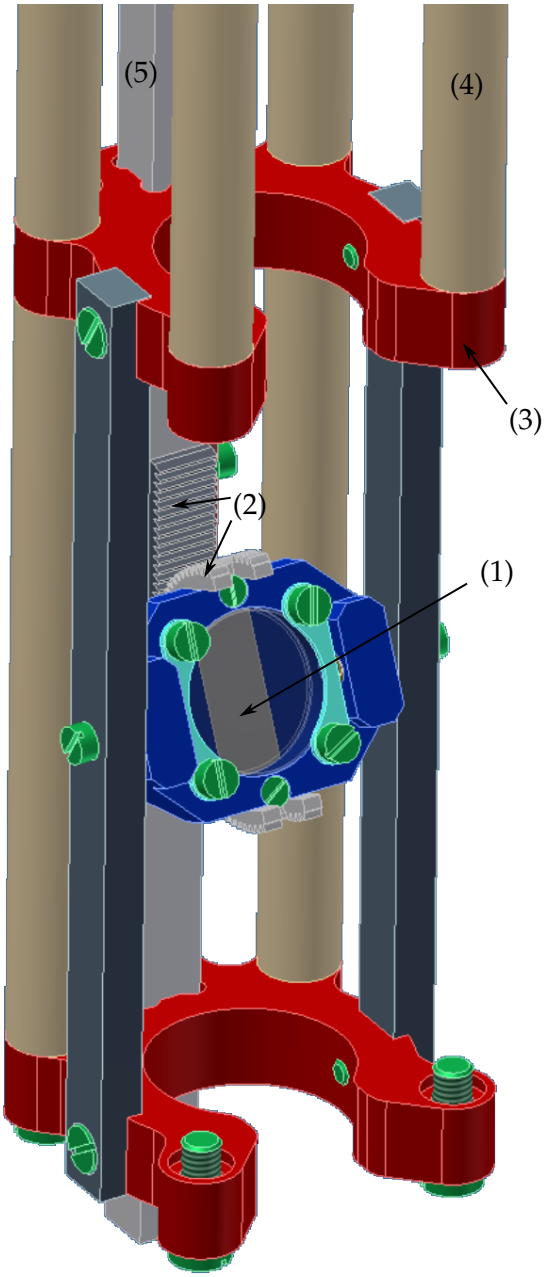

Figure 5.8: CAD render view of the mirror support structure. (1) Cold mirror and support structure, (2) piston and rod construction for tilting, (3) intermediate turtle support structure, (4) support rods, (5) tilting actuator. All parts are fabricated out of PAI. In the image the two front support rods (connecting the two turtle-shaped support structure depicted in red) are not shown for better display.

company, was installed to drive the linear rod. The inner support structure was fabricated out of poly-amide[1], which has a very low outgassing rate, low thermal expansion coefficient and is certified for operation at liquid argon temperatures. Because of overpressure requirements of the MicroBooNE cryostat, the feedthrough construction was successfully seal tested for 0.3 bar over-pressure.

An evacuated quartz glass pipe is required to facilitate an undisturbed entry of the laser beam into the liquid argon phase (see Section 5.2 for details). This pipe is positioned at centre of the rotatable feedthrough and held in place by three o-ring seals. The glass pipe is enclosed in a metal housing to prevent any damage during installation or operation. The failure of the glass pipe would result in the exposure of the inner cryostat to ambient air, introducing unwanted impurities into the liquid argon. Furthermore, glass parts falling into the cryostat could damage the TPC or the filtration system irreversibly.

Precision position encoders are installed on both movable axes. To measure the rotary position a commercially available encoder[2] setup from Heidenhain is installed. The device uses two markings for position encoding, one continuous marking for stepping (with a resolution of 0.001°) and a second one, spaced equally 2° apart for absolute position encoding. The encoder ring is mounted onto the outer side of the feedthrough flange, rotating whenever the mirror is rotated. The encoder head is held in place by a support beam fixed onto two rods attached to the non movable part of the feedthrough. This construction has the advantage that any backlash error due to gear movement is excluded and the measurement directly converts to the azimuthal angle used for downstream processing. Two limit switches are installed to ensure the rotary movement is confined in the safe range. To measure the polar angle, the linear movement of the rod is coupled to an absolute linear encoder [3], manufactured by Heidenhain. Again, two limit switches ensure safe operation. The linear movement is translated into a rotation by the piston and rod construction. This construction introduces uncertainties to the measurement position and a backlash. However, the backlash can be compensated by always approaching positions from the same direction. For the translation of the linear movement ΔL into a rotation $\Delta\phi$ the translation ratio s according to $\Delta L = s \times \Delta\phi$ was measured with a laser alignment device. A 45 deg movement was measured by positioning the mirror such that an alignment laser is exactly reflected back, then the mirror was moved 45 deg such that it overlaps with the laser beam of the alignment device. The obtained ratio was found to be $s = 0.3499 \pm 0.0002\,\mathrm{mm}/^\circ$. This translation ratio is used in the following for absolute measurements in the vertical direction. The dominant error in the vertical position measurement is therefore the accuracy of the encoder $\sigma_{linear} = \pm 1\,\mu\mathrm{m}$, which translates into a vertical rotation measurement accuracy $\sigma_{polar} = \pm 10.29''$. Both encoders rely on photoelectric reading of a measuring standard.

1 Duratron T4301 PAI
2 Heidenhain AK ERA 4480
3 Heidenhain LC 415

5.4 ELECTRONIC SYSTEM

The electronic subsystem is built to control the laser beam introduced into the detector. Furthermore, it supplies a trigger signal to the TPC and simultaneously records laser beam parameters, such as beam direction and energy. It can be divided in two intertwined parts. Firstly, all motors controlling the direction and shape of the beam. Secondly, the measurement part, which records the beam direction with two encoders installed on the feedthrough construction and supplies a trigger signal to the TPC by means of a photodiode. The electronic backend is individual, but identical for each laser system. An overview block diagram of all devices and connections is drawn in Figure 5.9.

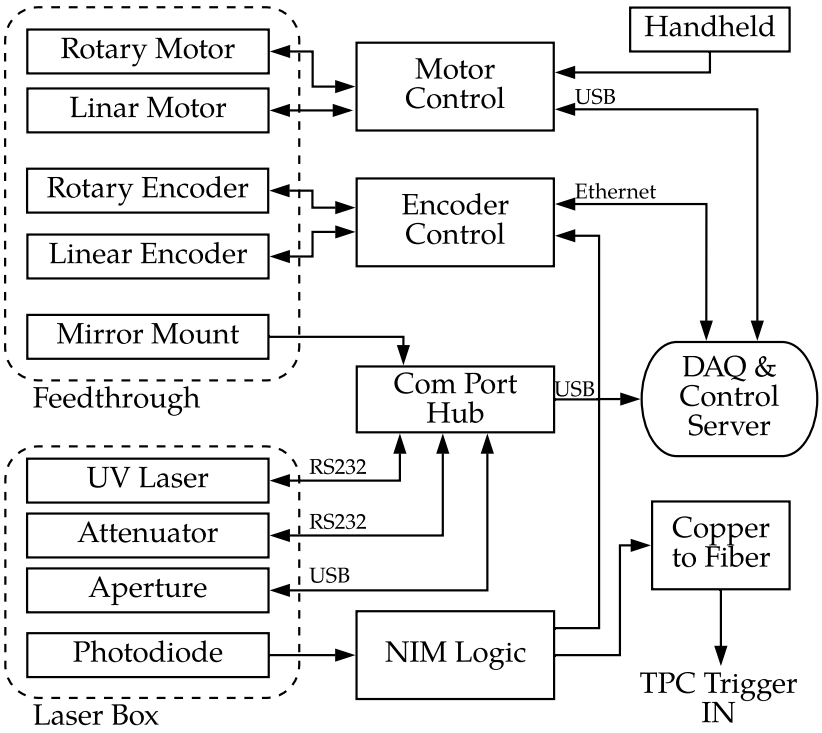

Figure 5.9: A block diagram of electric component used in the laser calibration system. The feedthrough and laser box form two separate installations, connected (trough various controllers) to the data acquisition and control server.

Controls for the laser box encompass the UV laser source, the attenuator and the aperture. Their function principles and use is documented in Section 5.2. Additionally a remote controllable mirror mount is present but not shown in the block diagram, due to single use during commissioning. The aforementioned devices are all connected to the Data Acquisition (DAQ) and control server trough a USB hub. All devices can be controlled trough the serial port with various standards, described below. The photodiode[1] signal is connected to a logic rack where the signal is discriminated and distributed to the position encoder and detector trigger inputs. To convert the photodiode signal with levels from 0 V to 5 V to Nuclear Instrumentation Standard (NIM) logic levels a discriminator is used. The discrim-

1 Thorlabs DET-10A

inator threshold level is set to 3 V and the NIM logic out is used as an output. The signal is split by a fan in/out module to a timer and two NIM to Transistor-Transistor Logic (TTL) converters. A signal pulse with a length of 20 ns, compatible with the MicroBooNE trigger input, is generated by the timer. The TTL output of the timer is connected to a TTL to fiber converter[1].

Additionally, a normal and an inverted signal is each fed to NIM to TTL converter, used as bipolar signals of the RS485 input of the encoder controller. The detector trigger line is propagated trough a fibre to ensure galvanic separation of detector ground reference and building ground, where the laser racks is connected. The detailed logic is shown in Figure 5.10. Firing the laser while Photomultiplier Tubes (PMTs) are in operation might cause irreversible damage to them, to prevent this scenario the interlock of the laser power supply is connected to a PMT High Voltage (HV) enable signal.

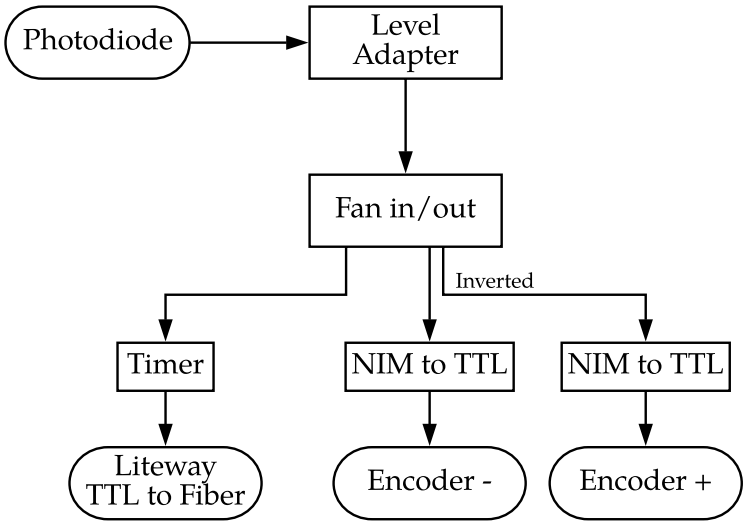

Figure 5.10: Block diagram of the photodiode signal discrimination and distribution.

The feedthrough hosts rotary and linear motors, accompanied by corresponding encoders, see Section 5.3 for mechanical details of the devices. Both stepper motors are driven by two identical motor controllers[2] with different drive current settings to respect the limits of the individual motors. Moreover, the limit switches of the motor installation are connected to the motor controller. Two encoders supply the necessary measurements for laser beam direction determination. The linear and rotary encoder are connected to a controller[3], which sends the acquired measurements as User Datagram Protocol (UDP) packages over an ethernet connection to the DAQ server. Two different operation modes are used for position data. The polling mode, where the encoders read the position at a fixed rate, is used during testing and calibration of the system. For detector scanning the external trigger input is used to initiate position readings. In both modes, along the absolute position measurements, the trigger count and a relative time stamp is recorded.

1 LuxLink DT-7201
2 Schneider Electric MForce MicroDrives
3 Heidenhain EIB741

Each laser system incorporates a dedicated 19-inch rack, hosting the DAQ server[1], the control units and power supplies of the installed devices. The Alternating Current (AC) power distribution is routed trough a Uninterruptible Power Supply (UPS)[2], to ensure a proper shut down procedure in case of a power outage. An interlock is implemented, such that after a power outage the system has to be switched on manually, preventing accidental laser firing. Direct Current (DC) power distribution is realized trough a custom built distribution system using several DC power supplies[3]. A MicroBooNE standard rack protection system is installed, which monitors temperatures and issues an alarm if smoke is detected. The unit is connected to the slow monitoring system of MicroBooNE. Another safety feature is the housing of the laser power supply, its dimensions are chosen such that if a cooling water leak occurs, all water is held inside it. Four fans are installed in the laser housing for cooling.

5.5 REMOTE CONTROL SYSTEM

The main objective of the remote control system is to achieve high repeatability of laser beam trajectories and configurations. An additional design driver for the control system was the requirement to operate the laser calibration system remotely. This emerges from the fact that calibration campaigns are performed during neutrino beam downtime, which can be announced with a lead time of as little as few minutes and last for only few hours. Therefore, a fast reaction time is needed to obtain laser calibration data whenever possible. Only by automation of the laser operation these time constraints can be met. Furthermore, because of safety considerations, the entire UV laser beam path is fully enclosed such that no UV light can harm people in its vicinity. The mechanical design implications to meet these standards, severely restricts manual access to the optical table feedthrough.

The following devices were included in the remote control system: the laser head, the two steerable mirrors, the attenuator, the aperture and the two stepper motors controlling the movement of the last (cold) mirror. Except the aperture, which was connected via USB, all systems were connected to a control server trough RS232 connections. See Section 5.4 for details. To control the individual devices via software, a python package was developed in an object-oriented approach. This allows each subsystem to be treated in the same way, enabling a unified way of accessing the devices. Since, all movement in the system is done by motors, a generic motor class was introduced. Furthermore, all motors are controlled trough a serial port, acting as a physical layer to various interaction protocols. The motor class accepts generic definitions for movement distances, speeds, directions and accelerations, once the stepping resolution is defined. Main functions implemented are relative and absolute movement instructions. Moreover, if applicable for the device, position reading, monitoring and movement abortion was implemented. The individual motor protocols are implemented trough pre- and postfixes. Testing capabilities are introduced in a way that serial port communications are looped

1 DALCO R1304BTL
2 Tripp Lite UPS SMART750RMXL2U
3 TDK Lambda Series

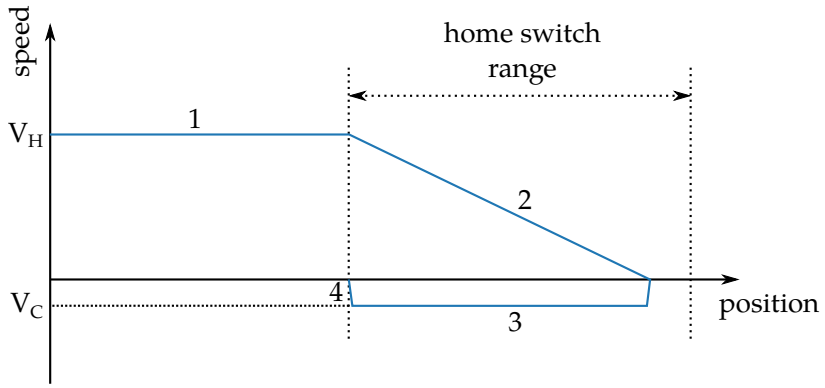

Figure 5.11: Homing procedure for all motor axes. In phase (1) the motor approaches the home switch at homing speed (VH). Once the home switch is reached, the motor decelerates during phase (2). In phase (3) the movement direction is inverted and the speed is lowered to minimum to creep speed (VI). When the home switch is released the movement is stopped immediately (4).

back and not sent to the device. This allows the correctness of the expected communication to be checked. The serial commands sent to the individual devices are blocking commands, but the reaction time is usually slow, hence no long waiting function calls exist in the control program.

For clear organization, a device class was introduced, holding meta information such as the name, and implementing the get and set functions for any parameter defined by the inheriting class. In an additional base class, used by all devices, the serial communication level is managed. At the same level logging and of all interaction with the devices and shell output is handled. In addition to devices, services were implemented. These are responsible for data formatting, data transmission and input/output handling. In the next section the data acquisition model is explained in detail.

To ensure precise repeatability, before each laser scan the rotary and linear motors are calibrated against a home switch. For this operation, one of the limit switches is approached at a slow speed V_H. When the homing switch is activated, the motor decelerates until halt. At minimum speed V_C the motor creeps in the opposite direction until the home switch is released again. Figure 5.11 illustrates this procedure. In this position the position counter is reset to zero.

This procedure was cross checked for repeatability using the absolute position encoders for both axes and systems. For the check the homing procedure was repeated one hundred times, each time the stop position was used as a measurement point, results are shown in Figure 5.12. A standard deviation of $\sigma_{l,1} = 0.011\,\text{mm}$ and $\sigma_{l,2} = 0.012\,\text{mm}$ was found for the linear motors. For the rotary motor the spread is higher, due to the higher gear ratio, $\sigma_{\phi,1} = 0.019°$ and $\sigma_{\phi,2} = 0.021°$. The homing procedure is performed automatically at the beginning of each run, during the warm up period of the laser. After a power outage or any miscommunication is detected, the homing has to be performed manually.

To conduct a laser scan with the laser system, a python program performs all operations. The operations stored in a file read at the beginning of the scan. This

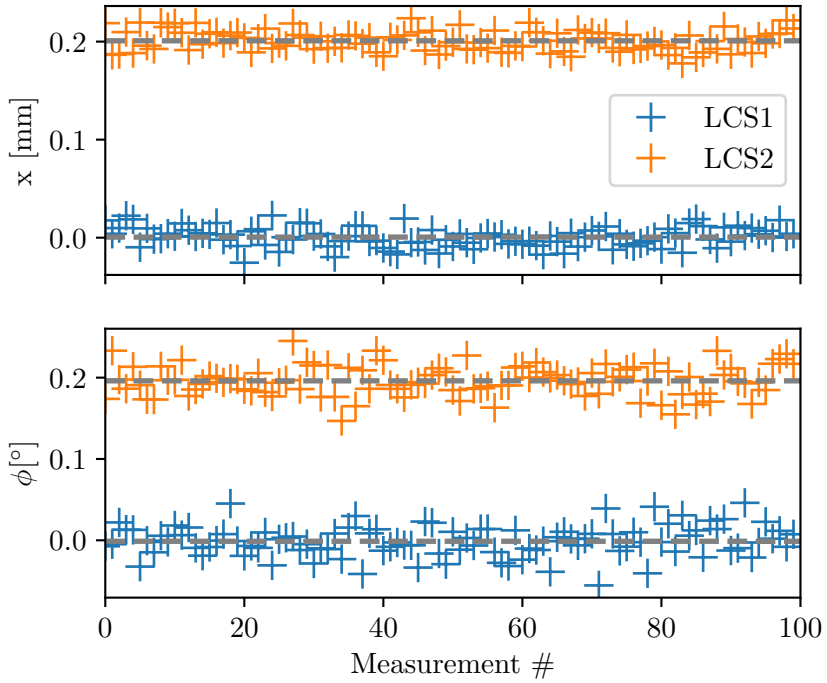

Figure 5.12: Homing procedure cross check for both axes of both laser calibration systems. The top plot shows the hundred readings of the linear encoders, the bottom plot the reading of the rotary encoder. Blue and orange colours indicate the two individual systems (LCS1 and LCS2). Laser system 2 measurements are offset by 0.2 mm and 0.2°.

file contains lines of instructions for each device. One set of instruction contains the following parameters:

- Index: Acceding identifier
- Horizontal relative movement: Distance to be moved by the rotary motor in this steps relative to the previous position.
- vertical relative movement: Distance to be moved by the linear motor in this steps relative to the previous position.
- vertical speed: Speed at which the rotary movement will be performed.
- Horizontal speed: Speed at which the linear movement will be performed.
- Shot frequency: Repetition rate ar which the laser is fired. Can be zero, then a single shot is fired. If negative, the firing will be started after the movement is finished.
- Numbers of Shots: Only relevant if the shot frequency is negative, this amount of shots will be fired after the movement is finished.
- Attenuator Position: Power setting of the laser beam.

- APERTURE POSITION: Absolute aperture position.

The accepted ranges of these parameters are summarized in Table 5.1. A laser scan is initiated by the start of the program supplying the scan pattern file described above and a run number. Additional options are possible but not necessary, these are mainly implemented for testing purposes:

- NO REF: Do not perform a reference run for the rotary encoder.
- NO WARM UP: Do not wait for the laser to warm up. Useful whenever the laser was warmed up manually or after a restart of the program.
- DRY RUN: Do not send any data to the devices, instead print them out to the shell.
- NO LASER: Ignore all instructions regarding the laser.
- LOCAL MODE: Do not send meta data to data assembler.
- INTERNAL TRIGGER: Use an internal 10 Hz trigger for the rotary and linear encoders. Photodiode signals are ignored.

NAME	DESCRIPTION	RANGE	INCREMENT
HorMov	relative horizontal step	−3 - 90°	0.001°
VerMov	relative vertical step	0 - 90°	0.001°
HorSpeed	horizontal step speed	0 - 5 °/s	0.001°
VerSpeed	vertical step speed	0 - 5 °/s	0.1 °/s
AttPos	beam energy	0 - 100 %	0.1 °/s
ShtFreq	shot frequency	−10 - 10 Hz	0.1 Hz
ShtCount	shot count	1 - 50 000	1

Table 5.1: Scanning pattern input definitions.

A flow diagram of a stardard laser scan is shwon in Figure 5.13. During the initialization phase, the laser is warmed up for 20 min and the rotary encoder performs an initial calibration to gain absolute positioning. The above described homing procedure for the rotary and linear motor is performed. After all calibrations are performed, the motors bring the cold mirror into the starting position. When the warm up time has passed and the laser is ready, the program starts to perform the instruction set one by one. As a first action the attenuator and the aperture are brought into the required positions. This updated configuration is sent to the data assembler (described in Section 5.6). This is followed by an update of the laser configuration (not yet shooting) based on the instruction set and an update of planned laser speeds is sent to the motor controller. Depending whether the shot frequency is greater than zero or not two different procedures are followed. If true, the laser shutter is opened and the laser starts firing, right after this action the relative movement is initiated and monitored. When the movement stops the

shutter is closed and the laser firing is ceased. If the shot frequency was zero or negative, the mirror movement is started without opening the shutter, when the movement stops one of the following two options is possible: if the shot frequency is set to zero, no shots are fired in this step. If the frequency is below zero, the absolute value is used to infer the shot frequency and the shot count is used to calculate the necessary time for the laser to be active. The shutter is opened and the execution halts for the necessary time. In a last step the step count is increased and the next instruction set is loaded. This procedure is repeated until all lines of the configuration file are processed. In a finalize step the motors are brought into an idle position and the laser is left in idle mode to cool down.

This approach allows a very versatile scanning pattern inputs. It is possible to scan the detector in a stop and go fashion, where the mirror is brought in position and after the movement is finished the laser is shot several times. Also possible is the pattern of firing while the mirror is moving at a constant speed. Furthermore it is easy to align the laser to a single position and fire the laser at a low rate.

5.6 DATA ACQUISITION

Data from several sources is stored when a trigger is issued by the photodiode. First and foremost the laser beam direction is recorded, additionally data from the remote controlling is stored along with this dataset. Data acquisition is initiated by the photodiode, which sends a signal trough NIM logic to the encoder controller (see Section 5.4 for details). The controller acquires positions of the two encoders connected to it and sends the data, including trigger count and measurement quality metrics, via an UDP package. On the server, a C program receives the UDP packages, and extracts the relevant information. A time stamp is assigned to the data package on arrival and is combined with supplemental data from remote control and written to disk. This program also controls the initial configuration of the encoder controller and handles position calibrations during the warm up period.

The main issue with data acquisition arises from the different times when data is updated. Obviously the laser firing is defining when data is stored, but remote control might update data much earlier. Therefore a two publisher and one subscriber, with an intermediate broker, architecture is used. The inter process communication protocol is used for communication between the different parts. The communication architecture is implemented using the zeroMQ[1] library. Two workers, the remote control script and the encoder, run as independent threads on the server. The workers send their data to an intermediate broker, which will confirm the reception of the data with an empty reply. Multiple subscribers can be connected to request the data to this broker. In the used configuration the data assembler is the only subscriber. Whenever new data from the encoder arrives the data assembler writes data to a text file. Other subscribers, such as slow controlling, could be implemented. The described data flow is illustrated in Figure 5.14.

The following data is stored to disk for later processing:

1 www.zeromq.org

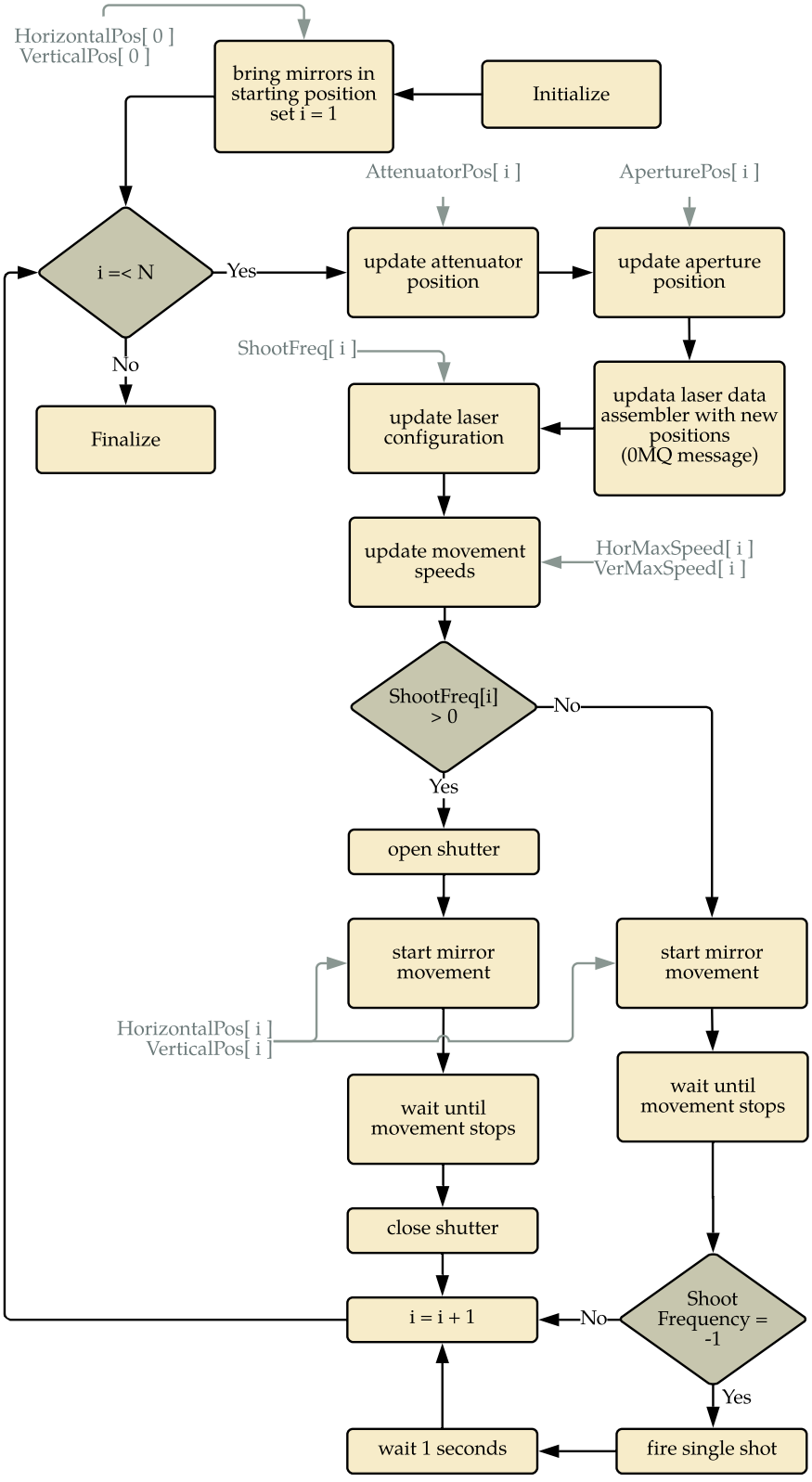

Figure 5.13: Flow diagram for laser run control.

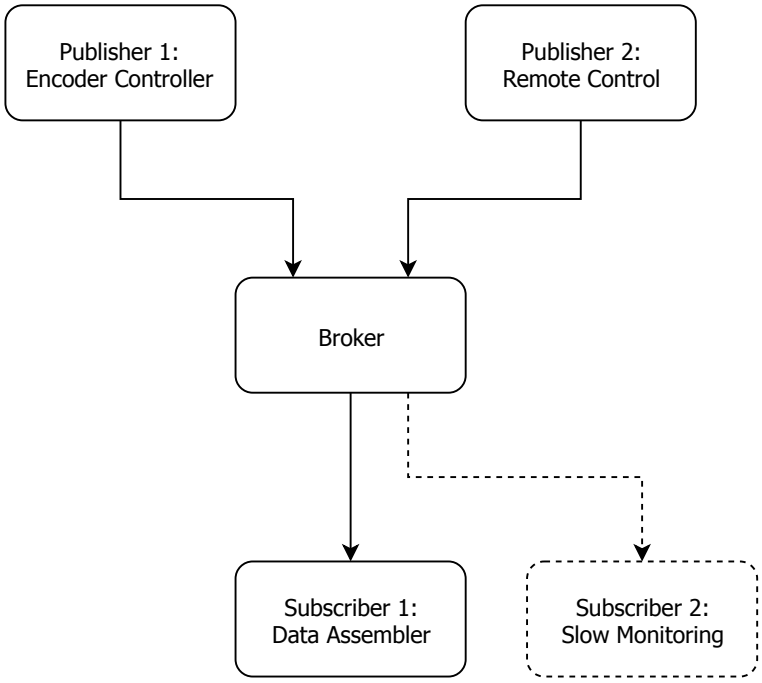

Figure 5.14: Publisher-subscriber pattern used for DAQ handling.

- Laser ID: Laser identification, 1 for upstream and 2 for downstream system
- Status: System status indication, 0 if everything is ok, 1 if encoder data is not available or corrupt, 2 if data from remote control is unavailable
- Linear Position: Raw linear encoder position
- Rotary Position: Raw rotary encoder position
- Attenuator Position: Attenuator position
- Aperture Position: Aperture position
- Trigger Time High: Absolute trigger time in s
- Trigger Time Low: Relative trigger time in µs
- Trigger Count: Trigger Count from first shot of the current run
- Step Count: Current configuration step number
- Laser Trigger Count: Total shots fired by the laser
- Position Axis 1 of M1
- Position Axis 2 of M1
- Position Axis 1 of M2

- Position Axis 2 of M2

To be able to connect the collected data with an individual TPC readout event, the time stamp is recorded as well. Under high load on the server the time stamping might vary. This was tested with the following procedure, the encoder controller was set to issue new positions with a rate of 10 Hz, simulating the maximal trigger rate achievable by the UV laser. To simulate high load the command line tool stress[1] was used. During the entire test period all processors of the server were fully loaded. The critical metric for this test is the time spread of the time stamp for successive measurements. If it is small enough, measurements from the laser and the detector can be combined without ambiguities. However, if the spread between time stamps of consecutive measurements is within the range of the actual time spacing of the measurements, in our case 0.1 ms, the two data frames can not be matched uniquely. The test revealed that the time spread of subsequent measurements σ_t is 12 µs, well below the minimal time spread of laser firings. As a time source for the laser DAQ a common Network Time Protocol (NTP) servers is used. The same server is supplying time to all other detector DAQ systems.

Matching offline recorded data from the laser side and the TPC side is based on the timestamp on each data set. Naive matching by event number is not feasible due to the possibility of trigger losses introduced by any device in the trigger generation chain (photodiode, discriminator, optical transport or trigger input). Hence laser data is matched offline against the TPC by timestamp. This is realized as a python script, which outputs an one dimensional array in where the index is the TPC event number and the stored value is the corresponding laser event number. This array can then be used during event processing and analysis, described in Section 6.4. Matches are found by stepping trough laser event timestamps t_{Laser} and finding TPC events with timestamps t_{TPC} within a time range 100 µs according to

$$|t_{Laser} - t_{TPC}| < 100\,\mu s. \tag{5.6}$$

The threshold of 100 µs was chosen well below the expected maximum laser firing repetition rate of 10 Hz or 100 ms. If no match could be found the array value was set to -1, so latter processing can skip the event in question. Figure 5.15 illustrates the procedure on a full laser scan. In the top graph, the time difference of consecutive trigger events for the laser and the detector are shown. Spikes of increased time-differences arise when the a horizontal scan step is finished and the azimuthal angle and possibly the laser attenuation is adjusted. During this time the laser is not firing, hence no trigger signals are issued. In the zoomed view an offset of 5 events for the location of the increased time difference for the laser and the detector is visible. As a test for the correct working procedure of the matching algorithm, the absolute time difference between laser and detector events is analyzed, plotted on the bottom of the aforementioned figure. The standard deviation of the time series is used to qualify the correctness of the matching, whenever lower than 50 µs, the matching was assumed correct.

1 linux.die.net/man/1/stress

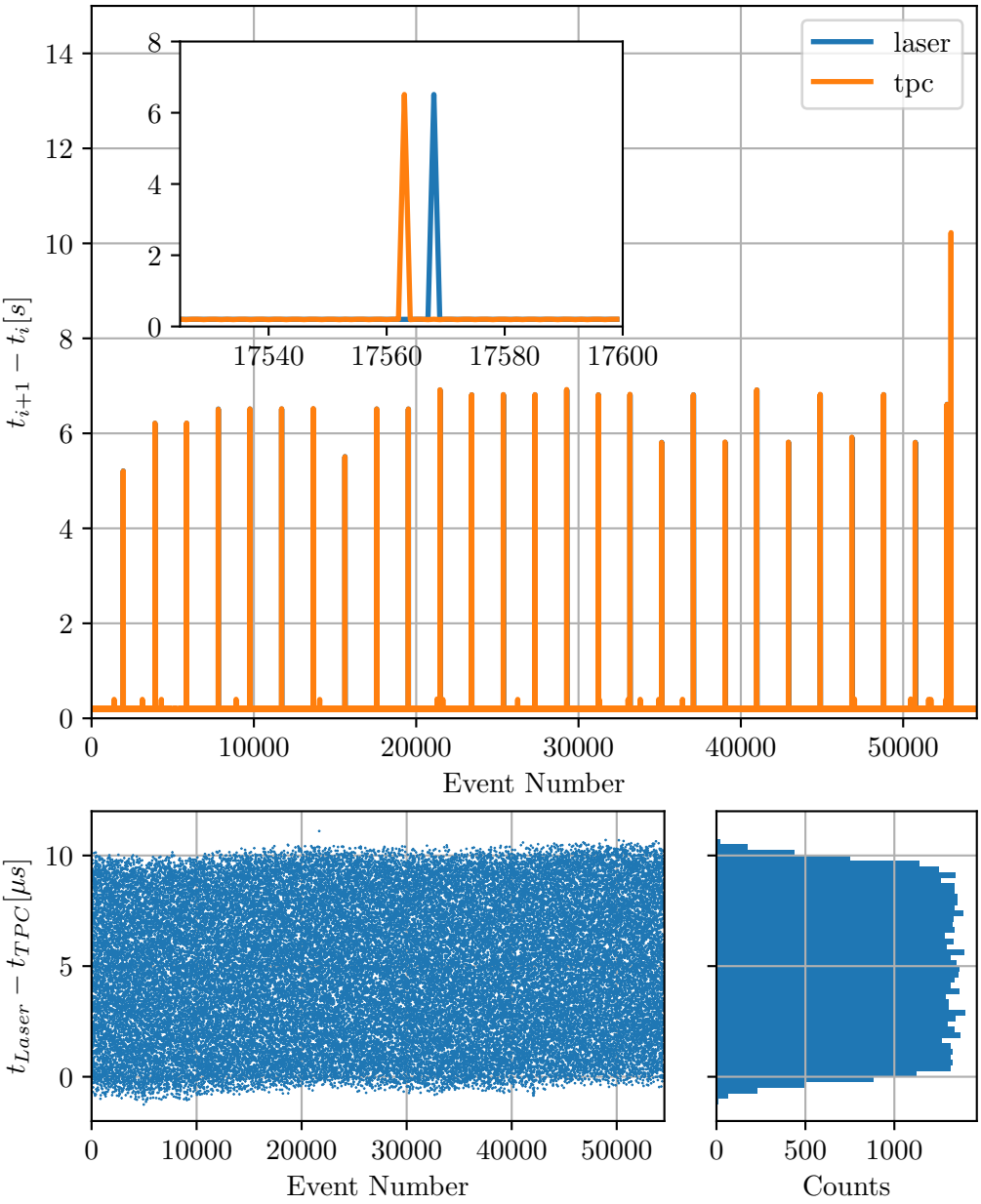

Figure 5.15: Event time alignment. The top graph displays the time steps between consecutive laser (blue) and TPC (orange) events. The zoomed in view shows an event misalignment of a larger step. On the bottom row, the individual time differences and a corresponding histogram of laser and TPC events after time matching is displayed.

5.7 COMISSIONING AND OPERATION

After successful commissioning the main parts of MicroBooNE, obtaining an operational LArTPC the laser system was commissioned. Two challenge arises during

installation. Firstly, because the laser system was installed after transportation of the closed cryostat (welded shut) to it's final location at Liquid Argon Test Facility (LArTF), the alignment of the UV beam onto the cold mirror could not be verified in place. The alignment had to be (re-)established without optical feedback at the cold mirror, this was achieved by observing the TPC signal while manually issuing laser firing commands. The remotely controlled mirror mounted on the optical feedthrough (M3 in Figure 5.3) was used to adjust the direction of the UV beam between laser firings. An array of possible M3 mirror positions was scanned until a coarse alignment of the laser beam onto the cold mirror was reached. These M3 positions were chosen such that the minimum step-size in between firings (based on the length of the mirror holder structure and mirror size) was not displacing the laser beam more than the size of the cold mirror at a previous position. The starting position of the array was chosen manually, by observing the green alignment laser reflections on the feedthrough, during installation work. These considerations lead to approximately 400 positions to scan. Each step will included a firing of the laser at several horizontal cold mirror positions (discussed below). By the presence of a laser track in the TPC (displayed in the online monitor) the alignment is verified. During this corase scanning the laser pulse energy attenuation was minimal and the aperture was also opened maximally. This configuration was chosen to increase the probability of an TPC response even if the cold mirror was only hit partially by the laser beam. In a finer alignment procedure, optimal laser alignment onto the cold mirror was achieved by stepping trough mirror M3 positions in an alternating (in x and y direction) pattern, while observing the laser track position and shape in the TPC for different cold mirror positions. The step-size of this procedure is chose much smaller than for the coarse alignment. Furthermore, the beam energy was optimized with respect to cold mirror positions as well as the ionization profile along the beam.

Secondly, as already anticipated above, the laser beam direction relative to the detector is unknown due to the thermal contraction of the TPC with respect to the last (cold) mirror. This makes the firing of several laser pulses for each M3 position necessary because the laser track could be absorbed by a field cage ring. The opening angle of the scanning pattern was chosen such that at least two field cage rings will be scanned, ensuring a gap is present in the scanned region.

After establishing the alignment onto the cold mirror, the coverage limits of the laser system were explored. The obtained limits were then used to confine the nominal scanning regions. Further adjustment had to be made before a laser scan with optimal setting could be performed, these steps are discussed in Section 5.8.

After completed commissioning and system calibrations, nominal data runs were performed. Because of the unknown precise position of the field cage rings with respect to the cold mirror, a conservative scanning procedure is deployed. The cold mirror is first brought in a position where the laser beam is pointing downward towards the cathode, then a horizontal scan is performed at a fixed firing rate and movement speed until the limit is reached. The polar angle is then decreased without firing, and a horizontal scan is performed in the opposite direction, with the same movement speed and firing rate. This horizontal procedure is repeated

until the limiting angle in the polar direction is reached. This pattern is conservative in the way that it does not take into account the position of gaps in the field cage structure, at the cost of an extended total scanning time. The movement speed was chosen slow with respect to the laser firing, nominal scans were taken with a stepping speed of $v_h = 0.1\,\mathrm{deg/s}$ and a firing rate of $f_l = 4\,\mathrm{Hz}$. The horizontal stepping speed can be neglected as only a few steps (with respect to horizontal steps) were performed in this direction. In this configuration a complete laser scan with both systems lasted for about 6 hours, scan time can be adjusted by varying v_h and f_l according to the need. Laser scans were mainly performed during planned long beam shut breaks, during which maintenance and upgrades were performed on the proton beamline. Furthermore, laser scans were performed when the any unplanned beam downtime long enough.

5.8 SYSTEM CALIBRATIONS

Several parameters have to be tuned before a laser scan can be performed. First and foremost the laser path has to be aligned onto the cold mirror (see Figure 5.3 for details). Secondly, because of the reflectivity dependence on AOI, a laser energy attenuation calibration has to be obtained. Lastly, the cold mirror position relative to the TPC has to be calibrated precisely after the cryostat is filled with liquid argon.

Laser path alignment onto the cold mirror was performed when the MicroBooNE TPC was fully operational and was one of the major tasks during commissioning work. All alignment work in the laser box and on the feedthrough side was completed beforehand. In this state the only unknown parameters is the correct position of the mirror on the top flange (M3 in Figure 5.3). If the mirror was positioned correctly, and the cold mirror is arranged such that laser is deflected into the detector, an ionization signal would be created by the laser. For this reason a cold mirror position was selected, during laser installation, that fulfilled this criterion. Because of thermal shrinkage of the detector the path into the detector might become blocked by a field cage ring, but with horizontal adjustments to the mirror direction, the path is likely to be unblocked. More challenging is the alignment onto the cold mirror. In a first step, using the visible alignment laser, mirror M3 is positioned such that the back reflections from the quartz pipe surfaces are overlapping. In this position the alignment is approximately parallel to the quartz pipe. This position is set as initial position for a stepwise spiral scan of directions, the step size in both azimuthal and elevation axis were chosen to be 2 mrad. This corresponds to a displacement of 6 mm at the distance where the cold mirror is located. For the scanning procedure the laser beam energy was set to maximum, to leave an ionisation signal even if only a small part of the beam would be reflected by the cold mirror. Likewise, the beam diameter was set to maximum to increase the cross section between the incoming beam and the unknown cold mirror position. This path alignment has to be performed for each laser separately. Once the laser alignment is established, mirror positions are stored permanently and further calibration work can be performed.

To compensate the loss of reflectivity at high AOI at the cold mirror (see Figure 5.4), the energy of the laser pulse has to be adjusted accordingly. The goal of this calibration is to find a pulse energy setting for any AOI, such that hits produced by the laser are similar to minimum ionizing particle tracks. Since MicroBooNE track reconstruction algorithms are optimized for these kind of tracks, this will allow the reuse of theses algorithms to obtain laser tracks in later stage analysis.

Although the mirror behaviour is well understood and the possibility of a prior (to full detector operation) calibration is feasible, a calibration was performed for both laser systems after full laser commissioning. With this approach any systematic difference between the laboratory conditions of a calibration and the MicroBooNE laser system is excluded. To operate in the widest high reflectivity range of the mirror, the p-polarized output path of the attenuator is selected. This leads to a flat reflectivity behaviour for AOI up to 60°. To obtain a laser energy setting for all polar angles, the following approach is used. The cold mirror is brought to a position where no field cage is blocking the path, in this position a polar angle scan from 10° to 75° is performed for laser energy settings from 10 % to 90 %. The scan vertical movement was kept at a constant low speed of 0.5 °/s while firing laser pulses at a rate of 4 Hz, culminating in 520 TPC events per energy setting. A pulse energy step size of 10 % was chosen, resulting in a total of 4680 events. All events associated with a calibration run are processed trough the laser hit finder described in Section 6.2, with the amplitude/width veto disabled. The hit finder only reconstructed hits in the regions where laser ionisation signal was expected. For further analysis the mean amplitude over width ratio of all reconstructed hits in an event is considered. Figure 5.16 accumulates all information in a 3D graph, in the x-y plane the pulse energy setting and the AOI span two dimensions. The third dimension shows the mean amplitude over width ratio of single events, here colors indicate the power setting to better distinguish adjacent measurement points. Individual hit amplitude over width ratios indicate whether a hit is dominated by its amplitude or by its width, relative to a baseline.

Such a baseline amplitude over width ratio can be establish for hits with low laser energy of 10 %, here the probability of ionization by the laser is very low, so reconstructed hits originate solely from cosmic muons constantly penetrating the detector. Additionally a baseline is established where the laser is triggering the TPC readout, while mirror M2 is tuned such that the laser path is directed into the laser box wall. 2000 events were recorded in this configuration and processed identically to the data taken with laser tracks present in the event. The result of both approaches agree with ratios of $r_{a/w,10\%} = 8.2 \pm 0.3$ and $r_{a/w,0} = 8.12 \pm 0.08$, respectively. The presence of laser tracks in the expected region is correlated with elevated amplitude/width ratios relative to the baseline. Ratios of 20 and above start to appear for smaller AOI as the pulse energy is increased. The ratio reaches levels of 40 and above for fractional pulse energies above 0.8 for most of the AOI range. In Figure 5.17 four 2D views displaying the raw wire signals in a confined region is shown. In these graphs the raw signal amplitude is shown as a colour scale, dark blue is close to the baseline, light blue towards red indicates higher amplitudes. The selected region is approximately 6 m wide and 50 cm high. The

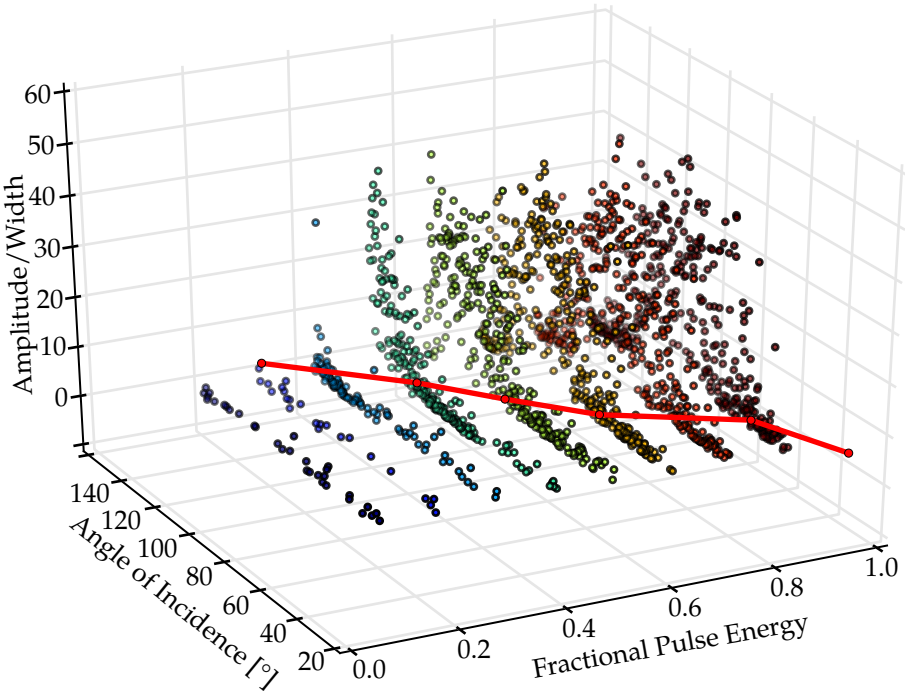

Figure 5.16: Event by event mean amplitude over width ratios for variable laser pulse energies and polar angles. The red line indicates the chosen calibration curve used for further laser studies.

laser beam enters from the left. In addition to the laser track, cosmic events are present in these views. For all four events the AOI is identical at 61°, but with increasing laser pulse energies of 20 %, 60 %, 70 % and 90 %. It can be observed that with higher pulse energies the signal amplitude increases as well. With low pulse energies of 20 % the ionization signal decays quickly along the laser path, the signal is lost in the noise level about 2/3 into the detector. At medium to high levels the ionisation signal is above noise level and similar to cosmic events, although the width of the signal is increased. At almost maximal energy the amount of induced charge reaches a level such that the pre-amplifiers become saturated and exhibit non-linear behaviour, corresponding to very high amplitude over width ratios.

The aim of the calibration is to produce laser signals of similar fashion to image b) in Figure 5.17 consistently over all polar angles. To achieve this, a pulse energy vs angle of incidence curve is chosen along the red curve in Figure 5.16. The curve follows the amplitude over width ratio value of 15 along all AOI. The curve is mostly linear, starts with a low energy settings at large AOI and increases towards larger pulse energies at smaller AOI. This behaviour corresponds well with the expected drop of reflectivity at smaller AOI. For further use, the calibration curve is implemented into the scan steering control software. The software automatically adjusts the settings of the attenuator to produce optimal ionisation signals in the TPC based on the desired polar angle in the scanning pattern.

The exact knowledge of the cold mirror position relative to the TPC is crucial for any processing of laser data. Without this information the true path of the laser

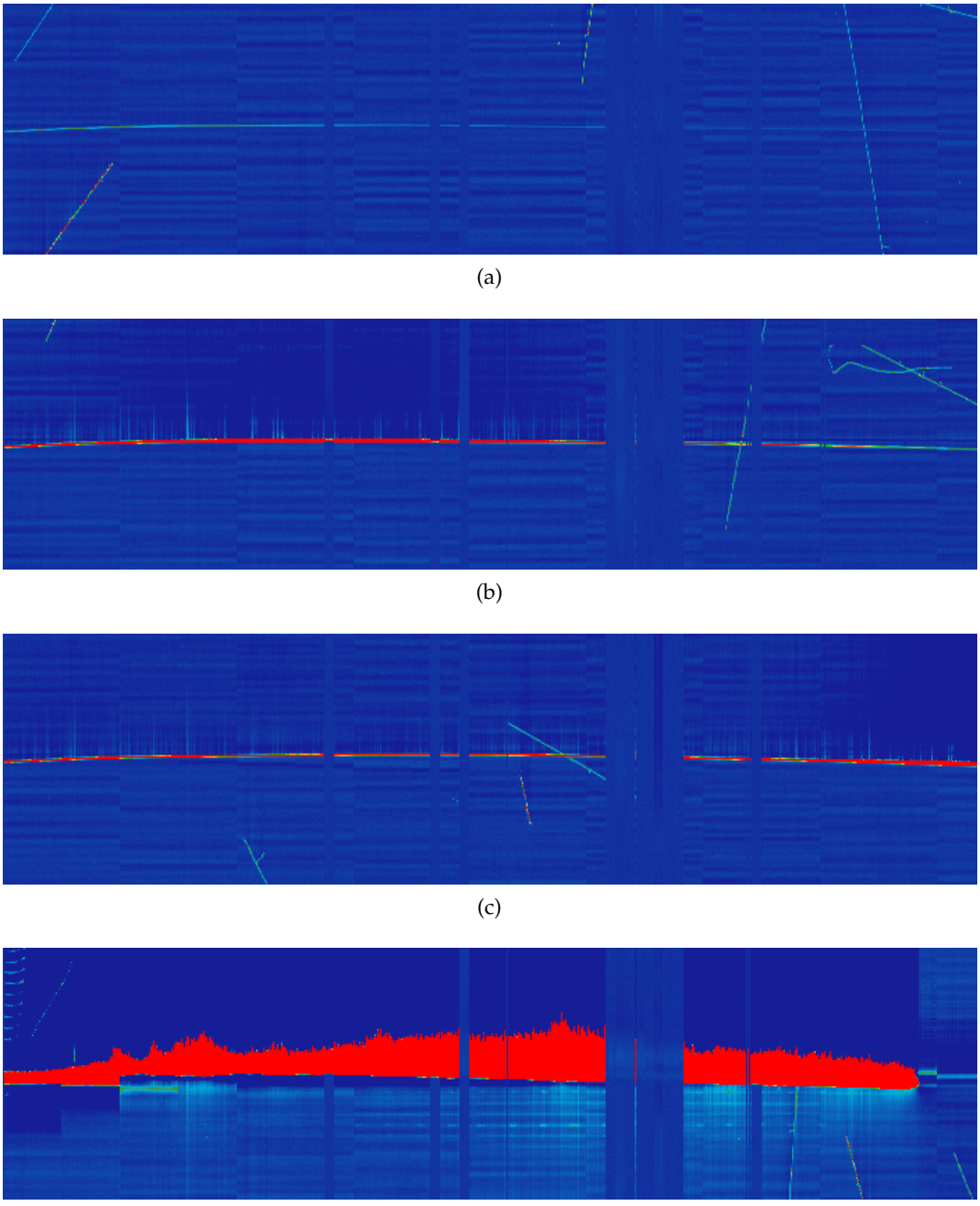

(a)

(b)

(c)

(d)

Figure 5.17: Four raw signal views for laser ionization signals at equal laser directions with increasing laser pulse energy (a) to (d). The selected region shows raw signal on the first 2000 collection wires (along the horizontal axis.)

is not well-defined and hence correction vectors cannot be determined precisely. The location of the mirror could have been measured when the TPC was inserted into the cryostat. However, the side location of the anchor point between the TPC and cryostat results thermal contractions that are hardly predictable. Therefore, the exact position has to be determined after the cryostat and TPC have reached liquid argon temperatures. The mirror position calibration is a two fold process. In a first step, relative distances to an arbitrary field cage ring are determined. In a second step, the absolute position of the reference field cage is fixed. Naturally this calibration has to be performed for both laser systems individually.

As base input, a data-set with multiple horizontal scans of the detector volume is used. A single horizontal scan consists of laser firings while the cold mirror is moving at a constant speed, scanning the azimuth range of the detector. During this movement the polar angle stays constant. The field cage rings will prevent laser beams entering the detector when aimed at them. Therefore, a horizontal scan will produce an on/off pattern of ionization signal either present or absent in the detector. This pattern is unique to a mirror position. It is also possible to calculate the expected pattern from any estimated mirror position, using basic trigonometry and the known ring diameter and ring-to-ring distances. Calculating the overlap of the estimated and observed pattern leads to an optimization problem. A sketch of the described procedure is shown on the right side of Figure 5.18. The measured pattern is extracted from collection wire data in a very narrow region at the entry point of the laser beam into the detector. This region is 200 wires wide (60 mm) and a drift time window of 200 µs. Hits are extracted from raw waveforms using the laser hit finder described in Section 6.2. The total number of hits present in the region is then used as a proxy for the presence or absence of a laser signal under the recorded azimuthal angle. The number of hits in the entry region is aggregated in a histogram with a bin size of 0.06° (blue crosses) shown in Figure 5.19 and Figure 5.20 (a). Regions with elevated hit counts clearly emerge between 5° to −25°, whereas for high angles the path into the TPC is fully blocked and laser beams can not enter. Moreover the width of the elevated count decreases as the angle increases, which agrees well with the assumption that the elevated hit count is produced by laser beams.

For the calibration of the mirror y-position a similar approach is deployed. As can be seen in Figure 4.6, two horizontal bars are installed for field cage support. This structure's position is well-defined and accessible with the laser system. Since its extension in the z-direction outward of the detector (also visible in Figure 4.6), this structure restricts the azimuth range of the laser system. An illustration of the procedure is sketched in Figure 5.18. For the y-position calibration a data-set is chosen where laser beams were introduced into the detector along a field cage opening. The scanned range includes polar angles from −70 deg to 70 deg, angles were aggregated into a histogram with bin size of 0.1 deg. To identify the presence or absence of laser tracks, the identical procedure as described above is deployed. In contrast to the x-z-calibration, only one large band where tracks enter the detector is present, with the boundaries defined by the support structure. Using the known distance ($D_{bar} = 97.335 \pm 0.200$ cm) and simple trigonometry, it is again possible to estimate the y-position.

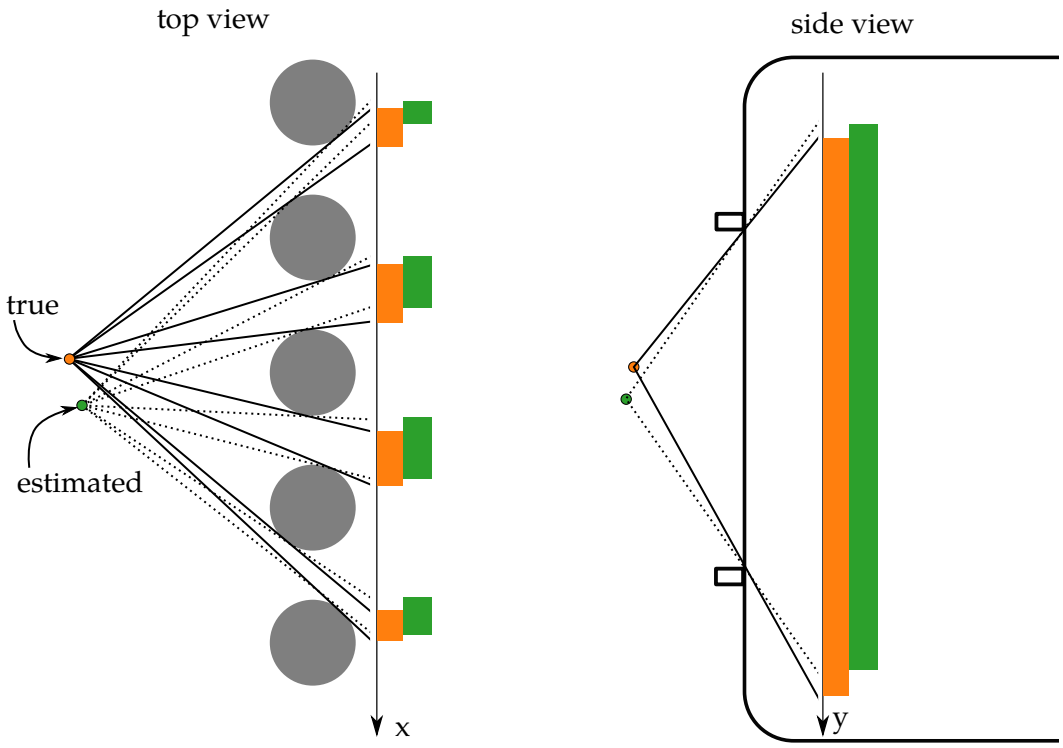

Figure 5.18: Sketch of the mirror position calibration procedure. On the left side, the top view (x-z-plane) is illustrated with the field cage rings in grey. The true laser position is illustrated in orange and solid lines, the true pattern under which laser tracks are visible is depicted in orange as well. In green and dashed lines an arbitrary estimated mirror position is introduced. The visible track range of the estimated position is shown as green band. On the right, a side view of the detector (x-y-plane) is shown. The laser range is restricted by the field cage support structure. Again the true and estimated laser positions are illustrated in orange and green, respectively.

Region edges with laser signal present are identified with a count threshold of 9 hits, the edge locations are indicated as red lines in Figure 5.19. In a final stage, the overlap of the measured and estimated widths is minimized using the the Nelder-Mead method of SCIPY [102]. This minimization is performed for all three space-dimension using the two independent data-sets. As initial estimators the known mirror position measured during installation is used. The results of the optimization problem for each laser system, together with the used data set is shown in Figure 5.19 for the upstream, and in Figure 5.20 for the downstream system. The mirror positions obtained with this method are summarized in Table 5.2.

SYSTEM	X[CM]	Y[CM]	Z[CM]
LCS1	103.8 ± 0.05	8.6 ± 0.05	-35.6 ± 0.05
LCS2	102.5 ± 0.05	8.2 ± 0.05	1080.2 ± 0.05

Table 5.2: Cold mirror positions after calibration

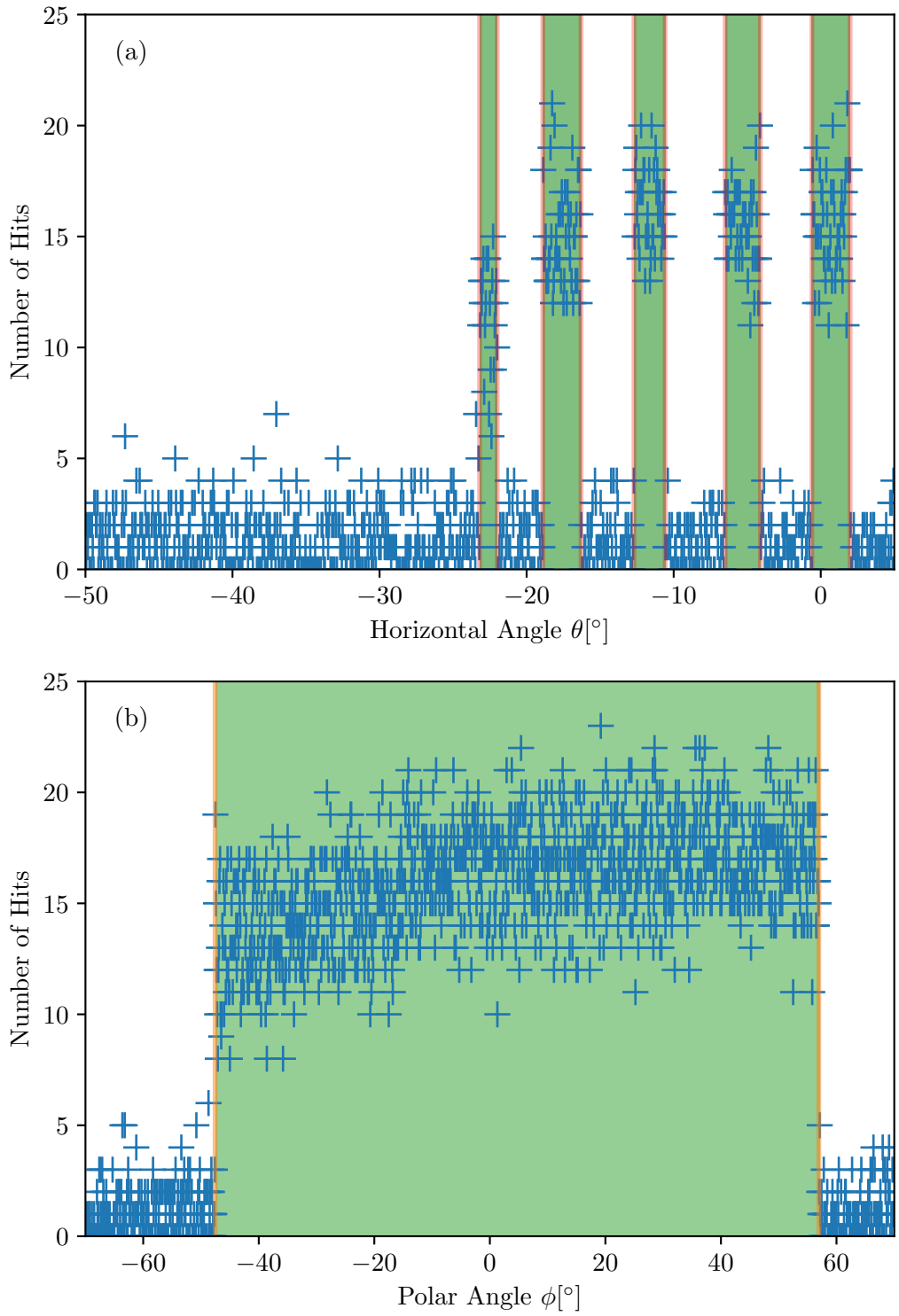

Figure 5.19: Cold mirror position calibration pattern for the upstream laser system. For azimuth (a) and polar angles (b). Blue crosses indicate the number of recorded hit for a given angle. Red bands show the direction under which gaps are measured. Green bands indicate the best location of the gaps under the best estimation of the mirror position.

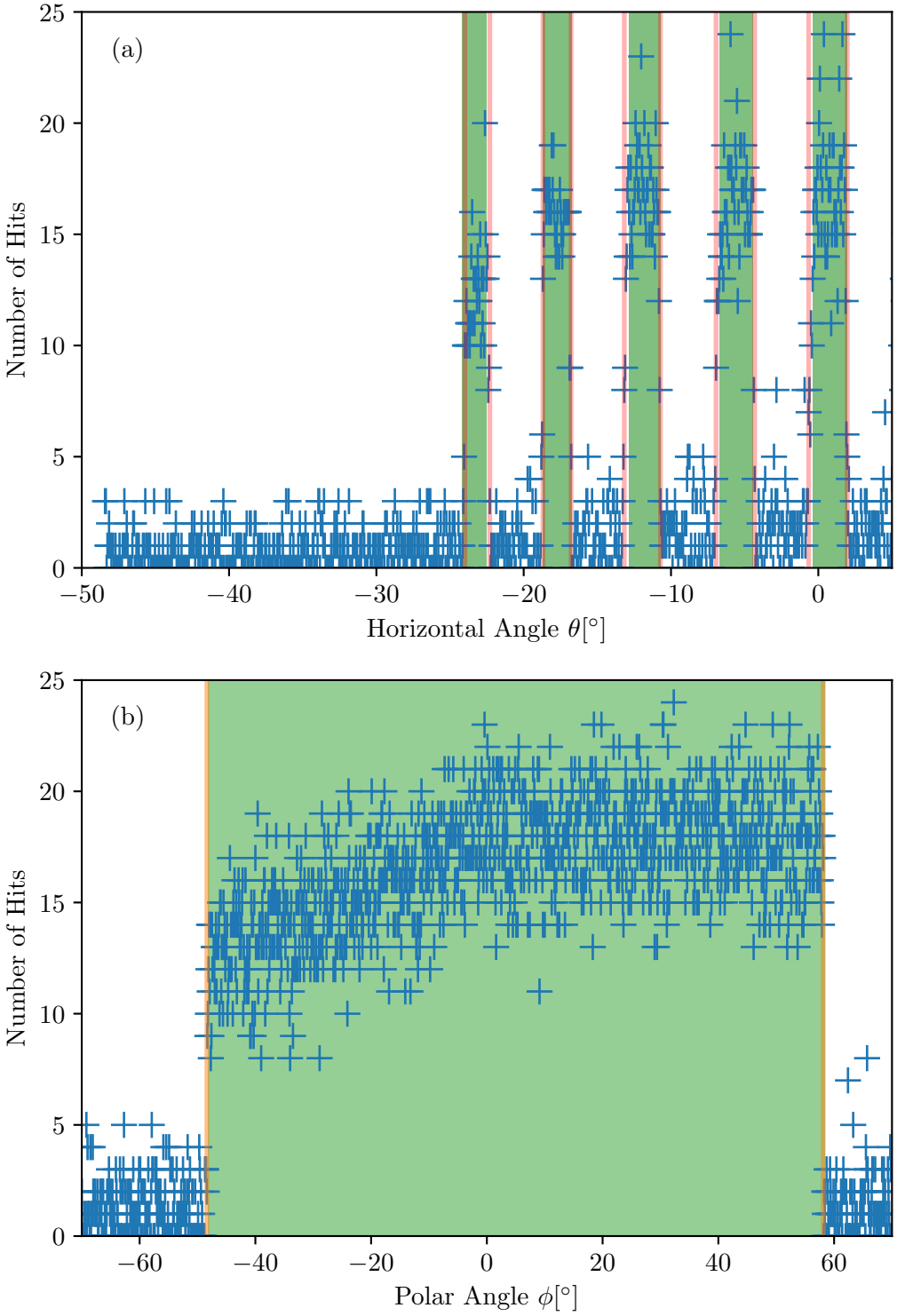

Figure 5.20: Cold mirror position calibration pattern for the downstream laser system. For azimuth (a) and polar angles (b). Blue crosses indicate the number of recorded hit for a given angle. Red bands show the direction under which gaps are measured. Green bands indicate the best location of the gaps under the best estimation of the mirror position.

6 ELECTRIC FIELD CALIBRATION

The most crucial detector properties of a time projection chamber is the electric drift field. The electric field governs the recombination rate of the electrons produced in the ionization process, impacting the electric signal formation. Immanently related to this is the scintillation light yield, electrons that are drifted away from the interaction site cannot participate in the scintillation process. Ultimately, both of these effects affect the calorimetric capabilities of the Time Projection Chamber (TPC). Furthermore, if the electric field is not uniform, ionization tracks will be distorted during the drift towards the readout plane. This leads to systematic errors in particle track reconstruction if not taken into account.

This chapter will introduce the electric field present in the detector and the various sources responsible for inhomogeneities of it. This is followed by several sections building up to the reconstruction of the electric field in the detector starting from raw data. First, hit finding and track reconstruction used to obtain laser 3D track signals is described. In the next section, the obtained track set is used to calculate residuals based on the information about the expected laser path. This is followed by the calculation and interpolation of a distortion map on a regular grid. Finally, the methodology used to derive the electric field based on the distortion map is introduced. All steps are illustrated in Figure 6.1. Additionally, parts as well as the full methodology is verified using a known electric field.

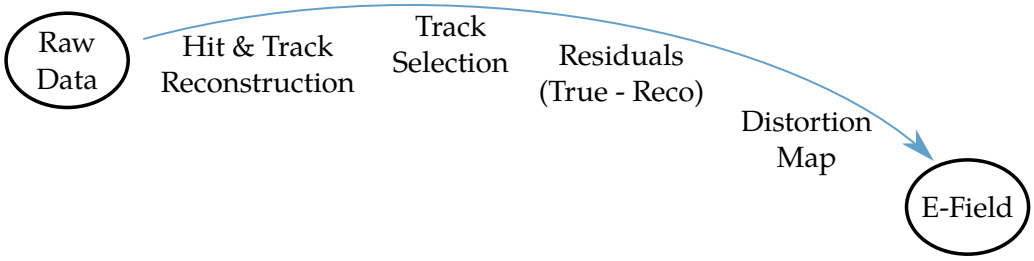

Figure 6.1: Different steps of the approach to reconstruct the electric field.

6.1 E-FIELD IN THE MIRCOBOONE DETECTOR

The MircoBooNE detector assembly is built such that the electric field points in a horizontal direction, see Figure 4.5, Figure 4.6 and Figure 4.7. At the anode ($U_{Anode} = 0\,\mathrm{V}$), three wireplane are installed for readout purposes. 2.56 m away from the anode, the cathode is installed, which can be held at various negative potentials. The nominal voltage, at which the TPC is operated during neutrino data taking is $-70\,\mathrm{kV}$. This anode-cathode configuration governs the main drift direction. To obtain an uniform electric field within the active volume, field cage rings are installed. 64 tubes, with a diameter of 2.5 cm, arranged around the volume be-

tween the anode and cathode, are held at an incremental potential such that field lines emerge and stay perpendicular to the cathode until they reach the anode. This ideal configuration allows for back-projection of the recorded wire signals to reconstruct a three dimensional track.

The goal of the following section is to understand and estimate the build up of space charge in the detector. First, the origin of the cosmic muons present in the MicroBooNE detector is discussed. Then the charge deposited in the detecor is estimated, which is then used as an input to E-Field simulations.

The bombardment of the earth by cosmic rays, which consist mainly of protons, alpha particles and heavier nuclei, induces hadronic interactions with the nuclei present in the atmosphere (mainly nitrogen and oxygen). A complete and thorough discussion of cosmic rays in the atmosphere can be found in [103] and references therein, what follows is a summary of the relevant processes for MicroBooNE. The primary particle interaction produce local showers, induced by mesons and other secondary particles produced in the collision. As the primaries pass trough the atmosphere further showers and secondaries are produced. The secondary particles consist of mainly π^+, π^- and π^0 but kaons and other particles are produced as well. These secondaries, if energetic enough, will themselfs form secondaries again, this process builds the backbone of the hadron cascade. However, these secondaries are all unstable, hence they decay, eventually stopping the cascade. Due to the increase of density when secondaries further penetrate the atmosphere, energy loss is increased and eventually the decay process overpowers the formation of new secondaries. Charged pion decays trough weak interactions into a muon and a muon-neutrino,

$$\pi^+ \to \mu^+ + \nu_\mu \quad \text{and} \quad \pi^- \to \mu^- + \bar{\nu}_\mu \tag{6.1}$$

with a lifetime of $\tau_\pi = 2.6 \times 10^{-8}\,\text{s}$. The lifetime of particles is enhance by the time dilation $\tau(E) = \gamma\tau_{0,\chi}$, with γ being the Lorentz factor known from special relativity. Neutral pions decay into gamma rays ($\pi^0 \to 2\gamma$) creating an electromagnetic shower via pair production and bremsstrahlung. The muons produced in the charged pion decay have a lifetime at rest of $2.2 \times 10^{-6}\,\text{s}$ and can survive great atmospheric depths if energetic enough. Hence the bulk of cosmic particles at the earth's surface is represented by muons.

The muon flux I at the earth surface is dependent on the energy and the azimuthal angle θ. Low energetic muon will decay before they reach the ground, while the flux at high energies at the surface is reflecting the primary particle spectrum. The dependency on the azimuthal angle is due to the increase in density from the extended path trough the atmosphere for high azimuth angles. Azimuthal dependency is very small, hence it is usually ignored. The muon flux has been measured and parameterized extensively in the last 50 years, [104] and references therein. An analytical approximation for the muon flux was given by Gaisser [105], which describes the muon flux at high energies and azimuthal angles up to 70 deg.

The expression was extended to include lower energies and higher azimuthal angles based on experimental data by [106], leading to

$$\frac{dI}{dE_\mu d\Omega} = 0.14\left(\frac{E_\mu}{GeV}\left(1+\frac{3.64GeV}{E_\mu(cos\theta^*)}^{1.29}\right)\right)^{-2.7}\left[\frac{1}{1+\frac{1.1E\mu\cos\theta^*}{115GeV}}+\frac{0.054}{1+\frac{1.1E\mu\cos\theta^*}{850GeV}}\right], \tag{6.2}$$

Where E_μ is the muon energy and θ^* the modified azimuthal angle. The two additive terms emerge from the pion and kaon contributions in the secondary spectrum. The modified azimuthal angle $\cos\theta^*$ is an empirical obtained fit that replaces $\cos\theta$ in the originally proposed equation and is given by

$$\cos\theta^* = \sqrt{\frac{(cos\theta)^2 + P_1^2 + P_2(\cos\theta)^{P_3} + P_4(\cos\theta)_5^P}{1+P_1^2+P_4}}. \tag{6.3}$$

From fits to data the parameters P_i were determined to,$P_1 = 0.102573$, $P_2 = -0.068287$, $P_3 = 0.958633$, $P_4 = 0.0407253$ and $P_5 = 0.81728$. Equation 6.2 gives the muon flux at sea level, it can be corrected for greater elevations taking into account the decrease in atmospheric depth. MicroBooNE is situated at 227 m above sea level [107], the atmospheric depth discrepancy to sea level is minimal, hence the effect is ignored. The analytical description in Equation 6.2 can be integrated over the solid angle to obtain the unit flux of muons in MicroBooNE, given an energy threshold. An energy threshold of 0.2 GeV is chosen, since muons below this energy travel approximately 14 cm in steel [20], hence most of muons in this energy range are absorbed in the bulk (liquid argon surrounding the detector, insulation, building etc.) above the MicroBooNE detector. The mean energy of muons at sea level is roughly 1 GeV [103], in this energy range muons are able to penetrate liquid argon roughly 4 m. Which is well above the The muon flux trough a horizontal area within these energy bounds is

$$I_H(E > 0.2GeV) = 1.72\times10^{-2}\,\mathrm{cm}^{-2}\mathrm{s}^{-1}. \tag{6.4}$$

This value well agrees with measurements [103]. To obtain the flux trough a vertical surface, a coordinate transformation is necessary, introducing an additional integration term, a detailed description is found in [108]. This leads to

$$I_V(E > 0.2GeV) = 0.55\times10^{-2}\,\mathrm{cm}^{-2}\mathrm{s}^{-1}. \tag{6.5}$$

With the knowledge of these two values it is possible to estimate the amount of muons passing trough the detector with the known geometry (see Section 4.3), using

$$R_{total} = R_{top} + R_{side} = lw\times I_H + 2(lh+wh)\times I_V \tag{6.6}$$

$$= 4560\,\mathrm{s}^{-1} + 3310\,\mathrm{s}^{-1} = 7870\,\mathrm{s}^{-1}. \tag{6.7}$$

To obtain the amount of produced charge, the mean track length per second in the detector has to be estimated. [108] estimates the mean track length based on a $\cos^2\theta$ approximation for the zenith flux distribution and horizontal slices much thinner than the total volume. The mean muon path length per second is then estimated to

$$\langle L\rangle = \frac{L_H}{R_{total}} \approx \frac{3}{2}\frac{I_H V}{R_{total}}. \tag{6.8}$$

where the total horizontal track length $L_H \approx \frac{3}{2} I_H V$ was estimated under the given assumption and $V = l \times w \times h$ is the volume. Using the above calculated total rate and horizontal flux together with the detector dimensions leads to $\langle L \rangle \approx 204\,\text{cm}$. In combination with the total rate this leads to an average total path length of all muons in the detector of $\langle R_L \rangle = \langle L \rangle \times R_{total} \approx 1.6 \times 10^6\,\text{cm/s}$ Assuming an minimum ionizing particle with a energy deposition per unit volume of 2.1 MeV/cm and the an average energy of 23.6 eV necessary to create an electron-ion pair, it is possible to calculate the average number of ions created per unit length

$$R_{ions} = \langle dE/dx \rangle / W_i \approx 90\,000\,\text{cm}^{-1}. \tag{6.9}$$

All created ion and electrons are subject to recombination, at the nominal electric field the recombination rate is 40 %, hence the number of ions produced is reduced by this factor. Combining the ion creation rate per unit length with the average total path length per second, it is possible to estimate the charge produced per unit time and volume

$$K = \frac{R_{ions} \times \langle R_L \rangle \times e}{V} \approx 2.2 \times 10^{-10}\,\text{Cs}^{-1}\text{m}^{-3}, \tag{6.10}$$

where e is the elementary charge.

With this source term, it is now possible to estimate the space charge distribution in the detector. Assuming an uniform electric field (ignoring effects from the introduced space charge itself), the ions slowly drift towards the cathode, where they are eventually absorbed. Hence the cathode represents a constant sink. For the following calculations the detector is assumed to be a infinite parallel capacitor, with the anode at $x = 0$ and the cathode at $x = D$. Also the space charge induced by the electron formed during ionization are ignored, since the charge is cleared much faster than the ions. The charge density is described by the (modified) charge continuity equation [109]

$$\frac{d\rho}{dt} = -\nabla \rho v_d + K - L, \tag{6.11}$$

where ρ is the charge density v_d is the drift speed, K and L are sink and source terms, respectively. Since we assumed a infinite parallel plate (drift direction is towards positive x) and we seek a steady-state solution, the equation simplifies to

$$\frac{d\rho v_d}{dx} = K, \tag{6.12}$$

where we put $L = 0$, since no sink is present. Trough simple integration, using the boundary conditions, the solution for the charge density

$$\rho(x) = \frac{Kx}{v_d} \tag{6.13}$$

emerges valid in in between the two parallel plates. This result can be interpreted in the following way. In a volume element at position x the charge produced during the time $t = x/v_d$ is equal to the charge that drifted from the anode (at $x = 0$) to x during this time t. Charge that was produced earlier already passed the volume element at x. With the drift speed $v_d = 0.6\,\text{cm}\,\text{s}^{-1}$ (at $E = 0.273\,\text{kV}\,\text{cm}^{-1}$) and the charge source derived in Equation 6.10, it is now possible to calculate the

ion charge density in the detector. At the anode ($x = 0\,\text{cm}$) the ion density is zero, since all ions are drifted away towards the anode and no new charge arrives from the opposite side. At the cathode ($x = 256\,\text{cm}$) the ion density is maximal $\rho(D) = 151\,\text{nC/m}^3$. The above discussion neglects the time-dependent terms in the continuity equation, a detailed discussion how space charge establishes over time is given in [109].

The derived space charge distribution is used as an input to a finite-element-simulation using COMSOL [110]. In the simulation the field cage geometry is approximated by a continuous boundary condition, corresponding to an ideal field cage geometry. The electric field is introduced with a potential of $U_{cath} = -70\,\text{kV}$ at the cathode. The anode plane is approximated with a continuous boundary condition $U_{anode} = 0\,\text{kV}$. A positive ion density according to the above derived relation is introduced. The impact of the ion space charge on the nominal field is shown in Figure 6.2 at two $z = 10\,\text{cm}$ and $z = 510\,\text{cm}$ in the x-y-plane. In the three rows the impacts on the three spatial directions of the electric field are shown as a ration of the nominal electric field E_0. At the edge of the detector, distortions in E_x and E_y are relatively small for all regions, this is due to the proximity of the slice to the side, where the boundary conditions introduce a field close to the nominal field. For the E_z case it is easiest to imagine the electric force acting on a negative charge probe located on the slice. Since most of the positive charge is present towards higher z, an attractive force towards the center is present, hence the field strength is diminished relative to the nominal field by roughly 15 %. For the central slice, the picture is more complex. Again the negative charge probe is instructive, for the E_x component the positive space charge density acting on the probe located at the cathode is present towards lower x, hence an attractive force is acting and the electric field is increased. Moving towards the cathode the attractive effect is offset more and more by the ions located behind the charge until the effect is reversed. When approaching the anode, the attractive force from all positive charge behind, towards the cathode, is reducing the nominal field. The distortion is obviously strongest at the cathode and anode with as much as 20 %. For the E_y case it is very similar, close to the top an attractive force by all space charge located below is acting on the probe hence an electric field pointing inwards is present. The effect is symmetric with a reversed sign for the bottom case. The maximal distortion of 15 % is again at the very edge of the detector. In the E_z case, the positive space charge for the central slice is equally distributed to the left and right, hence the two attractive forces acting on a probe charge cancel each other.

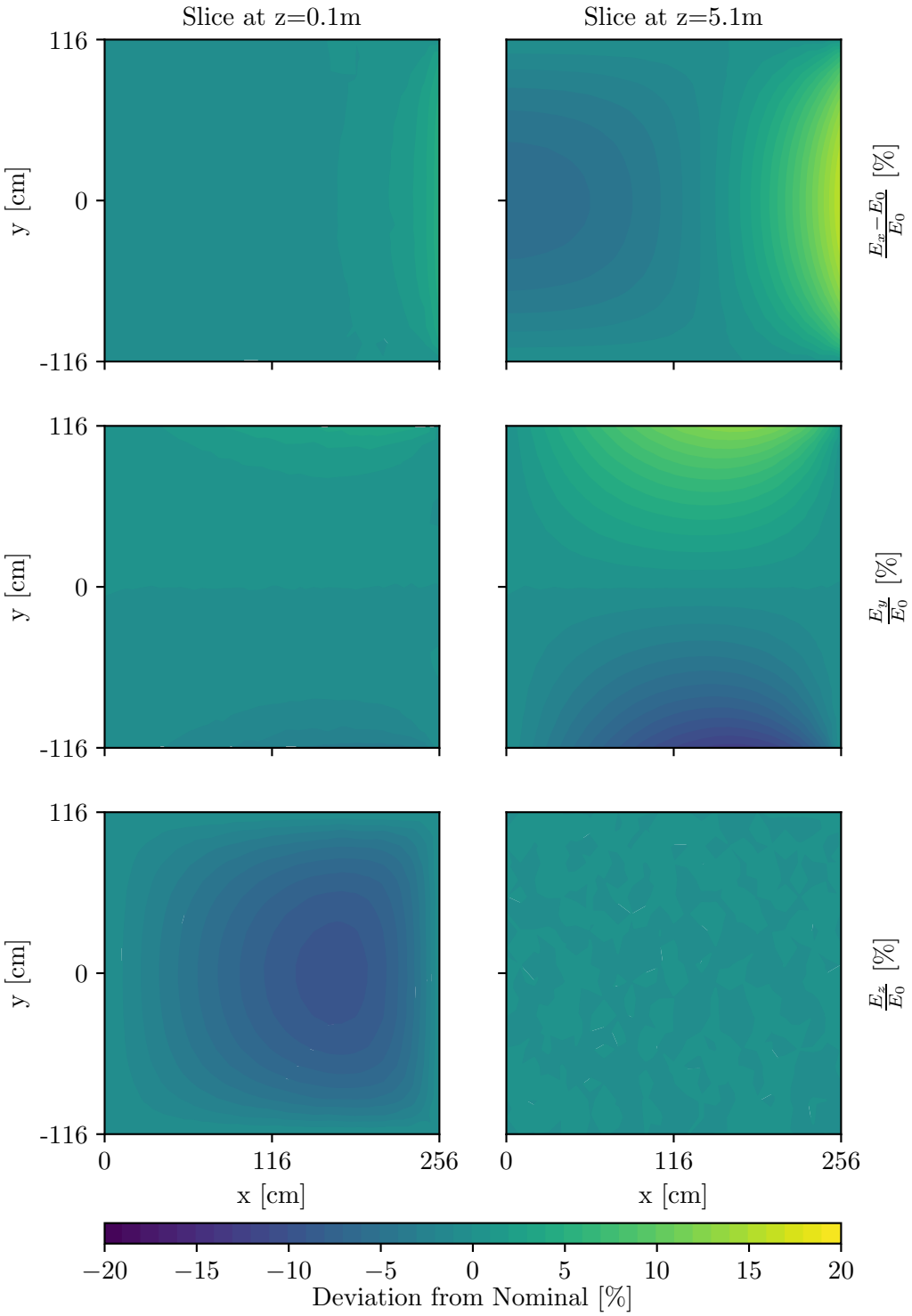

Figure 6.2: Simulated electric field deviations from nominal due to space charge in the MicroBooNE detecor for two x-y-slices. The left column shows slice close to the upstream face, the right column shows values for a slice in the middle of the detector. In the three rows, the deviation from the nominal field E_0 in the three spatial dimensions is shown in percent.

6.2 HIT FINDING AND TRACK RECONSTRUCTION

A laser scan consists of both laser systems scanning the active volume of the detector. A scan with an single laser system is denoted as a laser run. A laser run contains multiple TPC events, triggered by the firing of the Ultra Violet (UV) laser. To obtain a maximal converge of the TPC, under the premise of unknown precise location of the filed cage rings relative to the steering mirror position, the following scanning strategy is deployed. The polar angle is first brought to a maximal angle of 120° and then is successively decreased to 30° in a configurable stepsize. During each polar step, the mirror is moved azimuthally from either 3° to −45° or vice versa at a configurable fixed speed while firing the laser at a fixed, also configurable, repetition rate. Choosing a low horizontal scan speed with respect to the laser repetition rate, allows to obtain a maximal number of laser beams that enter the detector when aimed at a gap between field cage rings. For each event the laser direction is registered as described in Section 5.6. An estimated laser coverage based on the known laser position and the geometry of the field cage is shown in Figure 6.3. Furthermore, to prevent damage to the array of Photomultiplier Tubes (PMTs) by a high powered UV beam, the laser beam is not steered towards the anode.

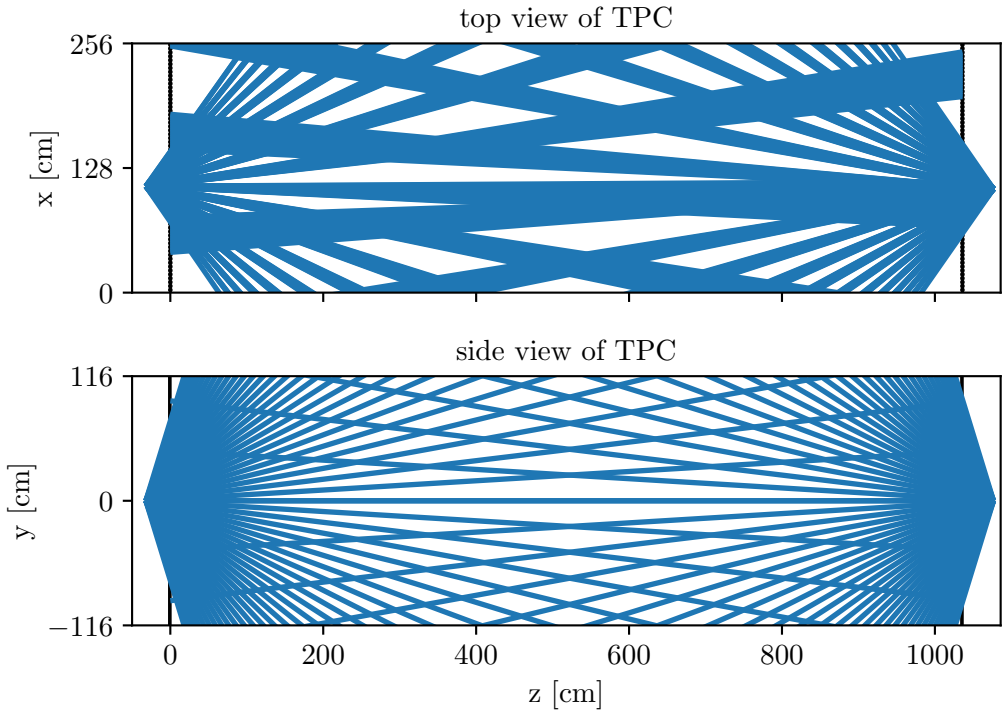

Figure 6.3: Estimated TPC coverage by the two laser systems.

The laser track reconstruction is partitioned into four steps: region of interest selection, hit reconstruction, laser detection and track reconstruction. These steps will be discussed in depth in the following paragraphs. Laser and TPC data are

combined by the procedure descibed in Section 5.6 before reconstruction is performed.

In a first step signals of all three wireplanes are cropped to a region of interest where the laser is expected. This is introduced to supress miss-identification of cosmogenic induced signals as laser tracks. Furthermore computational time of the following steps is greatly reduced, since the amount raw data to process is decreased. The selection is derived from the known laser true direction (see Section 5.6). Along the line defined by the laser entry and exit points a cylinder with radius $r_c = 50\,\text{cm}$ is introduced. The radius was chosen conservatively based on the maximum expected distortion amplitude of the order of 20 cm, estimated form simulation (see section Section 6.1). To ensure no accidental exclusion of laser tracks the radius was chosen twice as large as the maximal distortion. In all further steps only signals within this region of interest are considered.

In a second step the digitized signals of all thee wireplanes are searched for ionization signals (further called hits) individually. To identify hits a custom algorithm, optimized for laser induced signals, was developed. Existing hit finders are highly optimized for minimum ionizing particles and were found to be unable to handle larger signal amplitudes, resent in laser data. These high amplitudes were produced due to pulse energy fluctuations of the UV laser source and the non-linear reflectivity of the cold mirror. Raw signals differ from plane to plane, on the collection plane a single positive peak is present, whereas on the induction plane a bi-polar signal is induced (see section Section 3.7 for a detailed discussion). Before hit detection is performed, the baseline is subtracted from each wire. The baseline is obtained from calibration noise runs, performed independently of the laser calibration work. From the same data set the standard deviation of an individual wire was measured, which is used later. The method deploys several thresholds to identify hits. Signal amplitudes are scanned along increasing sample time. On collection wires, if the signal amplitude exceeds the threshold t_p, the subsequent samples are scanned until the amplitude falls below the threshold again. A new hit is defined within these time limits. The maximum amplitude (peak amplitude) and the associate sample time within these bounds is saved. On induction wires, two thresholds t_p and t_n (positive and negative) enclosing the signal are introduced. Again wire signals are scanned along increasing sample time, if the recorded amplitudes exceeds the negative threshold, the signal is scanned until it falls below the positive threshold again. These bounds are used to define the hits time extension. The middle point of the distance between maximum positive and negative amplitudes is used to define the hit's time locations. All aforementioned thresholds are chosen twice as large as the wires noise standard deviation $t_p = 2\sigma_i$ and $t_n = -t_p$ where i is the wire number. In addition to thresholds a peak to width ratio requirement is introduced per wireplane, to reject small amplitude and relatively long time-scale oscillations. The discussed algorithm is implemented as an LArSoft [111] producer module, an illustration of its working principle can be found in Figure 6.4. In Figure 6.5 all recovered hits for all planes in a laser event are shown. The detected hits contain information about the peak amplitude, width and digitization time of the found signal.

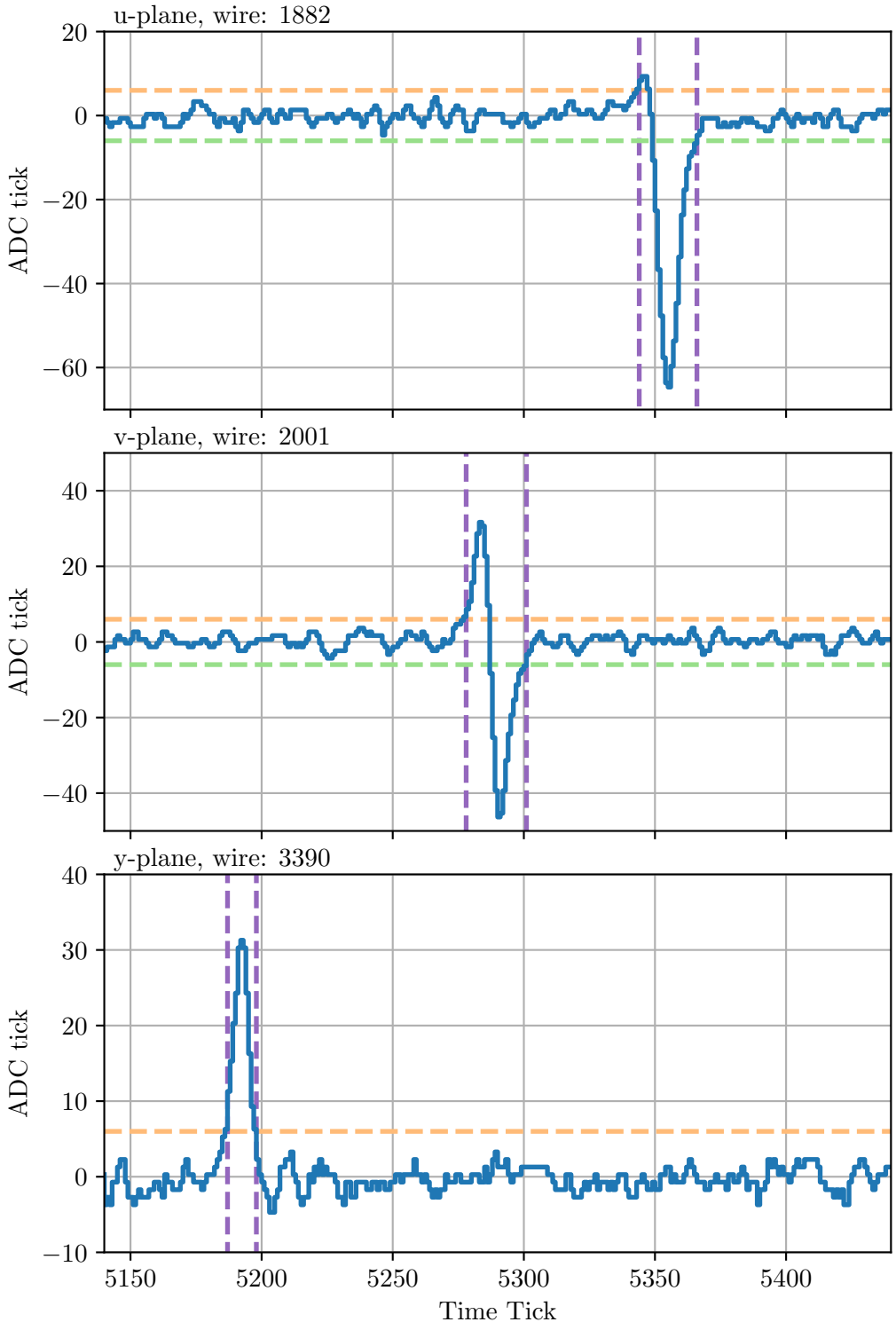

Figure 6.4: Illustration of the hit finder working principle for all three wire-planes (top: first induction (u), middle: second induction (v), bottom: collection (u)). An example wire signal is shown in blue, the applied threshold are shown in orange (t_p) and green (t_n). The time range of the identified hit is indicated in purple.

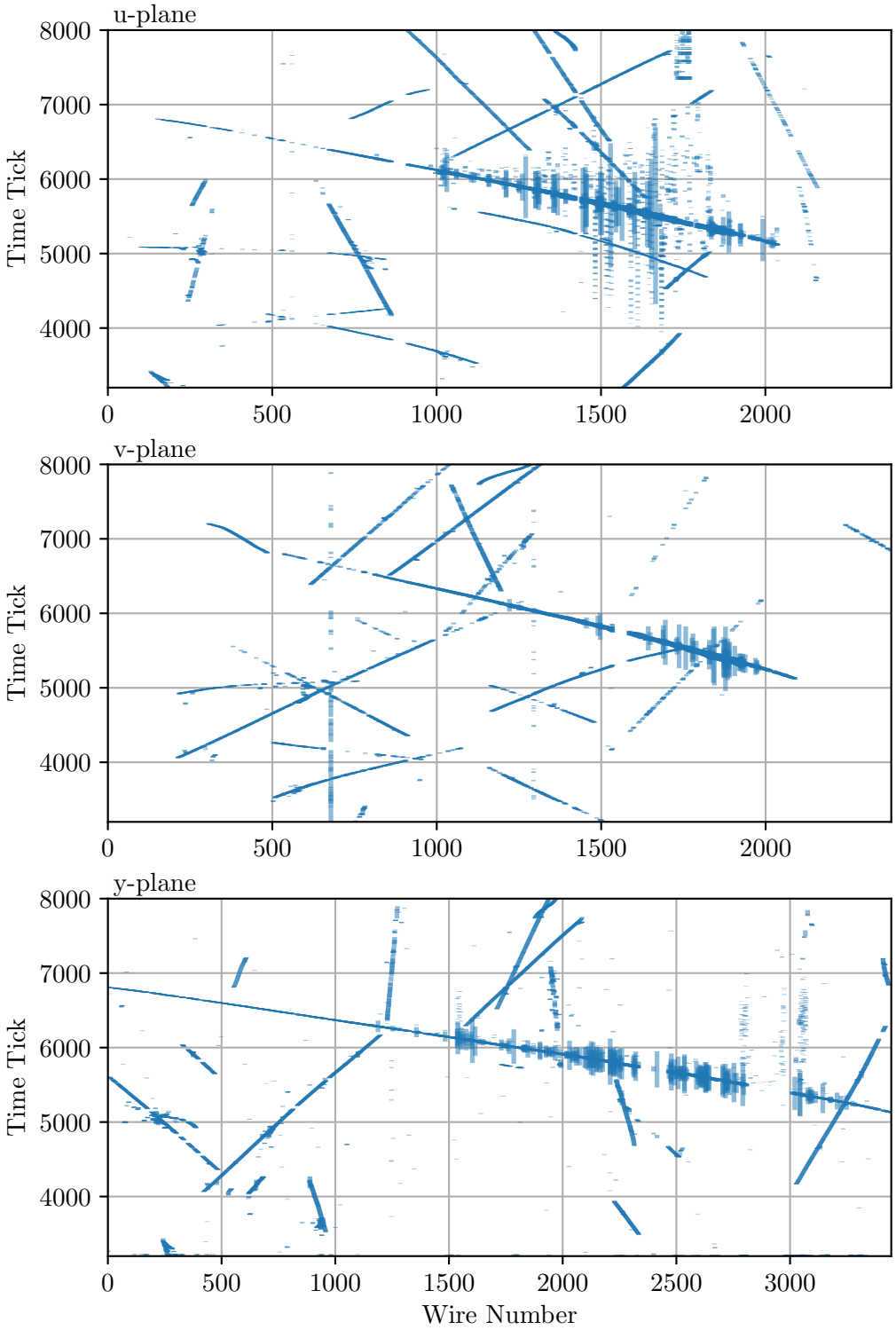

Figure 6.5: Hits reconstructed on all three wire-planes (top: first induction (u), middle: second induction (v), bottom: collection (u)) with the laser hit finder for a single laser event.

In a third step, the recovered hits on the three wire-planes are used to derive a three-dimensional trajectory, also denoted as a track. Several approaches to achieve this exist, hence a plethora of software algorithms was implemented with different stages of development and scope. Approaches include the use of Kalman filtering [112], machine learning [113], tomography [114] and pattern recognition [115]. Several of these algorithms were evaluated for laser track reconstruction, with varying success. The best performance in terms of track reconstruction efficiency and ease of use was provided by the Pandora software package, the detailed working principles of the algorithm can be found in [115]. For laser track reconstruction, only the subset of tools designed to identify minimum ionizing muons was applied on the laser hits provided by the previously discussed selection. The Pandora package was used as a standard way to obtain laser tracks from hits (in a single event) for all obtained data-sets. The main information present in a track, is the reconstructed trajectory and the corresponding error estimates. Until now, for each event (generated by a single laser firing) an assembly of tracks within the region of interest is present.

6.3 TRACK SELECTION

In the previous section the procedure to obtain tracks was discussed, in a next step, described herein, the so obtained set of tracks is further processed to identify or reject tracks be of laser origin or be per event with high efficiency. In each detector event only one or no laser track is present. For calculating a distortion map in a later stage, it is essential that a pure, in a sense that only laser tracks are matched with true laser information, data set is present. A single track wrongly associate with a true laser track, can disturb calculations significantly, especially if that track is traveling into regions not accessible by the laser. In this region no 'balancing' by other tracks in the vicinity is present and the residual is generally large for a misidentified track. To obtain a pure laser track data set, four selection criteria, described below, are applied to the input data set. Figure 6.6 illustrates these four steps of track selection graphically. In a first step, only tracks that have associate trajectory points within the expected entry region are selected. This region is defined by a box with 20 cm edge length, with the outer face's center aligned onto the expected entry point. The dimensions of the box are chosen based on the expected entry positions of the laser when scanning horizontally and vertically using the known mirror position (see Section 5.8). This is necessary because also accidental cosmic tracks in the region of interest (defined during hit finding) are reconstructed. In a second step, cosmic accidentals are further minimized. In this step the slope of the reconstructed track is compared to the expected slope of the true track. The slope is defined by the average of the mean slopes at the beginning and end of a track. The mean slope of the head (tail) of a track is constructed by fitting a line trough the 100 first (last) space points of the track. The cut criterion is set relaxed, reconstructed slopes that differ more than $\pm 50\,\%$ of the expected slope are excluded. In a final step, the tracks smoothness is taken into account. This cut is in place to eliminate tracks that show non-physical artifacts (oscillations, hard kinks, etc.) due to failing track reconstruction in earlier stages. Whereas a correctly

reconstructed laser track is expected to be relatively smooth, not undergoing any sudden direction changes, due to the continuity of the electric field in the detector. The data cut is applied on the maximum step size of a track along any wire plane, after subtracting the best linear fit, excluding any directional bias. A relatively rigors exclusion rule of $\Delta x \geq 1.2\,\text{cm}$, three times the wire spacing, is chosen here. The non-stringent cut is necessary, since the exact electric field is not known, although expected relatively uniform based on observed cosmic muon tracks. This is due to the fact that downstream distortion and electric field reconstruction are very sensitive to hard kinks. The step size vs z-distance of a full set of tracks (surviving the earlier cuts) is shown in Figure 6.6. On the basis of this data set, the distortion map and the electric field map is calculated, described in the following sections.

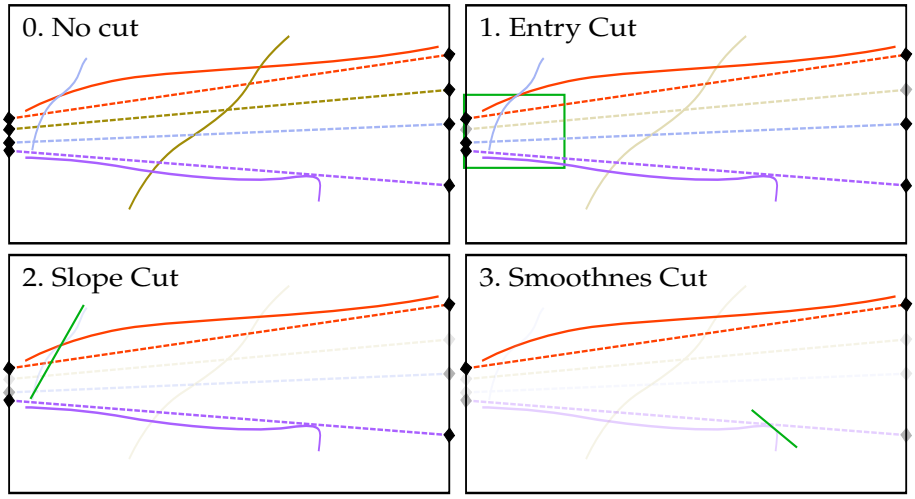

Figure 6.6: The three track selection criterion illustrated. (0) The input data set, dashed lines represent true laser information, full lines represent reconstructed tracks. Different colors indicate pairs of true and reconstructed track information. (1) Entry region (green box) selection. (2) Slope mismatch of true and reconstructed track. (4) Hard kink at the end of the reconstructed track

6.4 DISTORTION MAP RECONSTRUCTION

The input data set consists of a collection of laser tracks and its associate true information. This includes a laser scan from each laser systems (up- and downstream), described in the previous section. A single laser track is defined by a set of 3D space points, along the laser trajectory, obtained from track reconstruction. During track reconstruction a homogeneous electric field in the detector is assumed. Single tracks are not required to span the entire expected trajectory. This can occur whenever track reconstruction fails, due to missing wires or crossing trajectories from other sources, or the laser ionisation signal is too low for hit reconstruction. Furthermore, the true laser beam information, defined by the intersection points of the UV laser beam with the TPC boundary, is present in the input data set. The intersections are derived from the measurements of the polar and azimuthal angle described in Section 5.3. Additionally, in the truth information a laser system identifier is encoded. It is crucial that the input data set consists entirely of track

produced by a laser beam, not including any tracks from other sources. Otherwise, truth information is associate with a random trajectory, which will skew the calibration calculations towards higher displacements. This will become more clear in the following paragraphs.

In a first step, the displacement from truth information is calculated for each individual track in the input data set. To each space point a 3D vector $\vec{d}$ is associated corresponding to the estimated difference of the reconstructed $\vec{r}$ zand true position $\vec{t}$, according to

$$\vec{d}_i = \vec{t}_i - \vec{r}_i, \tag{6.14}$$

where i is the index of the reconstructed point within the single track. The true position $\vec{t}_i$, associated to the position $\vec{s}_i$ can be determined in several ways, but will always be located on the line defined by the entry and exit point of the laser beam into and out of the TPC. As a first approximation, the closest point on the truth line to the reconstructed point $\vec{r}_i$ is chosen as $\vec{t}_i$. Therefore, the displacement vector is defined by

$$\vec{d}_i = (\vec{L}_{entry} + \alpha_i \vec{T}) - \vec{r}_i \tag{6.15}$$

where,

$$\begin{aligned} \vec{T} &= \vec{L}_{exit} - \vec{L}_{entry}, \\ \alpha_i &= \frac{(\vec{r}_i - \vec{L}_{entry}) \cdot \vec{T}}{\vec{T} \cdot \vec{T}} \end{aligned} \tag{6.16}$$

Here the laser entry $\vec{L}_{entry}$ and exit $\vec{L}_{exit}$ points are introduced. The procedure is illustrated in Figure 6.7. This approach is robust in the way that reconstructed tracks not extending over the full truth range are handled without issues, the displacement vector can always be determined. With this procedure for every reconstructed point, a displacement vector is obtained.

A different approach, where the reconstruction track start and end points are matched to truth information, subsequently the intermediate points are mapped onto the truth line proportionally, is feasible. But this approach would not be robust against broken tracks, since track and truth ends are mismatched. This shortage could be overcome by implementing an algorithm ignoring broken tracks, however this would greatly reduce the number of used tracks, hence detector coverage decreases and statistical error increase.

Another alternative approach, where the crossing point of two laser beams, originating from opposite sides, is used as a ledger to determine the displacement of the reconstructed crossing point is conceivable. This would result in low coverage, since the region accessible by both laser system is small. Although this shortcoming, this procedure is used to verify the cold mirror position of the laser system in Section 6.7.

Residuals for Δx and Δy along the z-axis of the detector (for example runs 7267 and 7252) are displayed in Figure 6.8. The upstream and downstream data sets contain 911 and 1202 tracks, respectively. Since the upstream system is located at $z = -35.6\,\text{cm}$, tracks enter at $z = 0\,\text{cm}$ and propagate towards increasing z. The downstream system shows opposite behaviour, tracks enter at hgih-z and decrease

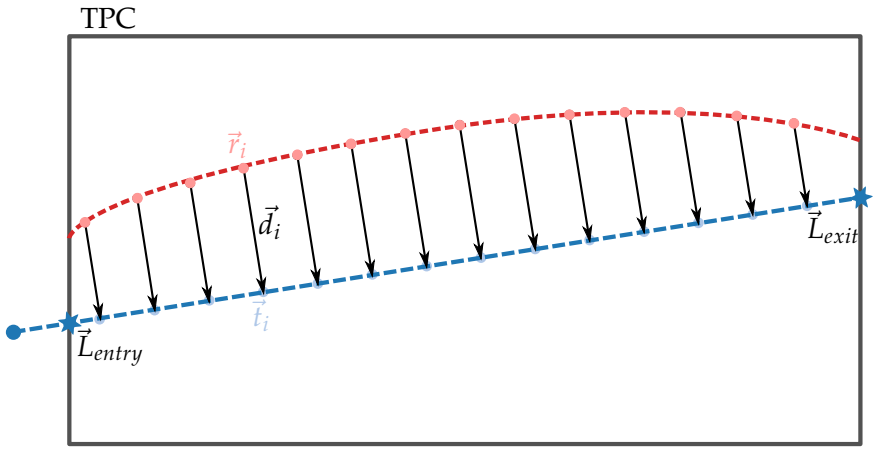

Figure 6.7: Illustration of the closest point approach. As a dashed blue line the true laser position is drawn, the red dashed line represents the reconstructed laser track. Red and blue dots show the associate points, respectively. Black arrows show the displacement vector $\vec{d}_i$

as they further progress. For the Δx graphs the color indicates the azimuth angle, where yellowish tracks are aimed straight, hence they travel the full span of the TPC. Greenish to purple colors indicate an increased azimuthal angle, aiming closer to the cathode, this makes the tracks stop at the cathode and therefore end at smaller and smaller z coordinates. For the Δy graphs the color indicates the polar angles, from yellow to pointing downwards (and hitting at the bottom) via greenish (spanning the full detector) to purplish pointing upwards. Already at this stage distortion effects are well visible. A clear symmetry between upwards and downward pointing tracks is observed in the Δy graphs. This is expected from a positive charge concentration at the center of the detector, electrons produced by tracks pointing upwards, are increasingly pulled towards the center (since the charge asymmetry increases) as they approach the top, resulting in a negative residual to the expected track. The same, with a inverted sign, is valid for track pointing towards the bottom of the track. In contrast, straight tracks are subject to a symmetric positive charge cloud, hence the forces cancel each other. For the Δx residuals the residual behavior is not symmetric, tracks pointing towards the cathode are 'bent back' to lower residuals. For electrons formed close to the cathode, the positive charge is between their current location and the anode, this leads to an increased field (hence increased drift velocity). As the charge drifts towards the anode, more and more positive charge is observed behind the current location, reducing the electric field and so reducing the drift speed. These two opposing effects partly compensate each other, leading to a decrease of distortion for charge produced close to the cathode. Therefore, the maximum distortion in x is found around $3/4$ along x.

Furthermore, nearby track residuals (with similar or same coloring) show high correlation, this indicates that the electric field is slowly varying as expected. This also indicates that track reconstruction and selection is working as expected, rejecting tracks with oscillating or other artefacts introduced by the hit and/or track reconstruction.

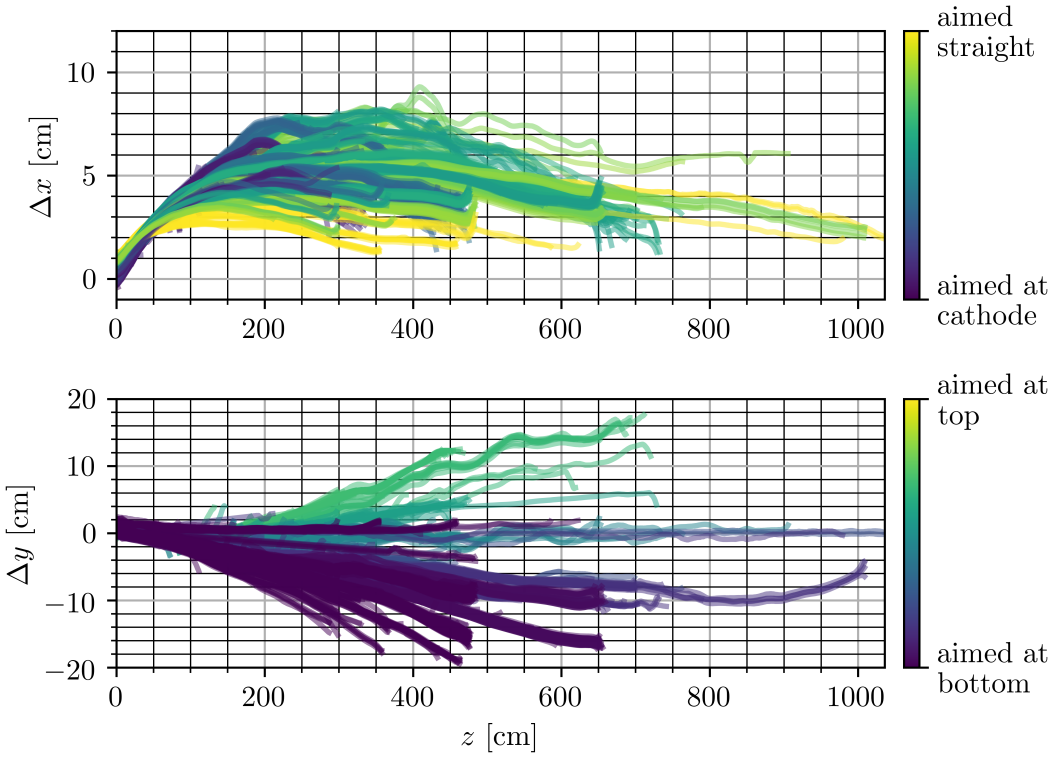

(a)

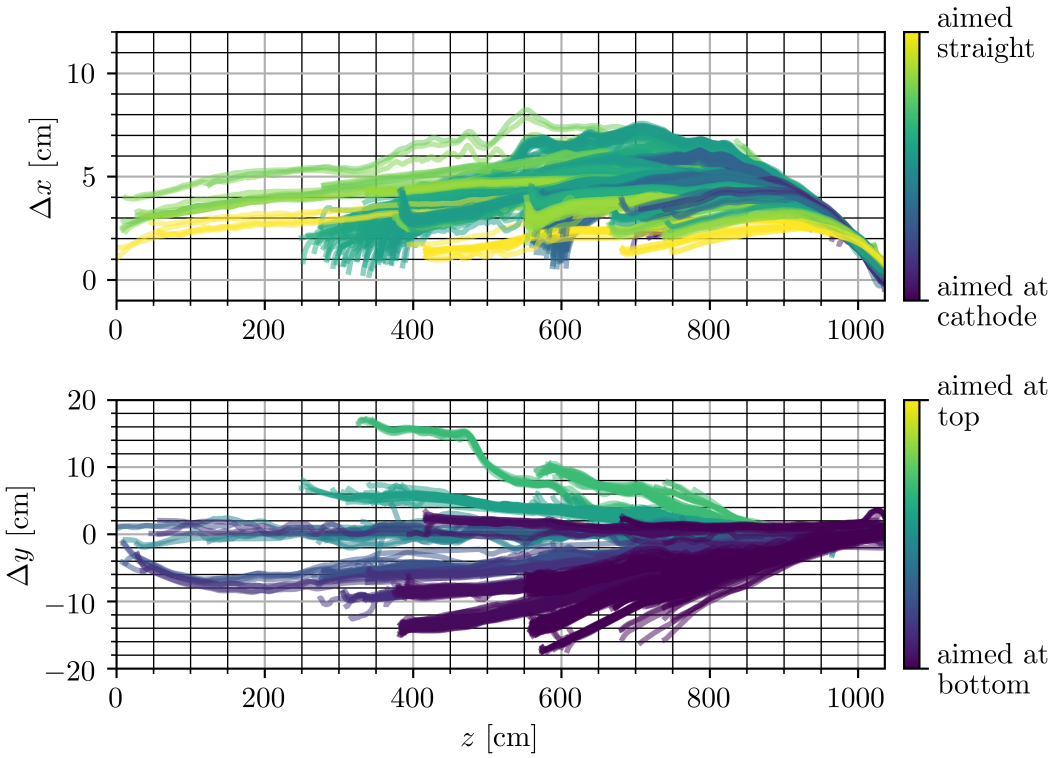

(b)

Figure 6.8: Δx and Δy track residuals relative to the true laser information along the z coordinate. For the upstream (a) and downstream (b) laser system. Different colors indicate the polar and azimuth angle. Different lengths of the tracks arise from beams hitting the top, bottom or cathode of the detector.

By now, a set of non-regular spaced points (along reconstructed laser tracks) with an associated distortion vector is available. For later processing and application of this distortion map a 3D regular grid in the detector is introduced, with a voxel size of $10 \times 10 \times 10\,\mathrm{cm}^3$. The voxel dimensions were chosen to restrict computational time and memory usage, it can be decreased if necessary. Distortion vectors for voxel central points $\vec{v}_j$ are interpolated from the surrounding true points and the associate displacement vectors. The interpolation is based on the four truth points that enclose the regular grid point in a tetrahedron. To obtain all possible and optimal tetrahedrons, before interpolation, a meshing stage is implemented. The meshing engine used in this mesh generator is based on Delaunay refinement [116], the engine is part of the CGAL (Computational Geometry Algorithms Library) C++ library [117].

For the interpolation step onto the regular grid, the barycentric coordinate system [118] is used. Here the four displacement vectors at the tetrahedron vertices are given by $\vec{V}_i$ with $i = 1 \ldots 4$, the 3D location of a vertex i is given by x_i, y_i, z_i. To interpolate the barycentric coordinates λ_i of an arbitrary point $\vec{P}$ is obtained via

$$\begin{pmatrix} \lambda_1 \\ \lambda_2 \\ \lambda_3 \end{pmatrix} = \mathbf{T}^{-1}(\vec{P} - \vec{V}_4), \tag{6.17}$$

where

$$\mathbf{T} = \begin{pmatrix} x_1 - x_4 & x_2 - x_4 & x_3 - x_4 \\ y_1 - y_4 & y_2 - y_4 & y_3 - y_4 \\ z_1 - z_4 & z_2 - z_4 & z_3 - z_4 \end{pmatrix}. \tag{6.18}$$

The fourth barycentric coordinate λ_4 can be inferred from the relation $\sum_i \lambda_i = 1$. With this information, the interpolation of the vector field $\vec{V}_P$ at $\vec{P}$ is then obtained trough

$$\vec{V}_P = \sum_i \lambda_i \cdot \vec{V}_i. \tag{6.19}$$

The method is computationally very inexpensive, with a single 3×3 matrix inversion necessary. One drawback of the described method is that only the closest displacement vectors are taken into account for the interpolation. With the relatively coarse regular grid (with a spacing of 10 cm) compared to the dense reconstructed points, with a spacing of roughly 3 mm (based on wire spacing), most of the reconstructed displacement vectors are ignored. To overcome this limitation, the set of displacement vectors is divided into n sub-sets, where data points associate with a track are devided into n sub-sets. For each sub-set the interpolation onto the regular grid is performed. The results of the sub-sets are then combined by summing up the individual displacement vectors and dividing by the number of sub-sets generated, essentially averaging over the sub-sets. At edges, where the displacement vectors coverage of the regular grid in a sub-set might not be consistent with the full set, no extrapolation is performed. Instead, no interpolation is performed at all, reducing the number of vectors contributing to the average for this particular point by one. The interpolation on individual sub-sets was performed in parallel using the OpenMP [119] framework. Based on the relative spacing of the two grids,

the number of sub-set was chosen to 25, leaving at least two reconstructed points between two points on the regular grid.

Since the laser is not fired towards the anode, but the electric field at the anode is well defined trough the set point of the bias voltage. Hence, an boundary condition describing zero distortion at the anode was introduced during the interpolation stage. Furthermore, space charge is expected to be the main contributor to distortions in the electric field, since no other geometry is present. Simulation shows that the distortion varies gradually and has no sharp jumps, which would not beo resolved by the interpolation between the anode boundary condition and the closest data point. The spacing between the anode and closest laser beams is roughly 50 cm, which results in increased detector coverage of roughly 20 %.

Additional improvement can be achieved by using the information from which side the laser track was introduced into the detector. Especially, the correction parallel to the laser track is difficult to resolve without using this information. An iterative back and forth approach where displacements are gradually adjusted from data from one side by the opposite side is implemented. The two displacement map from each side are denoted as D_1 and D_2 in the following. As an example, a k-iteration step approach is discussed. In a first step, the displacement based on one side is calculated using the above descibed procedure, leading to $D_{1,1}$, where the second index indicates the iteration step. In the second step, the so obtained displacement is applied onto the reconstructed track points from the opposing side reduced by a factor $\frac{1}{(n-(k-1))}$, where k is the index of the current step. To apply the correction, the meshing and interpolation routines described above are deployed. Based on this adjusted input set of reconstructed tracks, the displacement $D_{2,1}$ is calculated, in the third step. Closing the loop, based on the newly obtained distortion map, track inputs used to calculate D_1 are corrected by $D_{2,1}$. This loop, where distortions are back and forth adjusted by $D_{1,k}$ by $D_{2,k-1}$ is then continued n times. Finally in a last step the so obtained position is projected to the true position using the closest-point approach onto the line defined by the true beam information. With the two points, start of the iterative approach and true position found by the iterative approach, a resulting in a distortion map is obtained.

In Figure 6.9 the reconstructed distortion map for a central ($z = 512$ cm) and side ($z = 12$ cm) x-y in all three spatial coordinates is shown. In the side view the coverage is lower due to the geometric location of the laser systems. In the central slice, expected distortions from space charge are present, in drift direction (x dimension), the maximal distortion of 7 cm is located at 140 cm. This behaviour is expected due to cosmogenic induced space charge with an increasing density towards the cathode (see Section 6.1). Electrons produced close to the anode does not exhibit strong distortions, since most the local charge density is low and the maximum space charge is far away. Electron signals closer to the center is subject to a attractive force from the positive charge behind its location towards the cathode and an attractive force from all positive charge towards the anode, although smaller since the space charge is reduced towards the anode. For ionization signals closer to the cathode this effect is reduced by a faster drift in the first $1/3$ of the detector towards higher distortions and a subsequent slowing due to attractive force behind the covered drift distance down in the second $2/3$ closer to the anode. For the

distortion in y direction, the attractive force located along the central z axis of the detector. At the bottom and top edges the positive charge below or above causes an distortion on electrons towards the center of the detector. When moving along the top and bottom edge towards the anode, the effect reduces since the distance to the maximum of positive charge is increasing. At the center of the TPC positive charge is located above and below and the two attractive forces offset each other. In the z-direction at the edge the distortion is expected to be larger and at the central slice the effect of space charge should be minimal (since forces due to space charge cancel). The latter can be observed, whereas the first is not resolved due to coverage of the region by a single laser system.

6.5 ELECTRIC FIELD RECONSTRUCTION

In a final step the above discussed displacement map is used as a basis to recover the electric field. This is achieved using the fact that electrons produced in the detector will follow field lines until they are absorbed in the anode plane. Hence, all charge read out at a specific wire originated somewhere along the field line ending at it. In a homogeneous electric field, electrons follow a straight line (along x) to the readout wire. In an inhomogeneous electric field this does not hold, since field lines show a more complex behaviour.Recovering the electric field from the displacement map is a two fold process.

In a first step the electric field lines are recovered and then the magnitude of the electric field is determined. Recovering the electric field lines is straight forward since, as discussed above, distortions and field lines vectors are closely related. Assuming a linear field in between the regular spaced grid points introduced in Section 6.4, an electric field line can be recovered by calculating the vector connecting displacement vectors of two adjacent grid points in drift direction. Because the electric field is generally smooth the assumption is justified by the small step size of the the grid compared to the expected magnitude of the distortions. When this is performed for all adjacent displacement vectors $\vec{d}$, a set of field line vectors $\vec{R}_{i,j,k}$ is obtained, using

$$\vec{R}_{i,j,k} = \vec{d}_{i+1,j,k} - \vec{d}_{i,j,k}. \tag{6.20}$$

Here i, j and k are grid indices for the spatial coordinates in x, y and z, respectively. Their location in space is fixed to the mid point of the two displacement vectors and then interpolated onto the regular grid using the same method introduced in Section 6.4. A two dimensional illustration of the procedure for two rows of the regular grid is depicted in Figure 6.10, the index k is omitted (since constant). The drift direction is from right to left, from the cathode towards the anode. In the figure gray points denote the regular grid, black arrows show the reconstructed displacement vectors for the corresponding grid point and blue vectors show the derived field line vectors which are associate to the spatial coordinates indicated to the green points.

In a second step the magnitude of the electric field is determined under the same assumptions as before. In each step the distance traveled in the distorted picture is given by the length of $\vec{R}_{i,j,k}$, in the uniform case the traveled distance is constant Δx. The drift velocity in the two pictures is given by $\vec{v}_{i,j,k}$ and $\vec{v}_0$ and the time required

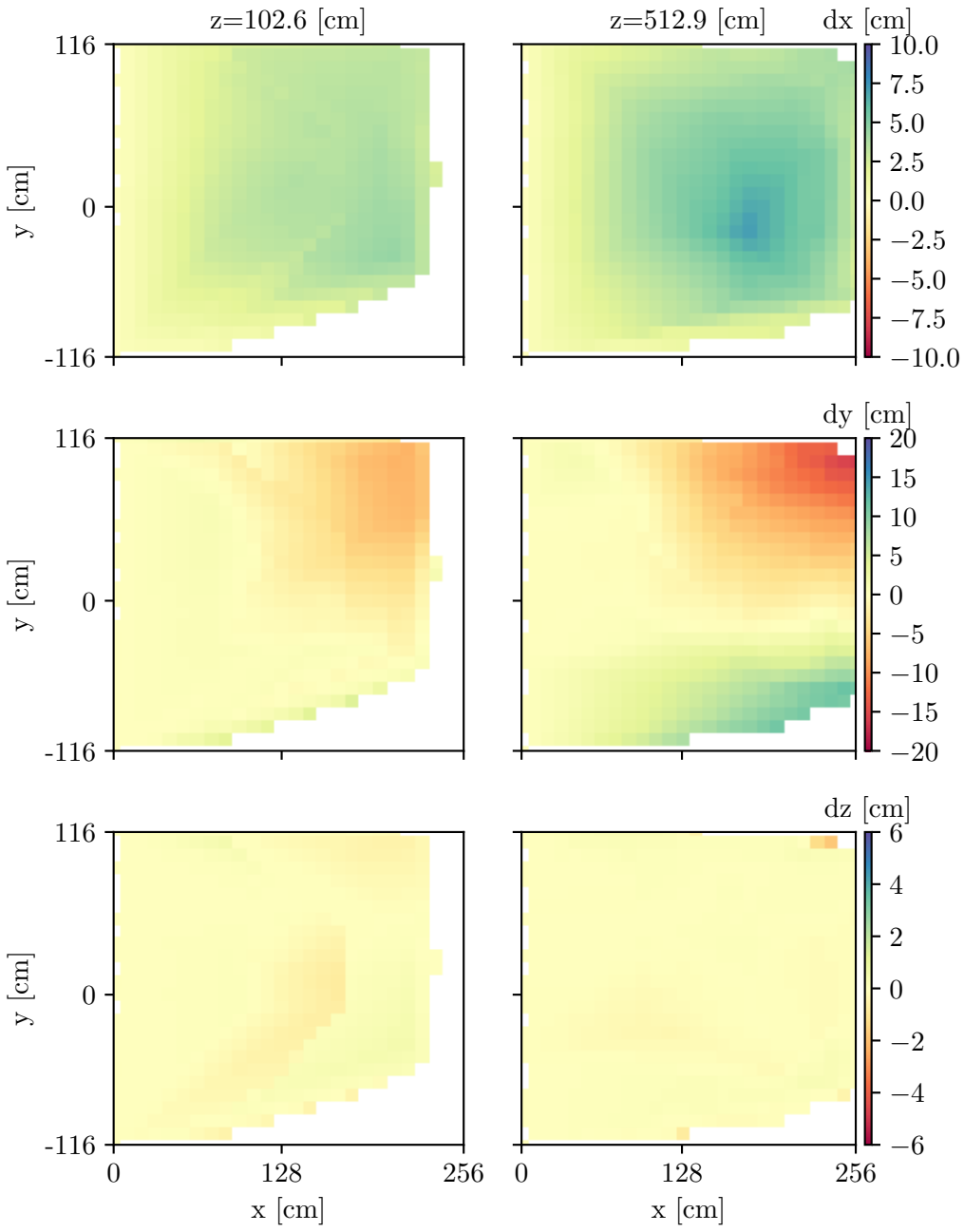

Figure 6.9: Distortion map for all three dimensions (top to bottom) at the side (left column) $z = 102\,\text{cm}$ and center (right column) $z = 512\,\text{cm}$.

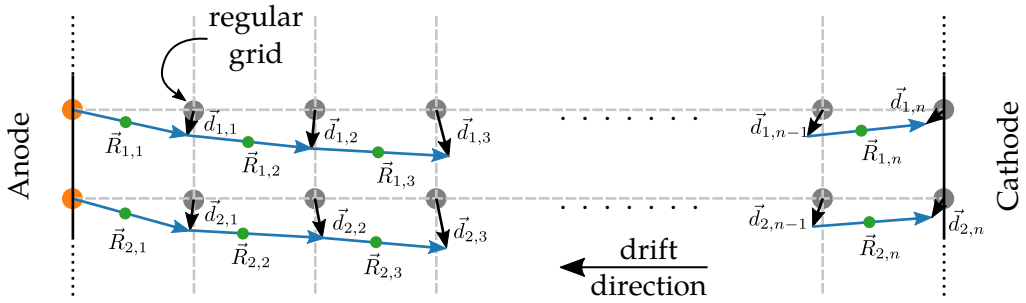

Figure 6.10: Illustartion of the approach used to recover the electric field based on the displacement map. See text for details.

to travel the given distance Δt is equal in both views. Hence the relation of the two pictures can be derived

$$\frac{|\vec{v}_{i,j,k}|\Delta t}{|\vec{v}_0|\Delta t} = \frac{|\vec{R}_{i,j,k}|}{\Delta x} \quad \rightarrow \quad |\vec{v}_{i,j,k}| = \frac{|\vec{R}_{i,j,k}|}{\Delta x}|\vec{v}_0| \tag{6.21}$$

With the right expression the magnitude of the drift field at the center of the vector $\vec{R}_{i,j,k}$ can be derived. The expression for the drift speed is independent of neighboring grid points. The drift velocity is related trough the electron mobility μ_e to the electric field (see Equation 3.19) in a non-linear fashion. The relation between drift field and drift velocity is parameterized by [71], hence the magnitude of the electric field can be derived from the inverted parameterization with the given drift velocity derived in Equation 6.21.

Figure 6.11 depicts the electric field distortion map relative to the nominal field $E_0 = 0.273\,\mathrm{V\,cm^{-1}}$ obtained with the above described method as a $z-x$ slice at $y = 0\,\mathrm{cm}$. The maximal reconstructed distortion in the x direction is 17 % located near the cathode, a decrease of the electric field towards the anode with a maximal magnitude of $-7\,\%$ is observed. In the y dimension a varying field distortion of $\pm 3\,\%$ is reconstructed, excluding boundary parts of the covered volume. The reconstructed z variation of the electric field has a magnitude of $\pm 1\,\%$ across the coverage. The spatial limitation arise from the up- and downstream location of the laser systems. Furthermore this configuration leads to artifacts in regions where the laser coverage from one side is exclusively responsible for the recovery of the electric field. Similar artifacts where the deviation has small jumps of 0.5 % can be observed where coverage is either dominated by one side or the other. Additional figures of the reconstructed distortion at different y distances are shown in Appendix C. Figure B.2 and Figure B.1 show distortion towards the bottom and top, where the distortion in x is similar to the one observed in the central slice. In the y direction distortions are enhanced towards negative and positive magnitudes on the two edges. The maximal relative distortions are 11 % in the top slice and $-12\,\%$ in the bottom slice. In the top slice a relatively uniform distortion is present in all three dimensions, still artifacts from the individual laser system coverage are visible. In th bottom region of the detector and especially in the y direction artifacts from the reconstruction method are clearly visible.

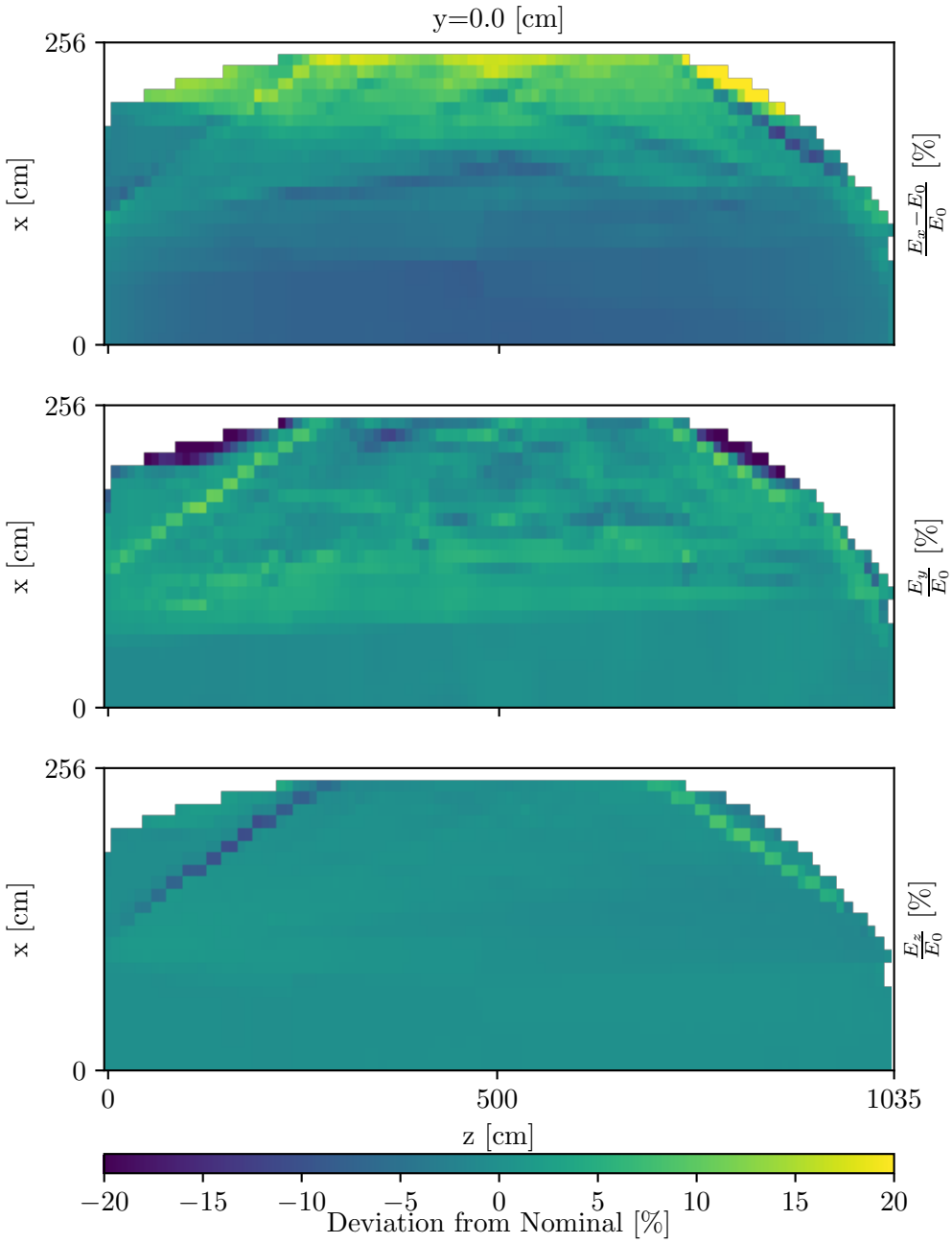

Figure 6.11: Distortions relative to the nominal electric field E_0 in three spatial directions for a slice at $y = 0\,\text{cm}$ in the z-x-plane.

6.6 VALIDATION AND ERROR ESTIMATION

Laser track simulations were implemented to verify the distortion map and subsequent electric field reconstruction under controlled conditions and to estimate systematic error due to the implemented procedure. Validation was performed at three stages of the E-Field reconstruction. First, synthetic tracks including distortions were used to verify the reconstruction chain, excluding effects of hit and track reconstruction. Secondly, the full chain is tested by the generation of laser-like ionization signal at a Geant4 [120] level, deploying the full Monte-Carlo chain of the MicroBooNE detector simulation. An illustration of the applied validation steps is found in Figure 6.12.

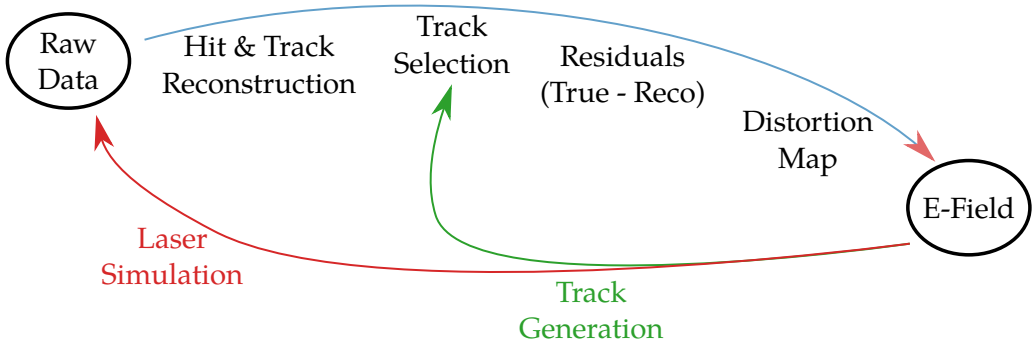

Figure 6.12: Location of the different validation stages introduced in the electric field reconstruction.

The basis for all introduced distortions is the simulated electric field introduced in Section 6.1. Based on this non-uniform electric field a displacement map is calculated [121], which is then used to apply displacement of charge at an arbitrary point in the detector. Slices of the displacement map in the x-z-plane at the center and edge of the detector are shown in Figure 6.13. Additional figures illustrating the displacement can be found in Appendix A.

A summary of all simulation set names and the different properties can be found in Table 6.1. Three fundamentally different track samples were produced.

The first set was produced with the motivation to exclude track reconstruction at all, such that the distortion and e-field reconstruction algorithms can be tested and verified. For this purpose a set of laser tracks, mimicking the coverage of the laser system, was produced. On the data set only space charge distortion was applied, excluding interaction simulation and track reconstruction. Due to this settings the data set is further denoted as perfect reconstruction. The so obtained tracks were fed into the track selection framework described in section 6.3, to cross check selection performance under ideal conditions. As expected all tracks passed the selection (1000 out of 1000 for each track sample), since no accidental cosmic particles were introduced as well as no reconstruction artefacts were present in this data set. The detector coverage of this data set is shown in the $z-x$, $z-y$ and $x-y$ projections in Figure 6.14 and Figure 6.15 for the upstream and downstream data set, respectively. Effects of the applied distortion are most prominently visible in the x-z-plane (bottom plot), here the laser tracks do not travel to the detector

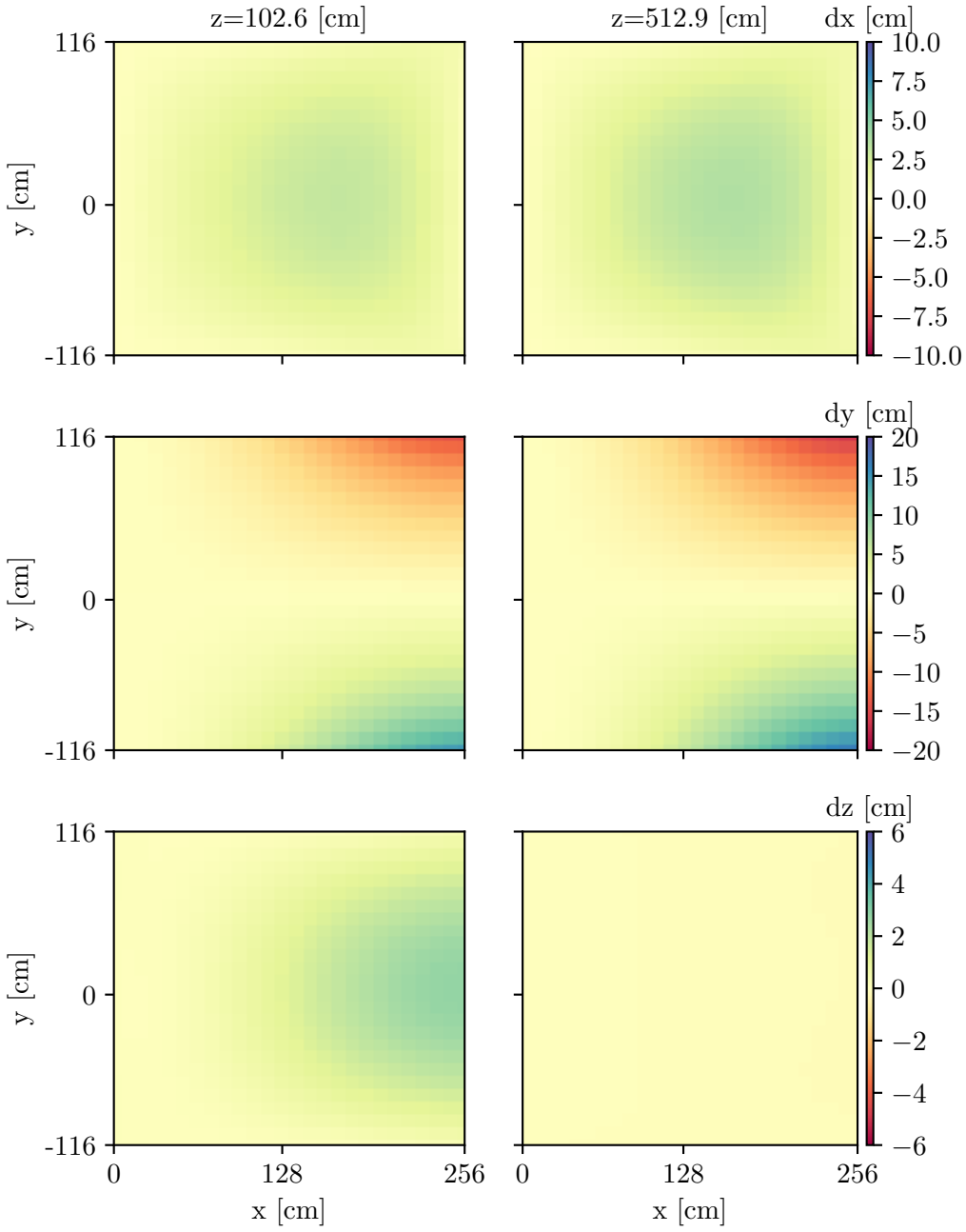

Figure 6.13: Introduced simulated distortions. Per row, each contour plot shows distortions in a spatial dimension. Values for a slice at the edge of the detector (at $z = 102.6\,\text{cm}$) is shown in the left column. In the right column values for a central slice, at $z = 512.9\,\text{cm}$, is shown.

boundary anymore. This is due to the attractive force by the space charge distribution at the center of the detector. The charge introduced at the top and bottom of the detector are subject to a asymmetric space charge distribution, pulling the charge towards the center. Charge produced in the central region of the detector observes a symmetric space charge, hence little to no distortion is present.

Distributions for the residuals ($\vec{x}_{true} - \vec{x}_{reco}$) for the three spatial coordinates for this data set are shown in Figure 6.16. It is instructive to introduce three sections of the detector to explain the distribution, $z < 200\,\text{cm}$ in blue (upstream end), $z > 835\,\text{cm}$ in orange (downstream end) and the central part where $200\,\text{cm} < z < 835\,\text{cm}$. Additional separations of the distribution can be found in Appendix C. In the Δx case, the distribution of all three regions overlap, this is expected since the distortion in drift direction is relatively flat over the full z range (see Figure A.1, Figure A.2 and Figure A.3). Furthermore, the three introduced regions are orthogonal to the distortions in Δx, leading to little fluctuations among them. In the Figure C.3 (a) the section of the TPC contributing to the spread is identified to be at the back (close to the cathode). The standard deviations of the three distributions are $\sigma_{x,d} = 0.2\,\text{cm}$, $\sigma_{x,u} = 0.2\,\text{cm}$ and $\sigma_{x,c} = 0.1\,\text{cm}$, where the second index denotes the region (u: upstream, d: downstream c: center). For the Δy case, the two distributions of the side regions overlap nicely, the central region shows a larger spread compared to the side regions. In Figure C.3 (a) it is visible that the large spread is originating from points close to the cathode of the detector, from (b) it becomes clear that equal contributions from top and bottom regions are contributing. Hence combining these insights the spread has its origins, at the top and bottom zones close to the cathode. This increased spread can be pinpointed to local effects, where only laser tracks from one side are present close to the cathode. The standard deviations of the three distributions are $\sigma_{y,d} = 0.5\,\text{cm}$, $\sigma_{y,u} = 0.5\,\text{cm}$ and $\sigma_{y,c} = 0.5\,\text{cm}$. A clear asymmetry is visible for the Δz residual distribution for the two sides of the detector. This is an expected behaviour, since the coverage on each side of the detector is dominated by laser tracks originating from the opposite side, since laser beams enter the TPC almost at a single location (on each side). The standard deviations of the corresponding deviations are $\sigma_{y,d} = 0.7\,\text{cm}$, $\sigma_{y,u} = 0.7\,\text{cm}$ and $\sigma_{y,c} = 0.2\,\text{cm}$. For all three spatial dimensions the standard deviation for the residuals is in the sub-centimeter region. In Figure C.4 the distribution of the magnitude of the residual $\vec{x}_{res} = \vec{x}_{true} - \vec{x}_{reco}$ is shown. In this figure it is again visible that larger residuals have their origin at the edges (top, bottom, cathode and the two sides) of the detecor. The overall standard deviation is $\sigma_{res} = 0.6\,\text{cm}$. From the above discussion follows that the displacement recovery methodology works best at the center and close to the anode, whereas the spread between introduced and recovered displacement increases closer to the cathode and the sides of the detector.

A second simulation data set was produced, the same input laser directions were used as in the first data set. Now the full signal formation is included in the simulation. This include ionization in liquid argon, drift to the anode (with standard Microboone settings) taking into account diffusion and lifetime, signal formation and detector response. Furthermore, the full standard laser reconstruction chain (described in Section 6.2) is used to obtain tracks from this data-set. Again, the

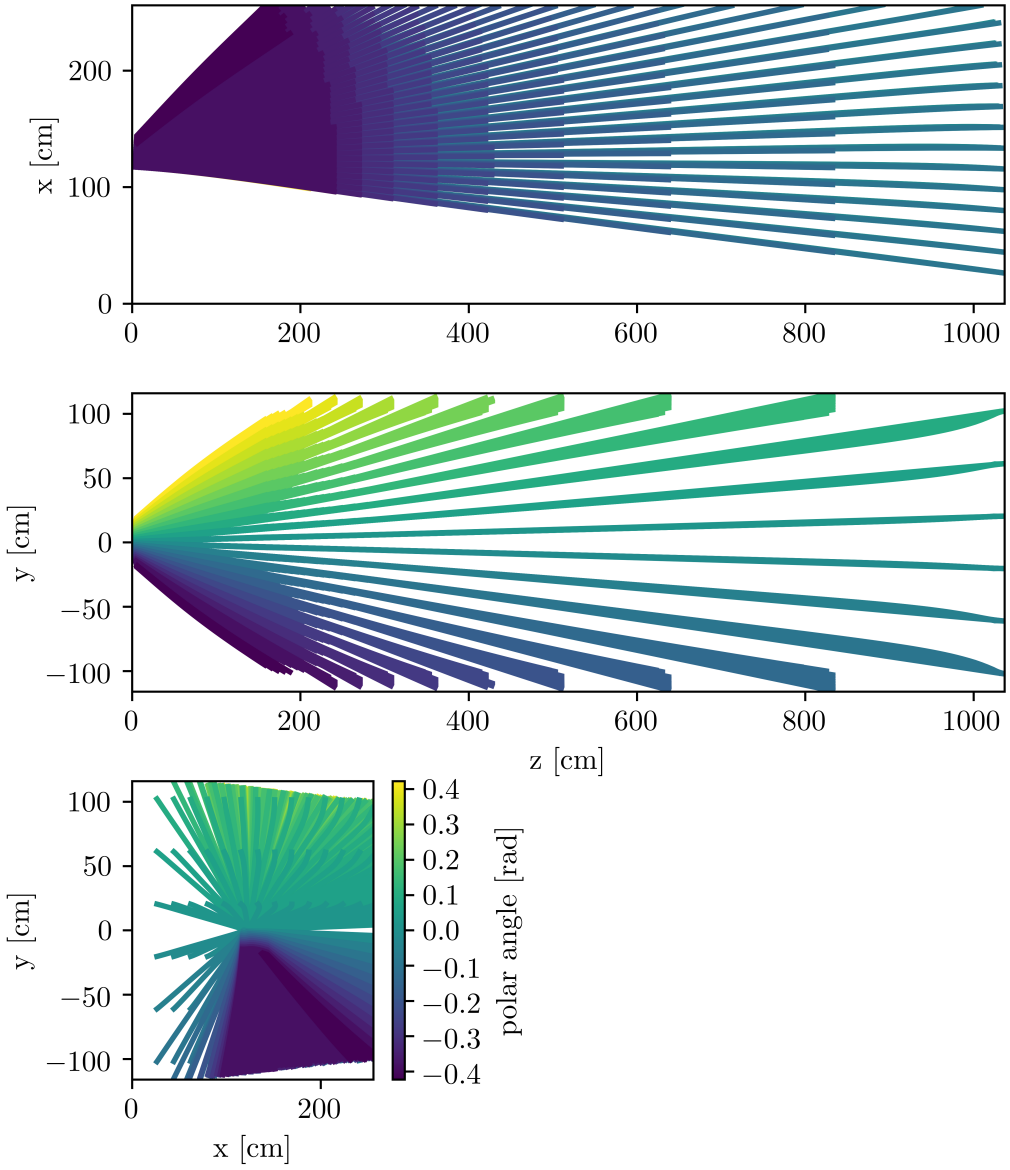

Figure 6.14: Coverage by the upstream laser system of detector with simulated laser tracks. The three graphs represent different views into the TPC, (top) x-z-plane, (middle) y-z-plane and (bottom) x-z-plane. Tracks were reconstructed ignoring all detector related effects (toy simulation). Different colors indicate polar angles.

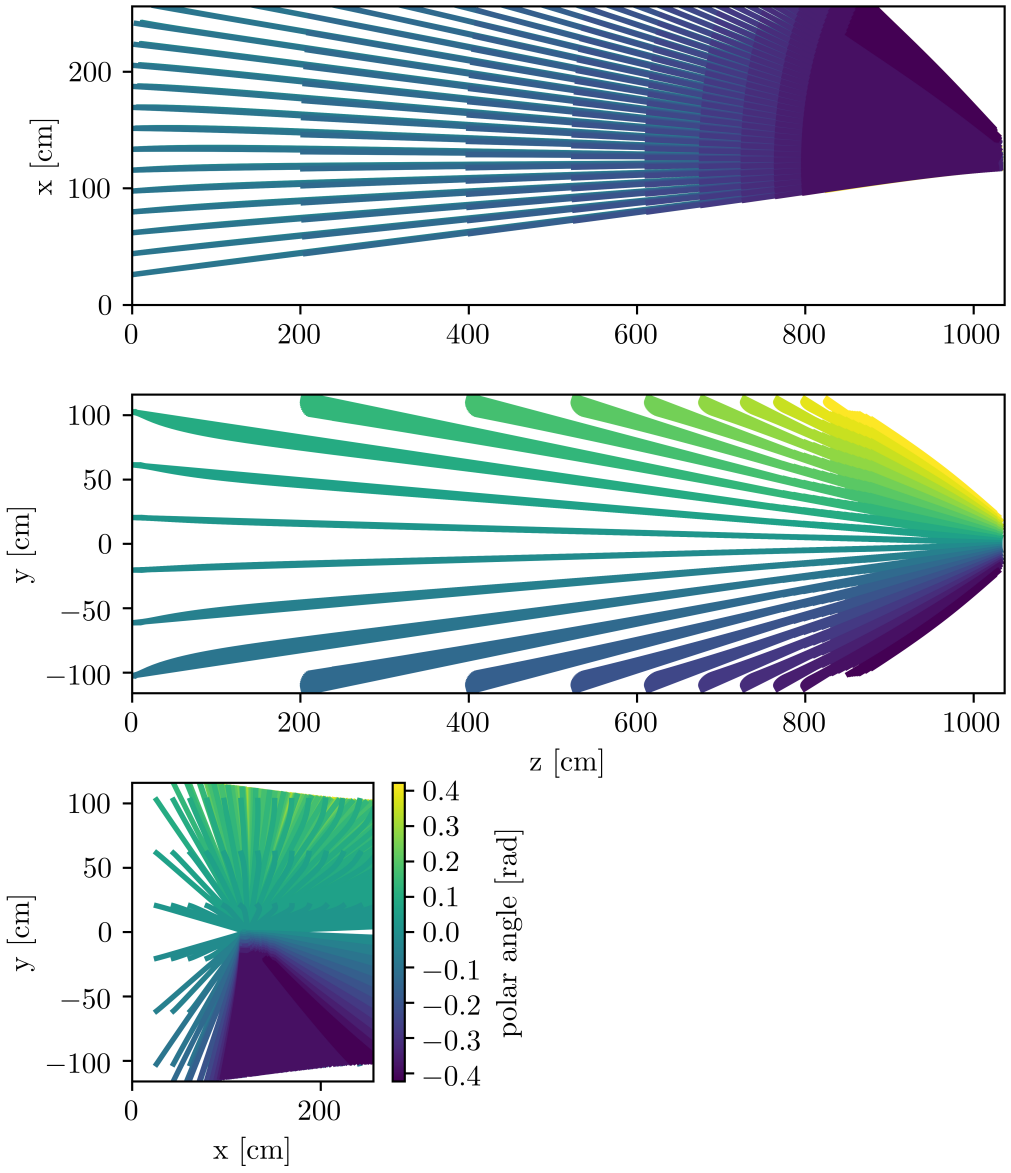

Figure 6.15: Coverage by the downstream laser system of detector with simulated laser tracks. The three graphs represent different views into the TPC, (top) x-z-plane, (middle) y-z-plane and (bottom) x-z-plane. Tracks were reconstructed ignoring all detector related effects (toy simulation). Different colors indicate polar angles.

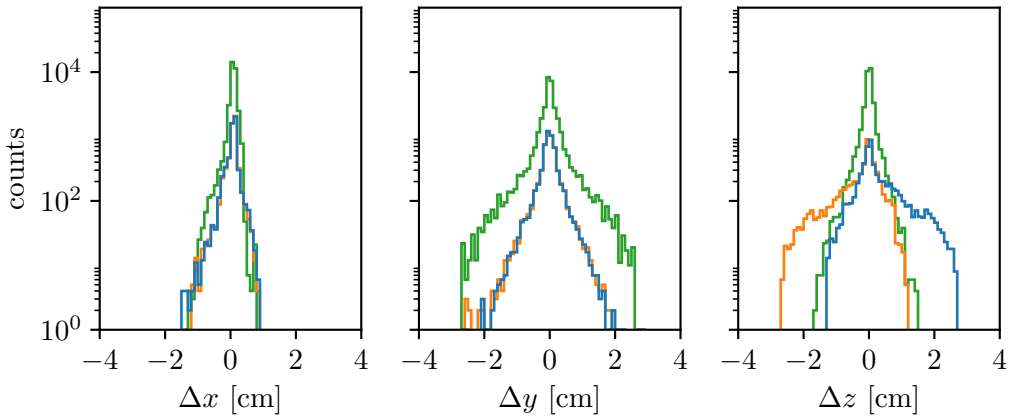

Figure 6.16: Residual ($\vec{x}_{true} - \vec{x}_{reco}$) distribution for each spatial dimension for the toy simulation. The three colors indicate contributions from different regions in the detector. Blue corresponds to regions on the upstream end $z < 200\,\text{cm}$, orange on the downstream end $z > 835\,\text{cm}$ and green the middle part where $200\,\text{cm} < z < 835\,\text{cm}$.

offline track selection is applied. The simulation of individual laser tracks was achieved by introducing minimum ionizing muons ($E_{mu} = 10\,\text{GeV}$) in the Larsoft simulation framework (which is using Geant4 internally). To ensure these muon tracks resemble laser tracks as close as possible, multiple coulomb scattering as well as delta electron production was disabled during the simulation stage. These settings ensure that the ionization signal for a laser track, produced by Geant4, is not overlaid by other track distorting effects. This data set was used as an intermediate step towards the third simulation sample described below.

In a third simulation sample, to further improve the resemblance of ionization signals to true laser tracks, two adjustments were made to the above discussed simulation stages. Individual track residuals for this data set are shown in Figure C.2. The first improvement concerns the laser width, whereas a minimum ionizing muon produces a very narrow spatial ionization track, the UV laser ionization signal is spatially extended over few millimeters (described in Section 5.2). Neither Geant4, nor the Larsoft framework expose direct control of the spatial extend of the ionization signal. Therefore, the longitudinal signal diffusion (with respect to the electric field) is used as a proxy to extend the electron signal that arrives at the readout wire. The UV laser beam width is tunable by means of an aperture (described in section Section 5.2). For all laser runs used for calibration purposes the beam width was set to $0.5 \pm 0.1\,\text{mm}$. Hence, an additional field independent term was added to the longitudinal diffusion, such that initial ionization signals (before drift) exhibit the width of the laser beam. The second adjustment aims to raise the ionization amplitude per unit volume, lowered by the previous adjustment, to levels expected by the laser. To achieve this, the amount of deposited charge for laser tracks is multiplied by a constant factor to resemble laser ionization levels again.

As with the simulation samples described above, tracks were reconstructed using the custom laser hit finder and the pandoara reconstruction framework (see

Section 6.2 for details). Then track selection was applied before distortion maps are calculated. Track selection excluded 460 tracks for the upstream and 480 tracks for downstream system, respectively. As shown for the toy simulation, the distribution of residuals $\vec{x}_{res} = \vec{x}_{true} - \vec{x}_{reco}$ is used to quantify the estimated error of the full chain. The distribution of the residual magnitude is shown in Figure 6.17, again three subplots are shown indicating different sections of the detector. The regions are; front to back (left) with $x < 50\,\text{cm}$ (blue), $x > 206\,\text{cm}$ (orange) and $50\,\text{cm} < x < 206\,\text{cm}$ (green); top to bottom (middle) with $y < 78\,\text{cm}$ (blue), $y > -78\,\text{cm}$ (orange) and $-78\,\text{cm} < y < 78\,\text{cm}$ (green); right to left with $z < 200\,\text{cm}$ (blue), $z > 835\,\text{cm}$ (orange) and $200\,\text{cm} < z < 835\,\text{cm}$ (green). A broadening of the residuals that has its origins at the back and side of the detector is visible in the same fashion as it was visible in the toy simulation case. The magnitude of the spread is increased due to addition of uncertainties by the full simulation chain including hit finding and track reconstruction. Especially track reconstruction at the end of tracks, visible as kinks at the end of tracks in Figure C.1, are contributing to uncertainties. Furthermore, the reduced information and hence coverage available, due to the exclusion of roughly 40 % of the introduced tracks effects the precision of the measurement. Still, the standard deviation for the total residual remains at a sub-centimeter level $\sigma_d = 0.8\,\text{cm}$.

In summary, it can be concluded that the deployed methodology to recover a distortion map from a set of 3D trajectories which are subject to this distortion is performing as expected with a mean systematic error in the sub-centimeter level. Furthermore, the methodology was successfully validated against the hit and track reconstruction methods applied on data. The method performs best in regions where trajectories from both sides are present. The largest uncertainties arise at edges (top, bottom and cathode), for which the laser track coverage is low and track reconstruction is not optimized.

SET NAME	DETECTOR SIMULATION	RECONSTRUCTION	OFFLINE SELECTION
Toy Simulation	-	-	✓
MIP-Like	✓	✓	✓
Laser-Like	✓	✓	✓

Table 6.1: Simulation set names and properties

From the above obtained distortion map it is now possible to derive an electric field map and compare it to the electric field that was used to derive the synthetic electric field in the first place. This allows to estimate the systematic errors due to the methodology. Because of the stage at which the distortion was introduced, this verification will exclude any reconstruction or selection systematic errors. In the same fashion as the analysis of the distortion map, the residuals between expected/simulated field $\vec{E}_{sim}$ and the recovered field $\vec{E}_{rec}$ are considered. For easier interpretation the residuals $\vec{E}_res = \vec{E}_{sim} - \vec{E}_{rec}$ are expressed as a ratio of the expected electric field $\vec{E}_{res}/\vec{E}_{sim}$ in percent.

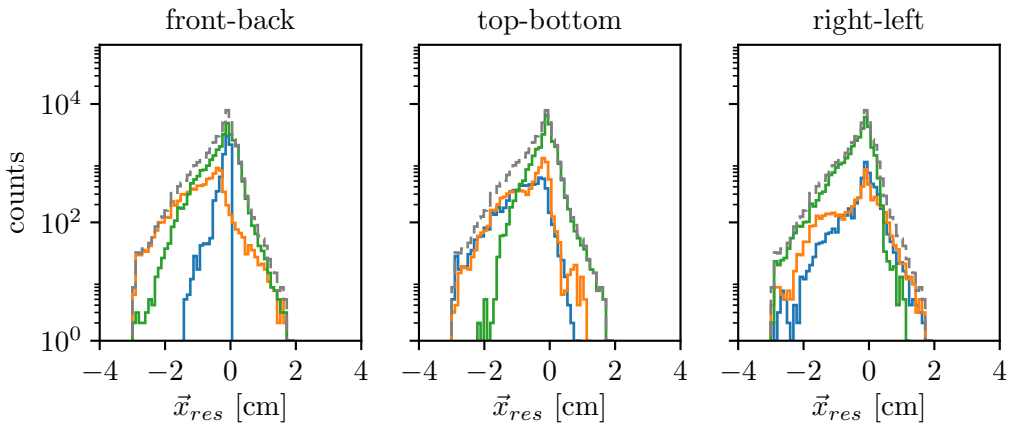

Figure 6.17: Total residual distribution for the full laser simulation. The three sub-figures all show the total distribution but with contributions from different geometrical sections of the detector The regions are; front to back (left) with $x < 50\,\text{cm}$ (blue), $x > 206\,\text{cm}$ (orange) and $50\,\text{cm} < x < 206\,\text{cm}$ (green); top to bottom (middle) with $y < 78\,\text{cm}$ (blue), $y > -78\,\text{cm}$ (orange) and $-78\,\text{cm} < y < 78\,\text{cm}$ (green); right to left with $z < 200\,\text{cm}$ (blue), $z > 835\,\text{cm}$ (orange) and $200\,\text{cm} < z < 835\,\text{cm}$ (green).

Firstly, the distortion map based on the toy simulation is used to recover the electric field. This approach can be interpreted as a test of the methodology under ideal conditions, where laser tracks are reconstructed with infinitesimally small error, giving a measure of the performance of the electric field recovery. The total residual distribution is show in the top row of Figure 6.18, where the three individual figures all show the total distribution (dashed line) along with contributions from different partitions of the detector (colored lines). The total distribution shows a dominant peak around zero with a standard deviation of $\sigma_{res} = 1.2\,\%$, low count tails of up to 12 % are present in both the negative and positive direction. Furthermore, it can be concluded that the front portion of the detector has a small variation, whereas the region close to the central cathode is responsible for most of the overestimated reconstructed field . The up- and downstream edges of the detector are responsible for most of the underestimation of the electric field. The very symmetric behaviour of the bottom to top and right to left pairs indicates that the method does not have any bias in these two directions. In contrast, the asymmetry in the front to back distributions is clearly due to the very different shapes of the distortions in these regions (ultimately related to the different charge densities). As already seen in the distribution of the distortion residuals, the method performs best in the central region of the detector, the uncertainty introduced by the recovery methodology of the electric field is 1.2 %.

Secondly, the electric field is recovered from the distortion map obtained by the full laser chain simulation. This allows insight into the systematic errors to the electric field recovery introduced by the track reconstruction and selection, distortion and electric field recovery algorithms. The total relative residual distribution is shown in the bottom row of Figure 6.18. A clear peak around the origin is

again visible in the total distribution, the standard deviation of the distribution is $\sigma_{res} = 1.7\,\%$. Again low count tails are present and have increased counts compared to the toy simulation. In general the observations from the toy simulation are confirmed or enhanced. The dominant contributions for overestimation is from the regions close to the cathode, again the regions close to the anode show a low spread. Residuals from the top and bottom partitions of the detector are very similar and do not contribute to tails. Since the the small peak identified to have its origin in the cathode region, does not contribute to the top or bottom partitions, it can be concluded that the central cathode region is responsible for the majority of the overestimation. The same argument can be used to exclude contributions from the left to right r of the distributions. In general an increase of the total spread and the low count tails of the distributions can be observed compared to the toy simulation. This is expected already from the increase seen in the distortion map residuals and the addition of more parts to the machinery.

6.7 VERIFICATION

To cross check the reconstruction chain and especially the mirror position calibration, a data-driven analysis is developed. If two true tracks share a crossing point, the ionisation path of the two laser tracks must cross as well. The deposited charge (by the two laser tracks) in the crossing point will be exposed to the same electric drift field. Unfortunately, it is very unlikely that two tracks share an exact crossing. Therefore as an approximation, the point of closest approach of two laser beams and two reconstructed laser tracks is chosen. Points of closest approach are determined for all reconstructed laser tracks from one side, against all laser tracks of the opposing side. An upper limit of 25 cm on the distance of closest approach is applied, because the expected electric field distortions are of similar order. Subsequently, for each found laser crossing pair the point of closest approach in the true information is determined as well. The distance for both points of closest approach in true information (Δ_{true}) and reconstructed tracks (Δ_{reco}) is calculated. These two distances are then subtracted to obtain the cross distanced

$$\Delta_{ij,cross} = \Delta_{ij,true} - \Delta_{ij,reco}. \tag{6.22}$$

Where i and j are the track indices of the upstream and downstream track. An example of crossing tracks and the above described points of closest approach is shown in Figure 6.19.

The distribution of cross distances is a metric for the performance of track reconstruction and mirror position calibration. For example if one mirror position has an offset in the Δx direction, the crossing distance distribution will be shifted systematically by Δx. Similarly, if during angle measurements a systematic shift is introduced, the distribution of cross distances will widen. To verify the procedure the cross distance distribution was calculated for several simulation data sets, where the mirror position and true laser information is available as a free parameter. Furthermore the mirror position and the angle conversion was varied, not affecting the reconstructed tracks, to investigate the effect of systematic errors in these calibration parameters. Two sample distributions without and with an offset

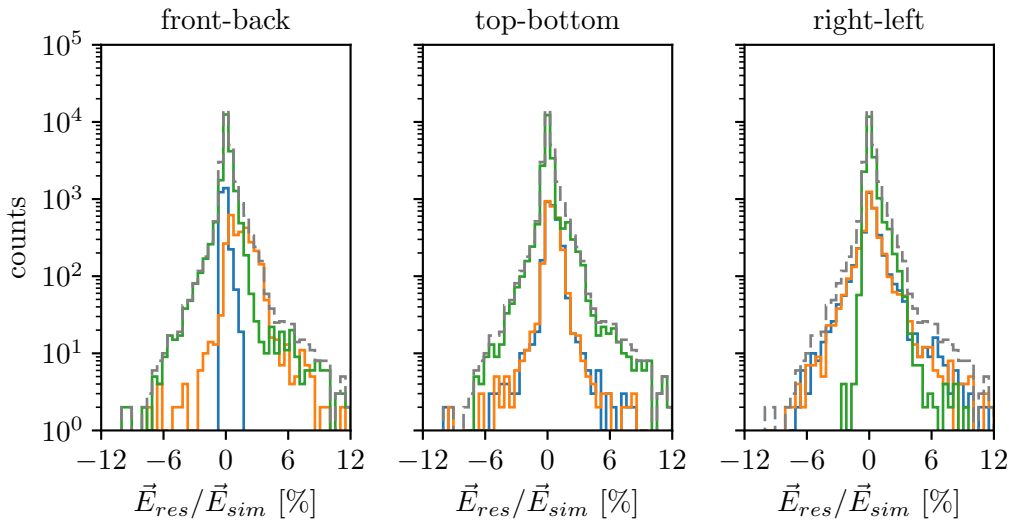

(a)

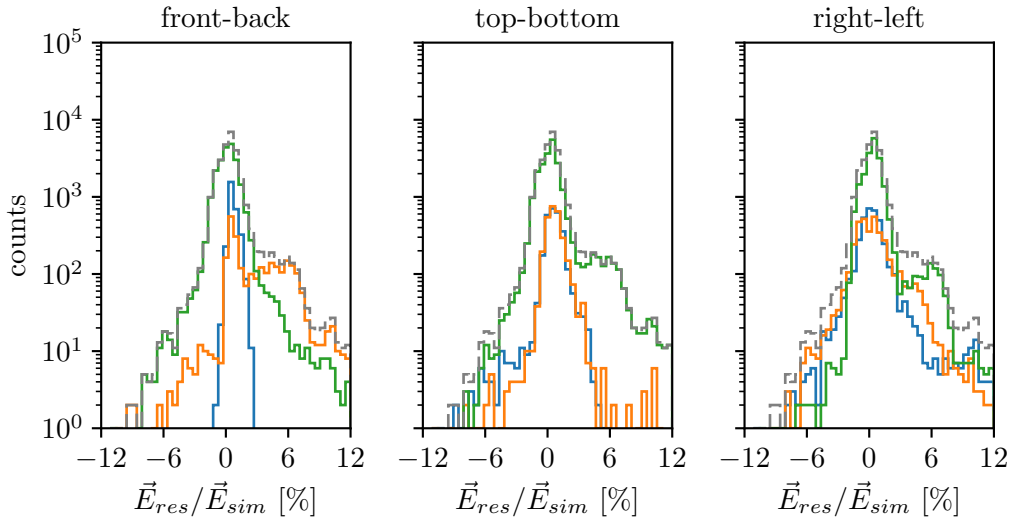

(b)

Figure 6.18: Relative electric field residual $\vec{E}_{res}/\vec{E}_{sim}$ distribution for the toy simulation (a) and full laser simulation (b). In all sub-figures the total distribution is shown as a dashed line. Contributions from different detector partitions are shown as colored lines in each sub-figure. The regions are; front to back (left) with $x < 50\,\text{cm}$ (blue), $x > 206\,\text{cm}$ (orange) and $50\,\text{cm} < x < 206\,\text{cm}$ (green); top to bottom (middle) with $y < 78\,\text{cm}$ (blue), $y > -78\,\text{cm}$ (orange) and $-78\,\text{cm} < y < 78\,\text{cm}$ (green); right to left with $z < 200\,\text{cm}$ (blue), $z > 835\,\text{cm}$ (orange) and $200\,\text{cm} < z < 835\,\text{cm}$ (green).

in drift direction ($\Delta x = 1\,\text{cm}$) are shown in Figure 6.20. The underlying dataset is identical to the described Toy Simulation introduced in Section 6.6. In the unbiased distribution a clear peak centred around 10 cm emerges. The tail towards positive values is introduced by crossing distances with large distance between true and

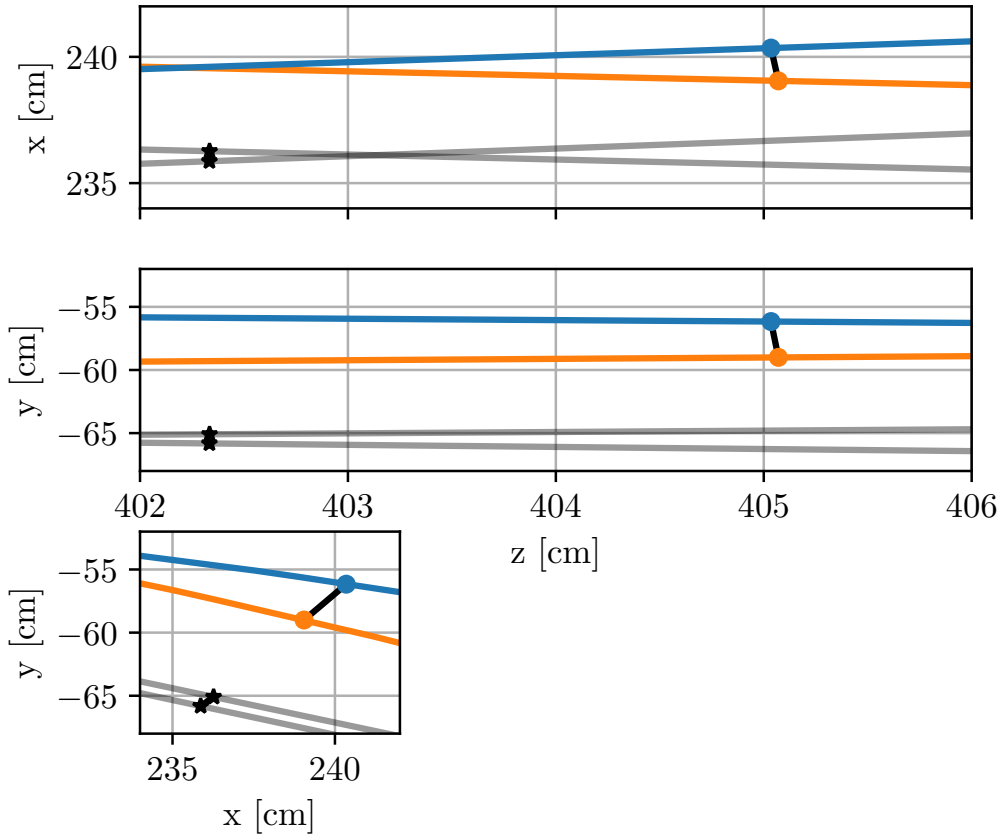

Figure 6.19: Cross distance calculations illustrated on an example. In blue and orange the upstream and downstream tracks are shown. In grey the true information of the laser beam is introduced. Dots indicate the points of closest approach for the tracks (blue and orange) and true information (black).

reconstructed crossing points. If a symmetric distortion was chosen, tails in both positive and negative cross distance were expected. Due to asymmetric nature of the distortion (shown in Figure 6.13), points towards the cathode ($x \lesssim 150\,\text{cm}$) exhibit large positive deviations from the expected crossing distance, whereas points closer to the anode have little to no distortion.
In the biased cross distance distribution peaks emerge roughly on positive and negative distances corresponding to the offset distance.

6.8 TIME DEPENDENCY STUDIES

The temporal variability of the electric field inside the detector is an important parameter to be determined. High temporal variability of the order of minutes, compared to a time scale of few hours for completing a laser run, will diminish the overall resolution of the laser calibration method. Fluctuations with longer time scales will determine how frequent laser runs have to be performed to obtain an updated electric field calibration. A main sources of fluctuations is the convective

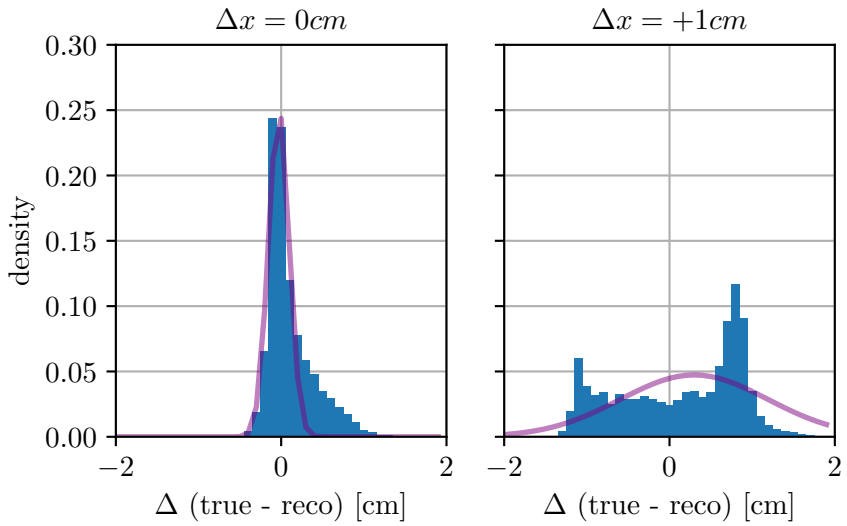

Figure 6.20: Two example cross distance distributions for toy simulation including best Gaussian fits (in purple). On the left no offset is applied, whereas on the right an offset of $\Delta x = 1\,\text{cm}$ is applied, which widens the distribution.

argon flow in the detector and the cosmic ray flux rate, both affecting the spatial distribution and the absolute amount of positive ions inside the drift volume.

To investigate temporal variation of the electric field, dedicated laser campaigns were conducted. During these, the laser beam direction was held constant and the laser was pulsed at a low rate of a few mHz. Fluctuations in the electric field during the data taking period will impact the drift time and path of deposited charge. In the case of a constant ionization path, the single source of variability is the fluctuation of the electric field. A run during which the laser direction was fixed over few hours to investigate short time scale fluctuations was conducted. Figure 6.21 indicates the chosen laser beam direction for the time dependency study. The direction nearly parallel to the wire plane was chosen to achieve full coverage of the TPCin the z-dimension. To keep the number of error sources as low as possible, only the raw waveform of individual wires were processed for this study. To simplify the waveform processing only collection wires were considered. With this approach uncertainties introduces by a full reconstruction chain, involving deconvolution, hit matching among planes and track reconstruction can be excluded. The electric field fluctuations will manifest itself in the shot to shot variation of the peak location on single wire waveform. In the following an ionization signal on an individual wire is denoted as a hit. Basic properties of a hit is its peak amplitude in mV, the peak sampling time and peak width, both in us. To infer the peak amplitude ADC 14-bit values are converted into mV. Additionally the ADC baseline is subtracted per event. With the known sampling time of 500 ns, ADC ticks can be converted to a time measurement. All times are measured relative to (laser) trigger time.

For this study, hits are created by fitting an Gaussian peak to the recorded waveform. Only waveform samples inside a time window of ±50 us of the expected

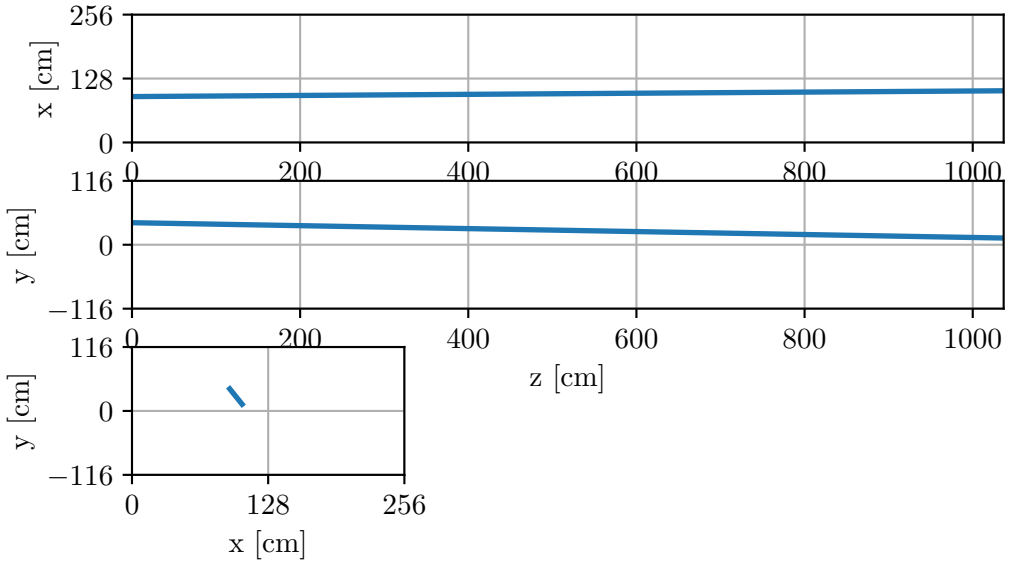

Figure 6.21: Expected location of the laser beam used for the time dependency study shown in three projections views of the detector. The laser is entering at the downstream end of the detector ($z = 1036\,\text{cm}$).

laser signal are considered for fitting, all other regions are ignored. Example waveform and corresponding Gaussian fits are shown in the top plot of Figure 6.22 for collection wires 500, 1750 and 3000 of the same event. In a next step individual peak locations of an entire run are aggregated per wire over time, displayed as a 2D histogram in the middle plot of the same figure. Summing over time not only shows the fluctuations but also reduces sensitivity to cosmic muons, which could be wrongly accounted as laser signal in the region of interest. Here the three wire locations aforementioned are indicated with dashed colored lines. Vertical gaps with missing data arise from non-operational wires. In the displayed run the downstream laser system was used, therefore the laser enters from the right side at wire 3255 and exits at wire 0. The width of the summed peak locations in the drift time dimension is an estimator for electric field fluctuations during the full run period. One can observe that the width stays constant in the central region of the detector, whilst the width decreases towards the edges of the detector. Per wire projections of the 2D histograms for the three selected wires are shown in the bottom plot of Figure 6.22. To estimate the width of the histograms Gaussian fits were applied, the peak location and the variance of the three best fits are, $\mu_1 = 943.63\mu s$, $\sigma_1 = 1.52\mu s$, $\mu_2 = 974.92\mu s$, $\sigma_2 = 1.83\mu s$, $\mu_3 = 993.95\mu s$, $\sigma_3 = 1.70\mu s$, with subscripts denoting the three wire locations. To obtain a conservative estimate on the maximum fluctuations, the wire showing the maximum variance $\sigma_{max} = 1.93\,\mu\text{s}$ at the location $\mu_{max} = 956.23\,\mu\text{s}$, is selected for further processing, corresponding to a variance in drift speed of 0.2 %. Using the inverse expression 3.19, the variation in time can be converted in a variation in electric field, under the premise that the drift distance stays constant, which is true by the experimental design. With the maximum fluctuation this results in a maximum electric field fluctuation of 0.6 % over 1.6 h.

For illustration, it is possible to translate the variance in time into a distance, using a similar path as described above assuming the operational field in MicroBooNE of 0.273 V/cm. This leads to wire variances of $\hat{\sigma}_1 = 1.8 \pm 0.3mm$, $\hat{\sigma}_2 = 2.1 \pm 0.3mm$, $\hat{\sigma}_3 = 2.0 \pm 0.3mm$ and a maximum variance of $\hat{\sigma}_{max} = 2.2 \pm 0.3mm$. Since only collection wires are considered in this study, the stability of the electric field is only measured in drift direction (x).

A potential systematic error source is a non-stable mirror position, introducing random start positions. Two observations discourage this. First, such a behaviour would introduce a cone structure with increasing width along the summed tracks, which is not observed. Second, a fluctuation of the mirror of only a few mm would already destroy alignment of the laser beam from the last warm mirror onto the cold mirror, due to the large distance between them and the small mirror diameter. Therefore, this scenario is very unlikely.

To further explore the data set, the time evolution of the peak location over the full run period can be considered. Identifying spatial and temporal correlations allows to quantifying the convective flow and turbulence respectively. To make correlation analyses possible, the mean laser path is extracted from the mean peak location determined above (corresponding to μ_w). This allows to normalize the time variation independent of the drift time. Furthermore data points which lie outside the $3\sigma_w$ region are removed from the dataset. σ_w is the variance of the previously determined Gaussian fit and w is the wire number. Figure 6.23 shows time evolution of the full run for wires separated by 100 wires for wire 0 to 3400, the color scale indicates the wire number. For display reasons each time evolution of a wire is offset by 10 µs with respect to the previous wire. The 100 wire spacing corresponds to 30 cm, horizontal gaps arise from unresponsive wires. Wires towards the detector edge exhibit lower overall fluctuations, as already discussed in the aforementioned paragraphs. It becomes apparent that neighboring wires display high correlation, whereas more distant wires do not correlate . A cross-correlation analysis between neighboring collection wires is performed to determine the spatial extension of the fluctuations. Figure 6.24 shows the cross correlation between 150 neighboring wires for four selected wires. The y-axis indicates the degree of correlation in arbitrary units, due to the fact that not at all time scales the number of data points is equal. The wire number can be converted into a distance in the z using the wire spacing. Qualitatively, it can be seen that correlations between wires extend over roughly 20 cm, hence it can be concluded that turbulent flow in the detector shows a spatial extend of this order. Additional 3D illustrations of the temporal fluctuations can be found in Appendix E.

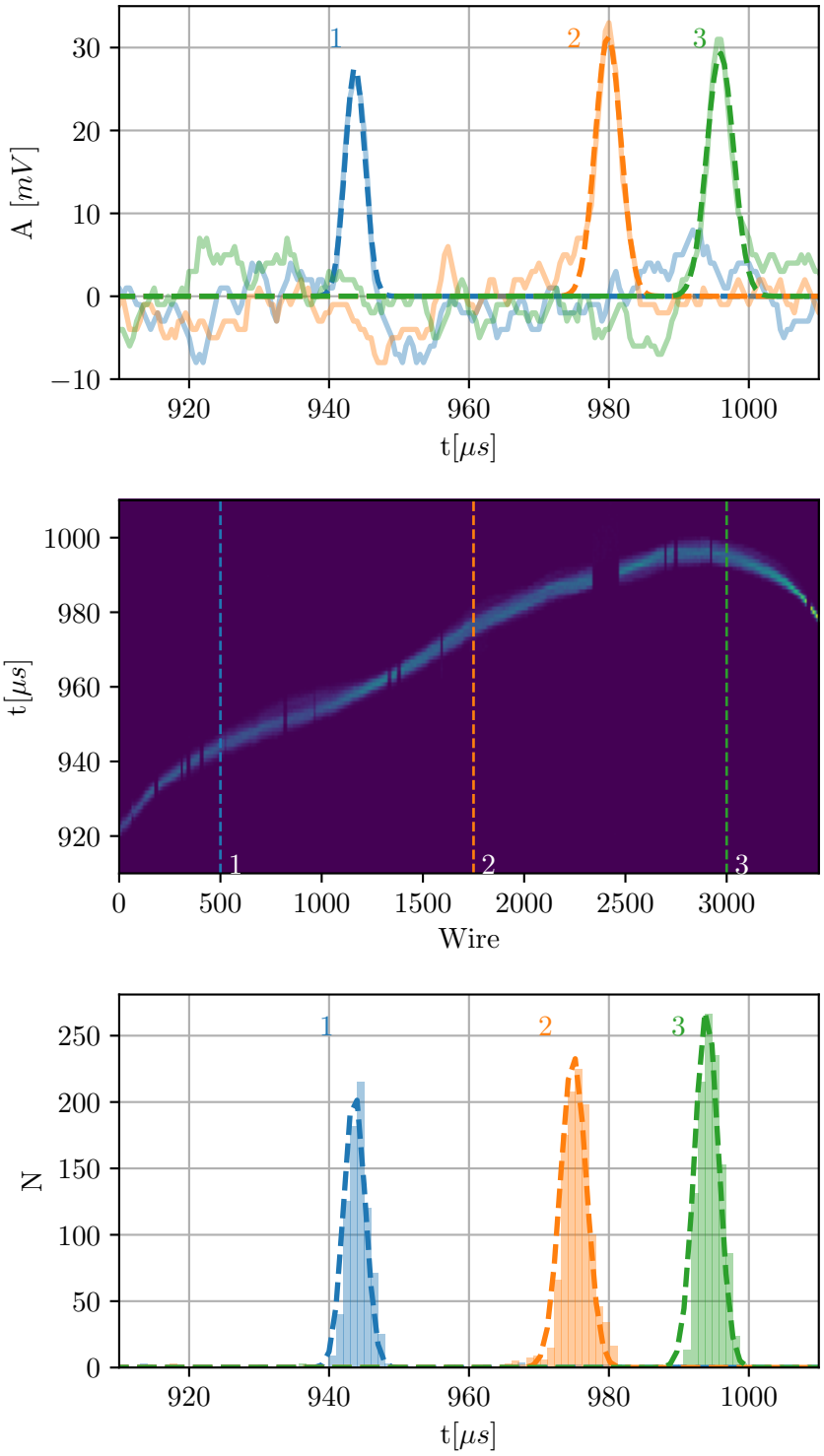

Figure 6.22: (Top) Display of raw waveforms of selected wires 500 (blue), 1750 (orange) and 3000 (green) of a single event. (Middle) Summed peak locations as a 2D histogram of 1500 events, the laser beam enters from the right. Indicated are the three location of the selected wires in the associate graphs above and below. (Bottom) Single wire histograms and best Gaussian fits of the summed peak locations for the three selected wires. The peak locations and the variance for each fit are (1) $\mu_1 = 943.63\mu s$, $\sigma_1 = 1.52\mu s$, (2) $\mu_2 = 974.92\mu s$, $\sigma_2 = 1.83\mu s$, (3) $\mu_3 = 993.95\mu s$, $\sigma_3 = 1.70\mu s$.

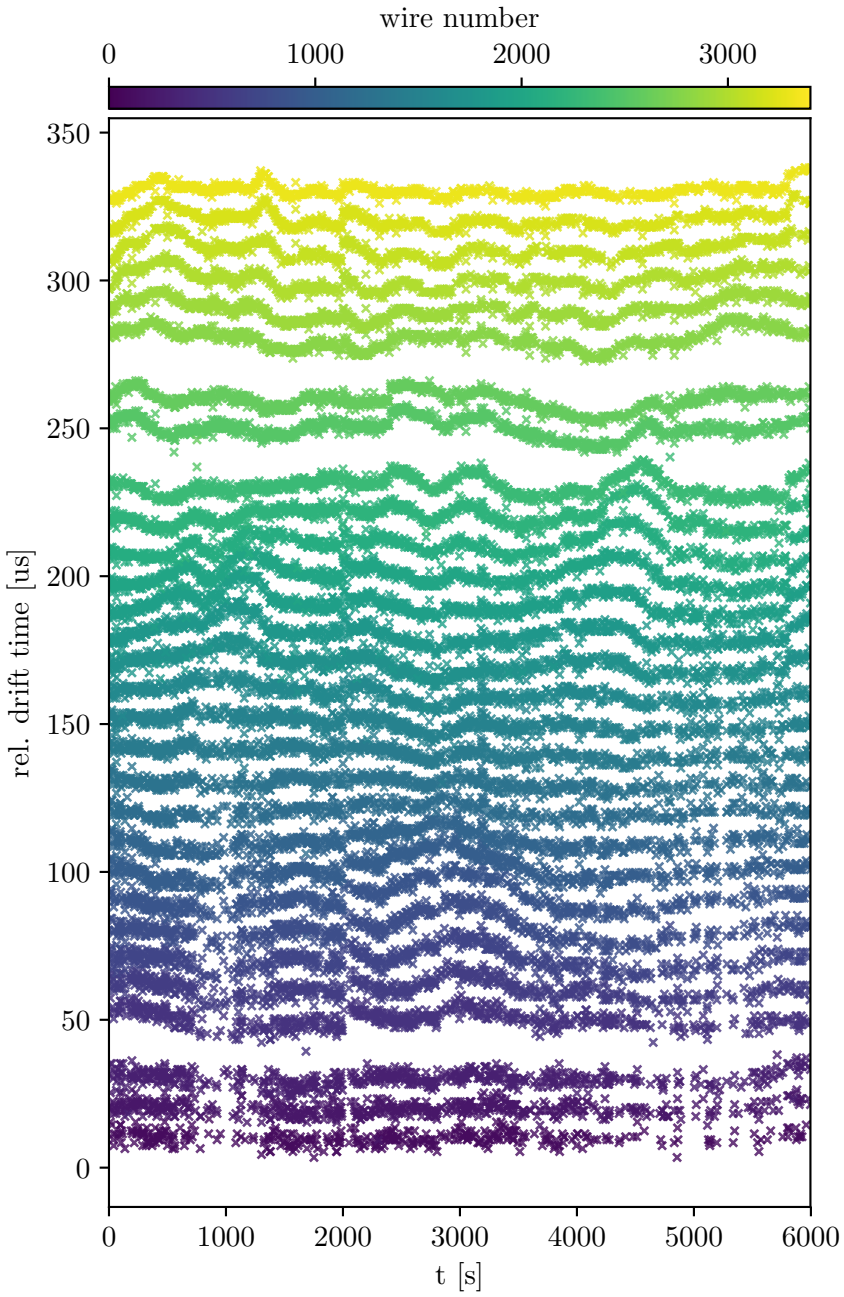

Figure 6.23: Peak location time evolution relative to mean position for selected wires. Wires 0 to 3400 with a spacing of 100 wires (corresponding to 30 cm) are shown, each colour represents a single wire. For better display to each wire an offset of 10 µs to the previous wire is applied. Horizontal gaps arise from unresponsive wires in the detector.

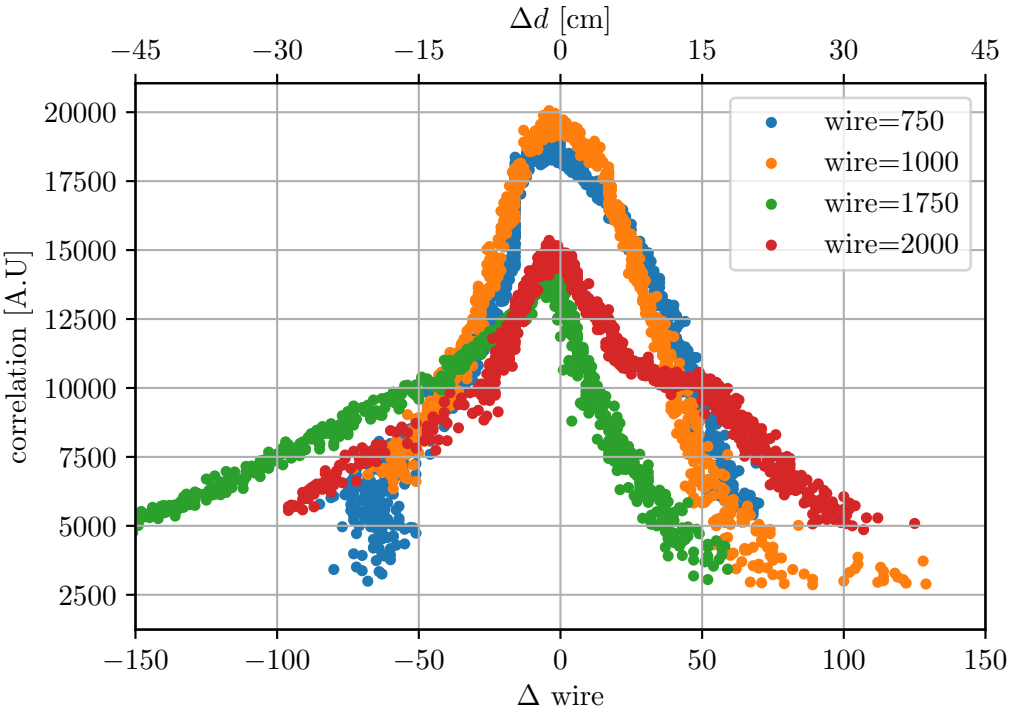

Figure 6.24: Neighboring wire signal correlations for four selected wires in different colors. The correlation is expressed in arbitrary units, the spatial extend (in z) is derived from the wire spacing.

7 CONCLUSION

In the framework of this thesis, an Ultra Violet (UV) laser system for electric field calibrations in Liquid Argon Time Projection Chambers (LArTPCs) was successfully developed, commissioned and deployed in the MicorBooNE detector.

The hardware includes the development of an optical table responsible for beam shaping and control, the optical feedthrough to introduce the UV laser beam into the cryostat and the mechanical system to control and measure the beam's direction into the LArTPC (pulished in [122]). On the software side, various motor drivers were implemented to remotely trigger, shape and steer the UV laser beam. All interfaces are brought together in a slow control system which orchestrates the sub-systems to obtain an optimal laser beam at a chosen location. In addition, a data collection model was implemented. It stores the UV laser beam's direction alongside meta-data of the calibration systems' state. The full system, consisting of two identical laser systems, was placed into operation within the final MicroBooNE commissioning efforts during summer 2015. The specific implementation within MicroBooNE was published as part of [52]. Two challenges had to be mastered before nominal calibration runs could be performed. Firstly, the position of the steerable mirrors relative to the detector had to be determined precisely. This had to be performed after the initial filling of the cryostat with liquid argon, since the LArTPC structure will thermally contract relative to the cryostat when cooled down. Therefore, a calibration strategy was developed to measure the mirror location based on the known TPC field cage (support) structure accessible by the UV laser beam. The presence and absence pattern of UV laser beam signals in the detector was matched to an expected pattern. Maximizing the overlap between estimated and recorded pattern lead to a best estimate for the mirror position. With this approach the mirror position could be identified with a precision of $\pm 0.5\,\mathrm{mm}$. Secondly, due to the steering mirror's reflectivity dependence on the Angle of Incidence (AOI), the UV laser beam's energy has to be modulated to compensate for these losses. This ensures optimal ionization of the liquid argon along the laser path for hit and track reconstruction. Dedicated runs, where the TPC response was recorded while the laser energy was adjusted, were performed. This data set was used to identify an optimal UV laser beam energy for any possible AOI.

With the calibrated system, a state is reached where UV laser beams introduced into the detector can be used to recover the spatial and electric field distortions. A dedicated laser hit reconstruction algorithm was developed to efficiently identify ionization signals on readout wires. Reconstructed tracks are selected based on multiple criteria to exclude accidental cosmic and poorly reconstructed tracks. With the remaining tracks a displacement map is recovered, which describes the difference between expected and recorded position, on a regular grid. The maximal recorded displacement in the drift direction is $d_x = 7.2 \pm 0.5\,\mathrm{cm}$ located at roughly 3/4 the distance to the cathode. The maximal distortion in the y dimen-

sion $d_y = -15.2 \pm 3.1\,\text{cm}$ and $d_y = 12.2 \pm 4.0\,\text{cm}$ is found at the top and bottom faces of the detector. Displacements in the z direction are more difficult to resolve due to the relative location of the two laser systems along the z-axis. At the center of the detector little displacement is recorded $r_z = 0.1 \pm 0.3\,\text{cm}$. The shape of the displacement is largely consistent with the expected distortions from the accumulation of space charge.

Finally, an electric field map is recovered from the displacement map. Again the impact of space charge dominates the observed distortions, with a magnitude relative to the nominal drift field of $-15 \pm 4\,\%$ and $14 \pm 3\,\%$ at the top and bottom edge, respectively. In drift direction the maximal deviation from the nominal field is found (as expected) close to the anode with a magnitude of $15 \pm 3\,\%$.

Studies of the temporal displacement variation over few hours were conducted. For this the UV laser beam direction was held constant over two hours while firing the laser at a few mHz. A spatial variation of $2.2 \pm 0.3\,\text{mm}$ over two hours was measured. Correlating the waveform of neighboring wires, a spatial extend of the fluctuation of up to 20 cm was observed. Currently, a publication describing the observed electric field distortion effects is in preparation.

MicroBooNE's primary objective is to investigate low energetic electron neutrino events ($p_\nu = 200\,\text{MeV/c}$ to $500\,\text{MeV/c}$), final state electrons with these energies have a residual range of 30 cm to 40 cm in liquid argon [123] (two to three radiation lengths). Hence, trajectory distortions of only a few cm will significantly influence the momentum resolution of the LArTPC. Furthermore, due to distortions in the electric field, fiducial volume cuts become non-trivial. The simple back-projection in drift direction, based on the time difference between scintillation and wire sensing does not yield correct results if field distortions are present. Therefore, normalization factors based on the knowledge of the exact fiducial mass have to consider field distortions. Of course, the volume could be restricted to regions with a uniform electric field. But, these regions have to be identified in the first place, and in a neutrino experiment would painfully reduce the signal rate. Currently, work is ongoing to implement corrections, based on the electric field obtained with UV laser calibration system, within the LArSoft [111] framework responsible for event reconstruction. This will pave the way to reduce systematic errors and ultimately improve the sensitivity of the detector.

In the near future, the next iteration of the UV laser calibration system will be installed in the LAr1-ND detector [124], which is part of the Short Baseline Neutrino Program at Fermilab [125]. All know-how gained during this thesis has greatly influenced the proposed design. Further ahead lies the construction of DUNE, a massive (40 kt) LArTPC [126] for long baseline neutrino oscillation studies. Although the build up of space charge is significantly reduced due to the detector's underground location, a UV laser calibration system is planned to map electric field distortions stemming from deformations of the field shaping structure. Furthermore, the UV laser calibration system is the only way to introduce a well-defined ionization signal in a LArTPC, enabling tests of the detector's integrity. This feature is particularly valuable if low event rates (signal and background) are expected.

A

SIMULATED DISPLACEMENT

Here additional figures displaying the used displacement distribution are shown, for details see Section 6.6. Additional slices in the *z*-*y* (Figure A.1, Figure A.2 and Figure A.3) and *x*-*z* (Figure A.4) are shown for different positions of the third coordinate.

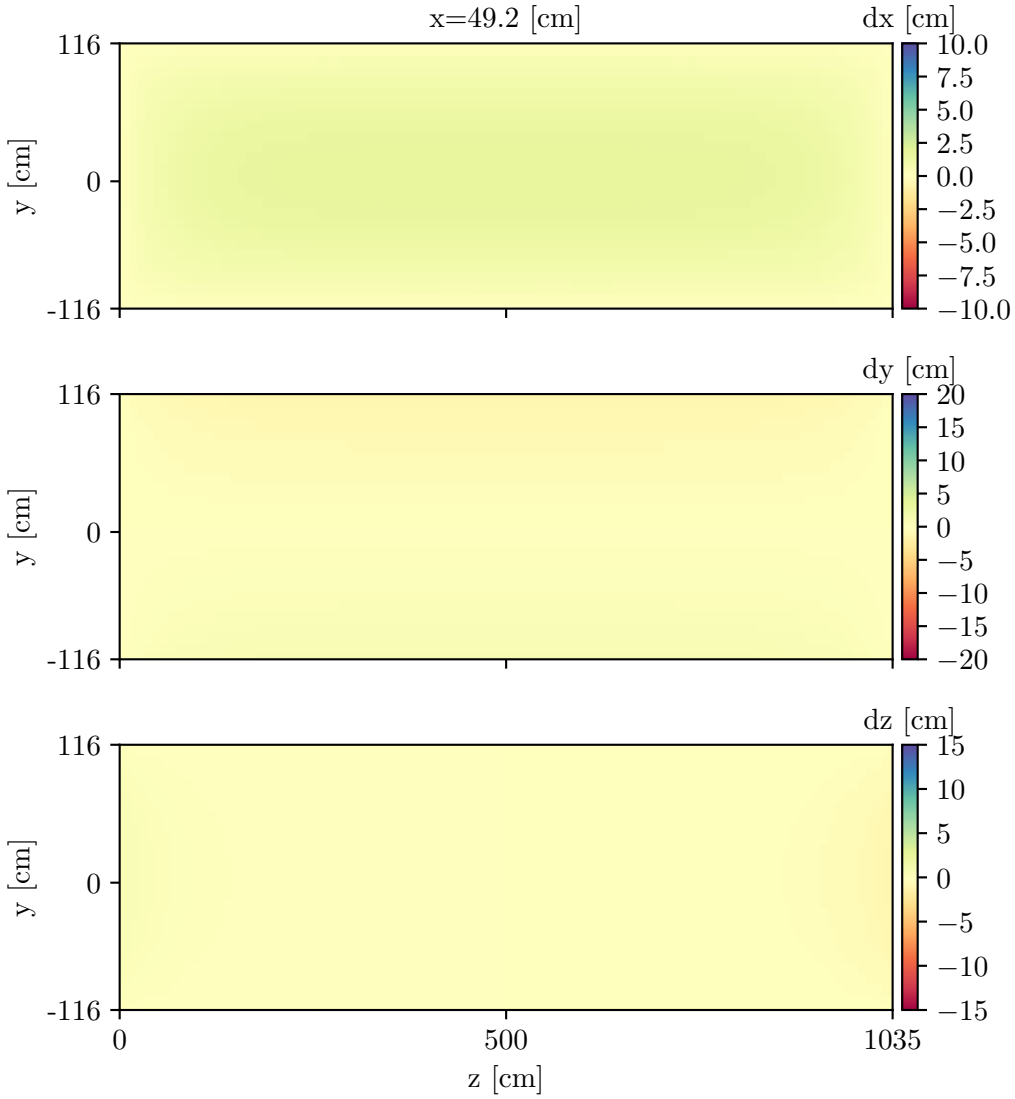

Figure A.1: Simulated displacement (zy-slices) at $z = 50\,\text{cm}$

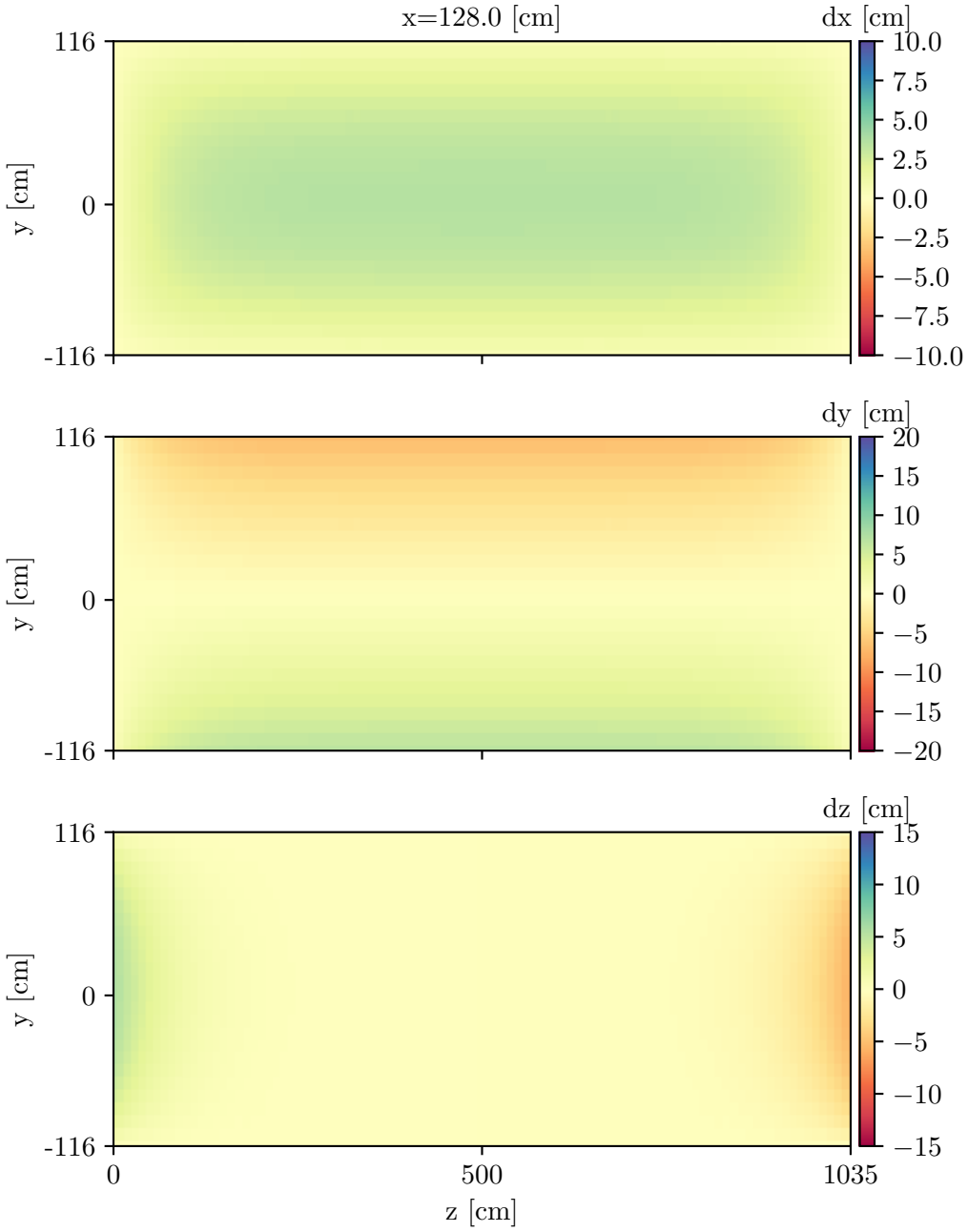

Figure A.2: Simulated displacement (zy-slices) at $z = 128\,\text{cm}$

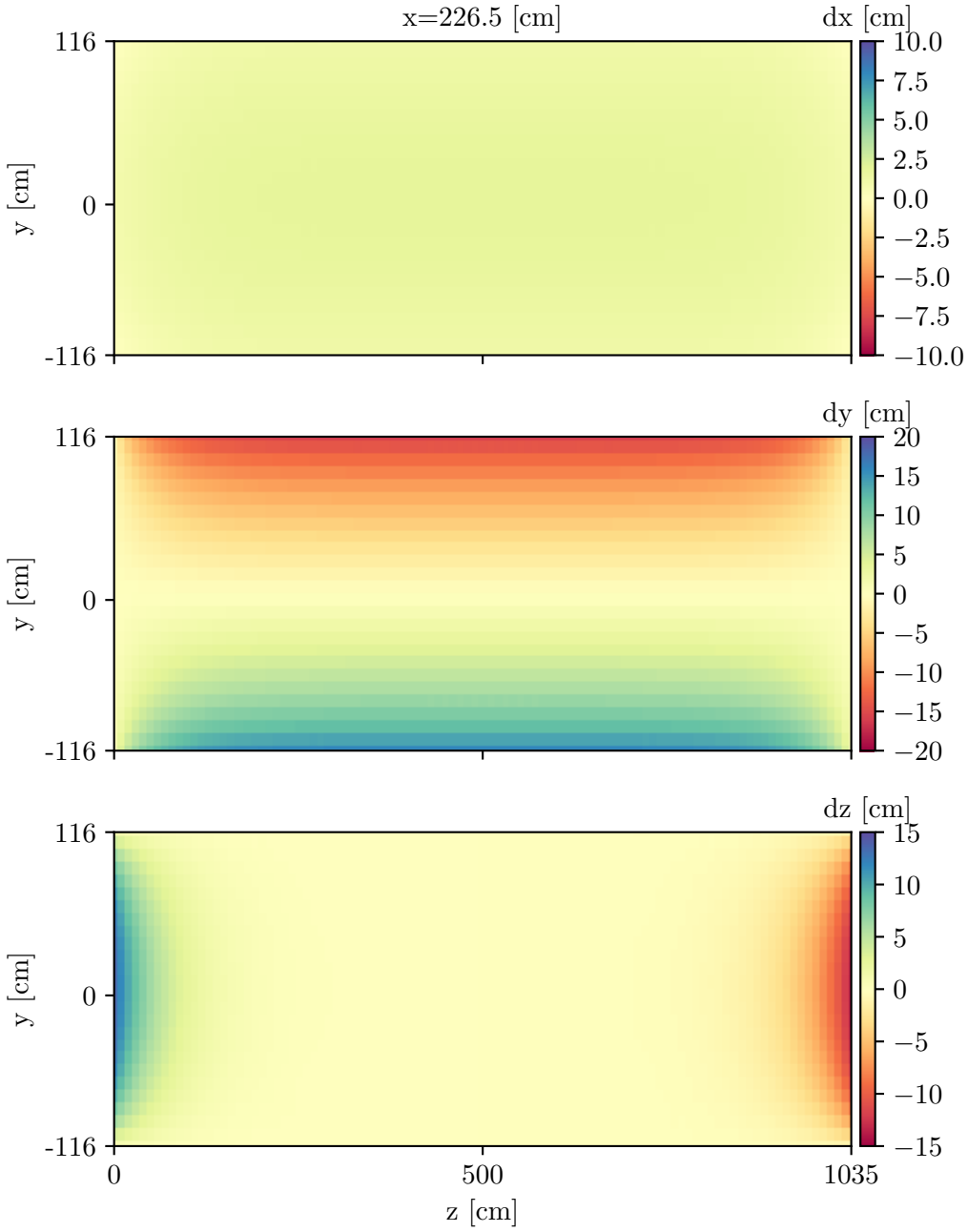

Figure A.3: Simulated displacement (zy-slices) at $z = 226\,\text{cm}$

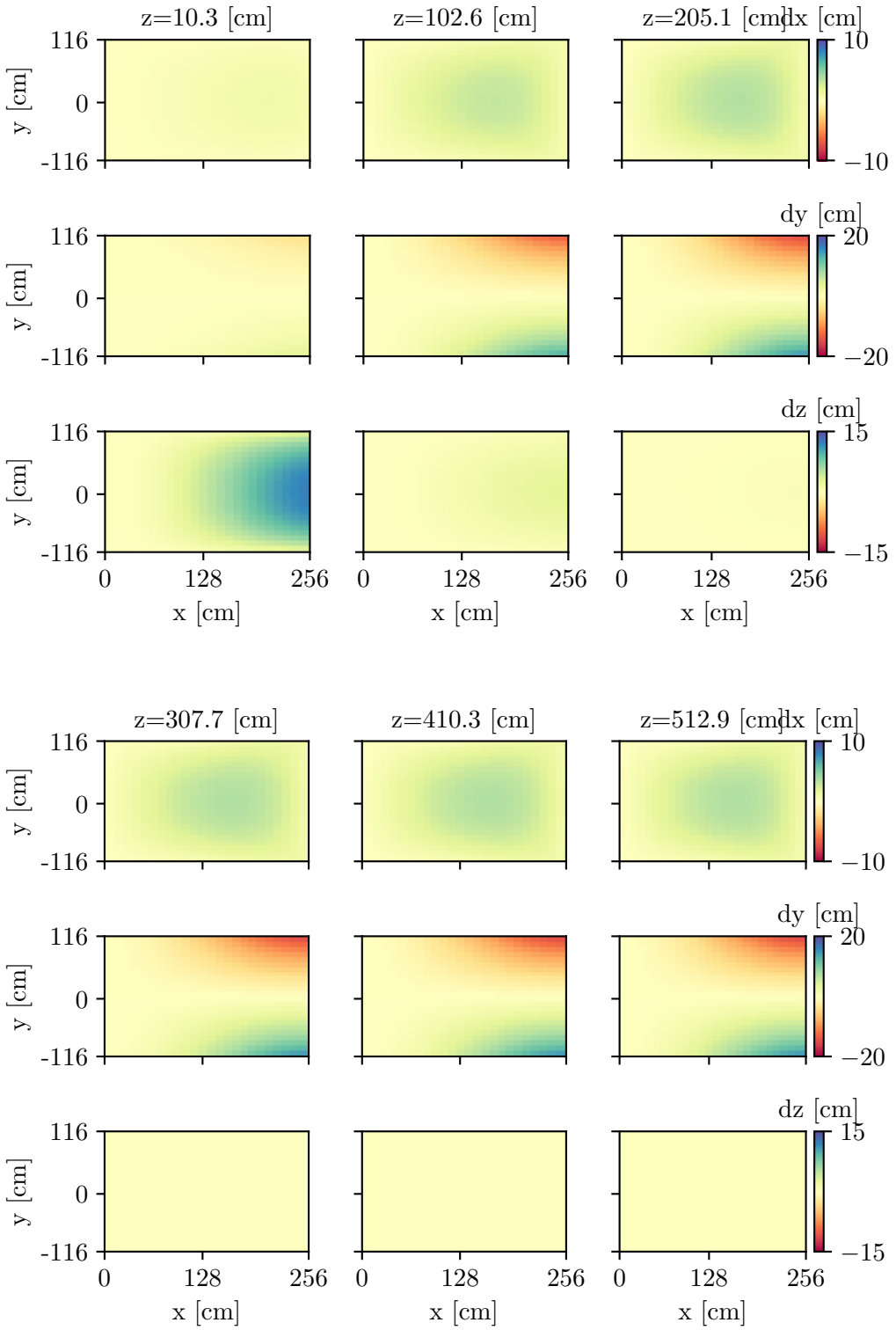

Figure A.4: Displacements for the xz-plane in the three spatial dimensions (rows) with increasing slice position in z (columns).

B

RECONSTRUCTED ELECTRIC FIELD

This chapter contains additional graphs depicting the reconstruced electric field using laser data.

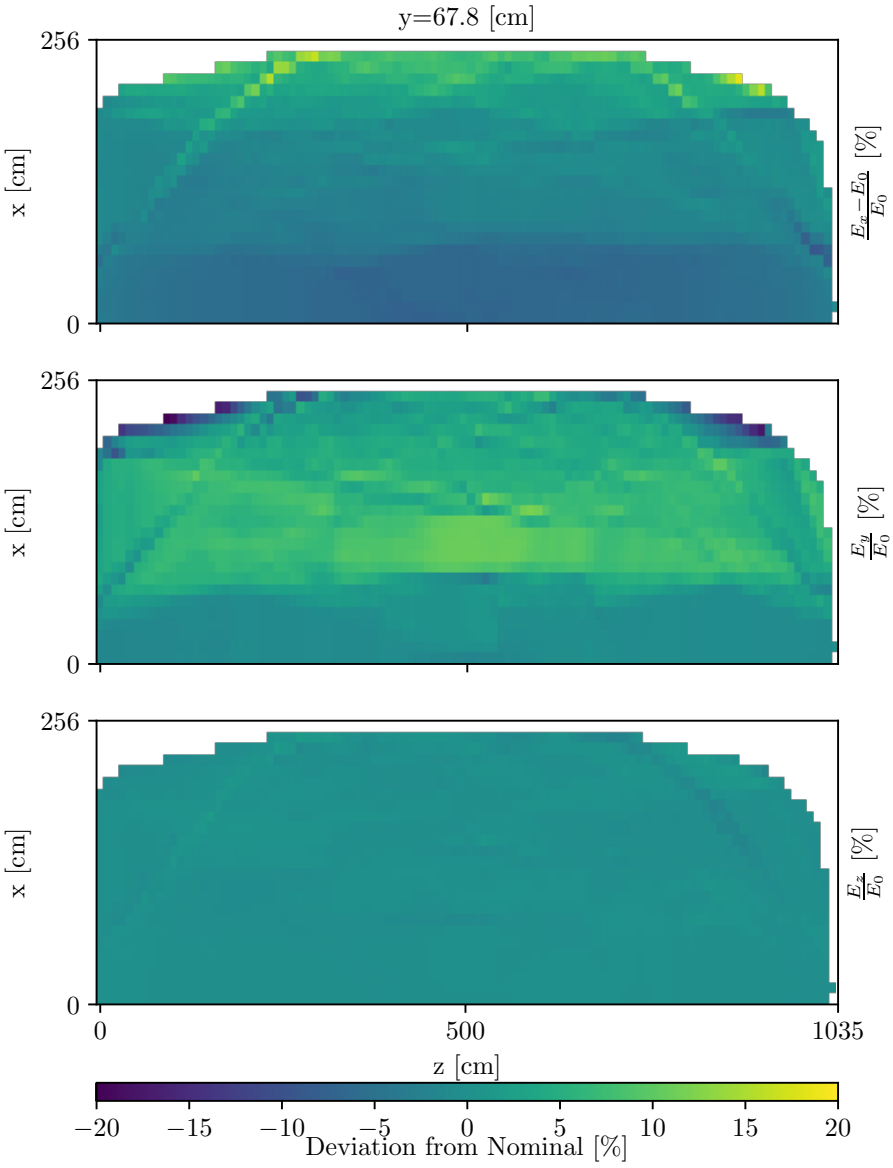

Figure B.1: Distortions relative to the nominal electric field E_0 in three spatial directions for a slice at $y = 67\,\text{cm}$ in the $z - x$-plane.

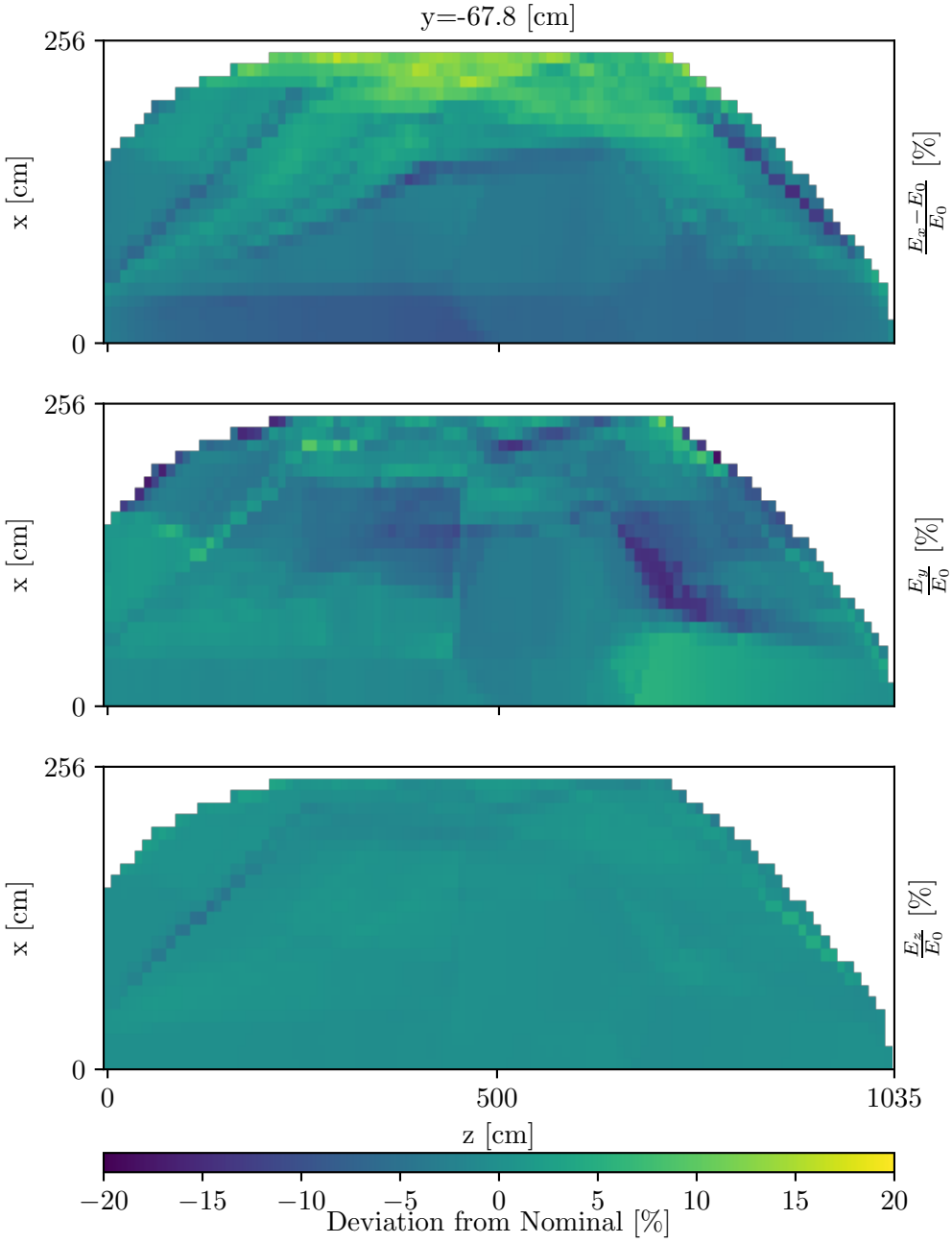

Figure B.2: Distortions relative to the nominal electric field E_0 in three spatial directions for a slice at $y = -67\,\text{cm}$ in the $z - x$-plane.

C

SIMULATION DATA

In the following additional data representations for the verification stage (Section 6.6) are presented.

Figure C.1 depicts the residuals for individual tracks in the x and y coordinate for the toy simulation per laser system. Different colors indicate varying polar (in the Δx) and azimuth (in the Δy) angles. A total of 1000 tracks are accumulated in this data set. In the same fashion, Figure C.2 the top, bottom or cathode of the detector. shows the residuals per laser system for the full laser simulation.

Figure C.3 depicts the residual distributions for the toy dataset, with colors indicating different sections of the detector, in (a) slices along x (front, center and back) and in (b) slices in y (top, middle, bottom) are selected.

Figure C.4 shows the distribution of the magnitudes of the residual $\vec{x}_{res} = \vec{x}_{true} - \vec{x}_{reco}$ for all grid points (where the reconstruction was possible). In the three sub-figures the contributions from different regions are indicated (see caption for details). The standard deviation for the total distribution (dashed line) is $\sigma_{res} = 0.6\,\text{cm}$.

Figure C.5 shows the distribution of the magnitudes of the residual for each spatial coordinate, in this case for the full laser simulation. Colors again indicate different regions of the detector, see caption of Figure C.4 for a description of the three regions.

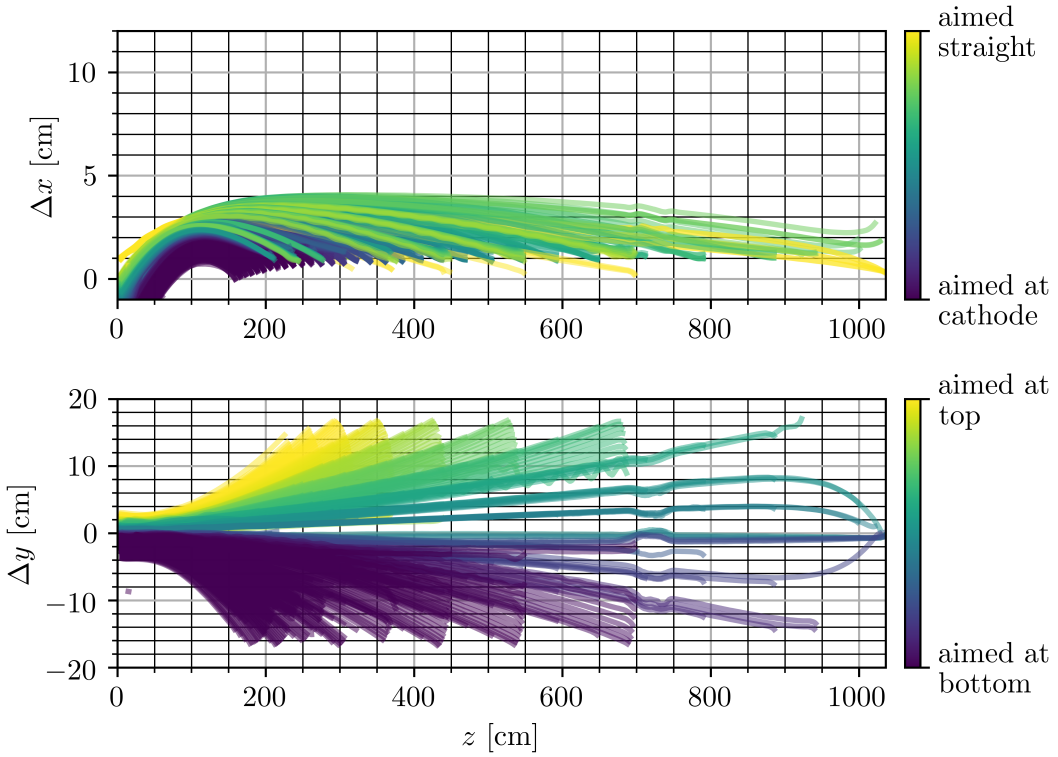

(a)

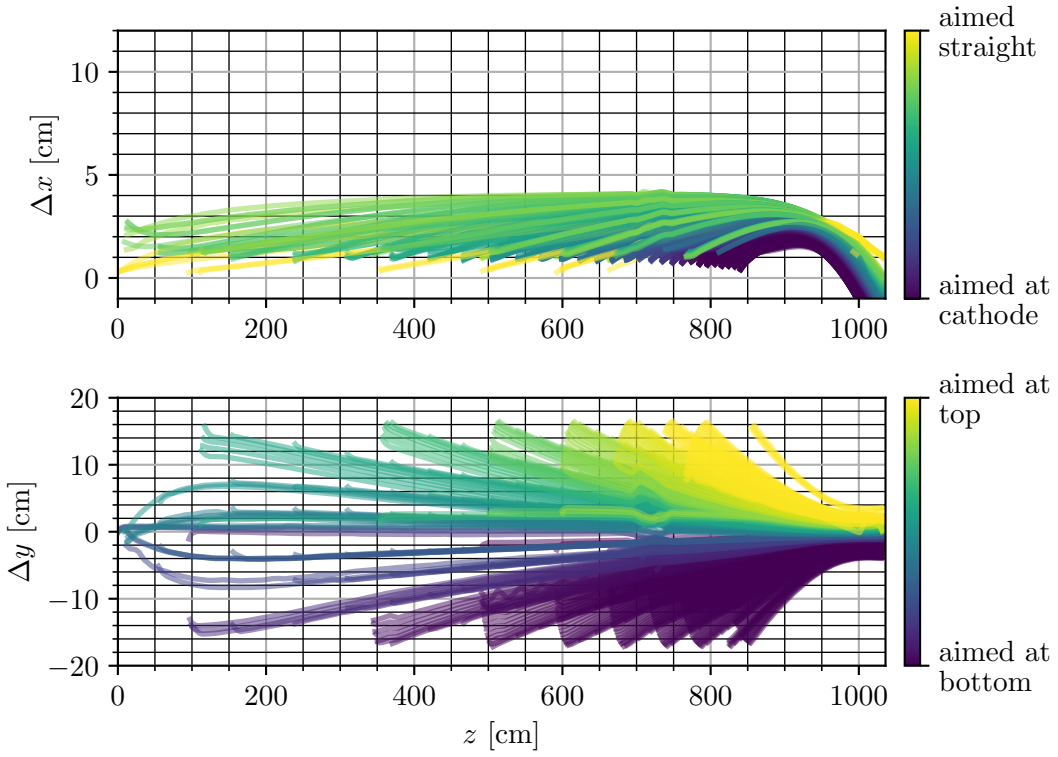

(b)

Figure C.1: Δx and Δy track residuals for the toy simulation relative to the true laser information along the z coordinate. For the upstream (a) and downstream (b) laser system. Different colors indicate the polar and azimuth angle. Different lengths of the tracks arise from beams hitting the top, bottom or cathode of the detector.

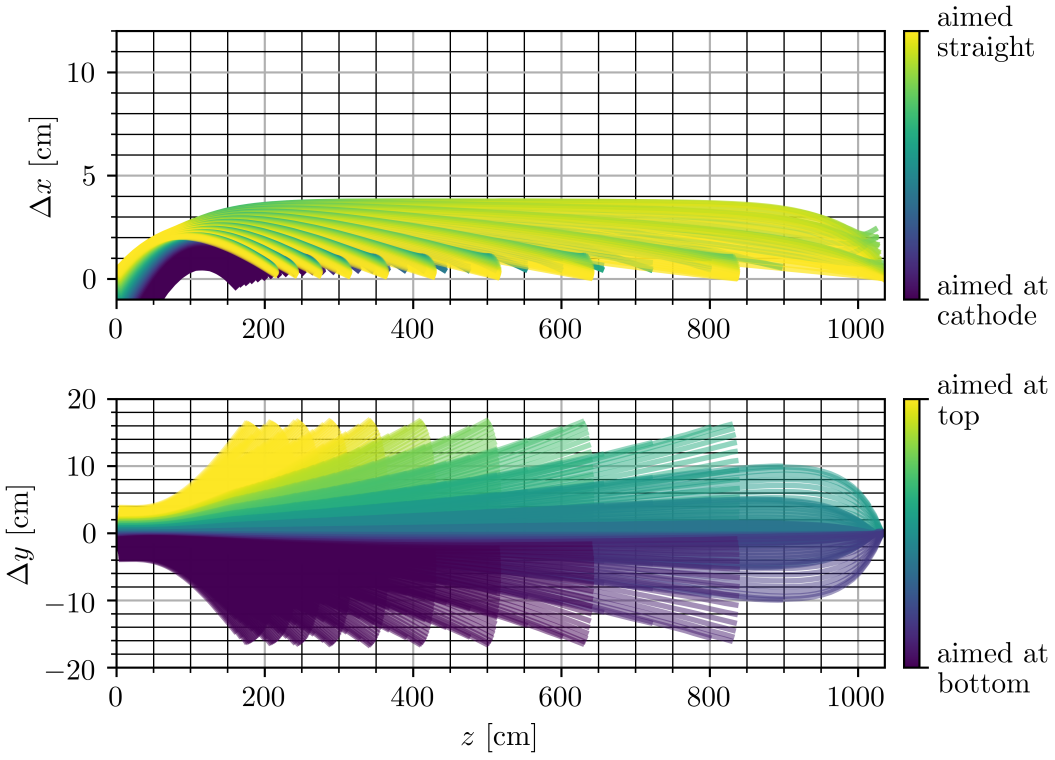

(a)

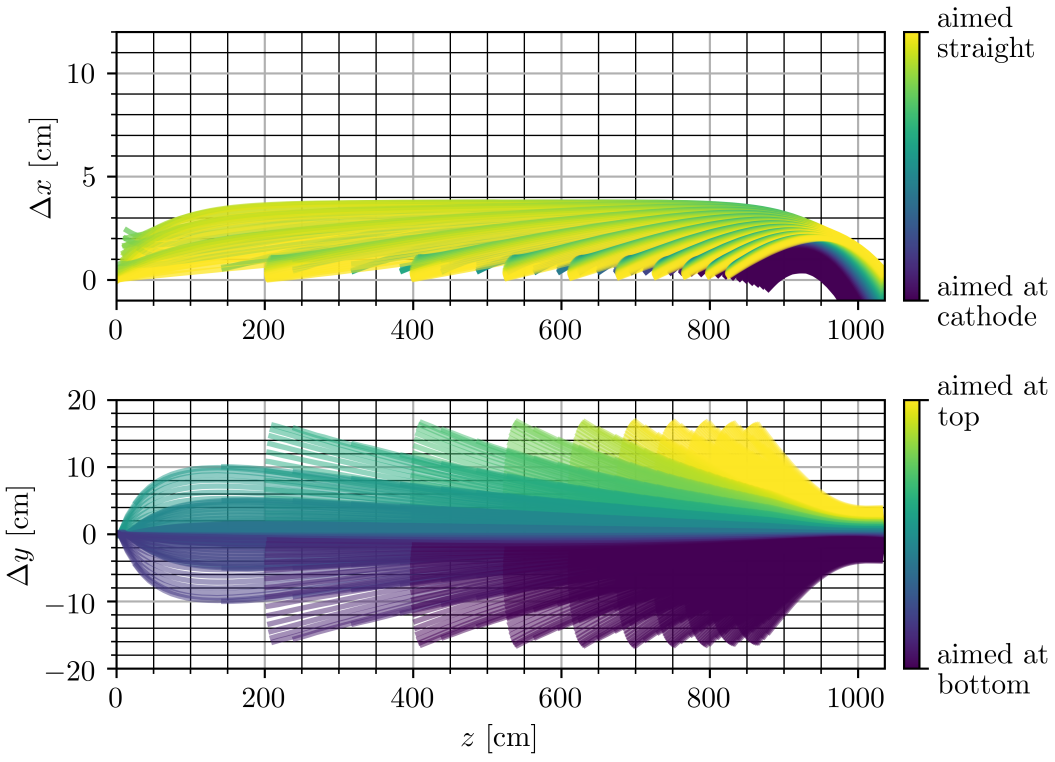

(b)

Figure C.2: Δx and Δy track residuals for the full simulation relative to the true laser information along the z coordinate. For the upstream (a) and downstream (b) laser system. Different colors indicate the polar and azimuth angle. Different lengths of the tracks arise from beams hitting the top, bottom or cathode of the detector.

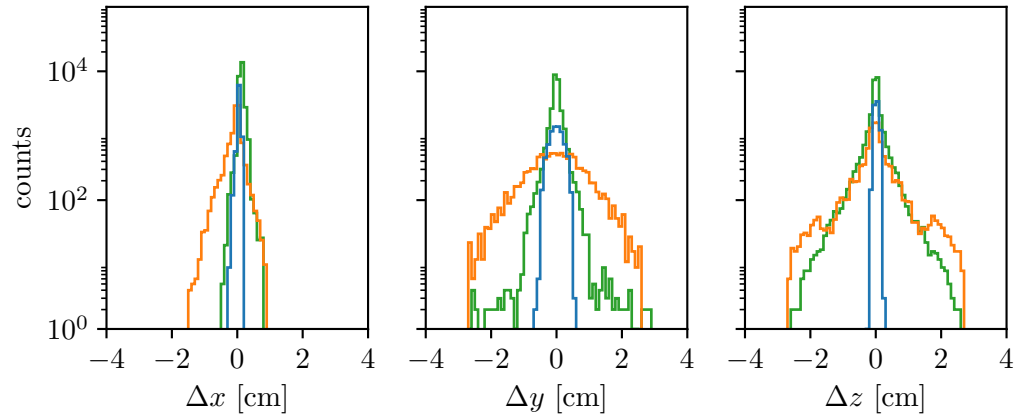

(a) front to back

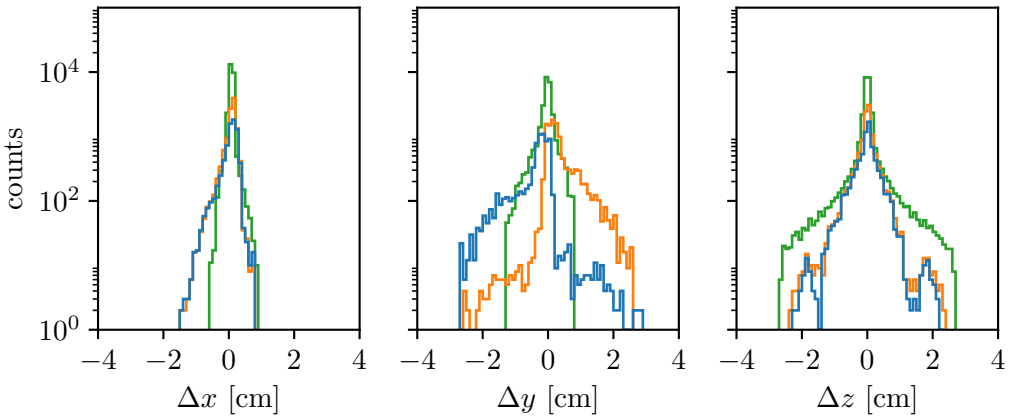

(b) top to bottom

Figure C.3: Residual ($\vec{x}_{true} - \vec{x}_{reco}$) distribution for each spatial dimension for the toy simulation. The three colors indicate contributions from different regions in the detector. In (a) blue corresponds to regions on the front end $x < 50\,\text{cm}$, orange on the back end $x > 206\,\text{cm}$ and green the middle part where $50\,\text{cm} < x < 206\,\text{cm}$. In (b) blue corresponds to regions on the top $y < 78\,\text{cm}$, orange on the bottom $y > -78\,\text{cm}$ and green the central part where $-78\,\text{cm} < y < 78\,\text{cm}$.

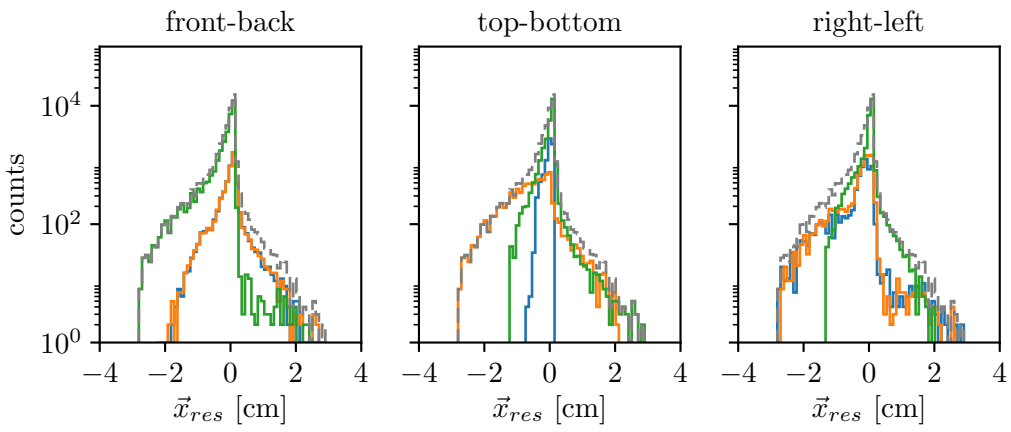

Figure C.4: Residual ($\vec{x}_{res} = \vec{x}_{true} - \vec{x}_{reco}$) distribution for the toy simulation. The three colors indicate contributions from different regions in the detector. The dashed gray line represents the summed distribution. Colors in the three sub-figures indicate contributions from different sections in the detector. The regions are; front to back (left) with $x < 50\,\text{cm}$ (blue), $x > 206\,\text{cm}$ (orange) and $50\,\text{cm} < x < 206\,\text{cm}$ (green); top to bottom (middle) with $y < 78\,\text{cm}$ (blue), $y > -78\,\text{cm}$ (orange) and $-78\,\text{cm} < y < 78\,\text{cm}$ (green); right to left with $z < 200\,\text{cm}$ (blue), $z > 835\,\text{cm}$ (orange) and $200\,\text{cm} < z < 835\,\text{cm}$ (green).

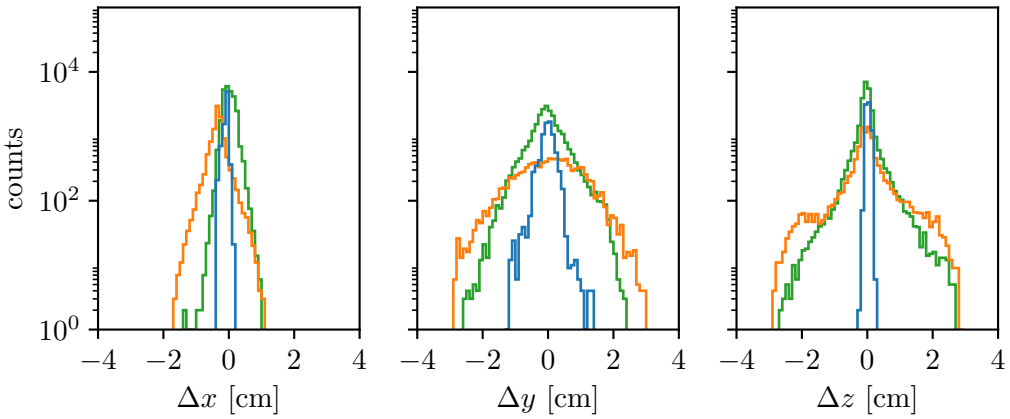

(a) fron to back

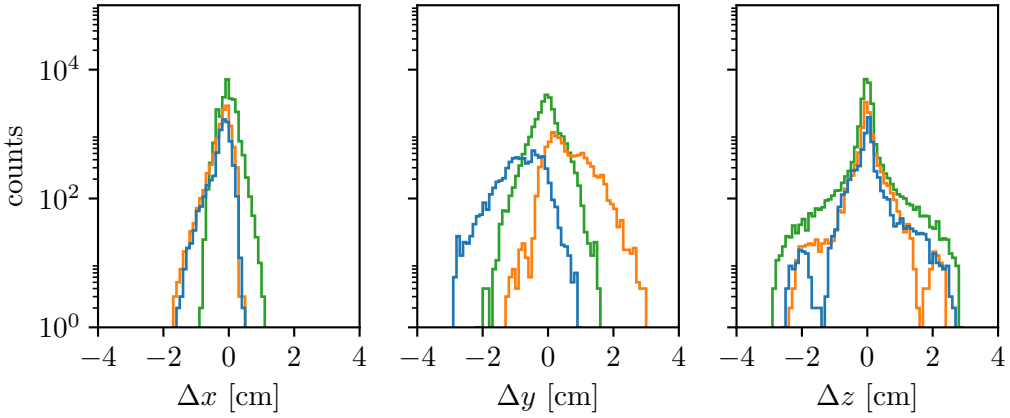

(b) top to bottom

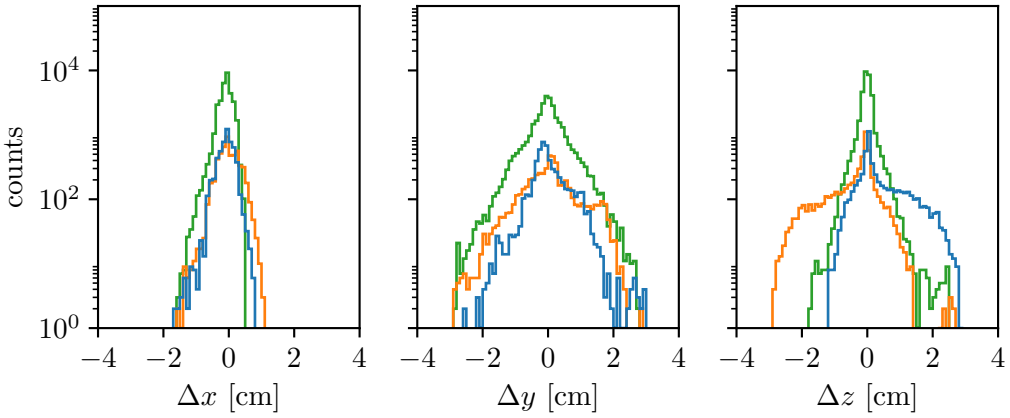

(c) up- to downstream

Figure C.5: Residual ($\vec{x}_{true} - \vec{x}_{reco}$) distribution for each spatial dimension for the full laser simulation. For the three regions described in Figure C.4.

D

CROSS DISTANCE DISTRIBUTIONS

This chapter holds additional information about the cross distance calculations described in Section 6.7.

DATA	OFFSET RANGE					FIGURE
SET	x [cm]	y [cm]	z [cm]	` []	Œ []	
Toy	−1–1	−1–1	0	0	0	Figure D.1
Toy	−1–1	0	−1–1	0	0	Figure D.2
Toy	0	−1–1	−1–1	0	0	Figure D.3
Toy	−2–2	−2–2	0	+0.1	0	Figure D.4
Toy	−2–2	−2–2	0	-0.1	0	Figure D.1
Toy	−2–2	−2–2	0	0	+0.1	Figure D.1
Toy	−2–2	−2–2	0	0	-0.1	Figure D.1
Toy	0	0	0	−0.5–0.5	−0.5–0.5	Figure D.1

Table D.1: Summary table of cross distance distributions, their associate offset ranges and figures.

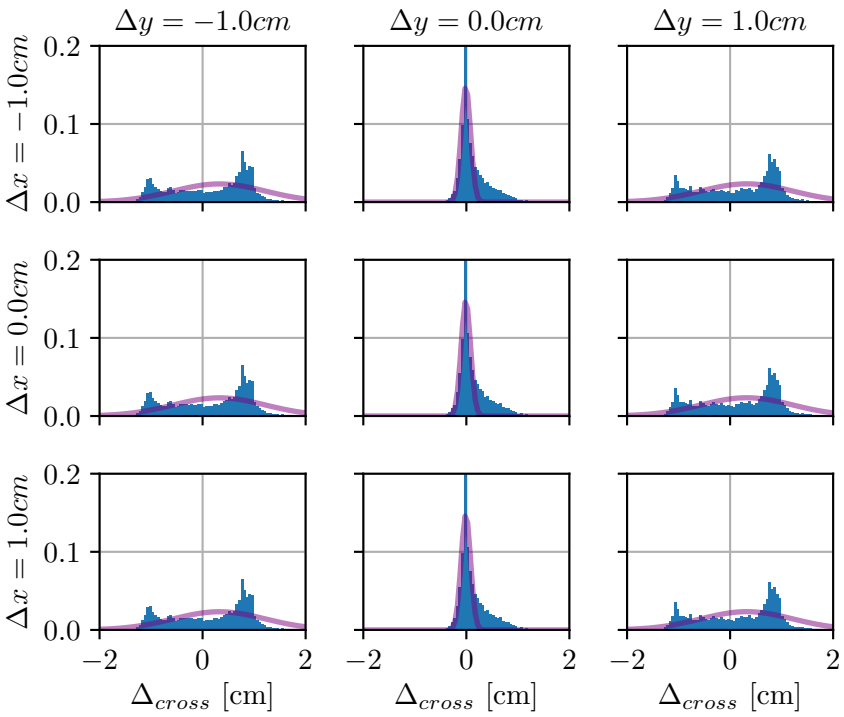

Figure D.1

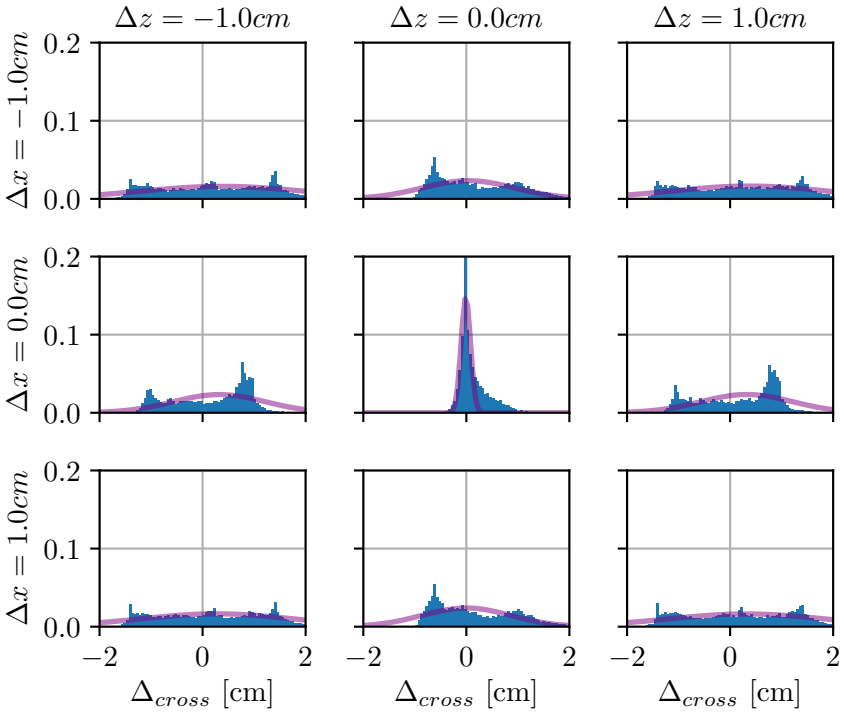

Figure D.2

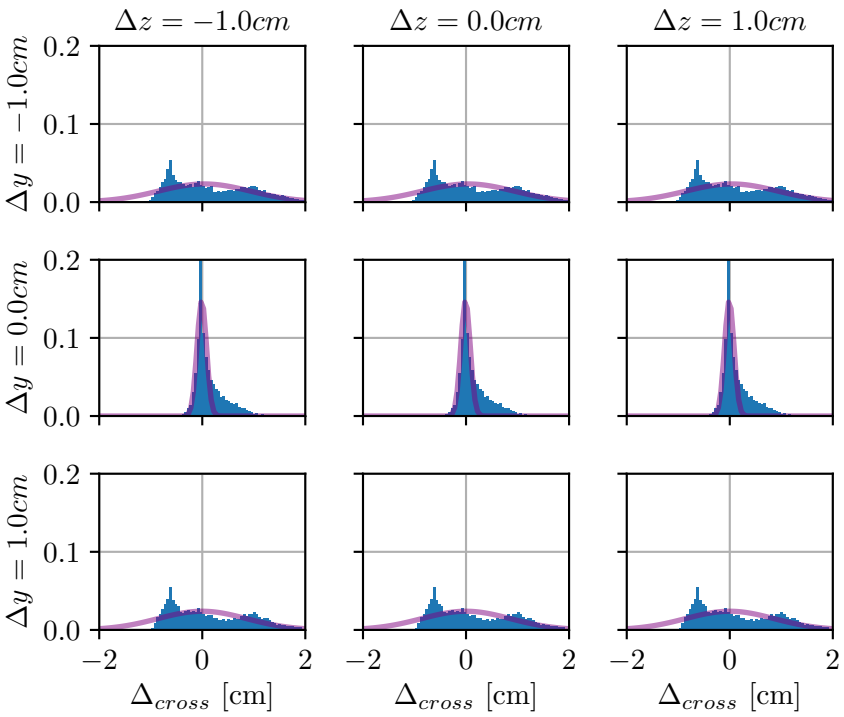

Figure D.3

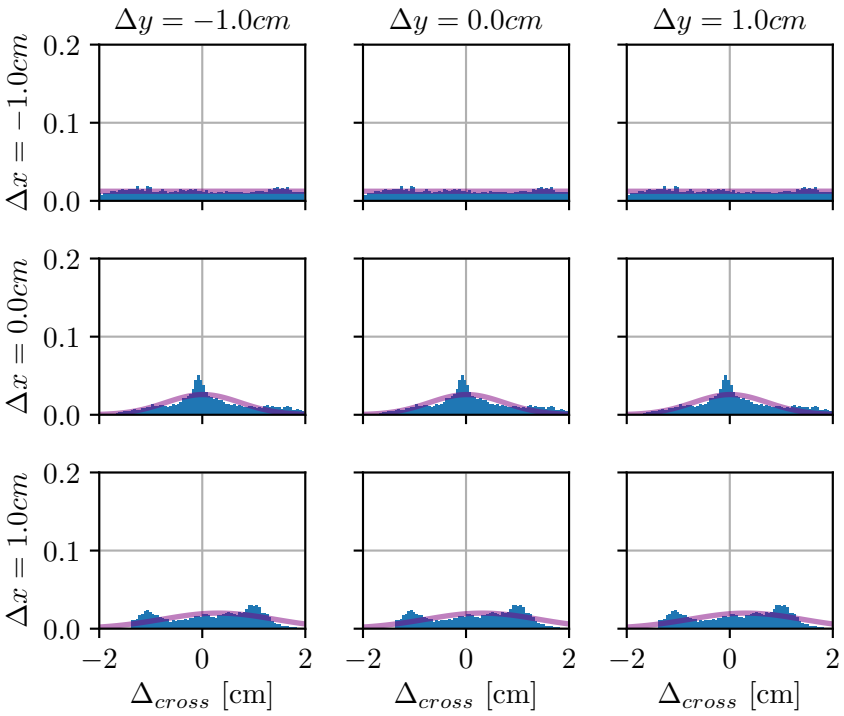

Figure D.4

E

TIME EVOLUTION

This chapter contains additional figures displaying the temporal fluctuations on a constant ionization track, generated by the laser being fired at a constant direction. For a detailed discussion see Section 6.8. In Figure E.1 a 3D plot is showing the variation of the peak location over time, in the plane the wire number is converted to a z-location using the known wire spacing, the sample time in s is the other dimension in the plane. The third coordinate is used to display the deviation from the mean peak location (defined and determined earlier). The maximum found deviation from the mean peak location is 12 µs at $z = 250$ cm and after a time of 3200 s. This corresponds to 1.38 cm assuming the nominal MicroBooNE drift field. In Figure E.2 the region with the maximum peak is enhanced. Following the peaks time evolution along $z = 250$ cm on can estimate the fluctuations period to be of the order of 1500 s or roughly 30 min. In addition to the variation in time, a scale for the corresponding spatial displacement (assuming the nominal drift speed) is given. Furthermore, the variation in time is converted to a relative variation of the nominal electric field under the assumption of a local linear drift speed relation.

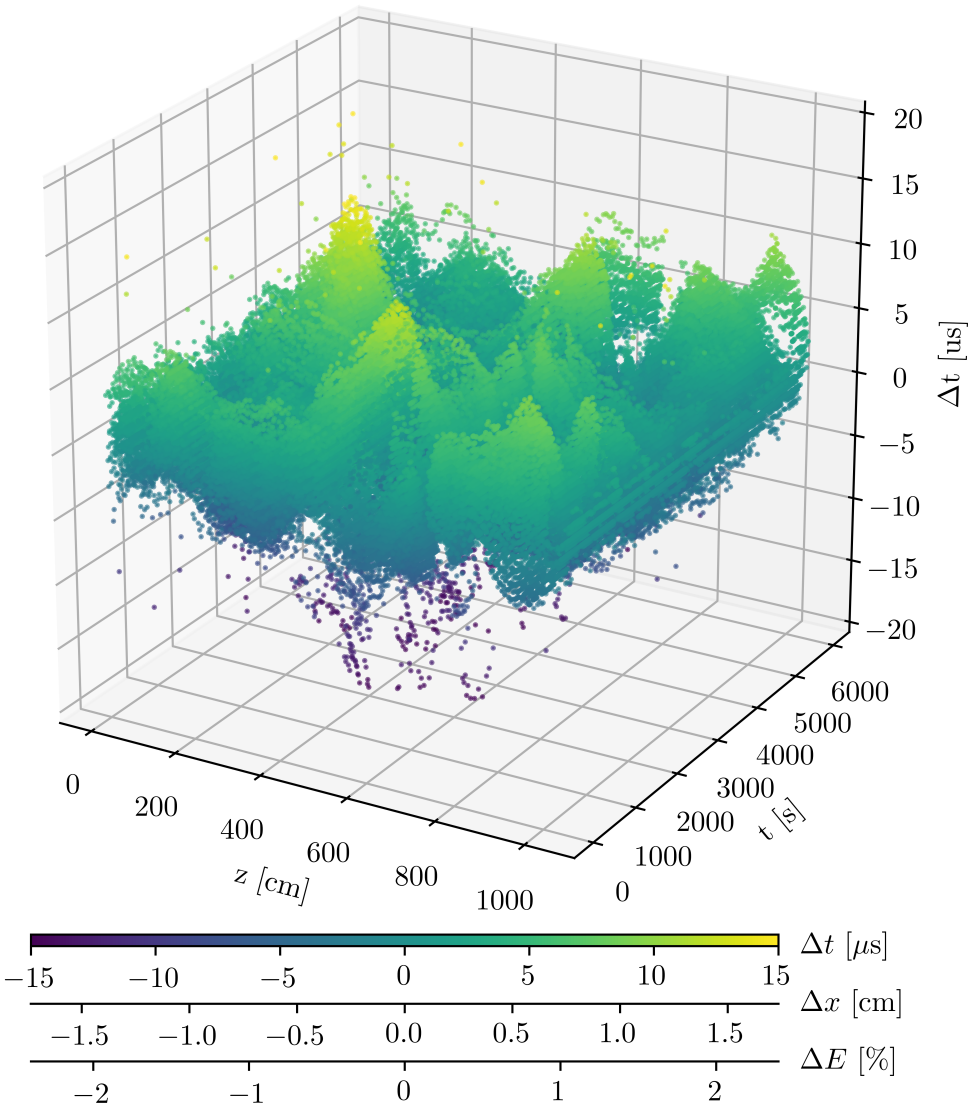

Figure E.1: Temporal evolution of the displacement. The color scale indicates the fluctuation in time, in distance (assuming the nominal drift field) or the variation of the nominal field (E_0).

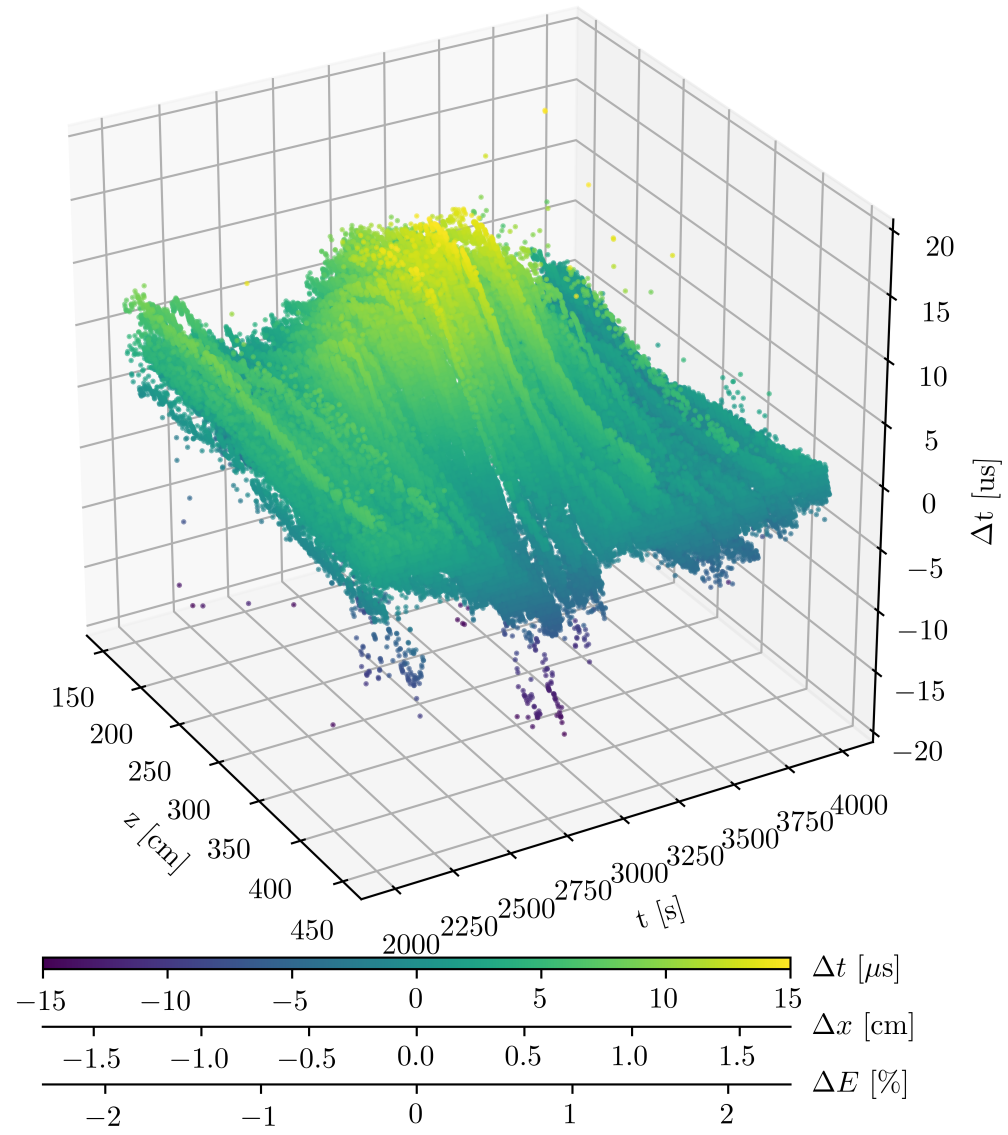

Figure E.2: Enlarged view of the temporal evolution of the displacement. The color scale indicates the fluctuation in time, in distance (assuming the nominal drift field) or the variation of the nominal field (E_0).

BIBLIOGRAPHY

[1] W. Pauli. "Dear radioactive ladies and gentlemen." In: *Phys. Today* 31N9 (1978), p. 27.

[2] F. Reines and C. L. Cowan. "A Proposed Experiment to Detect the Free Neutrino." In: *Phys. Rev.* 90 (3 1953), pp. 492–493. DOI: 10.1103/PhysRev.90.492.2. URL: https://link.aps.org/doi/10.1103/PhysRev.90.492.2.

[3] Raymond Davis, Don S. Harmer, and Kenneth C. Hoffman. "Search for Neutrinos from the Sun." In: *Phys. Rev. Lett.* 20 (21 1968), pp. 1205–1209. DOI: 10.1103/PhysRevLett.20.1205. URL: https://link.aps.org/doi/10.1103/PhysRevLett.20.1205.

[4] Bruce T. Cleveland, Timothy Daily, Jr. Raymond Davis, James R. Distel, Kenneth Lande, C. K. Lee, Paul S. Wildenhain, and Jack Ullman. "Measurement of the Solar Electron Neutrino Flux with the Homestake Chlorine Detector." In: *The Astrophysical Journal* 496.1 (1998), p. 505. URL: http://stacks.iop.org/0004-637X/496/i=1/a=505.

[5] R. M. Bionta et al. "Contained Neutrino Interactions in an Underground Water Detector." In: *Phys. Rev.* D38 (1988), pp. 768–775. DOI: 10.1103/PhysRevD.38.768.

[6] K.S. Hirata et al. "Experimental study of the atmospheric neutrino flux." In: *Physics Letters B* 205.2 (1988), pp. 416 –420. ISSN: 0370-2693. DOI: https://doi.org/10.1016/0370-2693(88)91690-5.

[7] K. Abe and others. "Indication of Electron Neutrino Appearance from an Accelerator-Produced Off-Axis Muon Neutrino Beam." In: *Phys. Rev. Lett.* 107 (4 2011), p. 041801. DOI: 10.1103/PhysRevLett.107.041801. URL: https://link.aps.org/doi/10.1103/PhysRevLett.107.041801.

[8] P. Adamson et al. "Measurement of Neutrino and Antineutrino Oscillations Using Beam and Atmospheric Data in MINOS." In: *Phys. Rev. Lett.* 110 (25 2013), p. 251801. DOI: 10.1103/PhysRevLett.110.251801. URL: https://link.aps.org/doi/10.1103/PhysRevLett.110.251801.

[9] Y. Abe et al. "Indication of Reactor $\overline{\nu}_e$ Disappearance in the Double Chooz Experiment." In: *Phys. Rev. Lett.* 108 (13 2012), p. 131801. DOI: 10.1103/PhysRevLett.108.131801. URL: https://link.aps.org/doi/10.1103/PhysRevLett.108.131801.

[10] F. P. An et al. "Observation of Electron-Antineutrino Disappearance at Daya Bay." In: *Phys. Rev. Lett.* 108 (17 2012), p. 171803. DOI: 10.1103/PhysRevLett.108.171803. URL: https://link.aps.org/doi/10.1103/PhysRevLett.108.171803.

[11] M. Guler et al. "OPERA: An appearance experiment to search for nu/mu ¡–¿ nu/tau oscillations in the CNGS beam. Experimental proposal." In: (2000).

[12] Ch. Kraus et al. "Final results from phase II of the Mainz neutrino mass search in tritium beta decay." In: *Eur. Phys. J.* C40 (2005), pp. 447–468. DOI: 10.1140/epjc/s2005-02139-7. arXiv: hep-ex/0412056 [hep-ex].

[13] V. N. Aseev et al. "An upper limit on electron antineutrino mass from Troitsk experiment." In: *Phys. Rev.* D84 (2011), p. 112003. DOI: 10.1103/PhysRevD.84.112003. arXiv: 1108.5034 [hep-ex].

[14] P. A. R. Ade et al. "Planck 2013 results. XVI. Cosmological parameters." In: *Astron. Astrophys.* 571 (2014), A16. DOI: 10.1051/0004-6361/201321591. arXiv: 1303.5076 [astro-ph.CO].

[15] User MissMJ. *Standard Model of Elementary Particles*. 2006. URL: https://commons.wikimedia.org/wiki/File:Standard_Model_of_Elementary_Particles.svg.

[16] M. Thomson. *Modern Particle Physics*. Modern Particle Physics. Cambridge University Press, 2013. ISBN: 9781107034266.

[17] C. Giunti and C.W. Kim. *Fundamentals of Neutrino Physics and Astrophysics*. OUP Oxford, 2007. ISBN: 9780191523229.

[18] K. Zuber. *Neutrino Physics, Second Edition*. Series in High Energy Physics, Cosmology and Gravitation. Taylor & Francis, 2011. ISBN: 9781420064711.

[19] Evgeny Kh. Akhmedov and Alexei Yu. Smirnov. "Paradoxes of neutrino oscillations." In: *Phys. Atom. Nucl.* 72 (2009), pp. 1363–1381. DOI: 10.1134/S1063778809080122. arXiv: 0905.1903 [hep-ph].

[20] M. Tanabashi, K. Hagiwara, K. Hikasa, and other. "Review of Particle Physics." In: *Phys. Rev. D* 98 (3 2018), p. 030001. DOI: 10.1103/PhysRevD.98.030001. URL: https://link.aps.org/doi/10.1103/PhysRevD.98.030001.

[21] Francesco Capozzi, Eleonora Di Valentino, Eligio Lisi, Antonio Marrone, Alessandro Melchiorri, and Antonio Palazzo. "Global constraints on absolute neutrino masses and their ordering." In: *Phys. Rev. D* 95 (9 2017), p. 096014. DOI: 10.1103/PhysRevD.95.096014. URL: https://link.aps.org/doi/10.1103/PhysRevD.95.096014.

[22] M.V. Diwan, V. Galymov, X. Qian, and A. Rubbia. "Long-Baseline Neutrino Experiments." In: *Annual Review of Nuclear and Particle Science* 66.1 (2016), pp. 47–71. DOI: 10.1146/annurev-nucl-102014-021939. eprint: https://doi.org/10.1146/annurev-nucl-102014-021939. URL: https://doi.org/10.1146/annurev-nucl-102014-021939.

[23] L.J. Wen, J. Cao, and Y.F. Wang. "Reactor Neutrino Experiments: Present and Future." In: *Annual Review of Nuclear and Particle Science* 67.1 (2017), pp. 183–211. DOI: 10.1146/annurev-nucl-101916-123318. eprint: https://doi.org/10.1146/annurev-nucl-101916-123318. URL: https://doi.org/10.1146/annurev-nucl-101916-123318.

[24] Nick Jelley, Arthur B. McDonald, and R.G. Hamish Robertson. "The Sudbury Neutrino Observatory." In: *Annual Review of Nuclear and Particle Science* 59.1 (2009), pp. 431–465. DOI: 10.1146/annurev.nucl.55.090704.151550. eprint: https://doi.org/10.1146/annurev.nucl.55.090704.151550. URL: https://doi.org/10.1146/annurev.nucl.55.090704.151550.

[25] T. K. Gaisser. "Review of atmospheric neutrinos." In: *Neutrino '96. Proceedings, 17th International Conference on Neutrino Physics and Astrophysics, Helsinki, Finland, June 13-19, 1996*. 1996, pp. 211–222. arXiv: hep-ph/9611301 [hep-ph].

[26] C Athanassopoulos et al. "The liquid scintillator neutrino detector and LAMPF neutrino source." In: *Nuclear Instruments and Methods in Physics Research Section A: Accelerators, Spectrometers, Detectors and Associated Equipment* 388.1 (1997), pp. 149 –172. ISSN: 0168-9002. DOI: https://doi.org/10.1016/S0168-9002(96)01155-2. URL: http://www.sciencedirect.com/science/article/pii/S0168900296011552.

[27] A. Aguilar-Arevalo et al. "Evidence for neutrino oscillations from the observation of anti-neutrino(electron) appearance in a anti-neutrino(muon) beam." In: *Phys. Rev.* D64 (2001), p. 112007. DOI: 10.1103/PhysRevD.64.112007. arXiv: hep-ex/0104049 [hep-ex].

[28] A. A. Aguilar-Arevalo et al. "Improved Search for $\bar{\nu}_\mu \to \bar{\nu}_e$ Oscillations in the MiniBooNE Experiment." In: *Phys. Rev. Lett.* 110 (2013), p. 161801. DOI: 10.1103/PhysRevLett.110.161801. arXiv: 1303.2588 [hep-ex].

[29] R. M. Sternheimer. "Energy Distribution of γ Rays from π^0 Decay." In: *Phys. Rev.* 99 (1 1955), pp. 277–281. DOI: 10.1103/PhysRev.99.277. URL: https://link.aps.org/doi/10.1103/PhysRev.99.277.

[30] Dieter Rein and Lalit M Sehgal. "Neutrino-excitation of baryon resonances and single pion production." In: *Annals of Physics* 133.1 (1981), pp. 79 – 153. ISSN: 0003-4916. DOI: https://doi.org/10.1016/0003-4916(81)90242-6. URL: http://www.sciencedirect.com/science/article/pii/0003491681902426.

[31] A. A. Aguilar-Arevalo et al. "Significant Excess of ElectronLike Events in the MiniBooNE Short-Baseline Neutrino Experiment." In: (2018). arXiv: 1805.12028 [hep-ex].

[32] Carlo Giunti and Marco Laveder. "Statistical Significance of the Gallium Anomaly." In: *Phys. Rev.* C83 (2011), p. 065504. DOI: 10.1103/PhysRevC.83.065504. arXiv: 1006.3244 [hep-ph].

[33] F. P. An et al. "Evolution of the Reactor Antineutrino Flux and Spectrum at Daya Bay." In: *Phys. Rev. Lett.* 118.25 (2017), p. 251801. DOI: 10.1103/PhysRevLett.118.251801. arXiv: 1704.01082 [hep-ex].

[34] F. P. An, Balantekin, et al. "Evolution of the Reactor Antineutrino Flux and Spectrum at Daya Bay." In: *Phys. Rev. Lett.* 118 (25 2017), p. 251801. DOI: 10.1103/PhysRevLett.118.251801. URL: https://link.aps.org/doi/10.1103/PhysRevLett.118.251801.

[35] Raymond R. Volkas. "Introduction to sterile neutrinos." In: *Prog. Part. Nucl. Phys.* 48 (2002). [,161(2001)], pp. 161–174. DOI: 10.1016/S0146-6410(02)00122-9. arXiv: hep-ph/0111326 [hep-ph].

[36] S. Schael et al. "Precision electroweak measurements on the Z resonance." In: *Phys. Rept.* 427 (2006), pp. 257–454. DOI: 10.1016/j.physrep.2005.12.006. arXiv: hep-ex/0509008 [hep-ex].

[37] T. Araki et al. "Measurement of neutrino oscillation with KamLAND: Evidence of spectral distortion." In: *Phys. Rev. Lett.* 94 (2005), p. 081801. DOI: 10.1103/PhysRevLett.94.081801. arXiv: hep-ex/0406035 [hep-ex].

[38] K. Abe et al. "Precise Measurement of the Neutrino Mixing Parameter θ_{23} from Muon Neutrino Disappearance in an Off-Axis Beam." In: *Phys. Rev. Lett.* 112.18 (2014), p. 181801. DOI: 10.1103/PhysRevLett.112.181801. arXiv: 1403.1532 [hep-ex].

[39] Feng Peng An et al. "Measurement of electron antineutrino oscillation based on 1230 days of operation of the Daya Bay experiment." In: *Phys. Rev.* D95.7 (2017), p. 072006. DOI: 10.1103/PhysRevD.95.072006. arXiv: 1610.04802 [hep-ex].

[40] A. A. Aguilar-Arevalo et al. "First measurement of the muon antineutrino double-differential charged-current quasielastic cross section." In: *Phys. Rev.* D88.3 (2013), p. 032001. DOI: 10.1103/PhysRevD.88.032001. arXiv: 1301.7067 [hep-ex].

[41] Jay N. Marx and David R. Nygren. "The Time Projection Chamber." In: *Phys. Today* 31N10 (1978), pp. 46–53. DOI: 10.1063/1.2994775.

[42] Georges Charpak, R. Bouclier, T. Bressani, J. Favier, and C. Zupancic. "The Use of Multiwire Proportional Counters to Select and Localize Charged Particles." In: *Nucl. Instrum. Meth.* 62 (1968), pp. 262–268. DOI: 10.1016/0029-554X(68)90371-6.

[43] C. Rubbia. "The Liquid Argon Time Projection Chamber: A New Concept for Neutrino Detectors." In: (1977).

[44] C. Thorn. "Properties of LAr." MicroBooNE Document Database. 2009.

[45] W. M. Haynes, ed. *Handbook of Chemistry and Physics*. 94th ed. CRC Press, 2013.

[46] B. L. Henson. "Mobility of Positive Ions in Liquefied Argon and Nitrogen." In: *Phys. Rev.* 135.4A (1964), pp. 1002–1008.

[47] G. F. Knoll. *Radiation Detection and Measurement*. 4th ed. Wiley, 2010.

[48] E. Aprile, A.E. Bolotnikov, A.I. Bolozdynya, and T. Doke. *Noble Gas Detectors*. Wiley, 2007. ISBN: 9783527609635.

[49] V. Chepel and H. Araújo. "Liquid noble gas detectors for low energy particle physics." In: *Journal of Instrumentation* 8.04 (2013).

[50] M.J. Berger, J.H. Hubbell, S.M. Seltzer, J. Chang, J.S. Coursey, R. Sukumar, D.S. Zucker, and K. Olsen. *XCOM: Photon Cross Section Database (version 1.5)*. 2018. DOI: https://dx.doi.org/10.18434/T48G6X. URL: http://physics.nist.gov/xcom.

[51] M. A. Hofmann. "Liquid Scintillators and Liquefied Rare Gases for Particle Detectors." PhD thesis. Technische Universität München, 2012.

[52] R. Acciarri et al. "Design and Construction of the MicroBooNE Detector." In: *JINST* 12.02 (2017), P02017. DOI: 10.1088/1748-0221/12/02/P02017. arXiv: 1612.05824 [physics.ins-det].

[53] C. Grupen and B. Shwartz. *Particle Detectors*. Cambridge Monographs on Particle Physics, Nuclear Physics and Cosmology. Cambridge University Press, 2008. ISBN: 9781139469531.

[54] H. A. Bethe. "Molière's Theory of Multiple Scattering." In: *Phys. Rev.* 89 (6 1953), pp. 1256–1266. DOI: 10.1103/PhysRev.89.1256. URL: https://link.aps.org/doi/10.1103/PhysRev.89.1256.

[55] L. Onsager. "Initial Recombination of Ions." In: *Phys. Rev.* 54 (8 1938), pp. 554–557. DOI: 10.1103/PhysRev.54.554. URL: https://link.aps.org/doi/10.1103/PhysRev.54.554.

[56] George Jaffé. "Zur Theorie der Ionisation in Kolonnen." In: *Annalen der Physik* 347.12 (), pp. 303–344. DOI: 10.1002/andp.19133471205. eprint: https://onlinelibrary.wiley.com/doi/pdf/10.1002/andp.19133471205. URL: https://onlinelibrary.wiley.com/doi/abs/10.1002/andp.19133471205.

[57] J. Thomas and D. A. Imel. "Recombination of electron-ion pairs in liquid argon and liquid xenon." In: *Phys. Rev. A* 36 (2 1987), pp. 614–616. DOI: 10.1103/PhysRevA.36.614. URL: https://link.aps.org/doi/10.1103/PhysRevA.36.614.

[58] Ulrich Sowada, John M. Warman, and Matthijs P. de Haas. "Hot-electron thermalization in solid and liquid argon, krypton, and xenon." In: *Phys. Rev. B* 25 (5 1982), pp. 3434–3437. DOI: 10.1103/PhysRevB.25.3434. URL: https://link.aps.org/doi/10.1103/PhysRevB.25.3434.

[59] R. Acciarri et al. "A study of electron recombination using highly ionizing particles in the ArgoNeuT Liquid Argon TPC." In: *JINST* 8 (2013), P08005. DOI: 10.1088/1748-0221/8/08/P08005.

[60] S. Amoruso et al. "Study of electron recombination in liquid argon with the ICARUS TPC." In: *Nucl. Instrum. Meth.* A523 (2004), pp. 275–286. DOI: 10.1016/j.nima.2003.11.423.

[61] J.B. Birks. *The theory and practice of scintillation counting*. International series of monographs on electronics and instrumentation. Macmillan, 1964.

[62] Akira Hitachi. "Exciton kinetics in condensed rare gases." In: *The Journal of Chemical Physics* 80.2 (1984), pp. 745–748. DOI: 10.1063/1.446781. eprint: https://doi.org/10.1063/1.446781. URL: https://doi.org/10.1063/1.446781.

[63] A Fedenev, A Morozov, R Kruescken, S Schoop, J Wieser, and A Ulrich. "Applications of a broadband electron-beam pumped XUV radiation source." In: *Journal of Physics D: Applied Physics* 37.11 (2004), p. 1586. URL: http://stacks.iop.org/0022-3727/37/i=11/a=013.

[64] Aharon Gedanken, Joshua Jortner, Baruch Raz, and Abraham Szoeke. "Electronic Energy Transfer Phenomena in Rare Gases." In: *The Journal of Chemical Physics* 57.8 (1972), pp. 3456–3469. DOI: http://dx.doi.org/10.1063/1.1678779. URL: http://scitation.aip.org/content/aip/journal/jcp/57/8/10.1063/1.1678779.

[65] Marlo Martin. "Exciton SelfTrapping in Rare Gas Crystals." In: *The Journal of Chemical Physics* 54.8 (1971), pp. 3289–3299. DOI: http://dx.doi.org/10.1063/1.1675342. URL: http://scitation.aip.org/content/aip/journal/jcp/54/8/10.1063/1.1675342.

[66] Robert S. Mulliken. "Potential Curves of Diatomic Rare Gas Molecules and Their Ions, with Particular Reference to Xe2." In: *The Journal of Chemical Physics* 52.10 (1970), pp. 5170–5180. DOI: http://dx.doi.org/10.1063/1.1672756. URL: http://scitation.aip.org/content/aip/journal/jcp/52/10/10.1063/1.1672756.

[67] Shinzou Kubota, Masahiko Hishida, Masayo Suzuki, and Jian-zhi Ruan(Gen). "Dynamical behavior of free electrons in the recombination process in liquid argon, krypton, and xenon." In: *Phys. Rev. B* 20 (8 1979), pp. 3486–3496. DOI: 10.1103/PhysRevB.20.3486. URL: http://link.aps.org/doi/10.1103/PhysRevB.20.3486.

[68] E. Morikawa, R. Reininger, P. Guertler, V. Saile, and P. Laporte. "Argon, krypton, and xenon excimer luminescence: From the dilute gas to the condensed phase." In: *The Journal of Chemical Physics* 91.3 (1989), pp. 1469–1477. DOI: http://dx.doi.org/10.1063/1.457108. URL: http://scitation.aip.org/content/aip/journal/jcp/91/3/10.1063/1.457108.

[69] Akira Hitachi, Tan Takahashi, Nobutaka Funayama, Kimiaki Masuda, Jun Kikuchi, and Tadayoshi Doke. "Effect of ionization density on the time dependence of luminescence from liquid argon and xenon." In: *Phys. Rev. B* 27 (9 1983), pp. 5279–5285. DOI: 10.1103/PhysRevB.27.5279. URL: http://link.aps.org/doi/10.1103/PhysRevB.27.5279.

[70] L. S. Miller, S. Howe, and W. E. Spear. "Charge Transport in Solid and Liquid Ar, Kr, and Xe." In: *Phys. Rev.* 166 (3 1968), pp. 871–878. DOI: 10.1103/PhysRev.166.871. URL: https://link.aps.org/doi/10.1103/PhysRev.166.871.

[71] W. Walkowiak. "Drift velocity of free electrons in liquid argon." In: *Nuclear Instruments and Methods in Physics Research Section A: Accelerators, Spectrometers, Detectors and Associated Equipment* 449.1 (2000), pp. 288 –294. ISSN: 0168-9002. DOI: https://doi.org/10.1016/S0168-9002(99)01301-7. URL: http://www.sciencedirect.com/science/article/pii/S0168900299013017.

[72] E. Buckley et al. "A study of ionization electrons drifting over large distances in liquid argon." In: *Nuclear Instruments and Methods in Physics Research Section A: Accelerators, Spectrometers, Detectors and Associated Equipment* 275.2 (1989), pp. 364 –372. ISSN: 0168-9002. DOI: https://doi.org/10.1016/0168-9002(89)90710-9. URL: http://www.sciencedirect.com/science/article/pii/0168900289907109.

[73] O. Bunemann, T. E. Cranshaw, and J. A. Harvey. "Design of grid ionization chambers." In: *Canadian Journal Research* 27a.5 (1949), pp. 191–206.

[74] V. Radeka et al. "Cold electronics for "Giant" Liquid Argon Time Projection Chambers." In: *Journal of Physics: Conference Series* 308.1 (2011).

[75] S. van der Meer. "A Directive Device for Charged Particles and Its use in an Enhanced Neutrino Beam." In: (1961).

[76] I. Stancu et al. "Technical Design Report for the 8 GeV Beam." In: (2001). DOI: 10.2172/1212167.

[77] Aguilar-Arevalo et al. "Neutrino flux prediction at MiniBooNE." In: *Phys. Rev. D* 79 (7 2009), p. 072002. DOI: 10.1103/PhysRevD.79.072002. URL: https://link.aps.org/doi/10.1103/PhysRevD.79.072002.

[78] M. Antonello et al. "A Proposal for a Three Detector Short-Baseline Neutrino Oscillation Program in the Fermilab Booster Neutrino Beam." In: (2015). arXiv: 1503.01520 [physics.ins-det].

[79] G. Carugno, B. Dainese, F. Pietropaolo, and F. Ptohos. "Electron lifetime detector for liquid argon." In: *Nuclear Instruments and Methods in Physics Research Section A: Accelerators, Spectrometers, Detectors and Associated Equipment* 292.3 (1990), pp. 580 –584. ISSN: 0168-9002. DOI: https://doi.org/10.1016/0168-9002(90)90176-7. URL: http://www.sciencedirect.com/science/article/pii/0168900290901767.

[80] H Chen, K Chen, G De Geronimo, F Lanni, D Lissauer, D Makowiecki, V Radeka, S Rescia, C Thorn, and B Yu. "Readout electronics for the MicroBooNE LAr TPC, with CMOS front end at 89K." In: *Journal of Instrumentation* 7.12 (2012), p. C12004. URL: http://stacks.iop.org/1748-0221/7/i=12/a=C12004.

[81] A Lebedev. "A laser calibration system for the STAR TPC." In: *Nucl. Instrum. Methods Phys. Res., A* 478.1-2 (2002), pp. 163–165.

[82] G. Renault, B.S. Nielsen, J. Westergaard, and J.J. GaardhOJe. "The Laser of the ALICE Time Projection Chamber." In: *Int.J.Mod.Phys.* E16 (2007), pp. 2413–2418. DOI: 10.1142/S0218301307008021. arXiv: nucl-ex/0703042 [NUCL-EX].

[83] Dariusz Miskowiec and Peter Braun-Munzinger. "Laser calibration system for the CERES Time Projection Chamber." In: *Nucl.Instrum.Meth.* A593 (2008), pp. 188–202. DOI: 10.1016/j.nima.2008.02.034. arXiv: 0801.4920 [nucl-ex].

[84] N.B. Delone and V.P. Krainov. *Multiphoton Processes in Atoms: Second Edition*. Atoms and plasmas. Springer, 2000. ISBN: 9783540646150.

[85] F.H.M. Faisal. *Theory of Multiphoton Processes*. Physics of Atoms and Molecules. Springer US, 1987. ISBN: 9780306423178.

[86] Claire McKenna and Hugo W van der Hart. "Multiphoton ionization cross sections of neon and argon." In: *Journal of Physics B: Atomic, Molecular and Optical Physics* 37.2 (2004), p. 457. URL: http://stacks.iop.org/0953-4075/37/i=2/a=013.

[87] N. Schwentner, E.E. Koch, and J. Jortner. *Electronic Excitations in Condensed Rare Gases*. Springer Tracts in Modern Physics. Springer Berlin Heidelberg, 2014. ISBN: 9783662152201.

[88] W. Tauchert and Werner F. Schmidt. "Energy of the Quasi-free Electron State in Liquid Argon, Krypton, and Xenon." In: *Zeitschrift für Naturforschung A* 30a (8 1975), pp. 1085–1087.

[89] W. Schmidt. *Liquid State Electronics of Insulating Liquids*. Taylor & Francis, 1997. ISBN: 9780849344459.

[90] I Badhrees et al. "Measurement of the two-photon absorption cross-section of liquid argon with a time projection chamber." In: *New Journal of Physics* 12.11 (2010), p. 113024. URL: http://stacks.iop.org/1367-2630/12/i=11/a=113024.

[91] W. F. Schmidt. "Electronic Conduction Processes in Dielectric Liquids." In: *IEEE Transactions on Electrical Insulation* EI-19.5 (1984), pp. 389–418. ISSN: 0018-9367. DOI: 10.1109/TEI.1984.298767.

[92] J. Abele et al. "The laser system for the STAR time projection chamber." In: *Nucl. Instrum. Meth.* A499 (2003), pp. 692–702. DOI: 10.1016/S0168-9002(02)01966-6.

[93] J. Sun, D. Cao, and J. Dimmock. "Investigating laser-induced ionization of purified liquid argon in a time projection chamber." In: *Nuclear Instruments and Methods in Physics Research Section A: Accelerators, Spectrometers, Detectors and Associated Equipment* 370.2-3 (1996), pp. 372 –376. ISSN: 0168-9002. DOI: http://dx.doi.org/10.1016/0168-9002(95)00822-5. URL: http://www.sciencedirect.com/science/article/pii/0168900295008225.

[94] A Ereditato, C C Hsu, S Janos, I Kreslo, M Messina, C Rudolf von Rohr, B Rossi, T Strauss, M S Weber, and M Zeller. "Design and operation of ARGONTUBE: a 5 m long drift liquid argon TPC." In: *Journal of Instrumentation* 8.07 (2013), P07002. URL: http://stacks.iop.org/1748-0221/8/i=07/a=P07002.

[95] A. Ereditato, D. Goeldi, S. Janos, I. Kreslo, M. Luethi, C. Rudolf von Rohr, M. Schenk, T. Strauss, M. S. Weber, and M. Zeller. "Measurement of the drift field in the ARGONTUBE LAr TPC with 266 nm pulsed laser beams." In: *Journal of Instrumentation* 9.11 (2014), P11010. URL: http://stacks.iop.org/1748-0221/9/i=11/a=P11010.

[96] A. Ereditato, D. Goeldi, S. Janos, I. Kreslo, M. Luethi, C. Rudolf von Rohr, M. Schenk, T. Strauss, M.S. Weber, and M. Zeller. "Performance of cryogenic charge readout electronics with the ARGONTUBE LAr TPC." In: *Journal of Instrumentation* 9.11 (2014), P11022. URL: http://stacks.iop.org/1748-0221/9/i=11/a=P11022.

[97] J. E. Sansonetti and W. C. Martin. "Handbook of Basic Atomic Spectroscopic Data." In: *Journal of Physical and Chemical Reference Data* 34.4 (2005), pp. 1559–2259. DOI: 10.1063/1.1800011.

[98] LV Keldysh et al. "Ionization in the field of a strong electromagnetic wave." In: *Sov. Phys. JETP* 20.5 (1965), pp. 1307–1314.

[99] R. Paschotta. *Encyclopedia of Laser Physics and Technology*. John Wiley & Sons, 2008. ISBN: 9783527408283.

[100] J. J. Degnan. "Optimization of passively Q-switched lasers." In: *IEEE Journal of Quantum Electronics* 31.11 (1995), pp. 1890–1901. ISSN: 0018-9197. DOI: 10.1109/3.469267.

[101] *IEC 60825-1:2014: Safety of laser products - Part 1: Equipment classification and requirements*. 2014.

[102] Eric Jones, Travis Oliphant, Pearu Peterson, et al. *SciPy: Open source scientific tools for Python*. [Online; accessed ¡today¿]. 2001–. URL: http://www.scipy.org/.

[103] Peter K.F. Grieder. "Chapter 1 - Cosmic Ray Properties, Relations and Definitions." In: *Cosmic Rays at Earth*. Ed. by Peter K.F. Grieder. Amsterdam: Elsevier, 2001, pp. 1 –53. ISBN: 978-0-444-50710-5. DOI: https://doi.org/10.1016/B978-044450710-5/50003-8. URL: http://www.sciencedirect.com/science/article/pii/B9780444507105500038.

[104] J. Kempa and I.MM. Brancus. "Zenith angle distributions of cosmic ray muons." In: *Nuclear Physics B - Proceedings Supplements* 122 (2003). Proceedings of the 12th International Symposium on Very High Energy Cosmic Ray Interactions, pp. 279 –281. ISSN: 0920-5632. DOI: https://doi.org/10.1016/S0920-5632(03)80398-5. URL: http://www.sciencedirect.com/science/article/pii/S0920563203803985.

[105] T.K. Gaisser. *Cosmic Rays and Particle Physics*. Cambridge University Press, 1990. ISBN: 9780521339315.

[106] Mengyun Guan, Jun Cao, Changgen Yang, Yaxuan Sun, and Kam-Biu Luk. "Muon simulation at the Daya Bay site." In: (2006).

[107] U.S. Geological Survey. *3DEP 1/3 arc-second*. 2018. URL: https://www.usgs.gov/core-science-systems/ngp/3dep.

[108] Hans Jostlein and Kirk T. McDonald. "Path Length of Muons Traversing an Arbitrary Volume." 2016. URL: http://puhep1.princeton.edu/~mcdonald/examples/muonpath.pdf.

[109] S. Palestini et al. "Space charge in ionization detectors and the NA48 electromagnetic calorimeter." In: *Nuclear Instruments and Methods in Physics Research Section A: Accelerators, Spectrometers, Detectors and Associated Equipment* 421.1 (1999), pp. 75 –89. ISSN: 0168-9002. DOI: https://doi.org/10.1016/S0168-9002(98)01193-0. URL: http://www.sciencedirect.com/science/article/pii/S0168900298011930.

[110] COMSOL Inc. *COMSOL Multiphysics Reference Manual version 5.3*. 2017. URL: www.comsol.com.

[111] Ruth Pordes and Erica Snider. "The Liquid Argon Software Toolkit (LArSoft): Goals, Status and Plan." In: *PoS* ICHEP2016 (2016), p. 182. DOI: 10.22323/1.282.0182.

[112] MicroBooNE Collaboration. *Reconstruction Performance Studies with MicroBooNE Data in Support of Summer 2018 Analyses*. 2018.

[113] C. Adams et al. "A Deep Neural Network for Pixel-Level Electromagnetic Particle Identification in the MicroBooNE Liquid Argon Time Projection Chamber." In: (2018). arXiv: 1808.07269 [physics.ins-det].

[114] Xin Qian, Chao Zhang, Brett Viren, and Milind Diwan. "Three-dimensional Imaging for Large LArTPCs." In: *JINST* 13.05 (2018), P05032. DOI: 10.1088/1748-0221/13/05/P05032. arXiv: 1803.04850 [physics.ins-det].

[115] MicroBooNE Collaboration. "The Pandora multi-algorithm approach to automated pattern recognition of cosmic-ray muon and neutrino events in the MicroBooNE detector." In: *The European Physical Journal C* 78.1 (2018), p. 82. ISSN: 1434-6052. DOI: 10.1140/epjc/s10052-017-5481-6. URL: https://doi.org/10.1140/epjc/s10052-017-5481-6.

[116] J. Ruppert. "A Delaunay Refinement Algorithm for Quality 2-Dimensional Mesh Generation." In: *Journal of Algorithms* 18.3 (1995), pp. 548 –585. ISSN: 0196-6774. DOI: https://doi.org/10.1006/jagm.1995.1021. URL: http://www.sciencedirect.com/science/article/pii/S0196677485710218.

[117] Susan Hert and Michael Seel. "dD Convex Hulls and Delaunay Triangulations." In: *CGAL User and Reference Manual*. 4.13. CGAL Editorial Board, 2018. URL: https://doc.cgal.org/4.13/Manual/packages.html#PkgConvexHullDSummary.

[118] H. Locarek-Junge and C. Weihs. *Classification as a Tool for Research: Proceedings of the 11th IFCS Biennial Conference and 33rd Annual Conference of the Gesellschaft für Klassifikation e.V., Dresden, March 13-18, 2009*. Studies in Classification, Data Analysis, and Knowledge Organization. Springer Berlin Heidelberg, 2010. ISBN: 9783642107450.

[119] OpenMP Architecture Review Board. *OpenMP Application Program Interface Version 4.5*. 2017. URL: http://www.openmp.org/.

[120] S. Agostinelli et al. "Geant4—a simulation toolkit." In: *Nuclear Instruments and Methods in Physics Research Section A: Accelerators, Spectrometers, Detectors and Associated Equipment* 506.3 (2003), pp. 250 –303. ISSN: 0168-9002. DOI: https://doi.org/10.1016/S0168-9002(03)01368-8. URL: http://www.sciencedirect.com/science/article/pii/S0168900203013688.

[121] The MicroBooNE Collaboration. *Study of Space Charge Effects in MicroBooNE*. Tech. rep. MICROBOONE-NOTE-1018-PUB. 2016. URL: http://microboone.fnal.gov/wp-content/uploads/MICROBOONE-NOTE-1018-PUB.pdf.

[122] A. Ereditato, I. Kreslo, M. Lüthi, C. Rudolf von Rohr, M. Schenk, Thomas Strauss, M. Weber, and M. Zeller. "A steerable UV laser system for the calibration of liquid argon time projection chambers." In: *JINST* 9.11 (2014), T11007. DOI: 10.1088/1748-0221/9/11/T11007.

[123] Stephen Seltzer. *Stopping-Powers and Range Tables for Electrons, Protons, and Helium Ions, NIST Standard Reference Database 124*. eng. 1993. DOI: 10.18434/t4nc7p. URL: http://www.nist.gov/pml/data/star/index.cfm.

[124] C. Adams et al. "LAr1-ND: Testing Neutrino Anomalies with Multiple LArTPC Detectors at Fermilab." In: *Proceedings, 2013 Community Summer Study on the Future of U.S. Particle Physics: Snowmass on the Mississippi (CSS2013): Minneapolis, MN, USA, July 29-August 6, 2013*. 2013. eprint: 1309.7987.

[125] M. Antonello et al. "A Proposal for a Three Detector Short-Baseline Neutrino Oscillation Program in the Fermilab Booster Neutrino Beam." In: (2015). arXiv: 1503.01520 [physics.ins-det].

[126] B. Abi et al. "The DUNE Far Detector Interim Design Report Volume 1: Physics, Technology and Strategies." In: (2018). eprint: 1807.10334.

ACKNOWLEDGEMENTS

Thanks to ...

... Igor Kreslo and Michele Weber for the opportunity to conduct this thesis and the constant support during the entire time of it's proceeding.

... Antonio Ereditato for welcoming me into the LHEP familiy.

... Jonathan Asaadi for being my external referee and Thomas Becher for chairing my doctoral defense.

... my office and lab companions Martin Auger, Yifan Chen, Sébastien Delaquis, Damian Göldi, Sabine Joos, David Lorca, Christoph Rudolf von Rohr, James Sinclair, Camilla Tognina and Marcel Zeller for exploring experimental physics and many other fun parts of life with me.

... everyone at LHEP for the always familiar atmosphere.

... my friends for keeping me sane.

... my parents, without their support, this would not have been possible.

... my son Kuno, for all the joy he brings to my life.

... my wife for her love, patience, and never ending support.

Thanks so much
for the wonderful gift.
I've always wanted an
apple corer.

Regards,
Joe Pommes

Declaration of Consent

on the basis of Article 30 of the RSL Phil.-nat. 18

Name, First Name:	Lüthi, Matthias
Matriculation Nr:	07-916-166
Study Program:	Physik Bachelor ☐ Master ☐ Dissertation ☒
Title of Thesis:	A Novel UV Laser System for Electric Field Calibration in Liquid Argon Time Projection Chambers
Supervisor:	Prof. Dr. Igor Kreslo Prof. Dr. Michele Weber

I declare herewith that this thesis is my own work and that I have not used any sources other than those stated. I have indicated the adoption of quotations as well as thoughts taken from other authors as such in the thesis. I am aware that the Senate pursuant to Article 36 paragraph 1 litera r of the University Act of 5 September, 1996 is authorized to revoke the title awarded on the basis of this thesis. For the purposes of evaluation and verification of compli-ance with the declaration of originality and the regulations governing plagiarism, I hereby grant the University of Bern the right to process my personal data and to perform the acts of use this requires, in particular, to reproduce the written thesis and to store it permanently in a database, and to use said database, or to make said database available, to enable comparison with future theses submitted by others.

Bern, 17.Januar 2019

Lüthi Matthias

CURRICULUM VITAE

Name:	Matthias Lüthi
Date of Birth:	8.February, 1986
2014 - 2018	Doctoral student under the supervision of Prof. Dr. Igor Kreslo and Prof. Dr. Michele Weber at the Laboratory for High Energy Physics of the University of Bern, Switzerland.
2012 - 2014	Master student under the supervision of Prof. Dr. Antonio Ereditato and Prof. Dr. Igor Kreslo at the Laboratory for High Energy Physics of the University of Bern, Switzerland.
2008 - 2012	Bachelor of Science in Physics at the University of Bern, Switzerland.
2006	Passerelle at Berner Maturitätsschule für Erwachsene
2001 - 2005	Professional Matura at the Berufsbildungszentrum Biel